

Effects of Turbulence on Aerofoils at High Incidence

by

Paterson John M^cKeough

Thesis submitted for the degree of Doctor of Philosophy in
the Faculty of Engineering, University of London.



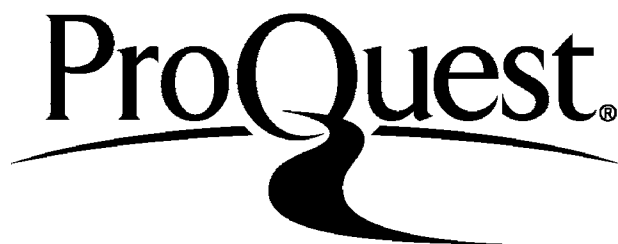
ProQuest Number: 10107314

All rights reserved

INFORMATION TO ALL USERS

The quality of this reproduction is dependent upon the quality of the copy submitted.

In the unlikely event that the author did not send a complete manuscript and there are missing pages, these will be noted. Also, if material had to be removed a note will indicate the deletion.



ProQuest 10107314

Published by ProQuest LLC(2016). Copyright of the Dissertation is held by the Author.

All rights reserved.

This work is protected against unauthorized copying under Title 17, United States Code
Microform Edition © ProQuest LLC.

ProQuest LLC
789 East Eisenhower Parkway
P.O. Box 1346
Ann Arbor, MI 48106-1346

ABSTRACT

Two effects of free stream turbulence on aerofoils at incidence were investigated:

(1) The mean loading effect. A survey of the literature dealing with the effects of turbulence on aerofoil mean loading and stalling was undertaken. This survey was supplemented by the results of an experiment in which three symmetric aerofoils, of different thicknesses, were tested in various turbulent flows. The effects of turbulence intensity and turbulence length scale were examined separately. For aerofoils with ultimate leadingedge stall, it was confirmed that the effect of turbulence on the maximum lift is approximately equivalent to the effect of increased Reynolds Number. The variation of this maximum lift with length scale was found to be greater than the $-1/5$ power law, suggested by a theory of G. I. Taylor.

(2) The unsteady loading effect. The higher order unsteady loads arising from the incidence of the aerofoil were investigated from both the theoretical and experimental viewpoints.

The higher order theory, which includes the effect of gust distortion by the mean flow field, was initially developed for a sinusoidal gust. This result was employed in two ways:

(a) It was applied directly to the problem of the periodic loading of turbomachine blades.

(b) It was used in the formulation, via Fourier analysis, of a higher order loading theory for an isotropic turbulent gust.

This latter theory predicts that the higher order admittance of lift (lift spectrum \div upwash spectrum) depends on the incidence, α , to the second power.

In the experiment, unsteady loads were measured on a rigid model at incidence α , and subjected to an approximately isotropic turbulent flow. The measured admittance of lift, due to incidence, was in reasonable agreement with the theoretical prediction.

ACKNOWLEDGEMENTS

This research was made possible by the personnel and technical resources of the Aeronautics Department, Imperial College, and by the sponsorship of the University of Queensland, Australia. The author is indebted to all concerned, particularly to:

- Mike Graham, whose supervision of the research was stimulating, helpful, and yet of a nature which allowed the author individual expression; and
- John Coles, the windtunnel technician, whose sense of humour remained intact, despite the author's attempt to demolish the 5' x 4' facility.

The thesis was written-up, in part, on Rasisaari, an island in a Finnish lake. The contributions of that island and of Älly, its other inhabitant, were not insignificant.

LIST OF CONTENTS

<u>Contents</u>	<u>Page Number</u>
CHAPTER 1. INTRODUCTION.	7
1.1 Effect of Turbulence on the Mean Loading of Aerofoils	7
1.2 The Unsteady Loading of Aerofoils	9
CHAPTER 2. LITERATURE SURVEY: MEAN LOADING.	26
2.1 The Laminar Separation Bubble	26
2.2 Types of Aerofoil Stall	28
2.3 Reynolds Number Effects on the Boundary Layer	32
2.4 Reynolds Number Effects on $C_{L_{max}}$ and $C_{D_{min}}$	35
2.5 Free Stream Turbulence Effects on the Boundary Layer	39
2.6 Free Stream Turbulence Effects on $C_{L_{max}}$ and $C_{D_{min}}$	41
2.7 Effects on the Flow about Bluff Bodies	45
2.8 Application of Taylor's Analysis to Aerofoils	50
2.9 Comparison with the Effects of Transition Wires	51
2.10 Separation on Aerofoils at High Speed	52
2.11 Summary	54
CHAPTER 3. THE MEAN LOAD EXPERIMENT.	56
3.1 The Aerofoils	56
3.2 The Turbulent Flows	58
3.3 Experimental Details	59
3.4 Results. Stall Type	65
3.5 Results. Mean Loading	69
3.6 Effective Reynolds Number	74
3.7 Conclusions Regarding the Mean Load Study	76

CHAPTER 4. THE UNSTEADY LOAD EXPERIMENT.	5.
4.1 Two Fundamental Design Decisions	78
4.2 The Aerofoil	82
4.3 The Turbulence	89
4.4 Signal Analysis	92
4.5 The Experimental Program	94
CHAPTER 5. FIRST ORDER TURBULENT LOADING.	95
5.1 The Experimental Admittance	95
5.2 Description of the Turbulence	97
5.3 The Theoretical Admittance to First Order	101
5.4 Comparison of Theory and Experiment	105
5.5 Results for the 3 inch Grid	108
5.6 Conclusions Regarding the First Order Turbulent Loading	109
CHAPTER 6. HIGHER ORDER THEORY FOR SINUSOIDAL GUST LOADING	110
6.1 General Assumptions	110
6.2 Method of Analysis	111
6.3 Theory for the Frozen Two-Dimensional Gust	113
6.4 Comparison with the Theory of Goldstein and Atassi	132
6.5 Conclusions Regarding the Higher Order Theory for a Frozen Two-Dimensional Gust	135
6.6 Extension to the Non-frozen Two-Dimensional Gust	136
6.7 Application to the Periodic Loading of Turbomachine Blades	137
6.8 Conclusions Regarding the Application to Turboblade Loading	143
6.9 Theory for the Frozen Three Dimensional Gust	144

	6.
CHAPTER 7. HIGHER ORDER TURBULENT LOADING	156
7.1 Higher Order Theory	156
7.2 Comparison of Experiment and Theory	163
7.3 Conclusions Regarding the Higher Order Turbulent Loading	169
CHAPTER 8. CONCLUDING COMMENTS.	171
LIST OF NOTATION	173
LIST OF REFERENCES	179
TABLES (4)	186
FIGURES (50)	190
PLATES (13)	240
APPENDICES	244
Appendix 1	244
Appendix 2	250
Appendix 3	252
Appendix 4	253
Appendix 5	259
Appendix 6	265
Appendix 7	271
Appendix 8	274
Appendix 9	275
Appendix 10	277
Appendix 11	280

CHAPTER 1. Introduction

In the flow of fluid about a body, an obvious effect of unsteadiness in the free stream is the production of unsteady aerodynamic forces on the body. A larger part of the present investigation deals with the unsteady loading of aerofoils at high angles of incidence to the mean flow. Although much theoretical and experimental attention has been devoted to the case of the thin aerofoil at zero mean incidence to the unsteady stream, the higher order effects due to incidence have been largely ignored. Two types of flow unsteadiness are dealt with in this study: the sinusoidal gust and the random turbulent gust, the two being related in that the former can be thought of as a Fourier component of the latter.

A further mean loading effect is produced as a result of the free stream unsteadiness interacting with the boundary layer on the body surface. This effect is particularly important for aerofoils at high incidence when boundary layer separation dominates the mean flow behaviour. In the present mean flow study, the type of free stream unsteadiness is restricted to random turbulence.

In both the unsteady-load study and the mean-load study, only two-dimensional aerofoils are considered; viz, unswept aerofoils of infinite aspect ratio.

1.1 Effect of Turbulence on the Mean Loading of Aerofoils.

In the early 1930's, some experiments were undertaken to determine the effects of free stream turbulence on the aerodynamic coefficients of aerofoils. Workers of that time were concerned with discrepancies between data from different wind tunnels, apparently attributable to differing levels of tunnel turbulence. The effects of turbulence were found to be significant, and all effort was made to

minimize this "background turbulence" level in later tunnels. Since this period, the specific problem of the effect of turbulence on the mean flow about aerofoils has been neglected. However there has been extensive work on the effects of free stream turbulence on boundary layers, directly, and on the flow about other body shapes (for example, Huffman, et. al. (1972), Bearman (1969)); and this work of course has relevance to the present problem.

1.1.2 Areas of renewed interest. Renewed interest in the effects of free stream turbulence on aerofoils has arisen in two areas:

(1) The design of new wind tunnels. The present generation of transonic wind tunnels is severely limited in Reynolds' Number capability. Furthermore, the effects of Reynolds Number on the transonic flow about aerofoils can be very significant, with the result that wind tunnel data may differ considerably from the full scale flight test data. New transonic tunnels with higher Reynolds Number capability are on the drawing boards. Achievement of the desired Reynolds Number by scale or by pressurization will result in a very expensive facility, so there is interest in methods of artificially increasing the Reynolds Number at transonic speeds. The high Reynolds Number simulation method which has been widely used in transonic testing in the past has been that which employs transition-tripping devices attached to the body surface. Yet free stream turbulence has often been observed to have an effect approximately equivalent to an increase in Reynolds Number; and so the introduction of turbulence has come under consideration as a possible method. So far, any definite conclusions regarding the suitability of this method have been precluded by the dearth of experimental information.

Transonic tunnels with ventilated walls have a higher level of background turbulence than their low speed counterparts. Thus there is a secondary interest in free stream turbulence effects in

relation to the design of new wind tunnels; viz, the effect of levels of turbulence normally encountered in transonic tunnels.

(2) The flow in turbomachinery cascades. Blades in turbomachines operate at high angles of attack in flows with a significant turbulence intensity. The aerodynamic characteristics of single blades and of cascades as a whole can be altered appreciably from their values in smooth flow.

1.1.3 The current investigation. It became apparent that the first requirement for a study of mean loading effects was a comprehensive literature review to identify the areas of inadequate knowledge. This review is presented, on a subject by subject basis, as Chapter 2 of the thesis. Subsequent to the review, an experiment was designed and undertaken with the aim of providing more conclusive information on the effect of turbulence on aerofoil mean loading. The details and results of the experiment comprise Chapter 3 of the thesis.

1.2 The Unsteady Loading of Aerofoils

Examples of situations to which an understanding of aerofoil gust loading can be usefully applied are:

- (1) the aeroplane wing in atmospheric turbulence ,
- (2) the compressor or turbine blade in the typically unsteady turbomachinery flow.

It is noteworthy that both the aeroplane wing and the turbo-blade are often at high incidence to the mean flow, the configuration on which attention is being focussed in this study. Atmospheric turbulence is best represented by a random turbulent gust; while flow fluctuations in a turbomachine have a broad band component (approximated by a random turbulent gust) and a narrow band, periodic component (approx-

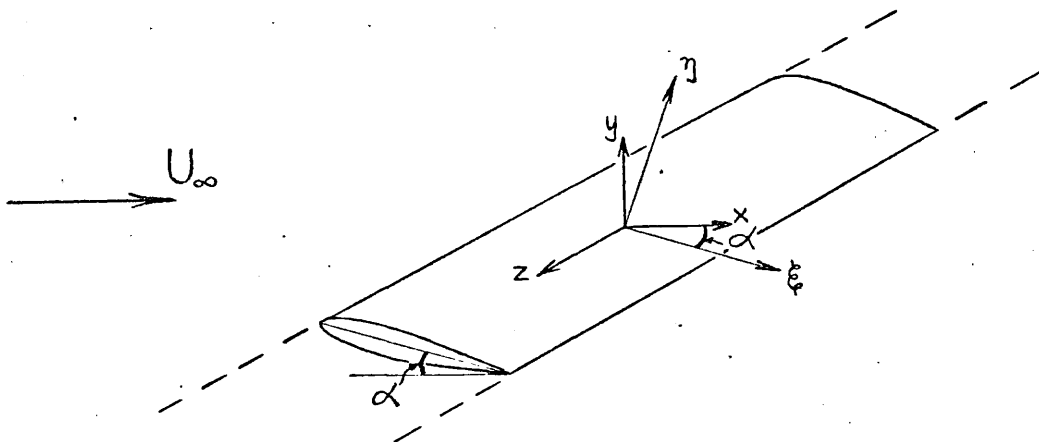
imated by a sinusoidal gust). In the theoretical analysis of gust loading, the cornerstone is the response to a general sinusoidal gust. This response can be used to determine the response to a known turbulent gust via the method of Fourier analysis.

1.2.1 Notation and definitions. Wavenumbers and distances which carry dimensions are written with overbars; for example, \bar{k}_1 and \bar{x} . In this report the following forms of non-dimensional wave-numbers and distances are widely employed: $k_1 = \bar{k}_1 c / 2$ and $x = \bar{x} 2 / c$ where c is the aerofoil chord length. Also the angular frequency and time are written as $\omega = \bar{\omega} c / 2$ and $t = \bar{t} 2 / c$ respectively, where $\bar{\omega}$ and \bar{t} carry the normal dimensions. (Note that ω and t are not dimensionless). Thus $\bar{k}_1 \bar{x} = k_1 x$, $\bar{\omega} \bar{t} = \omega t$, etc.

Two reference frames (with origin at the aerofoil midpoint) are employed:

- (1) stream-aligned co-ordinates : x, y, z .
- (2) aerofoil-aligned co-ordinates: ξ, η, z .

These co-ordinate systems are illustrated in the following sketch.



Components in the x, y and z directions are subscripted with $i = 1, 2,$ and 3 respectively.

A two-dimensional gust is here defined as one whose properties do not vary in the z -direction. There can be no component of gust velocity in this direction, and, further, this is the orientation of

the gust vorticity vector (although the gust may be irrotational). The more general three-dimensional gust has three components of both velocity and vorticity.

A frozen gust is defined as one in which there is variation of velocity in space but not in time (with respect to axes fixed in the fluid). An aerofoil translating this gust field with velocity, U_∞ , (or a stationary aerofoil onto which the gust is being convected at U_∞) "senses" a variation of velocity in time. For a sinusoidal gust of wavenumber, k_1 , in the x-direction, the frequency of this variation is given by: $\omega = k_1 U_\infty$. Although a truly frozen gust is not a practical possibility, the variation with time of many gusts found in practice is sufficiently slow for the assumption to be applied with good accuracy. G.I. Taylor first invoked this assumption, and in the literature it usually carries his name: Taylor's Hypothesis. If the gust is non-frozen, the aerofoil senses a different variation in time. An equivalent way of considering a non-frozen gust is as a frozen gust with a convection velocity which is not equal to the free-stream velocity, U_∞ . For the non-frozen sinusoidal gust considered in this way, the following two wavenumbers are introduced:

- (1) k_s , the spatial wavenumber in the x-direction.
- (2) k_f , defined by $\omega = k_f U_\infty$ where ω is the frequency sensed by the aerofoil.

The corresponding relative velocity between the gust and the aerofoil is then given by: $k_f/k_s \cdot U_\infty$.

The following quantities are used to denote orders of magnitude:

- (1) ϵ , the relative magnitude of the incident velocity fluctuations. For a sinusoidal gust, ϵU_∞ is defined to be equal to the amplitude; while, for a turbulent gust, it is equal to the r.m.s. of the fluctuating velocity in the x-direction. In this study it is assumed, throughout, that $\epsilon \ll 1$.

(2) α , the angle of incidence. Also, α is assumed $\ll 1$.

(3) k , the modulus of the wavenumber of a sinusoidal gust;

for example, for a three dimensional sinusoidal gust,

$$k = \sqrt{k_1^2 + k_2^2 + k_3^2} .$$

1.2.2 Order (ϵ) theories for sinusoidal gust loading. To formulate the response to this order, one need only consider a zero-thickness aerofoil at zero mean incidence, subjected to a gust whose velocity vector is in the y-direction; that is, an upwash gust (and then retain only first order terms in ϵ in the subsequent analysis). The unsteady theory retains the basic tenets of steady thin-aerofoil theory; for example, completely inviscid flow is assumed and the Kutta trailing-edge condition is satisfied at every instant.

The theory for the frozen two-dimensional gust was first developed by Sears (1941) using a conformal transformation method which was based on the earlier pioneering work of Wagner, Kussner, Theordorsen, and von Karman. Sears' result is summarized below:

The two-dimensional upwash gust is of the form:

$$\hat{v}_2 e^{i(\omega t - k_1 x)}$$

and $\omega = k_1 U_\infty$ (the frozen gust property).

Sears' result for the unsteady coefficient of lift, C_L , is:

$$C_L(t) = 2\pi \cdot S(k_1) \cdot \hat{v}_2 / U_\infty \cdot e^{i\omega t} , \quad \dots(1.1)$$

where Sears' response function, $S(k_1) = \frac{H_1(k_1)[J_0(k_1) - iJ_1(k_1)]}{H_1(k_1) + iH_0(k_1)} + iJ_1(k_1)$.

and the J's are Bessel Functions of the first kind and the H's are Haenkel Functions of the second kind.

In later years, the same result was obtained by directly solving the integral equation which arises from the boundary condition

on the aerofoil (for example, the solution presented by Bisplinghoff, et. al. (1955)). In Chapter 6 of the present dissertation, an analysis employing such a method is presented.

Jackson (1970) has measured the unsteady load on an aerofoil stationed near the wake of a cylindrical bluff body. The flow unsteadiness in this region approximated to a two-dimensional sinusoidal upwash gust; and Jackson found reasonable agreement between his measurement and the theoretical prediction of Sears.

Sears' theory can be simply extended for the case of a non-frozen two-dimensional gust. This extension was first reported by Kemp (1952) and the result is presented below:

- The gust is of the form:

$$\hat{v}_2 e^{i(\omega t - k_s x)} \quad \text{where} \quad \omega = k_f U_\infty .$$

The load response is:

$$C_L(t) = 2\pi \cdot S'(k_f, k_s) \cdot \hat{v}_2 / U_\infty \cdot e^{i\omega t} \quad \dots (1.2)$$

where the generalized Sears' function,

$$S'(k_f, k_s) = \frac{H_1(k_f) [J_0(k_s) - i J_1(k_s)]}{H_1(k_f) + i H_0(k_f)} + i \frac{k_f}{k_s} J_1(k_s) .$$

Kemp and Sears (1953, 1955) have theoretically analyzed the unsteady loading of turbomachine blades, produced by the interference of other blade rows. They considered the effect produced by:

- (1) relative motion between the mean flow fields of blades.
- (2) interference with vortex wakes from upstream rows.
- (3) interference with viscous wakes from upstream rows.

In each case it was possible to determine the effective unsteady upwash as a Fourier series with terms of the form $\hat{v}_2 e^{i(\omega t - k_s x)}$;

and, thus, the blade loading could be calculated using Kemp's result.

It should be stressed that the analysis of Kemp and Sears did not take

into account any effects which arise from the effective incidence of blades to the mean flow.

The order (ϵ) response for a three-dimensional sinusoidal gust can be formulated by analyzing the case of a yawed gust. This is an upwash gust with a two wavenumber dependence: k_1 in the chordwise direction and k_3 in the spanwise direction. Several workers have determined the response to a frozen yawed sinusoidal gust to various degrees of accuracy. Graham (1970) has formulated the problem using an exact unsteady lifting surface theory, and, with this formulation, he was able to calculate, numerically, the response function:

The yawed upwash gust is of the form:

$$\hat{v}_2 e^{i(\omega t - k_1 x - k_3 z)} \quad \text{with } \omega = k_1 U_\infty ,$$

and the load response is:

$$C_L(t, z) = 2\pi \cdot G(k_1, k_3) \cdot \frac{\hat{v}_2}{U_\infty} \cdot e^{i(\omega t - k_3 z)}$$

where $G(k_1, k_3)$ is the response function which Graham has calculated numerically.

Independently, Filotas (1969) derived an approximate closed form expression for $G(k_1, k_3)$. His theory also yielded an exact formula for the asymptote of $G(k_1, k_3)$ as $k_3 \rightarrow \infty$.

In the present notation this asymptote is given by

$$G_F(k_1, k_3) = \frac{2}{\pi} \frac{e^{-i(k_1 - \frac{1}{2} \tan^{-1} k_1/k_3)}}{\sqrt{k_1^2/\sqrt{k_1^2 + k_3^2} + 4k_3/\sqrt{k_1^2 + k_3^2}}} \dots (1.3)$$

Mugridge (1971) has derived an approximate analytical expression for

$$G(k_1, k_3) \quad \text{which is the correct asymptotic result for } k \rightarrow 0.$$

His analysis is a simple adjustment to that of Sears: it considers the effect of an additional (streamwise) component of vorticity in the wake. Mugridge's formula is re-derived, using a somewhat different approach, in Appendix 1. The formula is presented below in a form which is

useful for extension to other cases:

$$\begin{aligned}
 G_M(k_1, k_3) &= L(k_1, k_3) [J_0(k_1) - i J_1(k_1)] + i J_1(k_1) , \\
 \text{where } L(k_1, k_3) &= \frac{[1 + N(k_1, k_3)] J_1(k_1) - i Y_1(k_1)}{[1 + N(k_1, k_3)] [J_1(k_1) + i J_0(k_1)] + Y_0(k_1) - i Y_1(k_1)} , \\
 \text{and } N(k_1, k_3) &= \frac{k_3^2}{k_1 \sqrt{k_1^2 + k_3^2}} \cdot \left(1 - i \frac{2}{\pi} \log \left\{ \frac{k_1 + \sqrt{k_1^2 + k_3^2}}{k_3} \right\} \right) .
 \end{aligned}
 \quad \left. \vphantom{\begin{aligned} G_M(k_1, k_3) \\ \text{where } L(k_1, k_3) \\ \text{and } N(k_1, k_3) \end{aligned}} \right\} \cdot \cdot (1.4)$$

The theory for a non-frozen yawed gust follows simply upon the frozen gust analysis. When Graham's analysis is repeated for this case, it is found that, when the boundary condition is applied, terms arising from the gust depend on wavenumber, k_s , while those arising from the wake depend on k_f . $G'(k_f, k_s, k_3)$ can be calculated numerically with one simple alteration to Graham's program for the determination of $G(k_1, k_3)$. Similarly, the analysis of Mugridge can be generalized for the non-frozen gust. This generalization is also presented in Appendix 1 and the result is as follows:

The non-frozen yawed gust is:

$$\hat{v}_2 e^{i(\omega t - k_s x - k_3 z)} \quad \text{with } \omega = k_f U_\infty ,$$

and the load response is (with Mugridge's approximation):

$$C_L(t, z) = 2\pi G'_M(k_f, k_s, k_3) \cdot \frac{\hat{v}_2}{U_\infty} e^{i(\omega t - k_3 z)} , \quad \dots (1.5)$$

where

$$G'_M(k_f, k_s, k_3) = L(k_f, k_3) [J_0(k_s) - i J_1(k_s)] + i \frac{k_f}{k_s} J_1(k_s) ,$$

and the function, L , is defined above.

1.2.3 Order $(\alpha\epsilon)$ theories for sinusoidal gust loading. To formulate the response to this higher order in α , one must consider a zero-thickness aerofoil at mean incidence, α . Further complications are:

(1) components of gust velocity other than the upwash component (if they exist) can contribute to the load response to order $(\alpha\epsilon)$.

(2) if the gust has a wave-number dependence, k_2 , in the upwash direction, this can affect the load response to order $(\alpha\epsilon)$. (This dependence is irrelevant in the formulation of the order (ϵ) response because the aerofoil is at zero incidence to the mean stream)

(3) if the gust is rotational, it can be distorted by the mean flow field of the aerofoil. This effect is of order $(\alpha\epsilon)$.

Horlock (1968) first attempted to evaluate effect (1) for a two-dimensional gust. Later, Morfey (1970) presented a much simpler derivation of Horlock's result. Basically there are two additional load response terms (of order $(\alpha\epsilon)$) which arise from the gust component, \mathcal{U}_1 , parallel to the stream. The first is the obvious Sears-type response produced by the component of \mathcal{U}_1 which is perpendicular to the aerofoil chord. The second is a cross-product term involving \mathcal{U}_1 and the mean disturbance velocity field of the aerofoil (at incidence α). This term is not affected by a change in the relative velocity between the gust and the aerofoil; that is, it is the same for both frozen and non-frozen gusts. In the present notation, Morfey's result is:

the frozen two-dimensional gust considered by Morfey has components:

$$\hat{v}_1 e^{i(\omega t - k_1 x)}, \quad \hat{v}_2 e^{i(\omega t - k_1 x)} \quad \text{with} \quad \omega = k_1 U_\infty.$$

The load response is:

$$C_L(t) = C_{L_S} + C_{L_{A1}} + C_{L_M},$$

$$\left. \begin{aligned}
 \text{where } C_{L_S} &= 2\pi S(k_i) \frac{\hat{v}_2}{U_\infty} e^{i\omega t}, \text{ Sears' term, } O(\epsilon). \\
 C_{L_{A1}} &= \alpha 2\pi S(k_i) \frac{\hat{v}_1}{U_\infty} e^{i\omega t}, \text{ additional Sears' term, } O(\alpha\epsilon). \\
 C_{L_M} &= \alpha 2\pi M(k_i) \frac{\hat{v}_1}{U_\infty} e^{i\omega t}, \text{ Morfey's term, } O(\alpha\epsilon).
 \end{aligned} \right\} (1.6)$$

where

$$M(k_i) = J_0(k_i) + i J_1(k_i).$$

For the response to the corresponding non-frozen gust, $S'(k_f, k_s)$ replaces $S(k_i)$, and $M(k_s)$ replaces $M(k_i)$ in the above formulae.

Giesing (1968) has obtained a complete solution, numerically, for the case of an oscillating aerofoil in irrotational flow.

However this method, when applied to the problem of an aerofoil subjected to a sinusoidal gust, will not take account of all of the above-listed complications.

Very recently, Goldstein and Atassi (1975) have published a complete order $(\alpha\epsilon)$ analysis for the case of a frozen two-dimensional sinusoidal gust. Working independently, the author, as part of the present investigation, has developed a similar theory and extended it to encompass the following two cases:

- (1) the non-frozen two-dimensional gust ,
- (2) the frozen three-dimensional gust .

Further details of Goldstein and Atassi's work and a comparison with the author's analysis are given in Chapter 6.

Holmes (1971) has made measurements of the unsteady lift of an aerofoil at incidence in a stream with non-frozen transverse (v_2) and streamwise (v_1) periodic gusts. The gusts were irrotational and two dimensional, and the variation in the y direction was small; that is, $k_2 \approx 0$. As will be demonstrated in Chapter 6, when $k_2 = 0$ the higher order lift response is comprised of only the two terms derived by Morfey (equations (1.6)). Holmes found that the modulus of the higher order response due to incidence was reasonably well predicted by Morfey's theory.

1.2.4 Gust distortion by the mean field of the aerofoil. Consideration of this effect (denoted as "complication (3)" in the previous section) is necessary in any theory of gust loading which is complete to higher order in α .

1.2.4.1 General principles. Vorticity in a free stream (for example, a rotational gust) will be distorted by the mean flow field of a body placed in that stream. This is in addition to the "blocking effect" resulting from the satisfaction of the boundary condition on the body surface. The distortion effect can be readily visualized if vortex lines are used to represent the vorticity: the mean flow field of a body can stretch, skew, or convect (at different rates) the vortex lines.

Lighthill (1956) outlined a method for calculating the velocity field induced by a body placed in a stream containing "weak" vorticity. The vorticity is defined as being weak when the velocities associated with it are much less than the free stream velocity, U_∞ . In this case, the first order distortion effect is that produced by the irrotational flow field which satisfies the boundary condition for the free stream. This field is denoted by the vector, \underline{V}' . Lighthill's induced velocity field was comprised of four parts:

- (1) the flow field, \underline{V}' .
- (2) the irrotational flow field which satisfies the boundary condition for the free stream vorticity field (the blocking effect).
- (3) the Biot-Savart flow field resulting from the vorticity change due to distortion by (1).
- (4) the irrotational flow field which satisfies the boundary condition for flow field (3).

Clearly, the process can be carried on "ad infinitum", the order of the approximation increasing at each stage.

The distortion effect can be evaluated mathematically using

the vorticity transport equation, which, in turn is derived by taking the curl of the Navier-Stokes equation. For the calculation of the first order distortion effect (that is (3) above) for flows of high Reynolds Number the equation reduces to the following vector form:

$$\frac{\partial \underline{\zeta}^T}{\partial t} + (\underline{V} \cdot \nabla) \underline{\zeta}^T = (\underline{\zeta}^T \cdot \nabla) \underline{V} \quad \dots (1.7)$$

where $\underline{\zeta}^T$ is the vorticity vector, and $\underline{V} = \underline{U}_\infty + \underline{V}'$.

1.2.4.2 The rapid distortion of free stream turbulence. When equation (1.7) is applied to a random turbulent gust, the resultant theory is termed the "rapid distortion theory" and effectively assumes that each Fourier component of the turbulence is affected by the mean flow before it has time to exchange energy with other Fourier components or decay due to viscous action.

Hunt (1973) has rigorously determined the conditions under which equation (1.7) can be applied to turbulent flows external to a body:

$$(\text{ReNo})^{-1} \ll \epsilon \ll \min \left(\frac{L_1}{C}, 1 \right), \text{ and } (\text{ReNo})^{\frac{1}{2}} \gg \max \left(\frac{C}{L_1}, 1 \right).$$

where ϵ , here, is the turbulent intensity, $\frac{\sqrt{u_1'^2}}{U_\infty}$, and L_1 is the longitudinal integral length scale (a length scale of the energy-containing eddies).

If the Reynolds Number is large enough, as it often is in practice, the conditions reduce to:

$$\epsilon \ll \min \left(\frac{L_1}{C}, 1 \right)$$

The practical usefulness of the theory is limited when $\frac{L_1}{C} \ll 1$, as the allowable turbulence intensity, ϵ , is then very small.

1.2.4.3 Previous applications of the rapid distortion theory of turbulence. Ribner and Tucker (1953) and Batchelor and Proudman (1954) have analyzed the distortion of turbulence in its passage through a windtunnel contraction; and their results have since been corroborated by experiment. Considerable effort has also been devoted to the distortion of turbulence in simple shear flows.

Hunt (1973) has applied rapid distortion theory to the external flow about a circular cylinder. The complete general calculation was not computationally feasible, but certain asymptotes and other special cases were evaluated. Experiments by Bearman (1972) and Petty (1972) have supported certain of the main trends of the theory.

Graham (1975) has considered the distortion of a turbulent flow by the mean flow field of a porous plate (held perpendicular to the stream). Because the mean flow disturbance produced by the porous plate is relatively small (of the order of the resistance coefficient, K , of the plate), Graham was able to linearize the vorticity transport equation (equation (1.7)) and thus render the calculation tractable. He determined the theoretical effect of distortion on the spectrum of drag of the porous plate, and found this prediction to be in reasonable agreement with some experimental measurements.

1.2.4.4 Previous applications of distortion theory to sinusoidal gusts. In the theories of both Hunt and Graham, described above, the distortion of a single Fourier component (viz, a sinusoidal gust) is considered initially. Then Fourier Analysis is employed to establish the distortion effect for a general turbulent gust.

Goldstein and Atassi (1975) and the author specifically consider the distortion of a sinusoidal gust in their respective order ($\alpha \epsilon$) analyses of the sinusoidal gust loading of aerofoils. In a similar manner to Graham, a linearized version of the vorticity transport equation is employed; in this case linearized with respect to the small parameter, α , the angle of incidence of the aerofoil.

1.2.5 Formulation of the turbulence loading of aerofoils. When considering the turbulent loading of any body, it is convenient to calculate the ratio of the load spectrum to a velocity spectrum of the incident turbulence. This ratio is termed the admittance of the load. If the body reacts to the turbulence as a linear system, the admittance, at a particular frequency, will depend only on the length scale parameter, L/c . It is customary (for example, see Jackson (1970)) to define the admittance of the lift of an aerofoil as:

$$|A(k_1)|^2 = \left(\frac{U_\infty}{2\pi}\right)^2 \frac{\phi_{CL}(\bar{k}_1)}{\phi_{22}(\bar{k}_1)}, \quad \dots (1.8)$$

where $|A(k_1)|^2$ is the admittance,
 $\phi_{CL}(\bar{k}_1)$ is the spectrum of lift coefficient,
 $\phi_{22}(\bar{k}_1)$ is the spectrum of turbulent upwash,
 and $k_1 = \bar{\omega}c/2U_\infty$ is the reduced frequency.

1.2.5.1 Derivation of the admittance from the response function for a sinusoidal gust. This was first achieved by Liepmann (1955) for the particular case of the aerofoil. He used Sears result for the sinusoidal gust response, and thus assumed that each spanwise strip of the wing responds to the gust as if it were two-dimensional. This type of approximate formulation is known as "strip theory". The exact formulation will be based on the response to a general frozen three-dimensional sinusoidal gust.

The most direct derivation, pioneered by Ribner (1956), involves Fourier integrals. Roberts (1971) has rigorously derived the formula which specifies the load spectrum in terms of the response function for a general three-dimensional sinusoidal gust. This formula, as it applies to the unsteady lift of an aerofoil in turbulence, is presented below in tensor notation:

$$\phi_{CL}(\bar{k}_1) = \iint_{-\infty}^{\infty} \Omega_i^* \Omega_j \cdot \Phi_{ij}(\bar{k}) d\bar{k}_2 d\bar{k}_3, \quad \dots (1.9)$$

where (1) Ω_i is the response function for the i th component of the frozen sinusoidal gust; that is, if \hat{v}_i is the amplitude of this component:

$$C_L = \Omega_i \hat{v}_i e^{i\omega t} \dots (1.10)$$

(2) $\Phi_{ij}(\underline{k})$ is the three-dimensional wavenumber spectrum of the turbulence. In isotropic turbulence, $\Phi_{ij}(\underline{k})$ is a real function and $\Phi_{ij} = \Phi_{ji}$.

The corresponding formula for the admittance is then:

$$|A(k_1)|^2 = \left(\frac{U_\infty}{2\pi}\right)^2 \left(\frac{z}{c}\right)^2 \iint_{-\infty}^{\infty} \Omega_i^* \Omega_j T_{ij}(\underline{k}) \cdot dk_2 dk_3 \dots (1.11)$$

where $T_{ij}(\underline{k}) = \Phi_{ij}(\underline{k}) / \phi_{22}(\underline{k}_1)$ is the normalized three-dimensional spectrum.

It should be noted that Taylor's Hypothesis has been invoked in the derivation of (1.9): the spectrum formula has been established from the response function for a frozen sinusoidal gust. Thus the turbulence is considered to be a frozen pattern in space which is convected past the body by the free stream. A simplified derivation of equation (1.9) is provided in Appendix 2.

1.2.5.2 Admittance of lift to first order. This admittance can be formulated from the order (ϵ) three-dimensional sinusoidal gust response (and so the spectrum of lift is of order (ϵ^2)).

The sinusoidal gust in question is the frozen yawed upwash gust, and, as discussed in 1.2.2, the corresponding local lift response is:

$$C_L(t, z) = 2\pi \cdot G(k_1, k_3) \frac{\hat{v}_z}{U_\infty} \cdot e^{i(\omega t - k_3 z)}$$

For a section of the wing of span, $2b$:

$$\begin{aligned}
C_L(t) &= 2\pi \cdot G(k_1, k_3) \frac{\hat{v}_2}{U_\infty} \cdot e^{i\omega t} \cdot \frac{1}{2b} \int_{-b}^{+b} e^{-ik_3 z} d\bar{z} \\
&= 2\pi \cdot G(k_1, k_3) \cdot \frac{\sin k_3 a}{k_3 a} \cdot \frac{\hat{v}_2}{U_\infty} \cdot e^{i\omega t} \dots (1.12)
\end{aligned}$$

where a is the aspect ratio $= 2b/c$.

In the notation of equation (1.10):

$$\Omega_1 = \Omega_3 = 0, \quad \Omega_2 = \frac{2\pi}{U_\infty} \cdot G(k_1, k_3) \cdot \frac{\sin k_3 a}{k_3 a}, \text{ and}$$

Ω_2 is a function of k_1 and k_3 only.

Substituting into equation (1.11):

$$|A(k_1)|^2 = \frac{4}{c} \int_0^\infty |G(k_1, k_3)|^2 \cdot \frac{\sin^2 k_3 a}{(k_3 a)^2} \cdot \bar{S}_{22}(k_1, k_3) dk_3 \dots (1.13)$$

where $\bar{S}_{22}(k_1, k_3) = \tilde{\Phi}_{22}(\bar{k}_1, \bar{k}_3) / \phi_{22}(\bar{k}_1)$,

and $\tilde{\Phi}_{22}(\bar{k}_1, \bar{k}_3)$ is a two-dimensional upwash spectrum

which is related to the three-dimensional spectrum by:

$$\tilde{\Phi}_{22}(\bar{k}_1, \bar{k}_3) = \int_{-\infty}^{\infty} \Phi_{22}(\bar{k}) d\bar{k}_2$$

$\tilde{\Phi}_{22}(\bar{k}_1, \bar{k}_3)$, for isotropic turbulence, is an even function of \bar{k}_3 .

$\bar{S}_{22}(k_1, k_3)$ is the Fourier transform of a quantity which can be readily measured experimentally. This quantity is termed the normalized upwash cross-spectrum and is denoted here by $S_{22}(k_1, z)$. It is a frequency cross spectrum of the velocities at two points which are separated by a distance z , in the spanwise direction. The relationship between \bar{S}_{22} and S_{22} is:

$$\bar{S}_{22}(k_1, k_3) = \frac{1}{\pi} \int_0^\infty S_{22}(k_1, z) \cdot \cos k_3 z d\bar{z} \dots (1.14)$$

Jackson, Graham, and Maull (1973) have made a thorough comparison of this theoretical admittance with the admittance measured on an aerofoil mounted at zero incidence in a turbulent stream (The experiment was carried out by Jackson (1970)). To evaluate the theoretical admittance, $S_{22}(k_1, z)$ was measured and empirical curves were made to fit the data points. Formulae for $\overline{S}_{22}(k_1, k_3)$ were then derived by taking the Fourier transforms of the equations to these curves. Values of the theoretical admittance were obtained by a single numerical integration (equation (1.13) above). Using Graham's computation of $G(k_1, k_3)$ (refer to section 1.2.2), Jackson, et. al. found good agreement between theory and experiment for their particular case in which L_1/c was 0.42.

The approximate strip theory, already mentioned, assumes that the local lift response for a Fourier component of the turbulence is given by Sears' two-dimensional theory. Thus, with this approximation, $S(k_1)$ replaces $G(k_1, k_3)$ in equation (1.13):

$$|A(k_1)|^2 = \frac{4}{c} S(k_1)^2 \cdot \int_0^{\infty} \frac{\sin^2 k_3 a}{(k_3 a)^2} \overline{S}_{22}(k_1, k_3) dk_3 \quad \dots (1.15)$$

Hakkinen and Richardson (1957) have made measurements on a small aspect ratio aerofoil element to test strip theory, but their results were inconclusive. Jackson, et. al. have shown that strip theory overestimates the admittance when L_1 is of order c . However, as they have indicated, the discrepancy will become less as L_1/c increases; and thus strip theory will be useful in many practical situations where $L_1 \gg c$.

1.2.5.3 Admittance of lift to higher order in α . To the knowledge of the author there have been no previous measurements of the admittance of lift on an aerofoil at incidence α . Nor has there been any attempt to extend the theory to higher orders in α . Both of these aspects are dealt with in the present investigation.

1.2.6 The current investigation. The unsteady-load investigation

was undertaken with the aim of providing more information on the effect of incidence on the gust loading of two-dimensional aerofoils.

The approach used by Graham in his porous plate study was adopted for the theoretical analysis; that is, initially, the theory for sinusoidal gust loading was developed and, subsequently, it was extended to predict the loading induced by a random turbulent gust. This approach is particularly worthwhile for the aerofoil, as the intermediate results for sinusoidal gusts are directly relevant to some practical situations.

The theory for the turbulent gust was tested by an experiment similar to that of Jackson, but modified to allow measurements on the aerofoil at various angles of incidence to the mean flow. Some effort was directed at the ratification of the conclusions of Jackson, Graham and Maull for the aerofoil at zero incidence.

The chapter format for the unsteady load investigation is as follows:

Chapter 4: The experimental equipment, methods of measurement and analysis, and the experimental program are described.

Chapter 5: A comparison between the zero incidence experimental results and the established first order theory is presented.

Chapter 6: A second order theory for sinusoidal gust loading is developed. The frozen two-dimensional gust is considered first, and then the theory is extended in two directions:

(1) to the case of the non-frozen two-dimensional gust.

This result is applied to the problem of turboblade loading.

(2) to the case of the frozen three-dimensional gust.

Chapter 7: With the three-dimensional gust result of Chapter 6, a theory for turbulent loading to higher order in α is established. Finally a comparison is made between the theoretical and the experimental admittances of lift for an aerofoil at mean incidence, α , in a turbulent stream.

CHAPTER 2. Literature Survey: Mean Loading

In this survey, Reynolds Number and turbulence effects on various flows are reviewed, with the hope of establishing as complete a picture as possible of the likely effects of free stream turbulence on the aerodynamic coefficients of aerofoils. Also, the areas of current interest are expanded upon.

The following abbreviations are widely used:

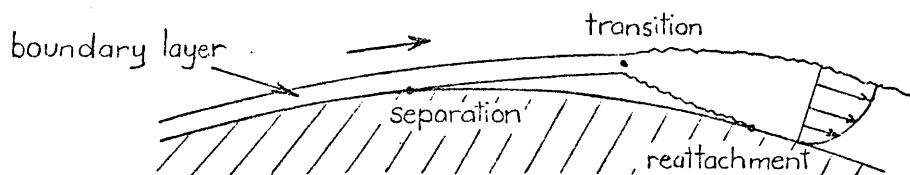
Re No. : Reynolds Number.

FST : free stream turbulence.

2.1 The Laminar Separation Bubble.

This bubble exists on various bodies in a particular broad Re No. range. For example, it is found on most round-nosed aerofoils at moderate incidence and at Re Nos. of practical interest. Aerofoil stall development can be critically dependent on the behaviour of a laminar separation bubble. Tani (1964) has compiled a comprehensive review of this subject.

2.1.1 General description. The bubble is formed as follows. The laminar boundary layer separates just downstream of the suction peak where the pressure gradient is strongly adverse. The separated laminar shear layer becomes quickly turbulent, and the subsequent expanding turbulent layer reattaches a short distance downstream. A typical bubble length, l , is $0.01c$ (c is the aerofoil chord length) on an aerofoil at a Re No. of the order of 10^6 . However, a better parameter, which covers a very wide range of Re No., is l/δ_{2s} where δ_{2s} is the boundary layer momentum thickness at separation. For a laminar separation bubble, l/δ_{2s} is of the order of 10^2 .



2.1.2 Observed bubble properties. Experimental investigation of the bubble has been extensive (for example, Gault (1955)). Pertinent properties of the bubble as observed on an aerofoil are:

(a) For a given incidence, the position of laminar separation is independent of Re No.. This is in accordance with laminar boundary layer theory.

(b) For a given Re No., the position of laminar separation moves upstream as the incidence increases. The bubble length decreases; and eventually the situation is reached where the turbulent shear layer fails to reattach. This phenomenon is known as "bubble bursting" or "nose stall".

(c) For a given incidence, the transition position is very dependent on Re No.. The length of separated laminar flow decreases with increase in Re No..

(d) Typically, the separated laminar flow length is 0.75 to 0.80 of the total bubble length. The pressure in the bubble is fairly constant beneath the separated laminar layer, but rises noticeably beneath the attaching turbulent layer.

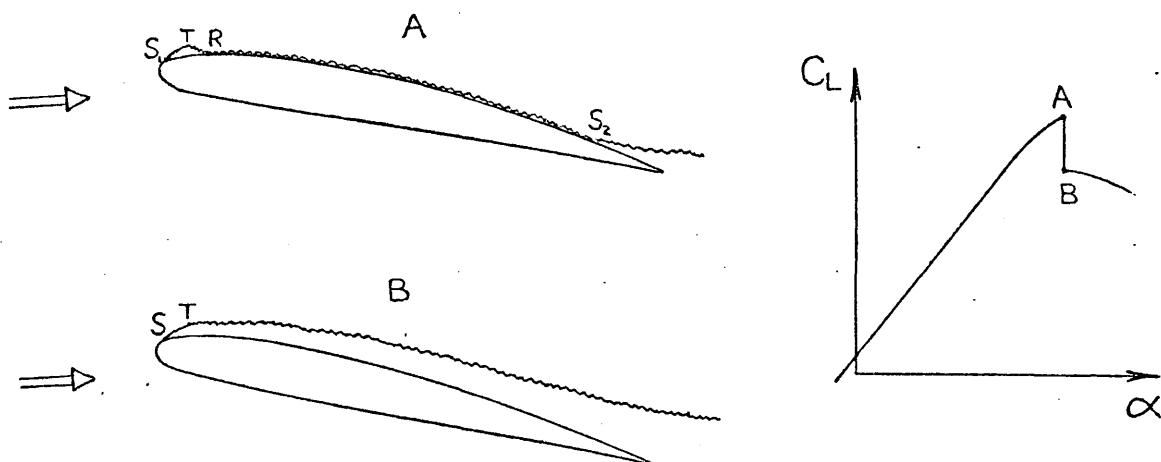
2.1.3. Criterion for bubble bursting. The earlier attempts to establish such a semi-empirical criterion (for example Tani (1939), Owen and Klanfer (1955), and Crabtree (1957)) were based on the assumption that, at some critical boundary layer Re No., there occurred a discontinuity in the movement of the transition position. Recent experimental evidence has been against the occurrence of any such discontinuity. Woodward, a

colleague of Horton (1969), found that transition in the separated laminar shear layer occurred in approximately the same position before and after bursting and he suggested that bursting occurs simply as a result of the sudden failure of the turbulent re-attachment. Horton has lent weight to Woodward's case with a semi-empirical analysis in which he assumed that the transition position varies smoothly with change in boundary-layer Re No.

2.2 Types of Aerofoil Stall. Low speed, 2 Dimensional

The early identification of stall types was carried out by Jones (1934) and in more detail, by McCullough and Gault (1951). McCullough (1955) later demonstrated the close relationship between the leading edge and thin-aerofoil stall.

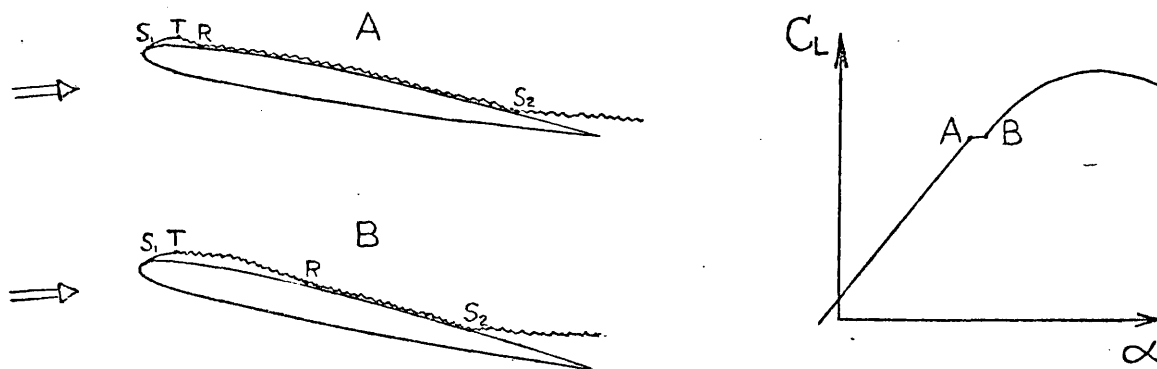
2.2.1 Leading edge (LE) stall. In this stall the maximum lift occurs just prior to bubble bursting, after which the separated shear layer remains clear of the aerofoil surface. The upper surface pressure distribution is altered considerably by a complete collapse of the suction peak; and the aerofoil experiences a sudden loss of lift.



2.2.2 Thin-aerofoil (TA) stall. After bubble bursting the separated shear layer re-attaches again further downstream. As was discussed in Section 2.1.3, the bubble bursts simply because the turbulent shear layer fails to reattach: the rate of turbulent layer expansion becomes insufficient in the steepening pressure gradient. For the thin sections which exhibit TA stall, bubble bursting occurs at a relatively low angle of incidence; and this, in turn, means that the pressure gradient further downstream is conducive to reattachment. The region so enclosed is termed a "long bubble". There is significant re-circulation in the region, and its initial length for an aerofoil at a Re No. of about 10^6 is typically $0.1c$. l/δ_{2S} is of the order of 10^4 .

The upper surface pressure distribution is altered: the suction peak becomes flatter and broader. There is little or no loss of lift, although a kink may be evident in the C_L vs. α curve.

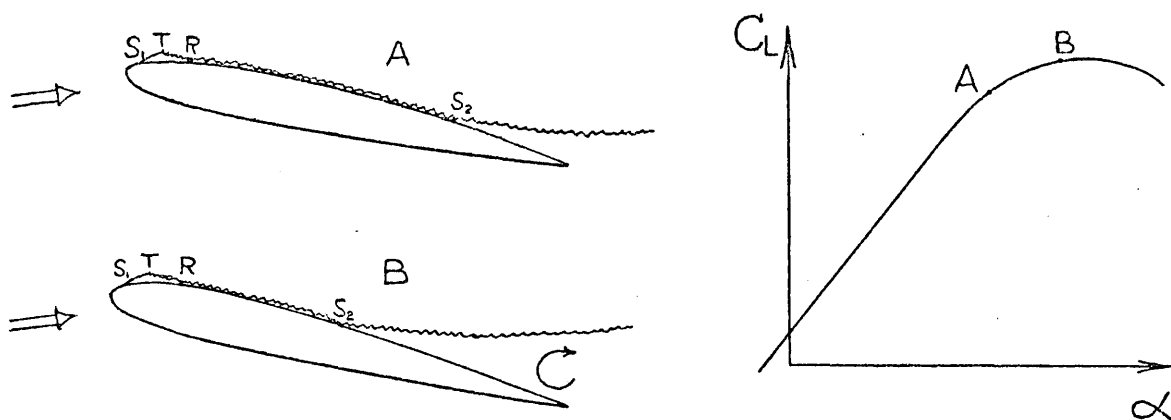
The bubble bursting occurs below C_L max. As the incidence is further increased the long bubble grows in extent, and at C_L max, it typically covers most of the aerofoil upper surface.



2.2.3 Trailing edge (TE) stall. In this stall, significant separation of the turbulent boundary layer occurs before any bubble bursting. As the incidence is increased, the separation point moves progressively forward from the trailing edge. There is no sudden flow change.

Certainly, in some cases, the transition point is ahead of the position where the laminar boundary layer would otherwise have separated; that is, natural transition without the existence of a laminar separation bubble. But, in other cases, the bubble is present as normal, yet it does not play an active role in the stall development.

Typically, at C_L max, the separation point has reached at least the mid-chord position.



2.2.4 Other stall types.

(a) A stall type found commonly in practice is one that has the features of both the leading edge and trailing edge types. As incidence increases, significant trailing edge separation occurs, but ultimately the laminar separation bubble bursts and there is a sudden loss of lift.

(b) "Reseparation" stall. This resembles the leading edge stall in many respects; but, instead of the laminar separation bubble bursting, the attached turbulent boundary layer separates suddenly a short distance downstream of the bubble. This stall type was first recognized by Wallis (1954), and analyzed in a semi-empirical way by Evans and Mort (1959).

2.2.5 Stall of turbo-machine blades. A turbo-machine blade can stall in any of the ways already described. The Re No. associated with a

turbo-blade flow is considerably less than that associated with an aeroplane wing flow, with the result that the laminar separation bubble tends to be much larger ($0.2c$ is a typical length). l/δ_{2s} is still of the order of 10^2 , as expected for a laminar separation bubble. These larger laminar separation bubbles can have an appreciable effect on the mean flow through turbo-machinery cascades.

2.2.6 Three dimensional effects in nominally two dimensional wind tunnel tests.

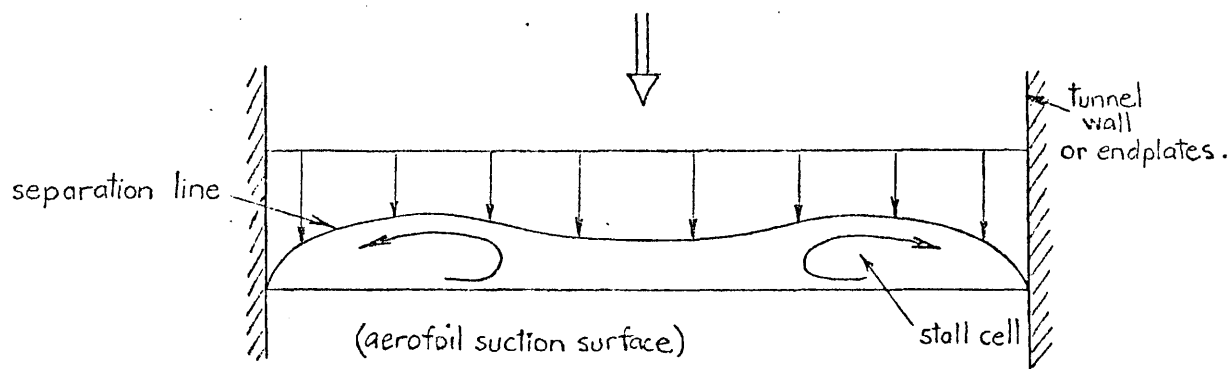
For many years, two dimensional stall development was assumed to occur on aerofoils which exhibited good two dimensional flow characteristics at lower incidences. Gregory, et. al. (1971) demonstrated that this assumption was far from correct, and identified three major problem areas:

- (1) Corner separations.
- (2) Three dimensional stall cells in separated flow regions near the trailing edge.
- (3) Three dimensional nose stall.

(1) The tunnel wall boundary layer causes a reduction in the circulation on the aerofoil near the wall, and this reduction can be sufficient to allow premature flow separation in the corner.

Corner separation can be avoided by normal methods of boundary layer control; for example, suction or blowing.

(2) Stall cells are regions of re-circulating flow in the plane of the aerofoil. They form, at incidences near that corresponding to maximum lift, in regions of separated flow which have developed from the trailing edge. The existence of such cells has been explained in terms of flow stability. Variation of lift in the spanwise direction leads to variation in upwash which can stabilize the variation in lift.



(3) When an aerofoil stalls via the bubble bursting mechanism, the initial stall tends to occur over only part of the span and generally in an asymmetric position. That the laminar bubble should break down initially at one particular spanwise location is not surprising, since the laminar bubble is very sensitive to local conditions. The explanation for the tendency of the breakdown to be confined to part-span follows that presented for the stall cells above. When part of the span stalls, lift is lost in that part and vorticity is shed into the wake. This vorticity induces a downwash on the still unstalled sections of the wing and this prevents the stalled region from spreading.

The stall cells and the three-dimensional nose stall have been observed on aerofoils with aspect ratios as high as 6. Obviously these effects will become more prominent when the aspect ratio is less. There appears to be no simple way of avoiding the development of such three dimensional effects in wind tunnel tests on aerofoils of moderate aspect ratio.

2.3 Reynolds Number Effects on the Boundary Layer

The Re No. can influence the position of transition and the development of the turbulent boundary layer, but it has no influence on the development of the laminar boundary layer.

In this discussion, three properties of the boundary layer will be considered; δ_2 , the momentum thickness; H , the shape

parameter; and C_f , the skin friction.

2.3.1 Effect on transition. Transition can occur either naturally on the aerofoil surface (natural transition) or via a laminar separation bubble (bubble transition). In either case, increasing the Re No. has the effect of causing earlier transition; that is, the transition position is moved upstream. This is in accordance with the theory of stability of laminar shear layers, and it has been confirmed experimentally. To first order, the effect can be thought of as a movement of the virtual origin of the turbulent boundary layer upstream (A more precise theory would have to include the altered pressure gradient effects) Thus, at a particular position on the body surface downstream of transition, the first order effect will be an increase in δ_2 of the turbulent boundary layer.

2.3.2 Effect on a wholly turbulent boundary layer. In zero pressure gradient, it is well-known that, at a particular position, δ_2 , H, and C_f are all decreased by an increase in Re No..

These trends remain approximately true in pressure gradients. Green (1973) has presented results of calculations for a turbulent boundary layer in a pressure gradient representative of the type which occurs on an aerofoil upper surface under high loading conditions. δ_2 and H were determined to be significantly reduced by an increase in Re No., particularly in the region of adverse pressure gradient.

2.3.3 Effect on a partly laminar, partly turbulent boundary layer on an aerofoil.

(a) Aerofoil at low incidence, such that the boundary layer is fully attached. It is the skin friction drag which is of prime interest here. From the foregoing, no definite conclusion regarding

the effect of Re No. can be made. The predominant contribution to the skin friction comes from the turbulent boundary layer. An increase in Re No. tends to decrease the C_f of the turbulent boundary layer, but the extent of the turbulent boundary layer is increased because of the movement upstream of the transition position. The C_f can be estimated quantitatively once a criterion for the position of transition has been established. A number of workers have attempted this for the case of a flat plate parallel to the stream. Prandtl (see Goldstein (1938)) developed a semi-empirical relationship between the C_f of a flat plate and the Re No., based on the assumption that transition occurs at a particular value of the Re No., $\frac{U_x}{\nu}$. He chose this particular value to fit some experimental data obtained by Gebers. The Prandtl-Gebers relationship for the overall C_D of a flat plate is presented in figure 4, and compared with the C_D curves for wholly laminar and wholly turbulent boundary layers on a flat plate.

(b) Separation of the turbulent boundary layer on an aerofoil at incidence. Separation depends on δ_2 and H: in simple terms, the likelihood of separation increases with increasing values of δ_2 and H. The precise dependence on δ_2 and H is very complicated. Again the effects of Re No. on transition and on turbulent boundary layer development produce opposing trends: the former increases δ_2 , while the latter decreases δ_2 and H. There is surprisingly little experimental evidence, presented in the literature, of the Re No. dependence of the separation of a partly laminar, partly turbulent boundary layer. Later, in section 2.4.3, some experimental load measurements are presented, from which it is possible to glean some information on the Re No. effects on turbulent boundary layer separation.

(c) Separation of the laminar boundary layer on an aerofoil at incidence (where "separation" refers to large-scale separation as opposed to separation within a laminar separation bubble). This

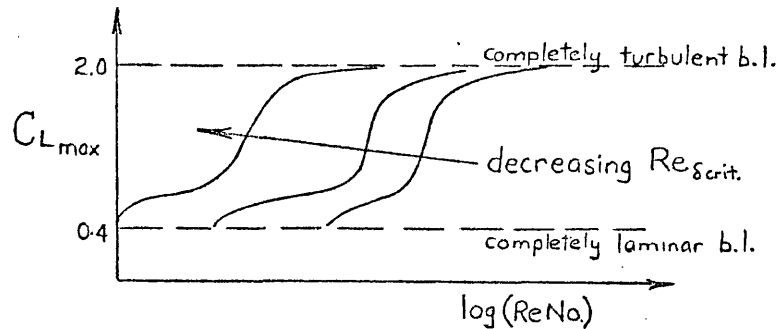
separation is controlled by transition and is very dependent on Re No.. When transition occurs naturally, laminar boundary layer separation is precluded when transition occurs upstream of the calculated laminar boundary layer separation position. Similarly, for bubble transition, the likelihood of bubble bursting is decreased the further upstream transition occurs. Thus, for both types of transition, an increase in Re No. allows the aerofoil to achieve a higher angle of incidence before laminar boundary layer separation (if at all).

2.4 Reynolds Number Effects on the C_{Lmax} and C_{Dmin} of Aerofoils

The stall type of a particular aerofoil can vary with Re No.. For example, at low Re No. the stall may be of the thin aerofoil type. As Re No. is increased bubble bursting is delayed until higher incidence and it is conceivable that the shear layer which separates near the nose may remain clear of the aerofoil surface: leading edge stall. And, at still higher Re Nos., bubble bursting may be delayed to such an extent that the separation of the turbulent boundary layer can dominate the stall: trailing edge stall or reattachment stall.

2.4.1 Leading edge stall (or the combined leading edge/trailing edge type). From the discussion in 2.3.3 it is clear that, for this stall type, C_{Lmax} will be very dependent on Re No., increasing with increasing Re No.. Von Karman and Millikan (1935) first attempted a theoretical prediction of the dependence of C_{Lmax} on Re No.. They assumed natural transition and ignored any separation of the turbulent boundary layer. The model was later improved by including the latter effect. Goldstein (1938) has presented the results of such calculations for an elliptic cylinder. The critical boundary layer Re No. for transition, $Re_{\delta_{crit}}$, was a parameter in these studies.

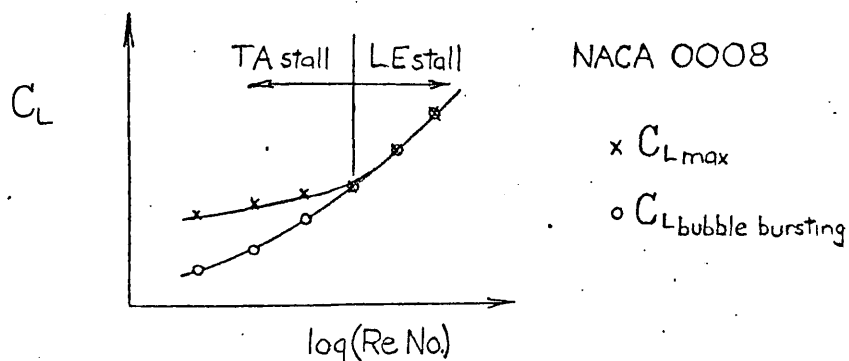
Goldstein's results are sketched below.



The high sensitivity of C_{Lmax} to $Re No.$, over a particular $Re No.$ range, is noteworthy. Some experimental results are presented in the next section.

2.4.2 Thin aerofoil stall. It is expected that the dependence of

C_{Lmax} on $Re No.$ will be less for the thin aerofoil stall than for the leading edge stall. The angle of incidence corresponding to bubble bursting will still be highly $Re No.$ dependent, but the maximum C_L is attained at a higher incidence when the long bubble extends over most of the aerofoil surface. It is expected that the angle of incidence corresponding to the latter condition will not be very sensitive to variation in $Re No.$. McCullough (1955) has experimentally confirmed these postulates. He has measured both the C_L corresponding to bubble bursting and the C_{Lmax} on a thin aerofoil over a wide range of $Re No.$. His results provide an excellent illustration of the relationship between the thin-aerofoil and leading edge stall types:



Further evidence of the small dependence of $C_{L\max}$ on Re No. for the thin aerofoil stall is given in Figure 1. These are experimental results of Stack (1931) for the very thin section, NACA 0006. This section most certainly has a thin aerofoil stall over this Re No. range, although Stack did not observe the stall types in his investigation.

2.4.3 Trailing edge stall. It was shown in Section 2.3.3 that there are opposing influences of Re No. on the separation of the turbulent boundary layer. It is known that trailing edge stall is exhibited by very thick sections at Re Nos. of the order of 10^6 . Some experimental results for $C_{L\max}$ for very thick sections have been reproduced in figures 2,3,6. Stack (1931) has made measurements on the NACA 0021, a very thick, symmetric section (figure 2) and on the USA 35A, a very thick, cambered section (figure 3). That the stall type for these sections is of the trailing edge type is confirmed by reference to the C_L vs. α curves published by Stack. Relf (1935) has made measurements on the Gottingen 387, a very thick, cambered section (figure 6). At a Re No. of 10^6 , the $C_{L\max}$ for the symmetric section is increasing slightly with Re No., while the $C_{L\max}$ for the cambered sections is decreasing slightly. Clearly, in the former case, the effect of Re No. on the turbulent boundary layer development is predominating; while, in the latter case, the Re No. effect on transition has the predominating influence. It is speculated that the difference of behaviour could be attributable to differing types of transition, bubble transition in one case and natural transition in the other.

It should be noted at this stage that these early experiments were carried out in variable density wind-tunnels on wing models of aspect ratio 6. The data was corrected to yield the "equivalent two-dimensional" values for the coefficients. Although the absolute values

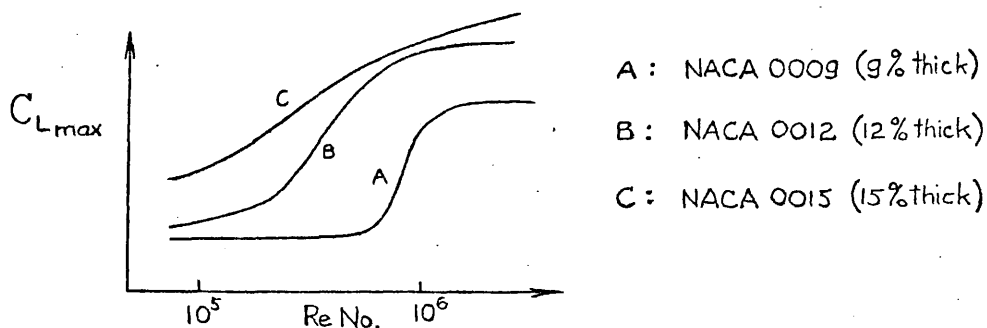
obtained in this way have since been found unreliable, they can be used quite validly to indicate relative trends; for example, variation with Re No..

Reseparation stall. From the analysis of Evans and Mort, it is inferred that the $C_{L\max}$ of aerofoils exhibiting this stall type will not be very dependent on Re No..

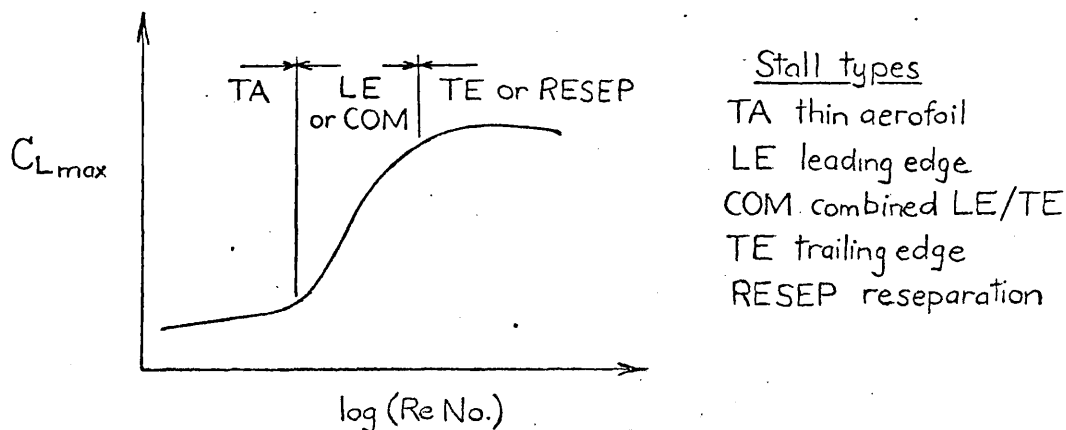
It is concluded that, for both trailing edge stall and reseparation stall, the maximum lift coefficient will have only a small dependence on Re No..

2.4.4 Overall Reynolds Number effect on $C_{L\max}$ of aerofoils.

Jacobs and Sherman (1937) have measured the $C_{L\max}$ on a number of aerofoils of moderate thickness over a wide range of Re No.. Some results are presented below.



The expected connection between the shape of a typical $C_{L\max}$ vs Re No. curve and the stall type is summarized in the next sketch:



2.4.5 Reynolds Number effects on C_{Dmin} . For symmetric sections, the minimum drag is composed ~~entirely~~ ^{mainly} of skin friction drag. Stack has measured the C_{Dmin} for a thin symmetric section (NACA 0006) and a thick one (NACA 0021) over a wide range of Re No.. These results are reproduced in figures 4,5. It can be seen that, for both sections, the dependence of C_{Dmin} on Re No. is small. For some Re Nos.,

C_{Dmin} is decreasing with increase in Re No., while, at other Re Nos, the effect is reversed. This is consistent with the reasoning in Section 2.3.3. Furthermore, the measured values for the thin section are in reasonable agreement with the theoretical curve for a double-sided flat plate (with Prandtl-Gebbers transition law). The measured values for the NACA 0021 section are considerably higher.

2.5 Free Stream Turbulence Effects on the Boundary Layer.

In a similar way to Re No., FST can influence transition and the turbulent boundary layer development; but the laminar boundary layer development is largely unaffected. (Lighthill (1954) has developed a theory of the laminar boundary layer in an unsteady stream. The velocities within the boundary layer and such properties as the local skin friction have time-dependent components in addition to the mean components which exist in a steady stream. The unsteadiness does not affect the mean development of the laminar boundary layer in this theory)

2.5.1 Effect on transition. Free stream turbulence enhances earlier transition, whether this be natural transition or bubble transition. The case of natural transition has been widely researched. Braslow (1966) has presented direct experimental evidence, showing that the critical boundary layer Re No. decreases smoothly for increasing

levels of free stream turbulence. Gault (1955) has investigated the effect of free stream turbulence on bubble transition, and found that the transition position is moved upstream by the introduction of FST.

At this stage an important general conclusion can be made. Whenever a property depends primarily on boundary layer transition, the effect of FST on that property will be equivalent to the effect of an increase in Re No..

As before, the first order effect of earlier transition on the turbulent boundary layer will be an increase in δ_2 .

2.5.2 Effect on a wholly turbulent boundary layer. The zero pressure gradient case has been the subject of several experimental investigations; for example, that of Huffman, et. al. (1972). The pertinent findings are that an increase in FST level increases δ_2 and C_f but decreases H, at a particular position on the surface. Green (1973) has determined that the effect on H of FST of 1% intensity is equivalent to a Re No. increase of some 60%.

Again it appears that the zero pressure gradient trends remain valid in flows in pressure gradient. Green has repeated the before-mentioned calculations for the aerofoil upper surface flow, using a boundary layer calculation method "speculatively modified to account for the effect of free stream turbulence". He determined that the FST effect was to significantly reduce H and to slightly increase δ_2 .

An important conclusion is that the effect of FST on the turbulent boundary layer is not equivalent to an increase in Re No.. However, as Green points out, other workers have argued that H is the parameter which controls separation on aerofoil rear surfaces; in which case the effect of FST on the separation of a wholly turbulent boundary layer will be similar to the effect of a Re No. increase.

Green emphasizes that the length scale of the FST in previous

experiments has been of the order of the boundary layer thickness. He suggest that "if the turbulence scale of the free stream were increased by an order of magnitude..... we might expect the boundary layer in this situation to respond to the predominant fluctuations as a large scale unsteadiness rather than as a source of turbulent energy."

2.5.3 Effect on a partly laminar, partly turbulent boundary layer on an aerofoil.

(a) Aerofoil at low incidence From the foregoing it is certain that an increase in FST level will cause an increase in the skin friction drag.

(b) Separation of the turbulent boundary layer on an aerofoil at incidence The FST effects on transition and on turbulent boundary layer development will both increase δ_2 , but the effect on turbulent boundary layer development will significantly decrease H . Thus there are opposing effects on the separation of the turbulent boundary layer.

(c) Separation of the laminar boundary layer on an aerofoil at incidence This separation is controlled by transition. Thus it is expected that the effect of FST will be equivalent to the effect of an increase in Re No..

2.6 Free Stream Turbulence Effects on the C_{Lmax} and C_{Dmin} of Aerofoils

2.6.1 Leading edge stall. The effect of FST will be equivalent to the effect of an increase in Re No.; namely, the C_{Lmax} will increase with increasing levels of FST. Millikan (1934) has measured the C_{Lmax} of the NACA 2412 aerofoil in flows of varying turbulence level and over a range of Re No.. His results are reproduced in figure 7. From the

dimensions of the turbulence-producing grid and the working distances from the grid, it is possible to estimate the intensities and the length scale of the FST, using data correlations for grids such as that due to Baines and Peterson (1951). These estimated intensities and length scale are included in the figure. (Methods for directly measuring the turbulence parameters were not available at the time of these early experiments). Millikan did not monitor the stall type, but, from other investigations of this and similar sections, it is fairly certain that the 2412 section does have, ultimately, a leading edge stall over the range of Re No. considered by Millikan.

Millikan's results indicate just how significant the effects of Re No. and FST can be for an aerofoil experiencing leading edge stall. At a given Re No., C_{Lmax} increases smoothly and continuously with increasing FST intensity. The effect of FST is in the same direction as the effect of increased Re No. as expected.

Relf (1935) has measured the C_{Lmax} of an R.A.F. 28 section aerofoil, which is of similar thickness to the NACA 2412, in smooth and turbulent flows. His results are presented in figure 6, where again the estimated intensities and length scales of the FST have been listed. These results are similar to those of Millikan for the 2412 section. Of particular interest is the extra information available as to the effect of different length scales of FST (Relf was not aware of this). The turbulent flows produced by Relf were of approximately the same intensity, but differed in length scale by a factor of 2. It is noteworthy that the effect of different length scales is significant, the effect of FST being greater for the smaller length scale.

2.6.2 Thin aerofoil stall. For the same reasons put forward in section 2.4.2, it is expected that the effects of FST on C_{Lmax} will be small. Stack has measured the C_{Lmax} of the very thin NACA 0006 section in a

turbulent flow (figure 1). It can be seen that the effect of FST is indeed small and has negligible dependence on Re No.. More precisely, the effect of FST is to decrease the C_{Lmax} slightly from its value in a nominally smooth stream. For a thin aerofoil, C_{Lmax} occurs when the long bubble extends over most of the aerofoil upper surface. Thus it is speculated that the FST effect is an example of the direct influence of stream turbulence on a separated turbulent shear layer: the FST produces a thicker layer at reattachment, hence a wider aerofoil wake and a lower C_{Lmax} .

2.6.3 Trailing-edge stall It was shown in 2.5.3 that FST affects both the transition and the development of the turbulent boundary layer and that the two effects have opposing influences on turbulent boundary layer separation. Furthermore, these opposing influences are different from those produced by an increase in Re No. (although Green has suggested that the differences will be small).

Consider now the experiments with very thick aerofoils, already referred to in section 2.4.3 (See figures 2,3,6). The NACA 0021 section, investigated by Stack, exhibits an increase in C_{Lmax} for an increase in FST level. The effect on C_{Lmax} is in the same direction as the effect of an increase in Re No., yet the increase in C_{Lmax} appears to be greater than would be expected by even a very large increase in Re No.. The U.S.A. 35A section exhibits a decrease in C_{Lmax} for an increase in FST level, which is also in the same direction as the effect of an increase in Re No.. However, Relf's results on a similar section, the Gottingen 387, are very different: FST increases the C_{Lmax} significantly while an increase in Re No. causes C_{Lmax} to decrease. The author has not been able to establish an explanation for this latter phenomenon. Obviously it casts doubt on Green's hypothesis that H is the boundary layer property which

controls separation under these conditions.

2.6.4 Concept of Effective Reynolds Number. When it became apparent that, often, the effect of FST was similar to the effect of an increase in Re No., it was found convenient to measure FST levels in terms of an effective increase in Re No.. This concept was widely applied as a method of designating the background turbulence level in wind tunnels. It was usual to define, for each wind tunnel, a turbulence factor, T.F:

$$\text{T.F.} = \frac{\text{Effective Re No. of the tunnel}}{\text{Actual Flow Re No.}}$$

Turbulence factors were commonly measured by determining the "critical Re No." of a sphere placed in the tunnel, and comparing this value with that for a sphere in smooth flow. (The flow about a sphere will be considered in detail in 2.7.1). The turbulence factor was considered as a constant for a particular tunnel over a wide range of Re No.. This method of correcting for FST effects was found to be of limited accuracy (understandable in terms of the discussion in 2.6.3), and greater effort was directed towards the reduction of background turbulence in wind tunnels.

2.6.5 FST effects on $C_{D\min}$

From the discussion in 2.5.3 it follows that, for symmetric sections, $C_{D\min}$ will be increased by the introduction of free stream turbulence. This is confirmed by the experimental work of Stack on the NACA 0006 and NACA 0021 aerofoils (Figures 4,5). If anything, the effect of FST is equivalent to an effective decrease in Re No.. It is interesting to note that, for the very thin aerofoil, the measured values of $C_{D\min}$ are in good agreement with the semi-theoretical curve for a double sided flat plate with wholly turbulent boundary layers.

2.6.6 F.S.T. effects on the flow in turbo-machine cascades. Large laminar separation bubbles can exist on turbo-blades at relevant Re Nos. and in smooth flow. (Refer 2.2.5). Yet, in real turbo-machine flows with high levels of FST, the existence of the bubble is often precluded by natural transition on the blade surface.

Evans (1971) has experimentally studied the transition on turbo-machine blades in various levels of free stream turbulence. He has confirmed that natural transition is promoted by either an increase in Re No. or an increase in FST. For example, at a Re No. of $2 \cdot 10^5$, a laminar separation bubble of length $\sim 0.2c$ exists with the FST intensity at 0.25%; but natural transition occurs when the turbulence intensity has been increased to 2.1%.

Large laminar separation bubbles can impair the aerodynamic efficiency of cascades. Kiock (1972) argues that cascade performance is optimum at some "critical level of free stream turbulence", a level which is sufficient to ensure natural transition of the boundary layers on individual blades.

2.7 Effect of Reynolds Number and FST on the Flow about Bluff Bodies

2.7.1 Spheres The drag of a sphere falls abruptly at a certain critical Reynolds Number, Re_{crit} . The flow change that occurs in the neighbourhood of Re_{crit} is similar to that associated with an aerofoil leading edge stall. At lower Re Nos. than Re_{crit} , separation of the laminar boundary layer occurs. At higher Re Nos., transition, via a laminar separation bubble, occurs, and the subsequent turbulent boundary layer separates at a position significantly further downstream; with the result that the wake is narrower and the drag is less.

The Re_{crit} value was found to be very sensitive to the FST

level. In fact, in the "pre-hot wire" days, it was used as a convenient measure of turbulence level. Dryden (1931) measured both Re_{crit} and the turbulence intensity ($\sqrt{v_i^2}/U_\infty$) in a number of tunnels and found that they roughly correlated.

Taylor (1936) improved the correlation by including a length scale parameter (L_1/D). He determined the functional dependence of Re_{crit} on $\sqrt{v_i^2}/U_\infty$ and L_1/D by theoretical considerations which assumed natural transition of the boundary layer. Because this analysis is relevant to the present study, it is summarized below:

1. From the theory of the laminar boundary layer, the velocity profile depends only on a parameter, Δ :

$$\Delta = \frac{\delta^2}{\nu} \frac{dU}{dx} = - \frac{\delta^2}{\rho U \nu} \frac{\partial P}{\partial x}$$

U : local stream velocity.
 δ : boundary layer thickness.

2. Taylor assumes that, in unsteady flow, this dependence holds at every instant, and writes:

$$\Delta + \Delta' = - \frac{\delta^2}{\rho U \nu} \frac{\partial(P+b')}{\partial x}$$

(Superscripted variables are the unsteady components)

The time varying part of the velocity profile should depend only on:

$$\Delta' = - \frac{\delta^2}{\rho U \nu} \frac{\partial b'}{\partial x}$$

3. Taylor considers the quantity, $\sqrt{\Delta'^2} = - \frac{\delta^2}{\rho U \nu} \sqrt{\left(\frac{\partial b'}{\partial x}\right)^2}$.

For isotropic, grid-produced turbulence one can connect the r.m.s. of the fluctuating pressure gradient to the r.m.s. of the fluctuating velocity and a length scale of the energy-containing eddies (for example, L_1):

$$\sqrt{\left(\frac{\partial b'}{\partial x}\right)^2} = \text{const.} \rho (\sqrt{v_i^2})^{\frac{5}{2}} L_1^{-\frac{1}{2}} \nu^{-\frac{1}{2}}$$

L_1 : longitudinal integral length scale.

Thus $\sqrt{\Delta'^2} = - \text{const.} \delta^2 U^{-1} (\sqrt{v_i^2})^{\frac{5}{2}} L_1^{-\frac{1}{2}} \nu^{-\frac{1}{2}}$ (2.1)

4. At the critical Re No., transition of the laminar boundary layer will occur at a particular angular position on the sphere. At this position, U/U_∞ is a constant, and Re_δ is a fixed fraction of Re ($Re = U_\infty D/\nu$; $Re_\delta = U\delta/\nu$). D : sphere diameter.

5. Finally: Taylor's basic transition assumption, namely, there exists a particular functional relationship between $\sqrt{\underline{\Lambda}^2}$ and Re_δ which defines transition:

$$\sqrt{\underline{\Lambda}^2} = f_1 \left(\frac{U\delta}{\nu} \right)$$

Substitution of equation 2.1 and re-arrangement leads to the final result:

$$Re_{crit} = f_2 \left[\frac{\sqrt{v_1^2}}{U_\infty} \cdot \left(\frac{D}{L_1} \right)^{\frac{1}{5}} \right]$$

Later experiments by Dryden, et. al. (1937), have verified that Re_{crit} and the parameter $\sqrt{v_1^2}/U_\infty \cdot (L_1/D)^{\frac{1}{5}}$ do correlate well over a wide range of $\sqrt{v_1^2}/U_\infty$ and L_1/D . Dryden, et. al. investigated the following ranges of the turbulence parameters:

$$\frac{\sqrt{v_1^2}}{U_\infty} : 0.007 \text{ to } 0.045 \quad \frac{L_1}{D} : 0.018 \text{ to } 0.464$$

Fairly reliable values of Re_{crit} in "still air" ($\sqrt{v_1^2}/U_\infty = 0$) are available. It appears that the data curve of Dryden, et. al. is approaching this value, smoothly and continuously, as $\sqrt{v_1^2}/U_\infty$ tends to zero. It is expected, then, that data for $0 < \sqrt{v_1^2}/U_\infty < 0.007$ will also correlate with Re_{crit} in the manner suggested by Taylor.

However it is not so certain that Taylor's relationship will hold for smaller scales of turbulence. In fact, Dryden's data in the range $0.018 < L_1/D < 0.046$ did not correlate well with other data. Dryden explained this by the fact that data for these lowest values of L_1/D was obtained at a distance of 1 foot from the screen, and "evidently 1 foot is too close a working distance for

spheres of this size". Examination of the details of Dryden's experiment reveals that the 1 foot distance was equivalent to a minimum of 20 mesh lengths. Thus the only doubt that can arise concerns the variation of intensity of the turbulence over the body length: this variation will be greater for the turbulence of smaller scale. From data given by Dryden, et. al. and other workers it is possible to estimate the variation of intensity over the length of the sphere for these low L_1/D flows: $\pm 20 - 25\%$ on $\sqrt{v_i^2}/U_\infty$. Although this variation is of the order of the before-mentioned discrepancy in the correlation, a realistic correction would be much smaller in magnitude, because one would expect the intensity at transition to be the important parameter. For a sphere, the transition position is very near to the vertical plane through its centre, the plane at which the intensity was measured. Thus there is a suggestion from the experimental work of Dryden, et. al. that Taylor's correlation is limited to $L_1/D > 0.05$.

From an intuitive standpoint, this is not surprising. For $L_1/D < 0.05$, L_1 is of order δ , the boundary layer thickness. The interaction of turbulence of this scale with the laminar boundary layer could well be more complicated than that assumed by Taylor in his analysis. Also there is the question of distortion of the turbulence by the mean flow field of the sphere: this effect will become more significant as L_1/D decreases.

Since Taylor formulated his analysis, it has become known that transition on a sphere proceeds via a bubble rather than naturally. Nonetheless, Taylor's Analysis is valid provided his transition assumption can be applied to the separated laminar shear layer. This seems reasonable. At Re Nos. relevant to the critical range of spheres, the laminar bubble length is small in comparison with the sphere diameter. Beneath the separated laminar shear layer the pressure is constant and there is little recirculating flow. It is reasonable to

suppose that, in this case, the separated shear layer resembles a normal attached laminar boundary layer.

2.7.2 Cylinders. Circular cylinders exhibit a similar critical drag range. Bearman (1968) has collected data for the Re_{crit} of circular cylinders in various turbulent flows and found that these values correlate well with $\sqrt{v^2}/U_\infty \cdot (D/L)^{1/5}$. The smallest value of L/D was approximately 0.12.

Goldstein (1938) presents pressure distributions which have been measured on circular cylinders in the critical range, for both smooth and turbulent free streams. These confirm that the effect of increased free stream turbulence is equivalent to the effect of increased Re No., not surprising since the type of flow in the critical range is controlled by transition. Some pressure distribution data is also presented for lower Re Nos. where complete separation of the laminar boundary layer occurs. The Re No. effect is small: the base pressure coefficient decreases slightly with increase in Re No. due to the more forward transition in the separated shear layer. Free stream turbulence produces a similar effect. Surry (1969) has recently confirmed that FST affects the subcritical flow of a circular cylinder in a way equivalent to an increase in Re No..

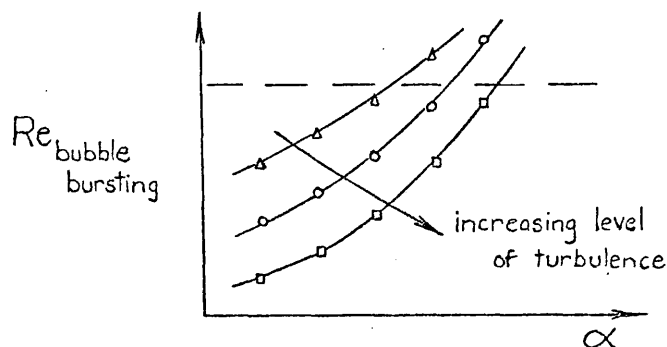
2.7.3 Flat plates perpendicular to the stream. Bearman (1968) has experimentally investigated the effect of FST on the mean flow about such plates. He found that FST lowers the base pressure appreciably, whereas an increase in Re No. has little effect. This contrasts with the observations of the flow about a circular cylinder at subcritical Re No. (reported above) where the effects of FST and Re No. were found to be similar. Bearman concluded that the turbulence, as well as causing earlier transition, promoted "much greater mixing

between the wake and the external flow."

2.8 Application of Taylor's Analysis to the C_{Lmax} of Aerofoils

The similarities between the flow change occurring on spheres in the critical range and "bubble bursting" stall of aerofoils are obvious.

Consider an aerofoil, with this type of stall, at fixed incidence and Re No. varying. For various levels of FST, the values of Re No. corresponding to bubble bursting can be measured. Then the incidence can be altered and the measurements repeated. In this way a graph similar to the following can be constructed:



The analysis of Taylor can be applied directly to the flow about an aerofoil at a particular incidence:

$$Re_{\text{bubble bursting}} = f \left[\frac{\sqrt{v_x^2}}{U_\infty} \cdot \left(\frac{c}{L} \right)^{\frac{1}{5}} \right]$$

Of more practical interest is the variation of C_{Lmax} with FST at a particular Re No.. The preceding graph can be used to interpret the variation of C_{Lmax} for aerofoils which ultimately stall by bubble bursting. The intersection of the dashed line with the curves gives the variation of $\alpha_{\text{bubble bursting}}$ with level of FST at a particular Re No.. C_{Lmax} is directly related to

$\alpha_{\text{bubble bursting}}$.

But clearly a statement like:

$$C_{Lmax} = f \left[\frac{\sqrt{v_x^2}}{U_\infty} \cdot \left(\frac{c}{L} \right)^{\frac{1}{5}} \right]$$

is not ~~necessarily~~ ^{obviously} true. Nor does it seem possible to devise an exact functional relationship of this simplicity. The analysis is greatly complicated by the movement of the laminar separation bubble upstream as the incidence is increased. At best, one could hope that C_{Lmax} correlated approximately with $\frac{\sqrt{\nu}}{U_\infty} \cdot \left(\frac{c}{L_1}\right)^{\frac{1}{2}}$.

For other stall types, the C_{Lmax} is not directly related to bubble bursting or transition, and no such approximate correlation is expected. For aerofoils with thin aerofoil stall, the C_L corresponding to bubble bursting should have the same dependence on the turbulence parameters as the C_{Lmax} for the leading edge stall aerofoils.

2.9 Comparison of the Effects of Transition Wires and the Effects of FST (Low speed flow)

Transition wires are widely used to simulate higher Re No. in wind tunnel flows. Thus a comparison of the effects of such devices with FST effects is useful for the assessment of a method of simulation which is based on the introduction of FST.

A correctly-designed transition trip device, when placed upstream of the natural transition position, will cause transition to occur at the device. In other words, the effect on transition will be in the direction of increasing Re No.. An increase in the level of FST can produce an equivalent effect on the transition.

However the effects of FST and transition wires on the subsequent turbulent boundary layer development are not exactly equivalent. In general, transition trip devices cause the turbulent boundary layer to be thicker than it would be if natural transition had occurred at the position of the device. Klebanoff and Diehl (1951) confirmed this for a flat plate, and also demonstrated that,

after an initial "settling down" period, the mean velocity profile of the boundary layer closely resembles the profile of the "undisturbed" boundary layer at the same thickness. On the other hand, FST decreases the value of the profile parameter, H , as well as increasing the boundary layer thickness, and thus the overall effect differs from that due to a transition device.

In general then, the chief limitation of both methods of high Re No. simulation is that the skin friction of the turbulent boundary layer is increased. The opposite trend is produced by a true increase in Re No.. However, Graham (1968) has shown that, over a wide range of Re No., it is possible to select a transition device which gives no effective increase in the momentum thickness of the turbulent boundary layer. Thus, by careful design, it may be possible to achieve, with transition devices, a better high Re No. simulation than is possible with FST.

Disadvantages of the transition trip device are:

(1) Prior knowledge of the transition position at the high Re No. of interest is required to effect an accurate simulation.

(2) The accuracy of the simulation must be reduced when the true high Re No. transition occurs via a laminar separation bubble.

With FST, it may be possible to determine, in one test, the effective Re No. of a particular turbulent flow and then assume that this effective Re No. will remain approximately unchanged in other tests. Further, it should be possible to correctly simulate higher Re No. bubble transition with FST.

2.10 Separation on Aerofoils at High Speed. Effect of Re No.

As the free stream Mach Number increases from zero,

(1) trailing edge separation occurs at lower angles of
incidence,

but (2) the behaviour of the laminar separation bubble is little affected.

More dramatic changes occur when the critical Mach Number is reached:

(1) the laminar separation bubble is suppressed, and (2) the supersonic region is terminated by a compression (often a shock), and the interaction of this compression with the boundary layer may induce a separation just downstream ("shock induced separation").

There are two basic supercritical flows in which separation effects are important. The first is found on wings at high incidence, with the free stream velocity small compared with velocity of sound; while the second is found on wings at lower incidence and higher Mach Number. Taylor (1973), for example, has described these two flows in detail, and emphasized that, for both, the effect of Reynolds Number on separation can be very significant. Some effort has been directed to the task of artificially simulating high Re No., transonic flows in low Re No. wind tunnel tests. An accurate simulation requires that the boundary layers at the shock and at the trailing edge should have profile shapes and thicknesses which match those at full scale. As yet, only first order simulations (in which the boundary layer is made to be turbulent at the shock, and is made to match the full scale boundary layer at the trailing edge) have been attempted. A first order simulation will only model correctly the initial separation. It is further limited in the range of flows to which it can be successfully applied. The transition trip device has been used most widely in previous simulations.

Clearly, a method of simulation based on increased levels of FST cannot be expected to be better than a first order simulation. A disadvantage of the transition trip device in transonic flows is

the local compression of the flow around the device itself. This problem would not arise for FST, but an FST method would have other difficulties, such as the problem of producing the turbulence in high speed flows.

2.11 Literature Review Summary.

The previous experimental studies of the FST effects on aerodynamic coefficients of aerofoils have been few in number and limited in their conclusions. In the literature review, these experimental results were supplemented by the knowledge of the effects of FST in other flows. In this way, a reasonable picture of the expected trends for aerofoil flows was constructed.

Nonetheless, having completed the review, the author felt it would be useful to investigate four aspects more thoroughly:

1. The magnitude of possible FST effects, as a function of the turbulence intensity and length scale.
2. The influence of FST on stall development and type.
3. The approximation of the effects of FST to an effective increase in Re No. (The review had indicated that exact equivalence could not be expected. But it was felt that a further evaluation of the degree of approximation would be useful).
4. Any fundamental differences between the FST effects for a turbulent flow with L_1 of order δ and those for a flow with L_1 of order C .

A relatively simple wind tunnel experiment was designed to provide further information on these four aspects. Only the FST effects on the overall mean loading and stall development of aerofoils were considered. Although the previous review emphasized the need for further, more fundamental investigation of FST effects on aerofoil boundary layers, this was considered to be outside the scope of the

present study.

The details and results of the current experiment are presented in the next chapter.

CHAPTER 3. The Mean Load Experiment

Simply stated, the objective of the experiment was to ascertain how the stall type and the mean loads on an aerofoil are affected by free stream turbulence. Preliminary experiments on aerofoils which already existed in the Aeronautics Department indicated that a reasonable variation in the stall type could only be obtained by employing several aerofoils of different thicknesses. (The wind tunnel that was used in this experiment is limited in its range of Re No. for a given model).

It was decided to test several such aerofoils in various turbulent flows at a particular Re No., and to compare with tests in nominally smooth flow at the same Re No. and at a higher Re No..

3.1 The Aerofoils.

3.1.1 Description A particular family of aerofoil sections was chosen; namely, the symmetric NACA 00 series. The preliminary investigations had shown that three stall types could be obtained with this aerofoil series for the range of thicknesses from 9 to 15%*c*. This range of thicknesses also covers most of the aerofoil thicknesses found in current low speed applications. Thus the following three sections were chosen:

NACA 0009 ,

NACA 0012 ,

NACA 0015 .

The Aeronautics Dept. 5 ft x 4 ft wind tunnel was used in this experiment. Considerations of the desired values of the Re No. and the turbulence length scale parameter L/ζ led to a choice of

1 foot for the chord length of the wings. The wings were constructed in the workshop of the Aeronautics Department.

3.1.2 Measurements The existing three component load balance was utilized for the mean load measurements. Load balancing and variation of incidence of a wing mounted on the balance can be achieved remotely. The control panel provides a convenient digital read-out of the angle of incidence, the lift force, the drag force, and the pitching moment.

Although a certain amount of information regarding stall type is provided by the mean load data, it was decided that a flow visualization technique should be employed for reliable determination of the stall type. Two methods were investigated in the preliminary experiments: the wool-tuft method and the oil/chalk method. The latter method has the advantage of providing a clear picture of the separated flow on the body surface. However it has the following disadvantages:

- its application is restricted to higher wind speeds.
- it provides a picture of the time-averaged flow only. No transient information.
- it is a time-consuming and tedious method.

The wool-tuft method was found to provide almost as much information about the separated flow regions without the above disadvantages. As a large number of visualization runs was planned for the main experimental program, the tuft method was felt to be the most efficient way of gathering the required information. The preliminary experiments, by allowing comparison with oil/chalk tests, did assist in the interpretation of tuft observations. Ten equi-spaced chordwise rows of tufts were employed in order to provide a flow picture of the whole wing span but without undue interference.

(Refer to Plate 1).

A permanent record of the flow visualization was achieved by photographing the moving tufts with a 2 second exposure time. The suction surface of the wing was the lower surface, as mounted in the tunnel. A photograph of the complete suction surface of the wing was achieved with the combination of a large mirror located on the tunnel floor and a camera located in the tunnel roof.

3.2 The Turbulent Flows

3.2.1 Description Two turbulence-producing grids, with very different mesh sizes, were designed and constructed for this experiment. The largest mesh size was limited by the distance between the beginning of the working section and the wing (as mounted on the balance). The large mesh size was fixed at 3 inches, which meant that the wing was located an acceptable 13 mesh lengths downstream of the grid. The grid of small mesh was designed to provide turbulence with length scale of the order of the boundary layer thickness. It was constructed from wire screening of mesh length $\frac{1}{8}$ inch mounted on a wooden frame. The dimensions of the frame matched the internal dimensions of the tunnel working section, thus allowing the grid to be placed at various distances upstream of the wing. For both grids, the ratio of mesh length to bar width was approximately 5.

With these two grids it was possible to investigate:

- (1) the effect of varying the scale of the turbulence, by using both grids ,
- (2) the effect of varying the intensity of the turbulence by varying the position of the $\frac{1}{8}$ inch grid relative to the wing.

3.2.2 Measurement A hot wire of the simple U-type (which responds

predominately to the longitudinal velocity fluctuations) was used. Analysis of the resultant signal for each flow yielded the "longitudinal" intensity, $\sqrt{v_1^2} / U_\infty$, and the longitudinal length scale, L_1 . Grid turbulence is known to be approximately isotropic at distances greater than about 10 mesh lengths downstream. Isotropy was not checked in this experiment but the minimum working distance from either grid was 13 mesh lengths.

The DISA anemometer system and auxiliary equipment were used in conjunction with the hot wire. The root mean square of the output signal was measured, and this value, when multiplied by a factor determined in the hot wire calibration, yielded the turbulence intensity. The length scale was determined from the normalized power spectrum, $\hat{\Phi}_{11}(n)$ of the signal. $\hat{\Phi}_{11}(n)$ was calculated using the digital method which has become established in the Department (and which is described in detail in 4.4). An example of $\hat{\Phi}_{11}(n)$ for one of the flows is presented in figure 8. The length scale can be calculated simply by:

$$L_1 = \frac{U_\infty}{4} \cdot \hat{\Phi}_{11}(0) .$$

This formula arises from the definitions of L_1 and $\hat{\Phi}_{11}(n)$ with the assumption that the turbulence is a "frozen" pattern which is convected downstream (Taylor's Hypothesis).

The hot wire was mounted on the tunnel centre line at the position corresponding to the position of the leading edge of the wing.

3.3 Experimental Details

3.3.1 Program. Two series of experiments were undertaken. In the

first, 4 flows were investigated:

- (1) Nominally smooth flow (free tunnel).
- (2) Flow produced with the 3 inch grid 40 inches from the wing.
- (3) Flow produced with the $\frac{1}{2}$ inch grid 40 inches from the wing.
- (4) Flow produced with the $\frac{1}{2}$ inch grid 4.5 inches from the wing.

The Re No. in each case was $0.26 \cdot 10^6$. In addition the smooth flow case was investigated at a Re No. of $0.76 \cdot 10^6$, which was the highest value possible in this tunnel. Hot wire measurements were made. Then, for each flow and each aerofoil, mean load measurements were taken over a wide range of angle of incidence. Concurrently with this, relevant flow visualization photographs were taken.

In the second series, four more flows, produced by the $\frac{1}{2}$ inch grid in four intermediate positions, were considered, with the aim of providing more information on the effects of variation in intensity. In this series, time did not permit hot wire or flow visualization investigations. The turbulence parameters, $\sqrt{v_1^2}/U_\infty$ and L_1/c were determined by interpolation between the measured values for the $\frac{1}{2}$ inch grid obtained in series 1. This interpolation can be done with confidence. Various workers (for example, Dryden (1937), Baines and Peterson (1950)) have demonstrated the power law decay of turbulence intensity behind grids; and, more specifically, Baines and Peterson have collapsed the data from a wide range of grids by plotting $\log(\sqrt{v_1^2}/U_\infty)$ against $\log(x/b)$, where x is the distance downstream from the grid and b is the bar size. The measured values of intensity from series 1 are in reasonable agreement with the curve of Baines and Peterson. Dryden (1937) and Bearman (1969) have demonstrated the linear variation of length scale with distance downstream of grids. Thus, intensity values for the series 2 flows were determined by logarithmic interpolation, while the length scale

values were estimated by simple linear interpolation.

Abbreviated notation will be used for the 9 flows, as outlined in the following table.

ABBREVIATION	DETAILS		
	GRID	DIST. FROM WING	Re. No. 10^{-6}
Smooth LR	-	-	0.26
Smooth HR	-	-	0.76
Grid L	3 inch	40 ins	0.26
Grid S, 1	$\frac{1}{8}$ inch	4.5 ins	0.26
Grid S, 2	$\frac{1}{8}$ inch	6.5 ins	0.26
Grid S, 3	$\frac{1}{8}$ inch	12 ins	0.26
Grid S, 4	$\frac{1}{8}$ inch	20 ins	0.26
Grid S, 5	$\frac{1}{8}$ inch	30 ins	0.26
Grid S, 6	$\frac{1}{8}$ inch	40 ins	0.26

3.3.2 Endplates. In the main experimental program, the wing was set between endplates. The chief consideration that prompted the use of endplates was the flow interference caused by the wooden frame of the small mesh grid, particularly when the grid was positioned near the wing. The interference of the tunnel wall boundary layer (with the frame absent) was determined to be insignificant. In the preliminary experiments, the aerofoils completely spanned the tunnel, yet there was no evidence of premature corner separations. With the aerofoil mounted on the balance, there existed a small gap between the ends of the wing and the walls. It is thought that "throughflow" in this gap provided a form of boundary layer control, not dissimilar to "blowing". One of the aerofoils, the NACA 0015, was

tested without endplates (aspect ratio = 5) and with endplates (aspect ratio = 4). The resultant C_L vs α curves for ^{the} two flows are presented in figure 9. It is seen that the primary effect of the endplates is a reduction in the lift curve slope, and this is, in fact, a consequence of the reduced aspect ratio rather than any changes in the wall boundary layer. A smaller wall boundary layer would tend to produce a higher C_{Lmax} and there is no indication of that in the figure.

Even in (ostensibly) very two dimensional flow conditions, the lift curve slope will be less than the theoretical value of 2π . The reason is that the vortex lines representing the aerofoil bound vorticity cannot terminate on the wall but must turn and lie in the plane of the wall. The effect of these vortex lines on the walls is less than the effect of trailing vorticity for a finite wing because there exists an image system for the vorticity on the wall which has a definite cancelling effect. Nonetheless the effect is measurable and it increases with decreasing aspect ratio. The results in figure 9 are an excellent illustration of the phenomenon.

The lift curve slopes (when corrected for blockage, etc) were (i) 5.8 for the wing with aspect ratio 5.0; and (ii) 5.4 for for the wing with aspect ratio 4.0. According to Goldstein (1938), a typical value for the lift curve slope in a two dimensional wind tunnel test is 5.7. In spite of the lower lift curve slope, it was decided that the main program would be conducted with endplates in order to avoid the uncertain interference effects of the frame of the small mesh grid.

The endplates were rectangular: 3 feet long by 2 feet in height. To allow the small grid to be positioned as close as 4.5 inches from the wing, it was necessary to design the endplates so that 7.5 inches of the leading section of the plates could be detached

when required. Plate 11 provides an overall view of the equipment: one of the wings mounted on the balance between the foreshortened endplates and the small mesh grid in position, 4.5 inches from the aerofoil leading edge. The disturbing effect on the flow of the grid frame can be appreciated from this photograph.

3.3.3 Dynamic head measurement. The dynamic head of the free stream must be monitored continuously during mean load measurements. The pitot tube should be positioned in such a location that the disturbance effect of the aerofoil is negligible. In the current experiment it was not always possible to satisfy this requirement and also ensure that the stream was not being disturbed by the proximity of a grid. However the latter problem was overcome by cross-calibrating the pitot near the grid with another pitot in the undisturbed stream (with the wing removed).

In the final reduction of data, another and, it is believed, more accurate method was used to correct for pitot errors due to the proximity of grids. The experiment demonstrated that the effect of FST on the lift curve slope is negligible: the pitot tube was well removed from the grid for the flow which, in general, produced the greatest FST effects. For other flows in which the pitot reading was affected by proximity to a grid, the pitot error was corrected for by matching the measured lift curve slope to the value determined in the flows with no pitot interference. Corrections made in this way were in reasonable agreement with those obtained directly from the cross-calibrations.

3.3.4 Tuft interference. Several mean load tests were conducted with and without tufts, and the effect of tuft interference was found to be very small. In fact, the effect was negligible prior to the stall.

Tufts were present in all the main experimental runs, even

those in which no visualization studies were conducted. Thus a precise description of this experiment would stipulate that aerofoils with tufts were the subject of the investigation.

3.3.5 Variation of intensity over the chord. This problem necessarily arises when turbulence of small length scale relative to the chord is being investigated. The variation can be readily accounted for when the effects of the free stream turbulence are primarily local; for example, the effects on transition. It is a simple matter to estimate the intensity of turbulence in any local region on the aerofoil surface. (This is considered further in section 3.5.1). The intensity variation is difficult to handle when the effects of FST are not confined to a local region; for example, when the effects both on transition and on turbulent boundary layer separation are important.

In this experiment, intensities were measured relative to the leading edge of the wing. Transition occurs near the leading edge at these Re Nos. Thus the measured intensities should approximate to the intensities of turbulence which affected the boundary layer transition.

3.3.6 Stall hysteresis. This phenomenon is associated with a stall in which there is a sudden loss of lift (that is, a flow change). Only the upper arm of the hysteresis loop was considered in this experiment: this arm includes the true value of C_{Lmax} . To ensure that a flow situation corresponding to a point on the lower arm was avoided, the required flow Re No. was always established first, with the aerofoil at zero incidence. The angle of incidence was then increased with no further alteration in Re No..

3.3.7 Support interference. The existing support system for the

balance was used. Some tests proved that both the disturbing effect of the shrouded supports on the mean flow and the effect on the mean loading of the exposed parts were negligible.

3.3.8 Wall corrections. The corrections referred to here are those which account for the differences between the loading produced by an infinite flow field and that produced by a flow in a duct; that is, a wind tunnel. The corrections recommended by Allen & Vincenti (1944) were applied. (These include wake blockage corrections). Only for lift measurements in the vicinity of $C_{L\max}$ were the corrections significant: in the range -2% to -4%.

The experimental results have been presented, for the most part, as uncorrected data. As the wall corrections are of the same order of magnitude and in the same direction for each aerofoil, the comparative study can be achieved without adjusting these raw mean load data. However the data for $C_{L\max}$ (Table 2) has been corrected for the wall effects to enable an accurate comparison with the $C_{L\max}$ data of other workers.

3.4 Results. Stall Type

The basic low speed stall types have been described in Chapter 2. Three of them were encountered in this experiment:

- combined trailing edge/leading edge type (COM stall)
- leading edge type (LE stall)
- thin aerofoil type(TA stall)

3.4.1 The COM Stall. Trailing edge separation began at several degrees of incidence below that corresponding to $C_{L\max}$. The separation was initially two-dimensional in nature; but, nearer the $C_{L\max}$ condition,

definite three dimensional stall cells had developed (as discussed earlier in section 2.2.6). This flow is illustrated by Plate 2.

The extent of trailing edge separation prior to the nose stall (i.e., C_{Lmax}) was strongly dependent on the aerofoil thickness and less dependent on the Re No. and FST effects.

In the COM stall, it is the bursting of the laminar separation bubble which limits the C_L . The separation line is seen to "jump" forward to a position near the aerofoil leading edge. Invariably, in this experiment, the nose stall initially occurred over only part of the span (Refer to plate 3). Nonetheless, the consequent loss of lift was always sufficient for the initial nose stall to be regarded as the flow phenomenon which determined the C_{Lmax} condition. As incidence was further increased, the nose stall became more extensive in the spanwise direction. This three dimensional development of the nose stall has been observed by other workers (refer 2.2.6).

For some experimental runs a slight unsteadiness in the flow near the leading edge (presumably in the region of the laminar bubble) was observed just prior to the nose stall.

A further feature of this nose stall was observed only in the turbulent flows of higher intensity. The initial nose stall (although still defining the C_{Lmax}) was unsteady in time as well as being localized in space. In other words, the nose stall occurred only intermittently. As the incidence was further increased, both the proportion of time in the stall and the spanwise extent of the stall increased. In some cases, the intermittent nose stall occurred at two positions; and the stall was observed to occasionally traverse the span between the two (refer to plates 4 and 5).

The period of the stall intermittency was of the order of a few seconds. Thus it is not clear whether the intermittency resulted

directly from the unsteady incident upwash (dynamic stall) or whether it was an indirect result of the interaction of the FST with the boundary layers. No evidence of this intermittency occurred in the smooth flow tests; but the smooth flow tests were limited to a maximum Re No. of $0.76 \cdot 10^6$ which was less than the effective Re No. of the higher intensity turbulent flows (refer to figure 26).

3.4.2 The leading edge stall. This stall was only observed for the smooth LR flow test on the 0012 aerofoil. It is a nose stall with little or no trailing edge separation. The nose stall developed asymmetrically in a similar way to that described above for the COM stall. (refer to plates 6 and 7).

3.4.3 The thin aerofoil stall. This was observed in all tests on the 0009 aerofoil. At an incidence in the range 8° to 10° , the upper surface flow had become unsteady, with greatest unsteadiness near the leading edge. In fact, the tufts near the leading edge were observed to undergo large sideways flicking movements (plate 8). This is thought to be indicative of the existence of the long separation bubble. Other workers (for example, McCullough and Gault (1951)) have reported that flow reversal occurs in these bubbles. In the present experiment, the tuft length was greater than the expected bubble height. It seems reasonable that tufts that are situated within a long bubble will be restricted to these sideways flicking movements.

The subsequent flow development was similar to that reported by other workers for the TA stall, with $C_{L \max}$ occurring when the long bubble had grown to encompass most of the aerofoil chord. However two types of initial bubble development were observed in this experiment. At lower Re Nos. and in FST flows of lower intensity, the stall development was remarkably two dimensional. The initial long

bubble extended across the complete span, and was of limited chordwise extent (perhaps $1/10c$). As the incidence was increased the bubble lengthened uniformly. (refer to plates 8 and 9).

At higher Re Nos. and in flows of higher turbulence intensity there was a tendency for the initial long bubble to consist of several spanwise sections, extending up to $\frac{1}{3}c$ in the chordwise direction. The bubble sections were generally asymmetrically located (refer to plate 10). It is not clear what phenomena were responsible for this structure of the long bubble: the formation of long bubbles is known to occur with little, if any, loss of lift and thus stabilizing downwash effects are not expected to be significant. As the incidence was increased the region of separation grew first in the spanwise direction, and then in the chordwise direction.

It should be noted that the final chordwise growth of the bubble was not well defined by the movement of tufts. The flow downstream of the bubble was quite unsteady. After the long bubble had grown to a length of about $\frac{1}{3}c$ it became difficult to distinguish between unsteady attached flow and genuine reversed flow in regions further aft.

3.4.4 Turbulent boundary layer separation. The movement of the separation line appeared to be controlled, primarily, by incidence. The effects of Re No. and FST were small. If anything, increase in either Re No. or FST slightly delayed the forward movement of the separation line. FST appeared to have a significant effect on the depth rather than the chordwise extent of the separation region. For a particular incidence, it was observed (from the tuft motion) that the depth was less for the higher levels of FST; and, in this way, the trailing edge separation development was effectively delayed. No appreciable effect on the depth of the separation region was apparent

for an increase in Re No..

No explanation of this phenomenon has been found. An explanation in terms of the interaction of FST with the aerofoil wake would contradict Bearman's observations for the effect of FST on the wake of a flat plate perpendicular to the stream.

3.4.5 Summary of Stall Types.

The results of four flows are summarized in table 1.

3.5 Results. Mean Loading

3.5.1 Lift Coefficient. The complete results for C_L as a function of α are presented in figures 10 to 13.

The shape of the curves correlates well with the stall type as determined in the visualization tests, the exception being for aerofoils exhibiting the intermittent nose stall. In this case, the curve is rounded contrary to a curve with discontinuity normally associated with a leading edge type of stall. A noteworthy feature is the pronounced "kink" in the curve for the 0009 aerofoil in smooth flow at the higher Re No. (figure 10). A kink is not evident in the other cases of thin-aerofoil stall (that is, for the 0009 aerofoil in other flows). Examination of the flow visualization results reveals that the kink corresponds to the first appearance of the long bubble, as expected. No conclusion can be drawn about a connection between the kink and a particular type of long bubble development (two-dimensional or three dimensional). The 0009 wing in the grid S, 1 flow exhibited similar bubble development but there was no kink apparent in the C_L vs α curve.

The effect of Re No. is presented in figure 10. The lift

curve slope is slightly higher for the aerofoils at the higher Re No.. The effect of Re No. is significant for the 0012 and 0015 sections. This is consistent with the bubble bursting type of stall that both exhibit. The Re No. effect for the 0009 section is smaller as expected; but it is greater than that for the thinner 0006 section as presented in figure 1.

The effects of the various turbulent flows are plotted in figures 11, 12, &, 13. No consistent effect of the turbulence on the lift curve slope is discernible. (This is true even when the data which has been corrected for pitot interference is ignored). The

C_{Lmax} results are summarized in table 2. In figure 14 they are plotted against the corresponding values of turbulence intensity. For each aerofoil in turbulence produced by the small grid, the measured values of C_{Lmax} increase smoothly and continuously with increase in turbulence intensity; in fact, for the 0009 and 0012 the relationship is approximately linear. Similar to the effect of Re No., the effect of FST is less for the 0009 section than for the others. There is nothing particularly universal about the slopes of these curves. The slopes are related to the slopes of the C_{Lmax} vs Re No. curves for the sections at the particular experimental Re No. . At a different test Re No. the slopes will, in general, be different. (refer fig.26) The data for the large mesh grid does not correlate with the data for the other grid: for a given intensity, the effect on C_{Lmax} is greater for the smaller length scale. Also plotted in this figure is data obtained from the results of Millikan for two Re Nos. (Refer to figure 7). It is seen that the measured values of C_{Lmax} for the 2412 aerofoil also have an approximately linear dependence on intensity.

In figure 15, values of the C_L corresponding to bubble bursting for the 0009 aerofoil are plotted against intensity.

Bubble bursting was indicated by the flow visualization studies, and

so data was only obtained for the four "series 1" flows. Nonetheless it does appear that $C_{L_{bb}}$ does vary in a similar way to the $C_{L_{max}}$ for the 0012 section; viz, a greater dependence on FST than that for the $C_{L_{max}}$ for the 0009 section. This is consistent with the experimental observations of McCullough (refer to section 2.4.2).

In figure 16, the $C_{L_{max}}$ data is plotted against the parameter of Taylor's analysis, $\sqrt{v_i^2}/U_\infty \cdot (c/L)^{1/5}$. Although the values obtained with the large mesh grid are brought closer to the data curves for the small mesh grid, the discrepancies are still significant. (In fact, Taylor's analysis is not strictly applicable to the 0009 section which exhibits a thin aerofoil stall). These results suggest that there is a lower limit on the value of L/c for applicability of Taylor's theory, even though only an approximate correlation of $C_{L_{max}}$ with $\sqrt{v_i^2}/U_\infty \cdot (c/L)^{1/5}$ was anticipated. There was a suggestion from the experimental results of Dryden, et. al. for spheres that a lower limit value was 0.05. This value would be consistent with the present trends. In these figures (14, 15, 16) the intensities are those measured at the "leading edge position". If the values are adjusted to yield the corresponding intensities at a position further downstream on the chord, the discrepancy between the small and large length scale data becomes larger.

It is relevant to consider how large the effect of distortion of the oncoming turbulence might be. For the small scale turbulence ($L/c \sim 0.03$), the effect of the aerofoil thickness on distortion will be of a similar magnitude to the effect of aerofoil incidence. Unfortunately, although the latter part of this thesis considers distortion produced by aerofoil incidence, it is restricted to an investigation of the effect on the unsteady loading: the distortion of the velocity field is not considered in detail. Some indication of the possible distortion effect due to thickness is provided by

theories for the distortion of turbulence along the stagnation streamline of a two dimensional body. As $L_1/c \rightarrow 0$, the uniform plane strain theory (for example, Batchelor & Proudman (1954)) can be applied, and the results are that the components, $\sqrt{v_1^2}/U_\infty$ and $\sqrt{v_3^2}/U_\infty$, are amplified continuously as the stagnation point is approached, while the component, $\sqrt{v_2^2}/U_\infty$ is attenuated. Bearman (1972) has measured such intensities along the stagnation streamline of a bluff body with L_1/c of the order of 1. He found that, even with this relatively high value of L_1/c , $\sqrt{v_3^2}/U_\infty$ was amplified considerably at a position near the edge of the boundary layer. Thus, in general, it is expected that the r.m.s. of at least one of the velocity components will be higher in the stagnation region. For the aerofoil, transition occurs near the leading edge, and so the value of $\sqrt{v_3^2}/U_\infty$ relevant to transition may be higher due to the distortion effect caused by thickness. The intensity amplification would be greater for the smaller scale turbulence, and thus could explain some of the discrepancy between the data for differing length scales presented in figure 16.

3.5.2 Drag Coefficient. Selected C_D results are presented in figures 17 to 20. In figure 17, the results for the three different sections in one particular flow are given. Increasing aerofoil thickness increases C_{Dmin} and delays the abrupt drag rise. For these sections the abrupt rise in drag follows upon bubble bursting. The differences between the leading edge and the thin aerofoil stalls are emphasized by a comparison of the drags at maximum lift. For the leading edge stall, this drag occurs just prior to drag rise; whereas, for the thin aerofoil stall, it occurs after the rise.

The results of four flows have been plotted in figures 18, 19, and 20 to highlight the effects of Re No. and FST. Increase of Re No. has, for each of the sections, lowered the value of C_{Dmin} and

delayed the drag rise; that is, the curves for the flow with FST cross over the curves for the nominally smooth flow. These trends are in accordance with previous findings as outlined in Chapter 2.

In figure 21, all the C_{Dmin} data is plotted against turbulence intensity. For each section, curves have been drawn through the small length scale data. The scatter of data points about these curves is greater than that for the corresponding C_{Lmax} curves, due to larger measurement errors.

The result for a repeated run is compared with the original measurement in the figure. This gives an indication of the accuracy of the C_{Dmin} determination in the present experiment. (C_{Dmin} was determined by plotting, in more detail, the data in the neighbourhood of zero incidence. Typical such curves are presented in figure 22). It is seen that the effect of the length scale of the turbulence is just as significant for C_{Dmin} as it is for C_{Lmax} (the data points for the large mesh grid are well removed from the curves for the small mesh grid). C_{Dmin} has a more complicated dependence on intensity than C_{Lmax} has: the rate of increase of C_{Dmin} with increasing intensity is less for the lower intensity values (less than about 2%) than for higher values. Whether this non-linearity arises from the turbulence effect on the transition or from the effect on the turbulent boundary layer development cannot be ascertained from the present results.

3.5.3 Pitching Moment Coefficient. For the sake of completeness, the results for the moment coefficient about the quarter-chord point are presented in figures 23, 24, 25. These results give little additional information: the trends for the abrupt decrease in nose-up moment follow those for the abrupt drag rise considered in the previous section. The accuracy of the measured moments at small incidence was

limited.

3.6 Effective Reynolds Number.

3.6.1 Maximum Lift Coefficient. Originally it had been hoped that it would be possible to test the universality of the effective Re No. concept by comparing the results for the different sections. However a thorough comparison on this basis was precluded by the lack of experimental data on the variation of C_{Lmax} with Re No. for these sections. In the 1930's extensive measurements were made on these aerofoils in variable density wind tunnels (for example, by Jacobs and Sherman (1937)), but, as pointed out earlier, the data from this era has since been found unreliable. Abbott and von Doenhoff (1945) have made reliable measurements but only for higher Re Nos. (greater than $3 \cdot 10^6$). The highest Re No. in the present experiment was $0.76 \cdot 10^6$. Only for the 0012 section has it been possible to elicit, from the experiments of other workers, reliable two-dimensional data in the Re No. range $0.76 \cdot 10^6$ to $30 \cdot 10^6$.

The following evaluation method of the effective Re No. concept was devised. Effective Re Nos. were determined with the data for the 0012 section only: C_{Lmax} values in the various turbulent flows were compared with the C_{Lmax} vs Re No. curve. For the other two sections, the measured C_{Lmax} values were plotted against these effective Re Nos. A test of the validity of the concept was whether these points lay on a smooth curve between the measured smooth flow values (Re No. $\leq 0.76 \cdot 10^6$) and the reliable smooth flow values from other sources (Re No. $\geq 3.0 \cdot 10^6$). This method has been applied in figure 26.

Two data points are significantly displaced from the curves

which correlate the majority of data: (1) For the 0009 section, the C_{Lmax} value obtained in smooth flow at the higher Re No. is below the curve of the data obtained in FST flows. Further evidence that this difference is a very real one is the fact that a kink in the C_L vs. α curve is only apparent for the higher Re No. smooth flow. Thus it is concluded that the effective Re No. concept is not accurately applicable to an aerofoil which stalls in the "thin-aerofoil way". This conclusion does not conflict with previous discussion: the review indicated that the effects of Re No. and FST on the C_{Lmax} of aerofoils with thin aerofoil stall would be small; but no indication of equivalence of the effects was given. (2) More disappointing is the displacement of the C_{Lmax} value for the 0015 section in Grid L flow from the main data curve. Another way of viewing this discrepancy is that the effect of this turbulent flow on the 0015 section is relatively greater than its effect on the other two sections. No source of measurement error which could explain a discrepancy of this size has been found.

The previous discussion has indicated that the effects of Re No. and FST on the C_{Lmax} of aerofoils with ultimate leading edge stall should be equivalent. Two areas of doubt have arisen in this study. The first is the above-mentioned discrepancy (2). The second is the intermittent nose stall which was observed only in flows with high turbulence intensity (although it is not conclusively known that an intermittent nose stall will not occur in smooth flow at high enough Re No.). Nonetheless, figure 26 does certainly demonstrate an approximate equivalence of the effects of FST and Re No. for the C_{Lmax} of the "LE stall" sections. When it is noted that the largest Re No. effects (at low speed) occur for this stall type, it is clear that the approximation should be useful for simulating many higher Re No. flows involving separation. Certainly an FST simulation method

can be applied to those flows in which transition trip devices have traditionally been used for the simulation.

3.6.2 Turbulent Boundary Layer Separation. In the current experiment, investigation of this separation was limited to flow visualisation (section 3.4.4). This visualization study high-lighted differences between the effects of Re No. and FST. Other workers have demonstrated that the effect of FST on the C_{Lmax} of aerofoils with trailing edge stall may or may not be in the same direction as the effect of Re No.. It is concluded that, in general, the effects of Re No. and FST on turbulent boundary layer separation will not be equivalent.

3.6.3 Minimum drag coefficient. The concept of FST being equivalent to an effective increase in Re No. has no relevance to C_{Dmin} . The effect of FST on C_{Dmin} is usually in the opposite direction to the effect of Re No.

3.6.4 Potential for effective Reynolds Number increase in wind-tunnels. Assuming that the concept can be applied validly, figure 26 reveals that the effective Re No. can be increased by a factor 6.0 with the small mesh grid in its nearest position to the wing. The maximum possible flow Re No. is reduced by a factor of approximately 2.0 due to the flow resistance of the grid. Nonetheless a useful factor of Re No. increase of about 3 is possible. No significant measurement problems are introduced by the existence of this sort of flow unsteadiness in the stream.

3.7 Conclusions Regarding the Mean Load Study

- (1) It is not universally true that the effect of FST is

equivalent to an effective increase in Re No. The present experiment has shown that, for aerofoils, the equivalence is approximately true for the lift of aerofoils which exhibit an ultimate leading edge stall. For these aerofoils in a typical low speed wind tunnel, the effective Re No. could be readily increased by a factor of three. A FST simulation of higher Re No. should be of the same order of accuracy as a method using a transition trip device. Unfortunately, in transonic flow testing, the transition device has been of only limited usefulness in the simulation of higher Re No..

(2) With the length scale of the turbulence fixed, the effect of FST on the aerodynamic coefficients increases smoothly and continuously with increase in turbulence intensity. The FST effect varies with the length scale of the turbulence, being greater for smaller scales. For length scales of the order of the boundary layer thickness, the dependence on length scale appears to be greater than the "1/5th power" dependence of Taylor's theory.

(3) High levels of FST can introduce unusual effects into the stall development; for example, the intermittent nose stall.

CHAPTER 4. The Unsteady Load Experiment

The basic requirements of the wind tunnel experiment were:

- (1) a rigidly-mounted two-dimensional aerofoil with variable incidence capability.
- (2) equipment for measuring the instantaneous load on the aerofoil.
- (3) production of a turbulent stream.
- (4) equipment for measuring the instantaneous velocity at several locations.
- (5) methods of eliciting the useful statistical properties of the fluctuating signals.

The 5' x 4' wind tunnel, used in the mean load experiment, was also employed in this unsteady load experiment.

4.1 Two Fundamental Design Decisions

4.1.1 The force transducers and their position relative to the aerofoil.

This question was considered in detail by Jackson (1970). Basically, two types of force transducer are suitable for this application: piezo-electric crystals and strain gauges. The former provide a better sensitivity and hence permit a more rigid system; and temperature drift, which is a serious problem for strain gauges, does not affect their performance. However, their greater size is a disadvantage. For the aerofoils of this application, the piezo-electric transducers must necessarily be mounted external to the wing. This, in turn, accentuates the problems of support interference with the flow and wing flexibility. Jackson decided in favour of piezo-electric crystals; and, by careful design, he was able to arrive at a sufficiently rigid aerofoil test element with minimal support interference.

Because Jackson's design had been proven in practice, a

similar force transducer and support system was adopted for the current investigation.

4.1.2 Dimensions of the turbulence-producing grid and the aerofoil

Following previous experimenters, it was decided that, in order to ensure satisfactory two-dimensionality of the mean flow field, the unsteady load should be measured on a part-span element of a wing which completely spans the tunnel. The problem was to optimize the following variables : s , the span of the test element, c , the aerofoil chord length, τ , the maximum aerofoil thickness, and M , the grid mesh length, within the following constraints:

(a) To ensure a sufficient magnitude of unsteady load on the element,

(i) L_1 , the turbulence length scale, should not be much less than s or c . Otherwise there is lack of correlation of the turbulence over the test element and the nett force is small.

(ii) With satisfactory correlation of the turbulence over the element, s and c should still be large enough to provide a measurable load. A preliminary calculation indicated that a turbulence intensity of the order of 5% would ensure a measurable load.

Typically, ten mesh lengths downstream of a grid, the intensity is of this order, and L_1 is of the order of $0.4 M$.

(b) To provide an adequate test of the theory,

(i) L_1 should not be much less than s or c , again for the reason of lack of correlation of the turbulence.

It is expected that any discrepancy between theory and experiment will become smaller as the correlation over the element tends towards zero.

- (ii) L_1 should not be much greater than c : otherwise the response to the gust is simply the quasi-steady response.
- (iii) L_1 should be of the order of c to provide a turbulence distortion of reasonable magnitude and to which the rapid distortion theory can be applied. When $L_1 \gg c$, the distortion is small. When $L_1 \ll c$, the rapid distortion assumptions in the theory break down (the levels of turbulence intensity are necessarily high).
- (iv) the thickness to chord ratio, τ/c , should be much less than 1. Both the already-established theory and the theory developed in this study are restricted to aerofoils of thin section. It was felt that τ/c should not be larger than 0.15.
- (c) To ensure adequate rigidity (that is, a high resonant frequency) of the test element, the ratio of span to thickness, S/c , should be made as small as possible. Jackson determined that the main resonance of his model with $S/c = 17.8$, was associated with spanwise flexing. His resultant resonant frequency was 460 Hz, which was only just beyond the highest turbulence frequency of interest. The natural frequency of spanwise flexing increases with decreasing S/c . (In fact, the theoretical natural frequency of the vibration of a simple beam depends on $\tau/S \cdot \sqrt{E/S\rho}$, where E is the modulus of elasticity and ρ is the material density. The test element was constructed with the aim of maximizing both τ/S and $\sqrt{E/S\rho}$, the latter is discussed further in the next section). Based on Jackson's experience, it was decided that τ/S should be less than 17.8.
- (d) To minimize flow interference of the support system (Jackson's tripod system was to be adopted), s should

be large.

- (e) To ensure satisfactory two-dimensionality of the mean flow, the total aspect ratio of the aerofoil should be at least 4. The total span is fixed at 5 feet by the dimensions of the wind tunnel, so the equivalent condition is that c should be less than 1.25 feet.
- (f) To minimize blockage effects, c should be small.
- (g) To keep the chord Reynolds Number in the range of practical interest, it was calculated that c should be made as large as the other constraints allow.
- (h) To be able to operate at least 10 mesh lengths downstream of the grid, the maximum M is about 6 inches. The working distance of 10 mesh lengths is the recommended minimum for reasonably isotropic turbulence and the limiting condition on M arises from the maximum working length available in the tunnel.

The following solution to the problem was arrived at:

$$c = 6 \text{ inches, } M = 6 \text{ inches, } s/c = 1.33, \tau/c = 0.15.$$

Jackson employed the same value of τ/c , but his value for s/c was twice as large. It was felt that the above design would have two advantages over Jackson's:

- (1) The resonant frequency would be higher ($s/c = 8.9$)
- (2) The lower value of s/c would provide a more rigorous test of the theory. In Jackson's experiment the value of s/L_1 was approximately 6.4 and thus the turbulence was not well correlated over a span-length.

In the present design, a further measure was taken to reduce support interference: part of the test element extended into the dummy wings on either side, and the forward support rods (of the tripod system) were connected to the extremity of these projections. The ultimate spanwise separation of these rods was 11 inches. The overall

aspect ratio of the aerofoil was 10, and the chord Reynolds Number of the experiment was $0.23 \cdot 10^6$.

4.2 The Aerofoil

4.2.1 Further details of the wing. Because the theory of this study does not specifically include the effect of camber, a symmetric aerofoil section was chosen; namely the standard NACA 0015 profile (also employed by Jackson).

Once the dimensions of the test element had been finalized, it was constructed so as to be as stiff and as lightweight as possible (in order to maximize E/ρ , and, in turn, the resonant frequency). A basic frame was cut from an aluminium block, and filled out with balsa wood. The matching dummy wings were cut from heavier timber. All construction work was carried out in the workshop of the Aeronautics Department.

A photograph of the measuring element of the aerofoil is presented as plate 12.

4.2.2 The support and load measuring system. There were two basic parts to the tripod support system:

(1) A massive "earthed" system resting on springs on the laboratory floor. This was comprised of (a) a weighted steel frame (the inertial mass) and (b) tapered pylons, bolted to the frame, passing through the tunnel floor, and terminating some distance below the model. Piezo-electric force transducers were clamped firmly to the top of these pylons.

(2) Light-weight connecting rods between the transducers and the measuring element of the aerofoil.

Two of the pylons and the inertial mass used in the current

experiment were a legacy of a previous experiment conducted, in the Department, by Edwards (1972). A feature of the inertial mass was that it rested on four large helical springs. These springs effectively isolated the support system from floor vibrations. The resultant resonant frequency of the inertial mass was negligibly small (about 0.5 Hz).

Plate 13 provides a view of the measuring element mounted on the supporting rods and pylons.

Two original features of the support system of the present experiment are now described in more detail:

4.2.2.1 Facility for incidence variation. This was achieved with two alterations to Jackson's basic design:

- (1) the rear pylon was provided with a capability for height and (to a lesser extent) longitudinal position adjustment.
- (2) the connecting rods were provided with a capability for rotation about their points of attachment to the aerofoil.

Details of these design features are illustrated in figure 27. It should be noted that, again, resonance considerations dictated the limited length (6 inches) of the connecting rods.

This design allowed the aerofoil to be set up at any incidence between -5° and $+20^{\circ}$, with facility for clamping all support connections for each set incidence. A basic intention of the design was that the connecting rods and the force transducers would be vertically orientated for all incidences of the aerofoil; that is, primary transducer response would always be to the load perpendicular to the stream: the lift force.

4.2.2.2 Transducer orientation and mounting. The piezo-electric force transducer responds primarily to the component of the applied force normal to the crystal. Yet it is also sensitive, to a lesser extent, to any transverse components. In the present experimental set-up, the primary response was to the aerofoil lift force, and the

secondary (undesirable) response was to the aerofoil drag force. A systematic effort was made to minimize the transducer sensitivity to this drag force.

This effort took the form of a preliminary experiment in which, by means of a specially constructed rig, normal and transverse loads could be applied to a transducer by the addition of weights. Two aspects were investigated:

(1) The use of diaphragms. For his experiment, Jackson designed a transducer "load cell" with two shim-metal diaphragms placed perpendicular to the connecting rod; the aim being to relieve the transverse forces and moments on the rod without affecting the normal forces. Edwards employed a load cell with a single diaphragm located immediately above the transducer. Various diaphragm thicknesses and configurations were examined in the present test, and notable results were as follows:

(a) With no diaphragms present, the sensitivity to transverse loads is linear.

(b) With a single diaphragm located some distance above the transducer, the sensitivity remained linear and was reduced by the presence of the diaphragm. The optimum thickness of the diaphragm was 0.005 inches; a thickness which produced negligible effect on the normal force sensitivity. This load cell configuration was adopted in the present experiment and is illustrated in figure 27.

(c) With a single diaphragm located immediately above the transducer (Edwards' configuration) the transverse force sensitivity became non-linear and could, in fact, be increased.

(d) With the twin configuration of Jackson, the sensitivity became non-linear and was decreased. There was no apparent advantage of this configuration over that of (b) above.

(2) The neutral axis orientation. The piezo-electric

transducer is insensitive to transverse loads applied along one particular direction. Each transducer, separately, was rotated in the experimental rig under transverse load, and the neutral axis was thereby determined and marked. The region of neutrality was found to be very narrow; significant transverse responses were encountered a few degrees either side of the neutral axis. The transducers were set up in the tunnel with their neutral axes aligned with the free stream direction. This was made possible by the design of the connecting rods: for any transducer orientation, all connections between the transducer and the aerofoil could be made firm. (refer to figure 27 for details).

Despite these efforts, the overall drag sensitivity of the test element, as installed in the tunnel, was about 10% of the normal force sensitivity. Jackson reported a similar figure for his equipment. This level of drag sensitivity is acceptable, as the unsteady drag forces on an aerofoil with attached flow will be an order of magnitude less than the unsteady lift forces. Further discussion of the possible error introduced by sensitivity to drag is given in sections 5.4.2 and 7.2.4.

4.2.3 Tunnel installation. Three aspects require further description: the installation of the dummy wings, the shrouding of the pylons, and the auxiliary electronics for the transducers.

Each dummy wing was supported by a single bolt at the tunnel wall and by four piano wires at the end adjacent to the test element. The bolt axis corresponded with the forward support axis of the test element, thus allowing mutual incidence adjustment of the test element and the dummy wings. The length of the piano wires was adjustable for this purpose. Near the test element, each dummy wing was specially cut out to accommodate the projection of the test element (for the forward connecting rods). A clearance of 1/16 inch existed between

all adjacent surfaces of the test element and the dummy wings. No attempt was made to seal the gap between the test element and the dummy wings in the main experimental program. A preliminary test, with the aerofoil at 10° incidence, had compared the lift spectrum with the gap unsealed with the spectrum with the gap sealed by "slit cellotape", and no measurable difference had been detected.

Sheet metal fairings were employed to shroud the support pylons from the flow. The rear fairing, like its partner, the rear pylon, was adjustable in height. The connecting rods, each $\frac{1}{4}$ inch in diameter, were thus the only parts of the aerofoil support system which were exposed to the flow. The shrouded pylons produced a measurable perturbation to the mean flow in the vicinity of the aerofoil. With the aerofoil removed, tests were undertaken to determine the perturbations to the dynamic head and to the mean flow direction at the aerofoil station:

- (a) Dynamic head. A pitot traverse over the test element position determined an increase of $+5.5\%$, fairly uniform over the span.
- (b) Flow direction. A yawmeter traverse determined an incidence in the range $+1^{\circ}$ to $+2.5^{\circ}$, the higher incidences being measured nearer the forward support pylons. However, the accuracy of this test was severely limited by the fact that only very small pressure differences were produced by a 1° rotation of the yawmeter.

The piezo-electric force transducer is used in conjunction with a charge amplifier which supplies, as output, an electric signal proportional to the instantaneous force on the transducer. In the present experiment, the outputs of the three charge amplifiers were summed, and the resultant signal was thus proportional to the nett lift force on the test element. Calibration was achieved simply by setting the amplifiers on "long time constant" and placing known

weights on the test element. The output was determined to be linearly dependent on the load and independent of the position of the load on the element. Calibration factors thus derived were in good agreement with those obtained directly from the rated transducer sensitivities and the set amplifier gains.

4.2.4 Resonant frequency of the test element. This was conveniently measured by first exciting the element, as installed in the tunnel, to vibrate at its natural frequency, and then analyzing the output signal. The excitation was achieved by a stream of tunnel air (no grid required) and the analysis by measuring the spectrum with an analogue "spectral analyzer". The resultant spectrum contained a well-defined peak at a frequency of 780 Hz: the resonant frequency of the test element as mounted on its supports. This result was regarded as quite satisfactory: the resonant frequency was well above the highest frequency of interest for the turbulent loading (about 300Hz).

4.2.5 Mean load characteristics. It was important to gain some knowledge of the mean lift characteristics of the model at the Reynolds Number and in the level of turbulence relevant to the unsteady load test. Direct mean load measurement with the test element was not possible, as the necessary length of time constant was not available on the charge amplifiers. Instead, during the mean load investigation described in Chapter 3 of the thesis, measurements were made on another NACA 0015 wing in approximately the same conditions of flow. Exact equivalence of the flows was precluded by the fact that the aerofoils were mounted at different locations in the tunnel working section. The following table compares the conditions of the two tests:

	UNSTEADY LOAD TEST	MEAN LOAD TEST
Reynolds Number	$0.23 \cdot 10^6$	$0.26 \cdot 10^6$
Turbulence Intensity	0.065	0.060
Aspect Ratio of the 2D Wing	10.0	5.0

The resultant mean C_L vs. α curve, corrected for wall interference effects, is given in figure 28. This curve provided the following useful information for the unsteady load study:

(1) Lift curve slope. The value yielded by the mean load test was 5.8 per radian. The higher aspect ratio employed in the unsteady test meant that the lift curve slope in this test was nearer to the theoretical value of 2π . (This dependence of the slope on aspect ratio has been explained in section 3.3.2). Thus the value of 5.8 can be regarded as the lower bound of possible values.

The theoretical lift curve slope value of 2π is also used in unsteady thin aerofoil theory. A possible correction to the theory to allow for the discrepancy between the theoretical and experimental lift curve slopes is discussed further in section 5.4.2.

(2) Effective incidence. The bulky support system of the test element induced an effective mean flow incidence to the aerofoil (refer to 4.2.3). A further estimate of this incidence was provided by the mean load data by virtue of the fact that it had been possible to determine the stalling angle of the test aerofoil by tuft visualization: a geometric incidence of 14° was the result. The mean test indicated a stalling angle of 16° (refer figure 28), though this value will be somewhat less when account is taken of the difference in aspect ratios. It was concluded that the average effective incidence was in the range: 0° to $+2^\circ$, a result which was consistent

with the yawmeter measurement described in section 4.2.3. This range of effective incidence was included in the theoretical calculations presented in Chapter 7.

(3) Mean load conditions at high incidence. The highest geometric incidence employed in the unsteady load test was 10° , corresponding to an effective angle of incidence to the mean flow of, at most, 12° . Reference to figure 28 shows that the aerofoil at this incidence was at the upper end of the linear C_L vs. α range.

In the unsteady load test, the intensity of turbulent upwash was equivalent to about 3.3 ^{or.m.s.} \wedge of incidence. Thus it was expected that the local incidence would occasionally venture above the stalling angle, but that the planform, as a whole, would not stall dynamically. This reasoning was supported by tuft observations which indicated that the flow was completely attached at the geometric incidence of 10° , and by the findings of the current mean load study (Chapter 3) which suggested that any dynamic stall behaviour would occur only at set incidences very close to the stalling angle. Nonetheless it was clear that, at some instants, the aerofoil would be operating at an incidence above the linear range of the C_L vs. α curve; and that, as a consequence, the effective lift curve slope at the highest set incidence may have been less than the slope of the linear range.

4.3 The Turbulence

4.3.1 The grids. The definitive load measurements were made in turbulence generated by a grid of mesh length, 6 inches. This grid had been designed by a previous worker in the Department. Its members were of square section and the mesh length to bar width ratio was 5.33. The full working section length of the wind tunnel was employed:

the grid was located at the entrance and the aerofoil near the exit, 13 mesh lengths separating the two.

Several unsteady load measurements were also conducted with the 3 inch grid, which had been designed for the mean load investigation of Chapter 3. The aim was to provide some information on the effect of a smaller turbulence length scale. The locations of the grid and aerofoil were as above, the resultant working distance being 26 mesh lengths.

4.3.2 The turbulence measurements. The required turbulence properties were as follows:

- (1) The one-dimensional upwash spectrum, $\phi_{22}(\bar{k}_1)$, was required for the experimental admittance calculation via equation (1.8).
- (2) The normalized upwash cross-spectrum, $S_{22}(k_1, z)$, was required for the zero incidence theoretical admittance calculation via equations (1.13) and (1.14).
- (3) The normalized three dimensional spectrum, $T_{ij}(\underline{k})$, was required for the higher order theoretical admittance calculation via the general equation, (1.11).

$\phi_{22}(\bar{k}_1)$ and $S_{22}(k_1, z)$ can be readily measured by experiment, whereas $T_{ij}(\underline{k})$ cannot. However, a formula for $T_{ij}(\underline{k})$ can be determined from a measurable spectrum with an assumption that the turbulence is isotropic. Wind tunnel turbulence will generally exhibit a certain degree of anisotropy; a degree which can be appreciated by a comparison of such measurable spectra as $\phi_{11}(\bar{k}_1)$ and $\phi_{22}(\bar{k}_1)$. In fact, a more reliable formula for $T_{ij}(\underline{k})$ has values of the turbulence parameters which are reasonably consistent with those of several different measured spectra. This latter policy was applied to the current study, the measured spectra being $\phi_{11}(\bar{k}_1)$, $\phi_{22}(\bar{k}_1)$, and $S_{22}(k_1, z)$.

$\phi_{11}(\bar{k}_1)$ can be determined from a signal proportional to the

longitudinal velocity fluctuations, v_1 ; $\phi_{22}(\bar{K}_1)$ from a signal proportional to the upwash fluctuations, v_2 ; and $S_{22}(k_1, z)$ from two simultaneous signals of the upwash at two stations separated, in the spanwise sense, by variable distance, z . In the first series of the present experiment, a U-type hot wire was employed to provide a v_1 signal; while, in the more comprehensive second series, X-type wires provided signals proportional to v_2 .

4.3.3 Hot wire details. The wires were used in conjunction with DISA brand anemometers and auxiliary units. The standard method of U-wire calibration was used. For the X-wires, the setting-up and calibration was achieved with the "matched wires" technique in which the difference signal of the two wires is made proportional to the upwash, and the calibration is conducted by a yaw test on the probe in a steady stream. A typical X-wire calibration curve obtained in this experiment is reproduced in figure 29.

The hot wire measurements were made with the wing removed, and at the flow speed of the load test (namely, 76 ft/sec). The wires were positioned on the spanwise line corresponding to the quarter-chord line of the aerofoil. Unsteady thin aerofoil theory predicts that the unsteady load will act through the quarter-chord point, and thus this position was most relevant for the turbulence measurements. With both grids, the variation of turbulence intensity over the wing chord was small: at most an 8% reduction in intensity from the leading edge to the trailing edge.

U-wire measurements were conducted with a single wire located near the tunnel centre-line. The U-wire probe was mounted on a rod fixed between the tunnel wall and one of the test element supports.

X-wire measurements were conducted, simultaneously, with two wires at different spanwise separations. A simple rig was designed to fulfil this task. It consisted of a support rod, completely

spanning the tunnel, and a traversing device. The two probes were mounted on the support rod: one at a fixed position near the tunnel centre, and the other free to traverse along it. The position of the latter probe was controlled, from outside the tunnel, by way of a traversing rod with a screw control. The whole assembly could be rotated about the support rod axis to facilitate the yaw calibration of the wires.

Drift of the tunnel temperature was a problem in the current experiment, the hot wire response being quite sensitive to changes in air temperature. With the grid installed and the velocity of the stream at 76 ft/sec the tunnel temperature did not stabilize, but continued to increase with running time. However, after about 25° C, the rate of increase became noticeably less. It was found that, by minimizing the run time, the temperature could be maintained in the range, 24.5° C to 26° C. (In fact, the run time could be made as short as 1 minute, a 40 second recording of the signal being sufficient for later analysis) Negligible change in the wire calibration occurred over this temperature range.

4.4 Signal Analysis

This section deals with the methods employed to elicit the spectra, $\phi_{CL}(\bar{k}_1)$, $\phi_{11}(\bar{k}_1)$, and $\phi_{22}(\bar{k}_1)$, and the cross spectrum, $S_{22}(k_1, z)$, from the respective signals.

The established digital analysis system of the Aeronautics Department (see Bradshaw (1975)) was utilized for the majority of the spectral analysis. The stages of this system are:

- (1) Analogue recording of the signal. For a subsequent cross-spectral analysis, simultaneous recording of the two signals on two recorder channels is required.
- (2) Digitizing of the signal(s) and recording of the digital

data. These operations are controlled by a PDP 8 computer, different programs existing for different numbers of simultaneous inputs.

(3) Analysis of the digital data on the Imperial College CDC 6400 computer. The spectral and cross-spectral analysis programs, currently in use in the Department, were written by Davies (1975). These programs employ the "Fast Fourier Transform" technique. The spectral program gives, as output, the spectrum normalized by the total power of the signal; while the cross-spectral program yields the "coherence" as one of its outputs. The coherence is the square of the modulus of the normalized cross spectrum.

In the present analysis, particular care was taken with the choice of Nyquist frequency and digitizing sampling rate, in order to minimize the aliasing error. The signals were "low-pass" filtered at the Nyquist frequency before digitizing.

Examples of output plots for a normalized load spectrum and an upwash coherence function are presented in figures 30 and 31 respectively. In the former, the model resonance peak at about 800Hz is clearly recognizable. Also in the same plot, another irregularity is discernible in the region of 50Hz. It is discussed further in section 5.1.2.

Normalized spectra were also obtained by analogue means using the Bruel and Kjaer brand "Wave Analyser". The spectra thus obtained provided a check of the digital analysis; and, in fact, very good agreement was found between spectra determined by both methods.

Absolute power spectra were ultimately required for the experimental admittance calculation. This necessitated accurate signal calibrations and a measurement of the absolute power of at least one signal at the pre-recording stage. The latter was

necessary because of changes of signal amplitude that can occur in the analogue recording and reproducing. This requirement for an absolute power measurement is a definite drawback of the Aeronautics Department system. In the current experiment a reliable estimate of power was obtained by the simple expediency of making the measurement with several of the more dependable R.M.S. meters (for example, DISA, Solatron, and Bruel & Kjaer brands).

4.5 The Experimental Program

The experiment was conducted in three series. The measurements of each series are outlined below:

Series 1: (a) Load measurements in the 6 inch grid turbulence at set incidences of the aerofoil of 0° and 10° .
(b) A U-wire flow measurement of the 6 inch grid turbulence.

Series 2: Flow measurements with two X-wires with a range of spanwise separation from 0.5 cm to 35.0 cm (6 inch grid turbulence).

Series 3: (a) A repeat of the 6 inch grid load measurements to determine reproducibility.
(b) Load measurements in the 3 inch grid turbulence at set incidences of 0° and 10° .
(c) Load measurements in the free tunnel (that is, in nominally smooth flow) over a wide range of incidence.

CHAPTER 5. First Order Turbulent Loading

This chapter compares the experimentally measured admittance of lift of an aerofoil at zero-incidence with the admittance predicted by the first order theory.

5.1 The Experimental Admittance

5.1.1 Data reduction. The absolute spectra of lift and upwash were determined from the measured normalized spectra as follows:

- At a particular reduced frequency, k_1 ,
the absolute spectral power = (normalized spectrum level) x
(r.m.s. of the signal)² x
(calibration factor)².

The admittance calculation then proceeded simply via the equation:

$$|A(k_1)|^2 = \left(\frac{U_\infty}{2\pi}\right)^2 \cdot \phi_{CL}(\bar{k}_1) / \phi_{22}(\bar{k}_1) \quad ;$$

the only further complication being that the dynamic head (and so, U_∞) were corrected for the support interference error described in section 4.2.3.

5.1.2 Results. The admittance results for the aerofoil mounted at zero incidence in the 6 inch grid turbulence (both series 1 and 3) are presented in figure 39. Considering that the data is plotted on log scale, the discrepancy between the results for series 1 and series 3 is not insignificant. The data curves cross over at a reduced frequency, k_1 , of the order of 1.0. For k_1 greater than 1.0, the series 1 estimate is greater than the series 3; while for k_1 less than 1.0, the reverse trend is evident. Within each experimental series, very good reproducibility of data was obtained.

The experimental procedures of series 1 and 3 were identical with one exception: in series 1 the load signal was low-pass filtered at the pre-analogue-recording stage with a "high roll-off" instrument set at a frequency of 400 Hz. However, one would expect that a correction for any error introduced by this filtering would tend to increase the observed high frequency discrepancy. Further, one series 1 load spectrum (an analogue measurement) was obtained without filtering, and this spectrum was in good agreement with the other series 1 zero-incidence results.

There is some cause to suspect that a difference existed between the installations of the test element in series 1 and 3. Some of the series 3 spectra exhibited a small irregularity (a "dip-peak" combination) in the vicinity of 50 Hz. This has already been referred to in section 4.4 in connection with the example spectrum of figure 30. The irregularity became more prominent in the low incidence smooth flow tests (figure 50 presents the relevant spectra) where the overall unsteady load was much less. The shape of the irregularity suggested structural vibration as the origin rather than a 50 Hz electrical "hum". The irregularity was not evident in the series 1 load spectra; yet there was no clue as to what changes in the aerofoil installation might have introduced the vibration into the series 3 tests. In turbulent loading spectra, the irregularity was invariably well imbedded; and thus it is difficult to understand how it could have been responsible for the discrepancies in admittance which were observed between the series 1 and series 3 results over a wide frequency range.

Nor does it seem possible that measurement errors could account for the discrepancy. The greatest uncertainty lay in the absolute spectral power, and the source of this uncertainty was the r.m.s. measurement (The calibrations of the hot wire and the load balance were found to reproduce accurately). The maximum r.m.s.

error was estimated at $\pm 5\%$ which could lead to an error of $\pm 10\%$ in the absolute power. Even if this maximum error were assumed for each series, the discrepancy in admittance could not be completely accounted for. Further, reducing the discrepancy at one end of the frequency range (by an alteration in the spectral powers) would, of course, increase the discrepancy at the other end.

Thus, though there was some evidence that the discrepancy could be due to some difference in aerofoil installation, it was felt that the evidence was insufficient for a complete dismissal of the results of either series.

A further relevant result is the zero-incidence load spectrum in smooth flow, measured in series 3 and plotted in figure 50. This unsteady load has been induced by unsteadiness in the nominally smooth stream and in the aerofoil wake, and by resonant vibrations of the model. The general level of this spectrum is two orders of magnitude lower than that of a typical turbulent load spectrum. Thus unsteady loads induced by boundary layers, wakes, etc. could be confidently ignored in the determination of the turbulence admittance function.

5.2 Description of the 6 inch Grid Turbulence

It is convenient, for the theoretical admittance calculation, to be able to represent various spectra of the turbulence by analytical formulae.

For the zero incidence calculation, such a representation is not necessary. One can measure the normalized cross spectrum of the turbulence and calculate a theoretical admittance directly from this data with a double numerical integration (via equations (1.14) and (1.13) given previously). However, if the data can be represented by a formula which is readily Fourier-transformable, the first integration can be achieved analytically, and the admittance can be determined with

a single numerical integration. This is the approach employed by Jackson, et. al. (1973) and by the present author.

As explained in section 4.3.2, the higher order theoretical calculation does require an analytical formula for the normalized three dimensional spectrum $T_{ij}(\underline{k})$, which, in turn, necessitates an analytical representation of at least one measured spectrum. (In the present study, to improve the reliability of the $T_{ij}(\underline{k})$ representation, all three of the measured spectra, $\Phi_{11}(\bar{k}_1)$, $\Phi_{22}(\bar{k}_1)$, and $S_{22}(k_1, z)$ were involved).

5.2.1 The von Karman description. Von Karman derived a semi-empirical formula for $\Phi_{11}(\bar{k}_1)$ for the case of grid-produced wind tunnel turbulence. (See, for example, Hinze (1959)). In the present notation, the formula is:

$$\Phi_{11}(\bar{k}_1) = \frac{1}{\pi} \cdot \bar{v}_1^2 \cdot L_1 \frac{1}{(1 + k_1^{*2})^{5/6}}, \text{ where } k_1^* = \frac{\Gamma(\frac{1}{3})}{\Gamma(\frac{1}{2}) \cdot \Gamma(\frac{5}{6})} 2 \left(\frac{L_1}{C}\right) \cdot k_1 \quad \dots (5.1)$$

In figure 32, the experimental data for $\Phi_{11}(\bar{k}_1)$ has been plotted, together with the von Karman curve for $L_1/C = 0.44$. This curve is clearly an acceptable representation of the data. The measured value of the intensity of the longitudinal fluctuations, $\sqrt{\bar{v}_1^2}/U_\infty$, was 0.065.

When the turbulence is isotropic, the various spectra are related to each other by analytical formulae. Batchelor (1953), for example, provides the derivation of several such useful formulae. Using one such result, a formula for $\Phi_{22}(\bar{k}_1)$ corresponding to the above expression for $\Phi_{11}(\bar{k}_1)$ can be derived:

$$\Phi_{22}(\bar{k}_1) = \frac{1}{6\pi} \cdot \bar{v}_2^2 \cdot L_1 \frac{(3 + 8k_1^{*2})}{(1 + k_1^{*2})^{5/6}} \quad ; \quad \bar{v}_2^2 = \bar{v}_1^2 \quad \dots (5.2)$$

In figure 33, the experimental data for $\Phi_{22}(k_1)$ has been plotted, together with curves of the above formulae for two values of L_1/C : 0.36 and 0.44. Generally, the fit of the formulae to the data is less

satisfactory than that achieved with the corresponding $\phi_{11}(\bar{k}_1)$ spectrum. The curve for $L/C = 0.36$ provides the best data fit over the frequency range of interest for the subsequent admittance calculation. (This range is also indicated in figure 33). The measured value of the upwash intensity, $\sqrt{\bar{v}_2^2}/U_\infty$, was 0.058.

A comparison of the $\phi_{11}(\bar{k}_1)$ and $\phi_{22}(\bar{k}_1)$ results revealed several indications of anisotropy:

- (1) $\bar{v}_2^2 \cong 0.8 \bar{v}_1^2$,
- (2) the shape of the curve through the ϕ_{22} data was noticeably different from that of equation (5.2), whereas, for the ϕ_{11} case, the shapes were quite similar,
- (3) the value of L/C which provided the best curve fit to the ϕ_{11} data was greater than that for the ϕ_{22} data.

Nonetheless, the excursions from isotropy could not be regarded as large.

An analytical expression for the normalized upwash cross spectrum, $S_{22}(k_1, z)$ can similarly be derived from equation (5.1) with an assumption of isotropy. (For example, refer to Harris's (1970) derivation of $S_{11}(k_1, z)$):

$$S_{22}(k_1, z) = \frac{z^{\frac{1}{6}} z^{*\frac{5}{6}}}{\Gamma(\frac{5}{6})} \left\{ K_{\frac{5}{6}}(z^*) - \frac{3z^*}{3 + 8k_1^2} K_{\frac{1}{6}}(z^*) \right\} \dots (5.3)$$

where $z^* = \frac{\Gamma(\frac{1}{2})\Gamma(\frac{5}{6})(1+k_1^{*2})^{\frac{1}{2}}}{\Gamma(\frac{1}{3})L_1} \bar{z}$, and the K's are Bessel functions of the second kind.

Jackson, et. al. have presented such a formula in their 1973 paper. In this report, it is subsequently referred to as the "VK formula" for

$S_{22}(k_1, z)$. Experimental data for $S_{22}(k_1, z)$ for three values of k_1 (covering the complete range of interest) has been plotted in figures 34, 35 and 36. In the former two figures, the data has been compared with the VK formulae for two values of L/C which yield a reasonable data fit; namely 0.40 and 0.44. In each case, the largest discrepancies

between the formula and the data occurred with the middle value of

k_1 ($= 0.804$) at large z . This fit did improve as the value of L_1/C increased, but discrepancies then appeared at small z . An L_1/C value of 0.44 was considered the highest for which the overall fit was reasonable (figure 35); and, in fact, the value of 0.40 was considered to provide the best VK fit (figure 34).

Finally, the corresponding formula for the normalized three dimensional spectrum can be deduced (see, for example, Roberts (1971)).

In tensor notation, it is:

$$T_{ij}(k) = \frac{55}{6\pi} \cdot \left\{ \frac{\Gamma(\frac{1}{3})}{\Gamma(\frac{1}{2}) \cdot \Gamma(\frac{5}{6})} \right\}^2 \cdot L_1^2 \cdot \frac{(1+k_1^{*2})^{1/6}}{(3+8k_1^{*2})} \cdot \frac{k^{*2}}{(1+k^{*2})^{1/6}} \cdot \left\{ \delta_{ij} - \frac{k_i^* k_j^*}{k^{*2}} \right\} \quad \dots (5.4)$$

$$\text{where } k^{*2} = k_1^{*2} + k_2^{*2} + k_3^{*2} \quad \text{and} \quad k_i^* = \left\{ \frac{\Gamma(\frac{1}{3})}{\Gamma(\frac{1}{2}) \cdot \Gamma(\frac{5}{6})} \right\} \cdot 2 \left(\frac{L_1}{C} \right) \cdot k_i$$

It was not possible to directly determine, by experiment, the value of L_1/C which would give the best matching of this formula to the 6 inch grid turbulence. However, from the other spectral measurements, it was confidently assumed that this best fit value would lie in the range 0.36 to 0.44; and the mean value of this range, namely 0.40, was selected for the higher order theoretical admittance calculation (described in Chapter 7).

5.2.2 Alternative formula for $S_{22}(k_1, z)$. This general formula, with five constants to be specified for each k_1 value, enabled an accurate curve fit for all the experimental data:

$$S_{22}(k_1, z) = z' K_1(z') - z'^2 K_0(z') / C_1 + C_2 \sin [C_3(z' - C_4)] \quad \dots (5.5)$$

$$\text{where } z' = C_5 \bar{z}, \text{ and } C_2 = 0 \quad \text{except when } C_4 \leq z' \leq \frac{\pi}{C_3} + C_4 .$$

This best fit formula is subsequently referred to as the "BF formula" for $S_{22}(k_1, z)$. The first two terms are a generalization of the

Vickery (1965) cross spectrum formula. This latter formula, alone, was found to agree reasonably with the data at low and high values of z , but to underestimate it at intermediate z values. The third term, a half cycle of a sine function, was added to achieve agreement in the latter region. Figure 36 presents three such data fits for three different values of k_1 .

Nonetheless, it was evident that some uncertainty existed in the $S_{22}(k_1, z)$ formulae (both the VK and BF types) at low k_1 and high z , where accurate experimental data was not available and yet where $S_{22}(k_1, z)$ was appreciably non-zero. In the next section, it is demonstrated that this uncertainty leads, in turn, to some uncertainty in the first order theoretical values of admittance at low k_1 .

5.3 The Theoretical Admittance to First Order.

5.3.1 Method of calculation. Equations (1.13) and (1.14), derived in section 1.2.5.2, were employed; namely:

$$|A(k_1)|^2 = \frac{4}{c} \int_0^{\infty} |G(k_1, k_3)|^2 \frac{\sin^2 k_3 a}{(k_3 a)^2} \bar{S}_{22}(k_1, k_3) dk_3 \quad \dots (1.13)$$

$$\text{and } \bar{S}_{22}(k_1, k_3) = \frac{1}{\pi} \int_0^{\infty} S_{22}(k_1, z) \cos k_3 z d\bar{z} \quad \dots (1.14)$$

The $\bar{S}_{22}(k_1, k_3)$ formulae corresponding to the VK and BF formulae for $S_{22}(k_1, z)$ were deduced by way of standard Fourier transforms:

(1) VK result

$$\bar{S}_{22}(k_1, k_3) = \frac{8}{3\pi} \cdot L_1 \cdot \left\{ \frac{\Gamma(\frac{1}{3})}{\Gamma(\frac{5}{6})} \right\}^2 \frac{(k_1^{*2} + k_2^{*2} + k_1^{*2} k_3^{*2})}{(1+k_1^{*2})^{\frac{1}{2}} (1+k_3^{*2})^{\frac{1}{2}} (3+8k_1^{*2})} \quad \dots (5.6)$$

where

$$k_3^+ = \frac{\Gamma(\frac{1}{3})}{\Gamma(\frac{1}{2}) \Gamma(\frac{5}{6})} \cdot \frac{L_1}{(1+k_1^{*2})^{\frac{1}{2}}} \cdot \bar{k}_3$$

$$(2) \text{ HF result } \bar{S}_{22}(k_1, k_3) = \frac{1}{C_5} \left\{ \left(1 + \frac{2}{C_1}\right) \frac{1}{2(k_3^2 + 1)^{\frac{3}{2}}} - \frac{1}{C_1} \frac{3}{2(k_3^2 + 1)^{\frac{5}{2}}} \right. \\ \left. + \frac{C_2}{2\pi} \left[\frac{\cos k_3' C_4 - \cos(k_3' C_4 + (C_3 + k_3') \frac{\pi}{C_3})}{C_3 + k_3'} + \frac{\cos k_3' C_4 - \cos(-k_3' C_4 + (C_3 - k_3') \frac{\pi}{C_3})}{C_3 - k_3'} \right] \right\} \quad (5.7)$$

$$\text{where } k_3' = \bar{k}_3 / C_5.$$

Several solutions for the sinusoidal response function, $G(k_1, k_3)$, were considered; namely, the numerical solution of Graham and the approximate analytical solutions of Mugridge, Filotas, and Sears (as detailed in 1.2.2). The necessary integration over k_3 to evaluate the admittance was performed numerically. The computer program written to achieve this, with Graham's program for $G(k_1, k_3)$ as a subroutine, is presented in Appendix 11. Special care was taken to ensure that the step size and range of integration were suitable for an accurate estimate of the integral.

5.3.2 Theoretical admittance with $G(k_1, k_3)$ evaluated exactly (that is, via the numerical method of Graham). These admittance values were calculated with both of the previously-detailed $\bar{S}_{22}(k_1, k_3)$ formulae. For the VK formula, three values of L/C were considered: 0.36, 0.40, and 0.44. The results of the calculations are plotted in figure 37.

At large values of k_1 , the admittances collapsed onto a single curve. This was expected because the higher frequency components of the unsteady load are independent of the large scale eddy structure. The admittance at lower frequency was more sensitive to the $S_{22}(k_1, z)$ data fit. For the VK case, the level of the admittance curves at low frequency increased steadily with increase in L/C as expected. The VK curve with $L/C = 0.44$ was nearest to the BF curve (though it should be remembered that $L/C = 0.40$ yielded the best VK fit to the $S_{22}(k_1, z)$ data).

An important realization was that the low frequency theoretical

admittance calculation is sensitive to the $S_{22}(k_1, z)$ data fit over a wide z range: from $z = 0$ to a value of z where the spectrum is small and asymptoting to zero. This fact is explained as follows:

(a) The integrand in equation (1.13) falls rapidly to zero from its value at $k_3 = 0$.

(b) Thus the admittance is very dependent on the integrand values near $k_3 = 0$.

(c) These values, in turn, depend on the values of $\bar{S}_{22}(k_1, k_3)$ near $k_3 = 0$.

(d) As $k_3 \rightarrow 0$, $\bar{S}_{22}(k_1, k_3) \rightarrow \frac{1}{\pi} \int_0^{\infty} S_{22}(k_1, z) dz$.

So the admittance is sensitive to the area under the $S_{22}(k_1, z)$ curve.

(e) And thus the admittance result is sensitive to the $S_{22}(k_1, z)$ data fit over the range of z in which $S_{22}(k_1, z)$ is appreciably non-zero.

As indicated in section 5.2.2, it was precisely when k_1 was small that the experimental $S_{22}(k_1, z)$ data was not available over a sufficiently wide z range. Thus, even when all the data was well represented by analytical formulae (the BF data fit), some doubt existed for the calculated admittance at the lowest frequencies.

The difficulty of obtaining accurate $S_{22}(k_1, z)$ data for low k_1 and high z will be present in any wind tunnel experiment. The results of Jackson, Graham, and Maul (1973) were limited in the same way. In a private communication, Graham has indicated that his calculated admittances at the lowest frequencies depended significantly on the type of curve which he used to fit the data. For the low k_1 determinations, he employed an exponential fit to the data as well as the VK fit described in the Jackson, et. al. paper, and he found significant differences between the admittances determined with each type of fit.

5.3.3. Theoretical admittance with $G(k_1, k_3)$ approximations. These

admittance values were calculated using the VK $\bar{S}_{22}(k_1, k_3)$ formula with $L_1/C = 0.40$. In figure 38, admittance values determined with the following approximate formulae for $G(k_1, k_3)$ are compared with those calculated with the "exact" response function of Graham:

- (1) $G_M(k_1, k_3)$, Mugridge's formula, defined in equation (1.4)
- (2) $G_F(k_1, k_3)$, Filotas' formula, defined in equation (1.3)
- (3) $S(k_1)$, Sears' formula, defined in equation (1.1).

This is the two-dimensional sinusoidal response function and when employed in place of the three dimensional function, yields the "strip theory" admittance (see 1.2.5.2)

The resultant admittance trends were consistent with the nature of the approximations:

- (1) Mugridge's formula led to an admittance in good agreement with the exact theory at the low frequency end, but one which approached the strip theory result at high frequency. These trends are understandable when it is remembered that Mugridge's approximation is an adjustment to Sear's formula and is the correct low frequency asymptote for $G(k_1, k_3)$.
 - (2) Filotas' formula yielded an admittance which, though over estimating the exact theory over the entire frequency range, approached the high frequency curve of that theory at a faster rate than the strip theory admittance. The Filotas formula is the correct high frequency asymptote for $G(k_1, k_3)$.
 - (3) Strip theory overestimated the exact theory over the complete frequency range of interest. Jackson, et. al. observed a similar trend with an L_1/C value of the same order.
- Overall, considering that most power is at the lower

frequencies, the Mugridge formula provided a reasonably accurate and very convenient approximation to the first order theoretical admittance, relevant to this experiment. In many practical situations, the L_1/C

value will be greater than 0.40 and the approximation will be still better.

5.4 Comparison of Theory and Experiment for the 6 inch Grid Turbulence

5.4.1 The comparison. Figure 39 compares the zero incidence experimental admittances (series 1 and 3) with the theoretical values calculated with the exact theory for $G(k_1, k_3)$ and with two $S_{22}(k_1, z)$ data fits (the BF fit, and the VK fit with $L_1/c = 0.40$).

The agreement between theory and experiment was reasonable. The theoretical admittance was close to the high frequency data of the series 1 experiment and to the low frequency data of the series 3. Yet, for either of the individual experimental series, the agreement was not as good as that obtained by Jackson, et. al.. The current experiment, with S/L_1 equal to 3.3, was a more rigorous test of the theory than the experiment of Jackson ($S/L_1 = 6.4$). Unfortunately, because of the scatter of experimental results, it was not possible to deduce whether the theory predicts the admittance more or less satisfactorily for the lower S/L_1 value.

5.4.2 Sources of discrepancy between theory and experiment.

(a) Turbulence description. The problem of obtaining a sufficiently accurate description for the theoretical admittance calculation at the lowest frequencies has been discussed in section 5.3.2.

(b) Aerofoil thickness. The order (ϵ) theory for $G(k_1, k_3)$ assumes an aerofoil of zero thickness, whereas a 15% thickness section was employed in the experiment. Thickness will affect the admittance in two ways: (1) The turbulence at the positions of the aerofoil upper and lower surfaces will be

less well correlated. (2) The turbulence will be distorted by the mean flow field of the thick aerofoil at zero incidence.

(c) Contribution of non-linear terms in ϵ . Terms in the sinusoidal lift response of higher order in ϵ can contribute to theoretical admittance. In Appendix 10, it is argued that a sinusoidal response term of order (ϵ^2) may contribute to $\phi_{C_L}(\bar{k}_1)$ to order (ϵ^3); in which case, its effect on the admittance would be measurable.

(d) Lift-curve slope. The mean lift curve slope at zero incidence was found to be in the range 5.8 to 2π , compared with the theoretical value of 2π (refer to section 4.2.5). Assuming that the true lift curve slope should replace 2π in the admittance calculation, the maximum possible correction to the admittance is -15%. If this correction is applied to the present results, the theoretical curve still lies within the range of scatter of the experimental data.

(e) Absolute spectral power. The uncertainty in this measurement has been discussed in 5.1.2, where the maximum experimental error was estimated at $\pm 10\%$.

(f) Variation of turbulence intensity over the chord. This variation was estimated at about 8% maximum (already mentioned in 4.3.3). Yet it was felt that the consequent error in the admittance was much less; the measured intensity at the quarter-chord position being a good representation of the effective intensity for load calculations.

(d) Drag. To a certain extent the load balance was sensitive to drag forces (refer to 4.2.2). An estimate of the likely discrepancy due to unsteady drag forces can be made on a quasi-steady basis, using the mean load results for the 0015 section. The local r.m.s. effective incidence of the turbulence

was approximately 3.3° . Considering the changes in drag and lift produced by this sort of mean incidence change about

$\alpha = 0^\circ$ yields $\frac{\Delta \text{DRAG}}{\Delta \text{LIFT}} = 0.006$. The sensitivity of the load balance to drag force was about 10% of the lift force sensitivity. Thus the quasi-steady error due to drag was a negligible $\pm 0.1\%$.

(h) Wall interference. This arises from the difference between the infinite flow field and the flow field constrained inside a duct (the wind tunnel in this case). Following the practice of the mean load experiment of Chapter 3, the corrections of Allen and Vincenti (1944) were applied. For the unsteady load experiment the wall corrections were found to be negligible even at the highest incidence.

(i) Effective incidence of the supports. In section 4.2.5, a value of, at most, $+2^\circ$ was arrived at. The higher order theory, which is described later in Chapter 7 and which corrects the zero incidence admittance for incidence effect, was applied for $\alpha = 2^\circ$. The admittance correction (which goes as α^2) was found to be negligible.

(j) Unsteady Kutta condition. That the Kutta condition holds in unsteady flow has been assumed in this and previous studies with no experimental proof. The issue has been further confused by the results of recent acoustic experiments involving flow over a trailing edge: some results have thrown doubt on the validity of the unsteady Kutta condition, while others (for example, those of Bechert and Pfizenmaier (1971)) have tended to confirm it. Unsteady thin aerofoil theory, derived with the Kutta assumption, has, in the past, been applied usefully to practical problems. It was thought that, at this time, the best approach was to assume the validity of the Kutta condition, and to admit the dependence on it of all

the developed theory.

Particularly in view of (a), (b), (c), (d) and (e) above, it was felt that the zero incidence experimental results gave no cause to doubt the validity of the first order theory of aerofoil turbulent loading.

5.5 Results for the 3 inch Grid Turbulence

The admittance results of this series 3 test are plotted in figure 40, together with the theoretical admittance calculated with the VK formula for $\bar{S}_{22}(k_1, k_3)$.

Detailed measurements of the turbulence were not made for this case. (For the mean load investigation, described in Chapter 3, parameters of the 3 inch grid turbulence were measured, but at stations further upstream). Stapountzis, a colleague of the author, has recently made hot wire measurements in both the 6 inch and 3 inch grid turbulences at the station relevant to the unsteady load experiment. Some of his measurements were analyzed in order to determine the ratio of the intensities and length scales for the two cases, and thus to estimate the parameters of the 3 inch grid turbulence. The results were:

$$\frac{\sqrt{v_2^2}}{U_\infty} = 0.037 \quad \text{and} \quad L_1/c = 0.38 .$$

As indicated in figure 40, the theory with $L_1/c = 0.38$ was in reasonable agreement with the experimental data. At the higher frequencies the theory has overestimated the admittance, the order of the discrepancy being similar to that of the corresponding series 3 test for the 6 inch grid turbulence (refer to figure 39).

Thus the results of the 3 inch grid test were consistent with the more reliable results of the experiment conducted with the 6 inch grid. Unfortunately, the actual value of the length scale of the 3 inch grid turbulence was greater than the value which had been

estimated during the planning of the experiment; with the result that this test provided no additional information for the study.

5.6 Conclusions Regarding the First Order Turbulent Loading.

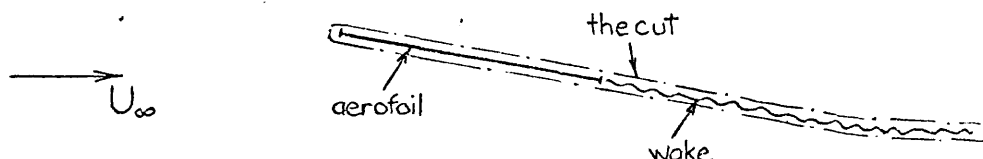
The present experiment has tended to confirm the conclusions of Jackson, Graham, and Maull (1973); namely that the first order theory provides a reasonable prediction of the admittance of lift of an aerofoil at zero mean incidence. Two additional aspects have been highlighted in this study:

- (1) The Mugridge formula is a useful approximation for the response function $G(k_1, k_3)$ required in the admittance calculation.
- (2) The predicted value of the admittance will tend to be less reliable at the lowest frequencies of interest for most practical problems (as a result of the difficulty of accurately describing the turbulence at those same frequencies)

CHAPTER 6. Higher Order Theory for Sinusoidal Gust Loading

6.1 General Assumptions

- (1) The flow is assumed entirely inviscid. The undisturbed flow (that is, with the aerofoil absent) consists of a free stream, U_∞ , and a gust velocity field. The gust may be irrotational or rotational; in either case, the disturbance flow field produced by the presence of the aerofoil is necessarily irrotational. (For example, Batchelor (1967) demonstrates that a flow field resulting from the satisfaction of a boundary condition is always irrotational).
- In the present case, the disturbance field is equivalent to that produced by a sheet of distributed vorticity on the aerofoil and in its wake. Thus the irrotational disturbance field is bounded by a "cut" which encloses the aerofoil and its wake:



- (2) This higher order theory is concerned only with the effect of mean incidence, α . The effect of thickness is ignored. In other words, the aerofoil considered in the analysis is a zero-thickness two dimensional aerofoil at incidence α .
- (3) The incidence, α , and the relative amplitude of the gust, ϵ , are both assumed to be much less than 1.0. Further it is assumed that ϵ is much less than α . This latter assumption permits terms of order (ϵ^2) to be neglected in comparison with those of order ($\alpha\epsilon$): the order ($\alpha\epsilon$) terms are the higher order terms of interest.

In practice this assumption that $\epsilon \ll \alpha \ll 1$ is meaningful from two view-points:

- (a) ϵ is often sufficiently small. In the current (high incidence) turbulent loading experiment (described in Chapter 4), the intensity of turbulence was "high", but even then, with $\epsilon \approx 0.06$ and $\alpha \approx 0.2$, the above assumption was approximately adhered to. In Appendix 10, the possible contribution of the order (ϵ^2) sinusoidal response term to the turbulent lift spectrum is considered further.
- (b) The order (ϵ^2) term is independent of incidence. Thus, when attention is being focussed on the difference between the unsteady loading at zero incidence and at non-zero incidence (as is the case of the present study) the order (ϵ^2) contribution need not be considered.
- (4) The Kutta condition is assumed to hold at every instant; and this allows the wake to be modelled by a sheet of distributed vorticity. In the order (ϵ) theories (for example, those of Sears and Graham described in 1.2.2), this vortex sheet is located on the extended aerofoil chord plane, which is also parallel to the direction of the free stream for the aerofoil at zero incidence. In the present order ($\alpha\epsilon$) theory, the initial assumption is that the wake vortex sheet lies along the extended chord plane. Later it is demonstrated that, to order ($\alpha\epsilon$), the precise spatial location of the wake is not important: the derived lift response would be the same if the wake were chosen to lie in the direction of the free stream.

6.2 Method of Analysis

Without satisfying the boundary condition on the aerofoil surface, the i th component of the instantaneous velocity at any point

can be written as:

$$V_i + v_i + \tilde{v}_i + O(\alpha\epsilon^2, \alpha^2\epsilon) ,$$

where V_i is the i th component of the undisturbed steady velocity: $O(1)$ or $O(\alpha)$,
 v_i is the i th component of the undisturbed fluctuating velocity: $O(\epsilon)$,
 \tilde{v}_i is the i th component of the additional fluctuating velocity
 produced by distortion of v_i by the mean flow field: $O(\alpha\epsilon)$.

When the boundary condition is applied, the instantaneous velocity can be written:

$$V_i^T = V_i + V_i' + v_i + v_i' + \tilde{v}_i + \tilde{v}_i' + O(\alpha\epsilon^2, \alpha^2\epsilon) \quad \dots (6.1)$$

where V_i' satisfies the boundary condition for the field, $V_i : O(\alpha)$,
 v_i' satisfies the boundary condition for the field, $v_i : O(\epsilon)$,
 \tilde{v}_i' satisfies the boundary condition for the field, $\tilde{v}_i : O(\alpha\epsilon)$.

The instantaneous vorticity can be written:

$$\mathcal{J}_i^T = \mathcal{J}_{i\infty} + \mathcal{J}_i + O(k\alpha\epsilon^2, k\alpha^2\epsilon) \text{ (outside the "cut")} \quad \dots (6.2)$$

where $\mathcal{J}_{i\infty}$ is the undisturbed vorticity: $O(k\epsilon)$.

\mathcal{J}_i is the additional vorticity produced by distortion: $O(k\alpha\epsilon, \alpha\epsilon)$.

(see, later, 6.3.3.1)

There are no mean components of vorticity (in this problem) and no components in the disturbance flow fields. $\tilde{\mathcal{V}}_i$ is the Biot-Savart velocity field of \mathcal{J}_i .

The basic method of the analysis is to substitute the above expressions for V_i^T and \mathcal{J}_i^T into the inviscid equations of fluid motion, and to solve with the aerofoil boundary conditions, retaining only terms of order (ϵ) and order $(\alpha\epsilon)$.

6.3 Theory for the Frozen Two-Dimensional Gust

This two-dimensional gust theory, as well as serving as an introduction to the more general, and more complicated, three-dimensional theory, is directly relevant to some practical unsteady loading problems.

6.3.1 Problem formulation

6.3.1.1 Frames of reference. The stream-aligned co-ordinate system, x, y, z , and the aerofoil-aligned system, ξ, η, z have been introduced in section 1.2.1. Components in the x, y , and z directions are subscripted with $i = 1, 2$, and 3 respectively, while, for the ξ and η directions, the subscripts remain as ξ and η .

6.3.1.2 The gust. A general two-dimensional gust, frozen in space, has velocity components:

$$v_1 = \hat{v}_1 e^{-i(k_1 x - k_2 y)}, \quad v_2 = \hat{v}_2 e^{-i(k_1 x - k_2 y)}$$

When such a frozen gust is convected onto the aerofoil at the free stream velocity, U_∞ , the components become:

$$v_1 = \hat{v}_1 e^{i(\omega t - k_1 x - k_2 y)} \quad \text{and} \quad v_2 = \hat{v}_2 e^{i(\omega t - k_1 x - k_2 y)} \quad \text{with} \quad \omega = k_1 U_\infty.$$

The corresponding gust components in the ξ, η, z co-ordinate system are given by:

$$v_\xi = \hat{v}_\xi e^{i(\omega t - k'_1 \xi - k'_2 \eta)} \quad \text{and} \quad v_\eta = \hat{v}_\eta e^{i(\omega t - k'_1 \xi - k'_2 \eta)},$$

$$\text{where} \quad \hat{v}_\xi = \hat{v}_1 \cos \alpha - \hat{v}_2 \sin \alpha,$$

$$\hat{v}_\eta = \hat{v}_2 \cos \alpha + \hat{v}_1 \sin \alpha,$$

$$k'_1 = k_1 \cos \alpha - k_2 \sin \alpha,$$

$$k'_2 = k_1 \sin \alpha + k_2 \cos \alpha.$$

\hat{v}_1 and \hat{v}_2 are, in general, complex, and, in order to satisfy the continuity condition $\left(\frac{\partial v_1}{\partial x} + \frac{\partial v_2}{\partial y} = 0 \right)$ are related by:

$$\hat{v}_2 = -\frac{k_1}{k_2} \hat{v}_1.$$

The vorticity associated with this gust is:

$$\zeta_{\infty} = \hat{\zeta}_{\infty} e^{i(\omega t - k_1 x - k_2 y)} = \hat{\zeta}_{\infty} e^{i(\omega t - k_1' \xi - k_2' \eta)},$$

where $\hat{\zeta}_{\infty} = ik_2 \hat{v}_1 - ik_1 \hat{v}_2 = ik_2' \hat{v}_\xi - ik_1' \hat{v}_\eta$ (from the definition, $\underline{\zeta} = \underline{\nabla} \times \underline{v}$)

In this two-dimensional gust theory, only this one component of vorticity can exist. This is emphasized in the subsequent analysis by the deletion of the subscript, 3, in the expressions for the gust vorticity; for example, $\zeta_{\infty} = \hat{\zeta}_{\infty} e^{i(\omega t - k_1 x - k_2 y)}$.

6.3.1.3 The instantaneous velocity at any point. This has already been synthesized:
(equation (6.1))

$$V_i^T = V_i + V_i' + v_i + v_i' + \tilde{v}_i + \tilde{v}_i', \quad \text{correct to order } (\alpha \epsilon).$$

6.3.1.4 Vorticity distribution on the aerofoil. The velocity fields, V_i' , v_i' , and \tilde{v}_i' , can be produced by replacing the aerofoil (as a boundary) by distributed vorticity on the chord line.

$$\text{Aerofoil bound vorticity} = K(\xi) + \gamma(\xi, t) + \tilde{\gamma}(\xi, t),$$

$$\text{where } K(\xi) \text{ produces the field } V_i' : O(\alpha)$$

$$\gamma(\xi, t) \text{ produces the field } v_i' : O(\epsilon)$$

$$\tilde{\gamma}(\xi, t) \text{ produces the field } \tilde{v}_i' : O(\alpha \epsilon)$$

Because γ and $\tilde{\gamma}$ vary with time, vorticity will necessarily be shed from the aerofoil, and the resultant wake will be a two-dimensional vortex sheet.

6.3.1.5 Boundary condition on the aerofoil.

On the aerofoil: $V_{\eta}^T = V_{\eta} + V_{\eta}' + v_{\eta} + v_{\eta}' + \tilde{v}_{\eta} + \tilde{v}_{\eta}' = 0$.

More particularly, owing to the formulation of the problem:

$$\left. \begin{aligned} V_{\eta} + V_{\eta}' &= 0 \\ v_{\eta} + v_{\eta}' &= 0 \\ \tilde{v}_{\eta} + \tilde{v}_{\eta}' &= 0 \end{aligned} \right\} \text{ on the aerofoil.}$$

6.3.1.6 Relationship between velocities and pressures. The relevant equation of motion, linking velocity and pressure is, in vector notation:

$$\frac{\partial \underline{V}^T}{\partial t} + (\underline{V}^T \cdot \nabla) \underline{V}^T = -\frac{1}{\rho} \nabla p \quad \dots (6.3)$$

where, for this two dimensional problem, $\underline{V}^T = V_{\xi}^T \hat{c} + V_{\eta}^T \hat{j}$ and \hat{c} , \hat{j} , and \hat{k} are the unit vectors in the ξ , η , and z directions, respectively.

This equation is the form of the Navier-Stokes equation for a frictionless, incompressible fluid with body forces, such as gravity, ignored.

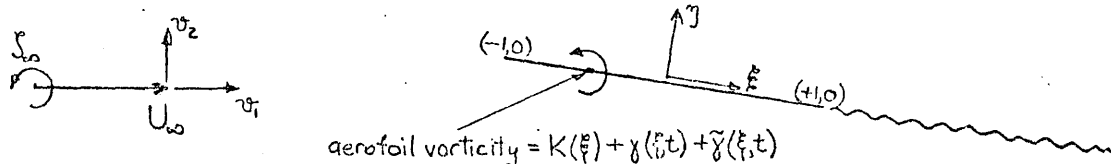
Using the identity: $\frac{1}{2} \nabla (\underline{V}^T \cdot \underline{V}^T) = (\underline{V}^T \cdot \nabla) \underline{V}^T + \underline{V}^T \times \underline{J}^T$,
where $\underline{J}^T = \nabla \times \underline{V}^T = \underline{J}^T \hat{k}$, in this case, equation (6.3) becomes:

$$\frac{\partial \underline{V}^T}{\partial t} - \underline{V}^T \times \underline{J}^T = -\nabla \left(\frac{1}{2} |\underline{V}^T|^2 + p/\rho \right) \quad \dots (6.4)$$

Integrating this equation with respect to ξ from $-\infty$ to ξ :

$$\frac{\partial}{\partial t} \int_{-\infty}^{\xi} V_{\xi}^T d\xi' - \int_{-\infty}^{\xi} V_{\eta}^T \underline{J}^T d\xi' = -\left(\frac{1}{2} |\underline{V}^T|^2 + \frac{p}{\rho} \right) \quad \dots (6.5)$$

6.3.1.7 Equations for the aerofoil lift. These are formulated by substituting, in equation (6.5), the velocities at two corresponding points on the aerofoil upper and lower surfaces ($-1 \leq \xi \leq +1$).



On the aerofoil surface: $V_y^T = 0$ and $V_\xi' = \mp \frac{K}{2}$, $v_\xi' = \mp \frac{\gamma}{2}$, $\tilde{v}_\xi' = \mp \frac{\tilde{\gamma}}{2}$ with the minus signs applying to the aerofoil top surface, and the plus signs to the lower surface. These latter relationships between the aerofoil vorticity and the surface velocities follow from the properties of a sheet of distributed vorticity.

Thus, on the upper surface: $V_{FU}^T = V_\xi - \frac{K}{2} + v_\xi - \frac{\gamma}{2} + \tilde{v}_\xi - \frac{\tilde{\gamma}}{2}$,
and on the lower surface: $V_{FL}^T = V_\xi + \frac{K}{2} + v_\xi + \frac{\gamma}{2} + \tilde{v}_\xi + \frac{\tilde{\gamma}}{2}$.

It follows that:

$$V_{FL}^T - V_{FU}^T = K + \gamma + \tilde{\gamma} \quad \dots (6.6)$$

$$\text{and } V_{FL}^{T^2} - V_{FU}^{T^2} = 2V_\xi K + 2V_\xi \gamma + 2V_\xi \tilde{\gamma} + 2Kv_\xi + O(\epsilon^2, \alpha\epsilon, \alpha\epsilon^2) \quad \dots (6.7)$$

When equation (6.5) is applied at the two corresponding points on the upper and lower surfaces, and one equation is subtracted from the other, the result is:

$$\frac{\partial}{\partial t} \int_{-1}^{\xi} [V_{FU}^T - V_{FL}^T] d\xi' = - \left\{ \frac{1}{2} [V_{FU}^{T^2} - V_{FL}^{T^2}] + \frac{p_U - p_L}{\rho} \right\} \quad \dots (6.8)$$

(The contribution of the integral from $-\infty$ to -1 is the same for the upper and lower points).

Substituting from equations (6.6) and (6.7) and writing $p = P + p'(t)$ yields:

$$-\frac{\partial}{\partial t} \int_{-1}^{\xi} (\gamma + \tilde{\gamma}) d\xi' = V_\xi K + V_\xi \gamma + V_\xi \tilde{\gamma} + Kv_\xi - \frac{(P_U + P_U') - (P_L + P_L')}{\rho} \quad \dots (6.9)$$

The time mean of equation (6.9) is:

$$0 = V_\xi K - \frac{P_U - P_L}{\rho} \quad \dots (6.10)$$

Subtracting equation (6.10) from equation (6.9) yields an expression for

the unsteady pressure difference across the aerofoil, correct to order $(\alpha\epsilon)$:

$$\frac{p_u' - p_l'}{\rho} = \frac{\partial}{\partial t} \int_{-1}^{\xi} (\gamma + \bar{\gamma}) d\xi' + V_{\xi} \gamma + V_{\xi} \bar{\gamma} + K v_{\xi} \quad \dots (6.11)$$

The unsteady aerofoil vorticity will be of the form: $\gamma(\xi, t) = \hat{\gamma}(\xi) \cdot e^{i\omega t}$.

Therefore: $\frac{\partial \gamma}{\partial t} = i\omega \gamma$ and $\frac{\partial \bar{\gamma}}{\partial t} = i\omega \bar{\gamma}$.

The unsteady upwards force/span,

$$F = \int_{-1}^1 (p_l' - p_u') d\xi.$$

Therefore:

$$F/\rho = - \left[i\omega \int_{-1}^1 \int_{-1}^{\xi} (\gamma + \bar{\gamma}) d\xi' d\xi + V_{\xi} \int_{-1}^1 (\gamma + \bar{\gamma}) d\xi + \int_{-1}^1 K v_{\xi} d\xi \right] \quad \dots (6.12)$$

It is convenient to divide F as follows:

$$F = F_p + F_D + F_M$$

where

$$\frac{F_p}{\rho} = - \left[i\omega \int_{-1}^1 \int_{-1}^{\xi} \gamma d\xi' d\xi + V_{\xi} \int_{-1}^1 \gamma d\xi \right],$$

$$\frac{F_D}{\rho} = - \left[i\omega \int_{-1}^1 \int_{-1}^{\xi} \bar{\gamma} d\xi' d\xi + V_{\xi} \int_{-1}^1 \bar{\gamma} d\xi \right],$$

$$\frac{F_M}{\rho} = - \int_{-1}^1 K v_{\xi} d\xi.$$

F_p is of order (ϵ) and is the primary response of the aerofoil to the undistorted gust. Not only does F_p contain the Sears' order (ϵ) response for the aerofoil at zero incidence, but it also contains some order $(\alpha\epsilon)$ contributions arising out of the additional terms (1) and (2), described in section 1.2.3. This further subdivision of F_p is conducted in the next section. F_D is of order $(\alpha\epsilon)$ and is the lift response to the "additional" gust produced by distortion. F_M is of order $(\alpha\epsilon)$ and is the cross product term previously derived by Horlock and Morfey (refer to 1.2.3).

It is a general result for a zero-thickness aerofoil in inviscid flow that the overall force, F , has a magnitude which can be calculated by the addition of pressures on the upper and lower

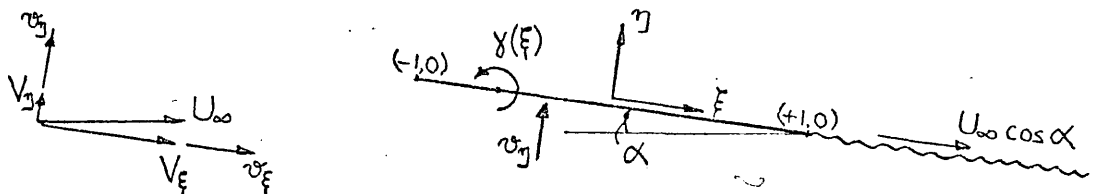
surfaces, and a direction which is always perpendicular to the instantaneous stream. The lift force, L , is defined as the force component perpendicular to the mean stream. The maximum error introduced by assuming $L = F$ is clearly of order $(1 - \cos \epsilon)$; that is, of order (ϵ^2) . This error can be ignored within the assumptions of the analysis.

The analysis for the higher order loading terms (F_D and F_M) can be simplified as follows: The aerofoil can be considered to be at zero incidence, with mean vorticity, $K(x) = -2 U_\infty \alpha \sqrt{\frac{1-x}{1+x}}$, distributed along the chord. This mean vorticity arises in the linearized theory for the steady flow about a flat plate at incidence, α . The errors introduced by this simplification are necessarily order $(\alpha^2 \epsilon)$ at least.

The final formulation of the problem is summarized below. A mathematical equation for each of the three components of unsteady lift (L_p , L_D , L_M) is presented, together with an illustration of the corresponding flow geometry:

(a) Primary lift, L_p

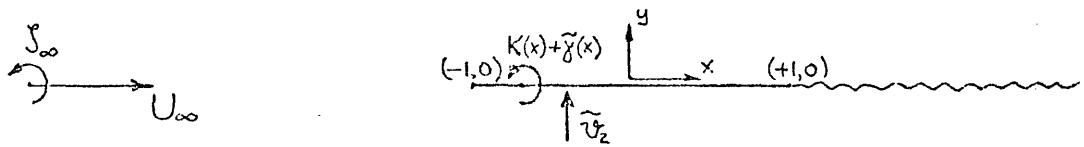
$$\frac{L_p}{\rho} = - \left[i\omega \iint_{-1}^1 \gamma(\xi') d\xi' d\xi + V_\xi \int_{-1}^1 \gamma(\xi) d\xi \right] \dots (6.13)$$



where $\gamma(\xi)$ satisfies the boundary condition for v_{η} (undistorted).

(b) Lift due to distortion, L_D

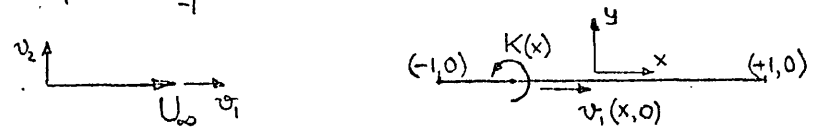
$$\frac{L_D}{\rho} = - \left[i\omega \iint_{-1}^1 \tilde{\gamma}(x') dx' dx + U_\infty \int_{-1}^1 \tilde{\gamma}(x) dx \right] \dots (6.14)$$



where $\tilde{\gamma}(x)$ satisfies the boundary condition for \tilde{v}_2 . \tilde{v}_2 is the additional upwash produced by distortion of ζ_∞ by the mean flow field. The mean flow field is that corresponding to the vorticity distribution, $K(x) = -2 U_\infty \alpha \sqrt{\frac{1-x}{1+x}}$, $(-1 \leq x \leq +1)$.

(c) The "Morfev lift", L_M

$$L_M / \rho = - \int_{-1}^{+1} K(x) \cdot v_1(x,0) \cdot dx \quad \dots \quad (6.14E)$$



where $K(x)$ is as above, and v_1 is the x-component of the undistorted gust.

6.3.2 Analysis for L_P . This analysis is an adaption of the theory of Sears. Sears' result can be derived in several ways: the current analysis employs the method of Bisplinghoff, et. al. (1955).

6.3.2.1 Wake analysis. It is initially assumed that the shed vorticity is conected along the extended aerofoil chord line by the component of the free stream velocity in that direction; viz, $V_\xi = U_\infty \cos \alpha$.

The wake vorticity is denoted by $\gamma_\omega(\xi) = \hat{\gamma}_\omega(\xi) \cdot e^{i\omega t}$; and, for simple convection at V_ξ , it must satisfy the equation:

$$\frac{\partial \gamma_\omega(\xi)}{\partial t} + V_\xi \frac{\partial \gamma_\omega(\xi)}{\partial \xi} = 0 \quad \dots \quad (6.15)$$

The total circulation in the flow must remain constant (Kelvin's Circulation Theorem).

With the Kutta trailing edge condition, this necessitates that:

$$\frac{\partial}{\partial t} \Gamma = - V_\xi \cdot \gamma_\omega(1) \quad \dots \quad (6.16)$$

where Γ is the unsteady circulation on the aerofoil = $\hat{\Gamma} e^{i\omega t}$
 where $\hat{\Gamma} = \int_{-1}^1 \hat{\gamma}(\xi) d\xi$, and $\gamma_w(1)$ is the wake vorticity at
 the trailing edge.

The simultaneous solution of equations (6.15) and (6.16) enables the
 wake vorticity to be expressed in terms of the aerofoil circulation:

$$\hat{\gamma}_w(\xi) = -i \frac{k_1}{\cos\alpha} e^{i \frac{k_1}{\cos\alpha} \xi} e^{-i \frac{k_1}{\cos\alpha} \xi} \hat{\Gamma} \dots (6.17)$$

6.3.2.2 Boundary condition. For the determination of L_p , the
 boundary condition must be satisfied for v_η ; that is, $v_\eta(\xi, 0) + v_\eta'(\xi, 0) = 0$
 on the aerofoil.

$$\text{Now, } v_\eta(\xi, 0) = \hat{v}_\eta e^{i(\omega t - k_1' \xi)} \quad (\text{refer to section 6.3.1.2}).$$

$v_\eta'(\xi, 0)$, a component of the "disturbance" velocity field,
 can be determined by an application of the Biot-Savart law to the
 corresponding aerofoil vorticity, γ , and wake vorticity, γ_w .

The result is:

$$v_\eta'(\xi, 0) = \frac{1}{2\pi} \int_{-1}^1 \frac{\gamma d\xi'}{\xi - \xi'} + \frac{1}{2\pi} \int_1^\infty \frac{\gamma_w d\xi'}{\xi - \xi'}$$

The boundary condition becomes (with substitution for γ_w
 from equation (6.17)):

$$\frac{1}{2\pi} \int_{-1}^1 \frac{\hat{\gamma} d\xi'}{\xi - \xi'} = -\hat{v}_\eta e^{-ik_1' \xi} + \frac{1}{2\pi} \int_1^\infty \frac{i \frac{k_1}{\cos\alpha} e^{i \frac{k_1}{\cos\alpha} \xi'} e^{-i \frac{k_1}{\cos\alpha} \xi'} \hat{\Gamma}}{\xi - \xi'} d\xi' \quad (6.18)$$

This integral equation can be solved for $\hat{\Gamma}$ with the help of the
 Söhnngen inversion formula.

When applied to equations (6.18), this formula enables $\hat{\gamma}$ to be
 explicitly expressed in terms of $\hat{\Gamma}$:

$$\hat{\gamma}(\xi) = \frac{2}{\pi} \frac{\sqrt{1-\xi}}{\sqrt{1+\xi}} \int_{-1}^1 \frac{\sqrt{1+\xi'}}{\sqrt{1-\xi'}} \frac{\hat{v}_\eta e^{-ik_1' \xi'}}{\xi - \xi'} d\xi' - \frac{1}{\pi^2} i \frac{k_1}{\cos\alpha} e^{i \frac{k_1}{\cos\alpha} \xi} \hat{\Gamma} \frac{\sqrt{1-\xi}}{\sqrt{1+\xi}} \int_{-1}^1 \frac{\sqrt{1+\xi'}}{\sqrt{1-\xi'}} \left[\int_1^\infty \frac{e^{-i \frac{k_1}{\cos\alpha} \xi''}}{\xi' - \xi''} d\xi'' \right] \frac{d\xi'}{\xi - \xi'} \quad (6.19)$$

When equation (6.19) is integrated with respect to ξ from -1 to +1,
 an equation in one unknown only ($\hat{\Gamma}$) results. (The mathematical
 details are very similar to those of the $\alpha = 0$ theory: refer to
 Bisplinghoff, et. al.). The solution for $\hat{\Gamma}$ is:

$$\hat{\Gamma} = \frac{4 \hat{v}_y [J_0(k_1') - i J_1(k_1')]}{i \frac{k_1}{\cos \alpha} e^{i \frac{k_1}{\cos \alpha} x} [H_1(\frac{k_1}{\cos \alpha}) + i H_0(\frac{k_1}{\cos \alpha})]} \quad \dots (6.20)$$

6.3.2.3 Determination of L_P . Equation (6.13), derived previously, is the relevant equation:

$$L_{P/\rho} = - \left[i \omega \int_{-1}^1 \int_{-1}^{\xi} \gamma(\xi') d\xi' d\xi + V_{\xi} \int_{-1}^1 \gamma(\xi) d\xi \right].$$

Using the mathematical identity, $\int_{-1}^{\xi} \int_{-1}^{\xi'} \gamma d\xi' d\xi = \int_{-1}^1 \gamma d\xi - \int_{-1}^1 \gamma \xi d\xi$, this equation transforms to:

$$L_{P/\rho} = - \left[i \omega \hat{\Gamma} - i \omega \int_{-1}^1 \xi \hat{\gamma} d\xi + V_{\xi} \hat{\Gamma} \right] e^{i \omega t} \quad \dots (6.21)$$

The integral, $\int_{-1}^1 \xi \hat{\gamma} d\xi$ is evaluated by multiplying equation (6.19) by ξ and integrating. The result is in terms of the circulation, $\hat{\Gamma}$:

$$\int_{-1}^1 \xi \hat{\gamma} d\xi = 2 \hat{v}_y \pi \frac{J_1(k_1')}{k_1'} - i \frac{(1 + i \frac{k_1}{\cos \alpha}) \hat{\Gamma}}{k_1 / \cos \alpha} + e^{i \frac{k_1}{\cos \alpha} x} \frac{\pi}{2} H_1(\frac{k_1}{\cos \alpha}) \hat{\Gamma} \quad (6.22)$$

Finally, by substituting equations (6.22) and (6.20) into equation (6.21), an expression for L_P in terms of the known gust properties is derived. Further substitution of $V_{\xi} = \cos \alpha$, $\hat{v}_y = \hat{v}_z \cos \alpha + \hat{v}_1 \sin \alpha$, and $k_1' = k_1 \cos \alpha - k_2 \sin \alpha$ enables the load to be expressed in terms of the gust properties referred to the x, y, z frame (refer to 6.3.1.2). The result is:

$$C_{L_P} = \frac{L_P}{\rho U_{\infty}^2} = 2\pi \left\{ \frac{H_1(\frac{k_1}{\cos \alpha}) [J_0(k_1') - i J_1(k_1')]}{H_1(\frac{k_1}{\cos \alpha}) + i H_0(\frac{k_1}{\cos \alpha})} + i \frac{k_1}{\cos \alpha} \frac{J_1(k_1')}{k_1'} \right\} \left\{ \frac{\hat{v}_z}{U_{\infty}} \cos^2 \alpha + \frac{\hat{v}_1}{U_{\infty}} \cos \alpha \sin \alpha \right\} e^{i \omega t}, \quad \dots (6.23)$$

where $k_1' = k_1 \cos \alpha - k_2 \sin \alpha$.

For $\alpha = 0$, this result reduces, as expected, to the Sears' formula (refer to 1.2.2).

Further simplifications to equation (6.23), correct to order are possible with the following substitutions:

$$\begin{aligned}\cos \alpha &\approx \cos^2 \alpha \approx 1.0, \\ \sin \alpha &\approx \sin \alpha \cos \alpha \approx \alpha.\end{aligned}$$

The validity of these substitutions (to order $(\alpha \epsilon)$) is evident when the trigonometrical functions are expanded as power series in α .

Further, it is clear that, with these simplifications, the expression for C_{LP} is not critically dependent on the wake model: if the wake had been assumed to be in the free stream direction, the final expression for C_{LP} would have been the same. This final expression is:

$$\begin{aligned}C_{LP} &= 2\pi \left\{ \frac{H_1(k_1)[J_0(k_1 - \alpha k_2) - iJ_1(k_1 - \alpha k_2)] + ik_1 J_1(k_1 - \alpha k_2)}{H_1(k_1) + iH_0(k_1)} \right\} \left\{ \frac{\hat{v}_2}{U_\infty} + \alpha \frac{\hat{v}_1}{U_\infty} \right\} e^{i\omega t} \\ &= 2\pi S'(k_1, k_1 - \alpha k_2) \left\{ \frac{\hat{v}_2}{U_\infty} + \alpha \frac{\hat{v}_1}{U_\infty} \right\} e^{i\omega t}, \quad \dots (6.24)\end{aligned}$$

where S' is the generalized Sears function, which arises also in the $O(\epsilon)$ theory for a non-frozen gust, and which has been defined in equation (1.2).

It is clear that the generalized response function, S' , will arise whenever the spatial wavenumber along the aerofoil chord differs from the wavenumber defined by: ω/U_∞ . For the $O(\epsilon)$ non-frozen gust theory, these two wavenumbers are k_s and k_f respectively. In the above analysis they are $(k_1 - \alpha k_2)$ and k_1 respectively.

6.3.2.4 Subdivision of C_{LP} . It is convenient to separate C_{LP} into its order (ϵ) and order $(\alpha \epsilon)$ components. As a first step:

$$C_{LP} = 2\pi S'(k_1, k_1 - \alpha k_2) \frac{\hat{v}_2}{U_\infty} e^{i\omega t} + \alpha 2\pi S(k_1) \frac{\hat{v}_1}{U_\infty} e^{i\omega t}.$$

Note that $S'(k_1, k_1 - \alpha k_2)$ has been replaced by $S(k_1)$ in the second term: the magnitude of this alteration is necessarily of order $(\alpha^2 \epsilon)$ at least.

$S'(k_1, k_1 - \alpha k_2)$ can be expanded as a power series in α , the first two terms of which are:

$$S(k_1) + \alpha S_A(k_1, k_2) ,$$

$$\text{where } S_A(k_1, k_2) = k_2 \left\{ \frac{H_1(k_1) [J_1(k_1) - iJ^+(k_1)]}{H_1(k_1) + iH_0(k_1)} + i \left[J^+(k_1) + \frac{J_1(k_1)}{k_1} \right] \right\} \dots (6.25)$$

$$\text{and } J^+(k_1) = [J_2(k_1) - J_0(k_1)] / 2 .$$

Details of the expansion are given in Appendix 3. The expression,

$S(k_1) + \alpha S_A(k_1, k_2)$ is the correct asymptotic form of $S'(k_1, k_1 - \alpha k_2)$ as α tends toward 0.

And thus:

$$\left. \begin{aligned} C_{LP} &= C_{LS} + C_{LA1} + C_{LA2} , \\ \text{where} \\ C_{LS} &= 2\pi \cdot S(k_1) \cdot \hat{v}_2 / U_\infty \cdot e^{i\omega t} , \\ C_{LA1} &= \alpha 2\pi \cdot S(k_1) \cdot \hat{v}_1 / U_\infty \cdot e^{i\omega t} , \\ C_{LA2} &= \alpha 2\pi S_A(k_1, k_2) \cdot \hat{v}_2 / U_\infty \cdot e^{i\omega t} . \end{aligned} \right\} (6.26)$$

C_{LS} is the first order (order (ϵ)) response, previously derived by Sears. C_{LA1} is of order ($\alpha\epsilon$), and is effectively a Sears-type response to the component of \hat{v}_1 which is perpendicular to the aerofoil chord (that is, it is a type (1) complication described in section 1.2.3). C_{LA2} is also of order ($\alpha\epsilon$), and is the extra response term which arises because the spatial wavenumber of the gust along the aerofoil chord line differs from ω / U_∞ (a type (2) complication).

6.3.3 Analysis for L_D

6.3.3.1 The vorticity transport equation. This is employed to determine the distortion of the gust vorticity. The exact, inviscid form of this equation can be derived by taking the curl of the equation of motion given earlier (equation (6.3)):

$$\frac{\partial \underline{y}^T}{\partial t} + (\underline{V}^T \cdot \nabla) \underline{y}^T = (\underline{y}^T \cdot \nabla) \underline{V}^T \quad \dots (6.27)$$

where, for this problem, $\underline{V}^T = V_1^T \hat{c} + V_2^T \hat{j}$ and $\underline{y}^T = y^T \hat{k}$.

Although, at the outset of this analysis, completely inviscid flow has been assumed, the assumption is more questionable when the transport of vorticity is being considered (the above equation, (6.27)) than when the relationship between velocities and pressures is being considered (equation (6.3)). For the latter, the predominate effects of viscosity are confined to the boundary layers where vorticity is generated due to the presence of the body surface. At Reynolds Numbers of practical interest for aerfoils with attached flow, the boundary layer is so small that the effect of viscosity on the lift is negligible. On the other hand, free stream vorticity will be affected by viscous action throughout the flow field, some viscous dissipation of vorticity occurring simultaneously with the mean field distortion described by equation (6.27). Other workers (for example Hunt (1973) and Graham (1975)) have compared the orders of magnitude of the dissipation effect and the distortion effect; and have found that, in many practical situations, the Reynolds Number and the scale of the gust are sufficiently large to allow the dissipation to be ignored in comparison with the distortion. For the case of free stream turbulence, the conditions are that $(\text{Re No.})^{-1} \ll \epsilon \ll \min(\frac{L}{c}, 1)$ and $(\text{Re No.})^{\frac{1}{2}} \gg \max(\frac{c}{L}, 1)$ (refer to the previous discussion of the rapid distortion theory, section 1.2.4.2).

Anyway, with the inviscid assumption, equation (6.27) is completely correct. For the case of the two-dimensional gust, only the z component of this equation is non-trivial:

$$\frac{\partial y^T}{\partial t} + V_1^T \frac{\partial y^T}{\partial x} + V_2^T \frac{\partial y^T}{\partial y} = 0. \quad \dots (6.28)$$

Now, as defined in sections 6.2 and 6.3: $\mathcal{J}^T = \mathcal{J}_\infty + \mathcal{J}$ and $\mathcal{J}_\infty = \int_{-\infty}^{\infty} e^{i(\omega t - k_1 x - k_2 y)}$. . . (6.29)

If the gust distortion system is a linear one, the distorted velocity will be of the form:

$$\tilde{v}_i = \hat{v}_i(x, y) \cdot e^{i(\omega t - k_1 x - k_2 y)} \text{ where } \hat{v}_i \text{ is of order } (\alpha E) \quad \dots (6.30)$$

\tilde{v}_i is the Biot-Savart velocity field for \mathcal{J} , so that \mathcal{J} is of the form:

$$\mathcal{J} = \hat{\mathcal{J}}(x, y) \cdot e^{i(\omega t - k_1 x - k_2 y)} \quad \dots (6.31)$$

$$\text{where } \hat{\mathcal{J}}(x, y) = ik_2 \hat{v}_1 - ik_1 \hat{v}_2 + \frac{\partial \hat{v}_2}{\partial x} - \frac{\partial \hat{v}_1}{\partial y}.$$

Because \hat{v}_i will change by an order of magnitude over the order of an aerofoil chord length, the latter two terms of $\hat{\mathcal{J}}$ are of order (αE) . The former terms are of order $(k\alpha E)$.

Consequently,

$$\left. \begin{aligned} \frac{\partial \mathcal{J}}{\partial x} &= (-ik_1 \hat{\mathcal{J}} + \frac{\partial \hat{\mathcal{J}}}{\partial x}) e^{i(\omega t - k_1 x - k_2 y)} \\ \text{and} \quad \frac{\partial \mathcal{J}}{\partial y} &= (-ik_2 \hat{\mathcal{J}} + \frac{\partial \hat{\mathcal{J}}}{\partial y}) e^{i(\omega t - k_1 x - k_2 y)} \end{aligned} \right\} (6.32)$$

Using the above results and reasoning, the first term in each case (for example, $-ik_1 \hat{\mathcal{J}}$) is of order $(k^2 \alpha E, k\alpha E)$ while the second term is of order $(k\alpha E, \alpha E)$.

Also, from section 6.2:

$$\left. \begin{aligned} V_1^T &= U_\infty + V_1' + v_1 + v_1' + \tilde{v}_1 + \tilde{v}_1' \\ V_2^T &= V_2' + v_2 + v_2' + \tilde{v}_2 + \tilde{v}_2' \end{aligned} \right\} (6.33)$$

Substituting from equations (6.29), (6.32), and (6.33) into equation (6.28), and retaining terms of order $(k^2 \alpha E)$, $(k\alpha E)$, and (αE) yields:

$$U_\infty \frac{\partial \hat{\zeta}}{\partial x} - ik_1 V_1' \hat{\zeta}_\infty - ik_2 V_2' \hat{\zeta}_\infty = 0 \quad \dots (6.34)$$

$$O(\alpha \epsilon, k \alpha \epsilon) \quad O(k^2 \alpha \epsilon) \quad O(k^2 \alpha \epsilon)$$

Consider now the three cases:

- (1) k of order (1). In this case, the three terms in equation (6.34) are of similar order, and the equation is certainly valid.
- (2) k is much less than 1. The equation tends to $U_\infty \frac{\partial \hat{\zeta}}{\partial x} = 0$; that is, the distortion tends to zero, as expected. The equation is clearly applicable to this case too.
- (3) k is much greater than 1. In this case, $\frac{\partial \hat{\zeta}}{\partial x}$ is necessarily of order $(k^2 \alpha \epsilon)$, the order of the other terms. This means that some of the order-of-magnitude analysis leading to equation (6.34) needs reassessment when $k \gg 1$. When this is attempted, it is found that other non-linear terms, ignored in the original analysis, need to be included. In other words, the linearization of the vorticity transport equation, resulting in equation (6.34), is not valid when $k \gg 1$. Even if the equation were valid, its application when $k \gg 1$ would be of doubtful accuracy because, in a real flow, viscous effects would become important with the scale of the gust much less than the aerofoil chord.

The linearized vorticity transport equation, (6.34), can be readily integrated:

$$\hat{\zeta}(x, y) = \left\{ ik_1 \int_{-\infty}^x \frac{V_1'}{U_\infty} dx' + ik_2 \int_{-\infty}^x \frac{V_2'}{U_\infty} dx' \right\} \hat{\zeta}_\infty \quad \dots (6.35)$$

6.3.3.2 Outline of the method of analysis. The distortion produced by a sinusoidal distribution of mean vorticity, $K'(x) = e^{-i\lambda x}$, is determined first. With this input, the resultant distorted upwash

gust, \hat{v}_2 , is of a simple sinusoidal form; and the lift response to this, C'_{LD} , can be readily determined via equation (6.14).

(Whereas, if one attempts to analyze directly for $K(x) = -2U_\infty \alpha \sqrt{\frac{1-x}{1+x}}$ the solution of equation (6.14) is difficult). Fourier analysis methods are used to determine the required lift response, C_{LD} , corresponding to $K(x) = -2U_\infty \alpha \sqrt{\frac{1-x}{1+x}}$ from the expression for C'_{LD} .

However, the Fourier integration in the final step is improper unless precautions are taken. The singularity in the integrand has its origins in the $\int_{-\infty}^x \frac{v'_2}{U_\infty} dx'$ term in equation (6.35). A lifting aerofoil produces a vortex-like disturbance to the mean flow; that is $v'_2 \sim \frac{1}{x}$ as x tends to $\pm \infty$. Thus, for any body with significant mean lift, $\int_{-\infty}^x \frac{v'_2}{U_\infty} dx'$ is improper. Graham (1975) encountered a similar problem in the $\int_{-\infty}^x \frac{v'_1}{U_\infty} dx'$ term for a body with significant mean drag.

Following Graham:

$$\int_{-\infty}^x \frac{v'_2}{U_\infty} dx' \text{ is replaced by } \int_0^x \frac{v'_2}{U_\infty} dx' + \int_{-\infty}^0 \frac{v'_2 - v_2(y=0)}{U_\infty} dx', \quad \dots (6.36)$$

From equation (6.35):

$$\begin{aligned} \hat{S}^T &= (1 + ik_1 \int_{-\infty}^x \frac{v'_1}{U_\infty} dx' + ik_2 \int_{-\infty}^x \frac{v'_2}{U_\infty} dx') \hat{S}_\infty \\ &= \hat{S}_\infty e^{i(k_1 \int_{-\infty}^x \frac{v'_1}{U_\infty} dx' + k_2 \int_{-\infty}^x \frac{v'_2}{U_\infty} dx')} \end{aligned} \quad \text{correct to order } (k\alpha\epsilon).$$

The latter step can be proved by expansion of the exponential as a power series. Thus replacing $\int_{-\infty}^x \frac{v'_2}{U_\infty} dx'$ as above, merely alters the overall phase of the solution for the nett vorticity, \hat{S}^T , by a constant $e^{-ik_2 Y}$ (to order $(k\alpha\epsilon)$),

where $Y = \int_{-\infty}^0 \frac{v_2(y=0)}{U_\infty} dx'$, an indeterminate constant.

The phase of the final lift response ($C_{LP} + C_{LD} + C_{LM}$) will thus be referenced to a gust, $\hat{S}_\infty e^{-ik_2 Y}$, rather than the gust, \hat{S}_∞ , originally considered. With a vortex-type mean disturbance in an

infinite field, the gust which arrives at the aerofoil has originated at the point, $(-\infty, -\infty)$. The introduction of the phase shift, e^{-ik_2Y} , means that the gust phase at the aerofoil is related to the gust phase at the point, $(-\infty, \text{some finite } y \text{ value})$. This adjustment does have relevance to real physical flows contained in finite fields. For example, in a wind tunnel experiment, measurements of the gust can obviously not be made at $(-\infty, -\infty)$. One can effectively measure the gust at " $x = -\infty$ " by removing the aerofoil but one has to be content with a measurement at finite y , or, in the case of a turbulent gust, to assume homogeneous turbulence.

In the next sub-section, the principle steps of the analysis and the general form of the results are given. The analysis is repeated with full mathematical details in Appendix 4.

6.3.3.3 The analysis

The mean perturbation velocities, V_1' and V_2' , produced by the vortex distribution, $K(x) = e^{-i\lambda x}$, are evaluated by an application of the Biot-Savart Law in its one-dimensional form:

$$V_1' = -\frac{y}{2\pi} \int_{-\infty}^{\infty} \frac{e^{-i\lambda x'} dx'}{(x-x')^2 + y^2}, \quad V_2' = \frac{1}{2\pi} \int_{-\infty}^{\infty} \frac{e^{-i\lambda x'} (x-x') dx'}{(x-x')^2 + y^2}$$

The integrals can be evaluated analytically.

A corresponding expression for $\hat{S}(x, y)$ is derived by substitution of these results into equation (6.35). The integrals, $\int_{-\infty}^x \frac{V_1'}{U_\infty} dx'$ and $\left\{ \int_0^x \frac{V_2'}{U_\infty} dx' + \int_{-\infty}^0 \frac{V_2' - V_2'(y=0)}{U_\infty} dx' \right\}$, can also be determined analytically.

The extra upwash, $\tilde{v}_2(x, 0)$ produced by distortion (that is corresponding to \hat{S}) is determined by an application of the Biot-Savart Law in its two-dimensional form:

$$\tilde{v}_2(x, 0) = \frac{1}{2\pi} \iint_{-\infty}^{\infty} \frac{\hat{S}(x', y') e^{i(\omega t - k_1 x' - k_2 y')}}{(x-x')^2 + y'^2} dx' dy'$$

The analytical evaluation of this double integral is straight-forward but tedious. The final result has analytical expressions which are

different in different parts of the complete λ range from $-\infty$ to $+\infty$.

The lift response, C'_{LD} , to the upwash, $\tilde{v}_2(x,0)$, is derived by solving the following equation (equation (6.14) formulated previously):

$$L'_{D/\rho} = - \left[i\omega \int_{-1}^1 \int_{-1}^x \tilde{\gamma}(x') dx' dx + U_\infty \int_{-1}^1 \tilde{\gamma}(x) dx \right] \quad \dots (6.14)$$

Terms in the derived $\tilde{v}_2(x,0)$ expression are of two basic forms:

$$(1) \quad \hat{v}_2 e^{i(\omega t - k_1 x)},$$

$$(2) \quad \hat{v}_2 e^{i(\omega t - [k_1 + \lambda]x)},$$

where \hat{v}_2 is a function of k_1 , k_2 , and λ in this case.

The solution of equation (6.14) for an upwash of the form (1) is provided by the theory of Sears:

$$C'_{LD} = 2\pi S(k_1) \hat{v}_2 / U_\infty e^{i\omega t},$$

while the solution for an upwash of the form (2) is given by the generalized Sears result, first reported by Kemp:

$$C'_{LD} = 2\pi S'(k_1, k_1 + \lambda) \hat{v}_2 / U_\infty e^{i\omega t}.$$

The formulae for the response functions, $S(k_1)$ and $S'(k_1, k_1 + \lambda)$ have been detailed in section 1.2.2.

Thus, formulae for C'_{LD} can be written down directly from the derived $\tilde{v}_2(x,0)$ formulae. For convenience, C'_{LD} is divided into its even and odd parts as a function of λ , denoted by C'_{LE} and C'_{LO} respectively:

$$C'_{LD} = C'_{LE} + C'_{LO}$$

$$\text{where } C'_{LE} = \pi \hat{J}_\infty / U_\infty \cdot B_E(k_1, k_2, \lambda) e^{i\omega t}, \quad \dots (6.37)$$

$$\text{and } C'_{LO} = \pi \hat{J}_\infty / U_\infty \cdot B_O(k_1, k_2, \lambda) e^{i\omega t}.$$

The functions B_E and B_0 are listed in the appendix.

The final lift response, C_{LD} is determined from C'_{LD} using a Fourier integral technique. From the properties of Fourier transforms it can be shown that, if C'_{LD} is the response to $K'(x) = e^{-i\lambda x}$, then the response to a general $K(x)$ is given by:

$$C_{LD} = \frac{1}{\sqrt{2\pi}} \int_{-\infty}^{\infty} \bar{K}(\lambda) \cdot C'_{LD}(\lambda) d\lambda, \quad \dots (6.38)$$

where $\bar{K}(\lambda) = \frac{1}{\sqrt{2\pi}} \int_{-\infty}^{\infty} K(x) e^{i\lambda x} dx.$

This is the mathematical expression of the process (valid for a linear system) of building up the response to a general input by superposition of the responses to the sinusoidal components of that input.

For the particular case of $K(x) = -2U_{\infty} \alpha \sqrt{\frac{1-x}{1+x}}$, equation (6.38) becomes:

$$C_{LD} = U_{\infty} \alpha \int_{-\infty}^{\infty} [J_0(\lambda) + iJ_1(\lambda)] C'_{LD}(\lambda) d\lambda \quad \dots (6.39)$$

Substituting from equation (6.37), and for $\hat{J}_{\infty} = ik_2 \hat{v}_1 - ik_1 \hat{v}_2$ (refer 6.3):

$$C_{LD} = \alpha \cdot 2\pi \cdot D(k_1, k_2) \left\{ k_1 \frac{\hat{v}_2}{U_{\infty}} - k_2 \frac{\hat{v}_1}{U_{\infty}} \right\} e^{i\omega t} \quad \dots (6.40)$$

$$\text{where } D(k_1, k_2) = \int_0^{\infty} [iJ_0(\lambda) B_E(\lambda) + J_1(\lambda) B_0(\lambda)] d\lambda.$$

A complete analytical evaluation of $D(k_1, k_2)$ has not been achieved, although there was some evidence that this may be possible (Analytical results were found for simpler integrals of the same type). In this study, numerical integration was employed for the evaluation of $D(k_1, k_2)$: some results are discussed in section 6.4.

6.3.4 Analysis for L_M . An analytical expression for L_M can be found directly from the formulation of section 6.3.1:

$$L_{M/\rho} = - \int_{-1}^1 K(x) \cdot v_1(x,0) dx,$$

$$\text{where } K(x) = -2U_\infty \alpha \sqrt{\frac{1-x}{1+x}} \text{ and } v_1(x,0) = \hat{v}_1 e^{i(\omega t - k_1 x)}.$$

$$\text{Thus, } L_{M/\rho} = 2U_\infty \alpha \hat{v}_1 e^{i\omega t} \int_{-1}^1 \sqrt{\frac{1-x}{1+x}} e^{-ik_1 x} dx.$$

The integral can be determined analytically and the final result is:

$$C_{LM} = \alpha \cdot 2\pi \cdot M(k_1) \frac{\hat{v}_1}{U_\infty} e^{i\omega t} \quad \text{where } M(k_1) = J_0(k_1) + iJ_1(k_1). \quad \dots (6.41)$$

This response term has been previously derived by Horlock and Morfey (refer 1.2.3)

6.3.5 Summary for the frozen, two-dimensional gust

The total unsteady lift coefficient to order (αE) is:

$$C_L = C_{LS} + C_{LA1} + C_{LA2} + C_{LD} + C_{LM},$$

$$\text{where } C_{LS} = 2\pi S(k_1) \frac{\hat{v}_2}{U_\infty} e^{i\omega t} : \text{order}(E)$$

$$C_{LA1} = \alpha 2\pi S(k_1) \frac{\hat{v}_1}{U_\infty} e^{i\omega t} : \text{order}(\alpha E)$$

$$C_{LA2} = \alpha 2\pi S_A(k_1, k_2) \frac{\hat{v}_2}{U_\infty} e^{i\omega t} : \text{order}(\alpha E)$$

$$C_{LD} = \alpha 2\pi D(k_1, k_2) \left\{ k_1 \frac{\hat{v}_2}{U_\infty} - k_2 \frac{\hat{v}_1}{U_\infty} \right\} e^{i\omega t} : \text{order}(\alpha E)$$

$$C_{LM} = \alpha 2\pi M(k_1) \frac{\hat{v}_1}{U_\infty} e^{i\omega t} : \text{order}(\alpha E)$$

(6.42)

with, from the continuity condition, $\frac{\hat{v}_2}{U_\infty} = -\frac{k_1}{k_2} \frac{\hat{v}_1}{U_\infty}$.

Examination of the formulae in detail shows that $S_A(k_1, 0) = D(k_1, 0) = 0$. Thus for a simple upwash gust of the type, $v_2 = \hat{v}_2 e^{i(\omega t - k_1 x)}$, all the order (αE) response terms disappear; that is, the Sears result is correct to

order ($\alpha \epsilon$) for this particular gust.

6.4 Comparison with the Theory of Goldstein and Atassi

6.4.1 Description of their theory. Goldstein and Atassi (1975) have recently developed a complete order ($\alpha \epsilon$) theory for the case of a frozen, two-dimensional gust. They employed a rigorous asymptotic expansion method, and were able to present general equations (involving integrals) which could, in theory, be solved to yield the higher order unsteady lift of an aerofoil of arbitrary section at incidence. However they solved the equations in detail only for the particular case of the zero-thickness aerofoil. Their solution for this case was fully analytical.

In their analysis, the unsteady velocity, pressure etc. were expanded as asymptotic series in α . The expansions were shown to be not uniformly valid at large distances from the aerofoil; and, thus separate, matching inner and outer expansions were constructed. The inner expansion was substituted into the general inviscid vorticity transport equation, and, by retaining terms to only order ($\alpha \epsilon$), a linearized equation resulted. This equation was solved with the boundary conditions on the aerofoil and at infinity. The latter was not the same condition as that applicable to the outer solution, but a modified condition which allowed matching of the inner and outer solutions. Goldstein and Atassi effectively solved for $\mathcal{V}_i + \mathcal{V}'_i + \tilde{\mathcal{V}}_i + \tilde{\mathcal{V}}'_i$ (the present notation) together. A further complication was that their solution was not uniformly valid at the aerofoil leading edge and trailing edge; and this necessitated an application of the method of strained co-ordinates (which in turn, introduced an extra term into their solution). Finally an equation of motion was used to relate velocities to pressures and thus enable the determination of the

unsteady lift on the aerofoil.

Three further aspects of their analysis are noteworthy:

(1) No mention was made of any limiting conditions (in respect of the gust wavenumber, k) for the validity of their linearized vorticity transport equation.

(2) The inner solution, by itself, did not tend towards the correct quasi-steady solution as $k_1, k_2 \rightarrow 0$. This was consistent with another statement of Goldstein and Atassi that their solution was "not uniformly valid in frequency space". The correct asymptote was recovered by reversing those adjustments to the inner solution which had resulted from the matching of the inner and outer solutions. This contrasts with the present solution for C_L which does tend to the correct quasi-steady asymptote ($2\pi [\hat{v}_2/U_\infty + 2\alpha \hat{v}_1/U_\infty]$) as $k_1, k_2 \rightarrow 0$; a result which implies that the present solution is uniformly valid in frequency space.

(3) The outer solution for the unsteady velocity did not tend towards the correct undistorted gust as $X \rightarrow -\infty$, but to a gust which differed from this by a constant phase difference. Goldstein and Atassi stated that the latter "is frozen relative to an observer moving along the steady state potential flow stream-lines with a speed U_∞ while the former "is frozen w.r.t. an observer moving along the real axis with this speed." For a body with significant lift, the steady streamlines which arrive at the body originate at the point $(-\infty, -\infty)$; and, thus, this problem is equivalent to the singularity problem of the present analysis described in 6.3.3.2. In fact, in their analysis for the zero thickness aerofoil, Goldstein and Atassi referenced the overall phase of their solution to a datum which is exactly equivalent to the datum resulting from equation (6.36) of the current analysis.

6.4.2 Comparison of results. Goldstein and Atassi calculated a higher order response function, \mathcal{R} , of the form (in the current notation):

$$\mathcal{R} = \frac{C_L^{(0)*}}{2\pi\alpha E} e^{-i\omega t} \quad \dots (6.43)$$

where $C_L^{(0)*}$ is the complex conjugate of the order (αE) contribution to C_L . The complex conjugate is required because Goldstein and Atassi consider a gust which has the opposite sign for the frequency, ω .

Thus:

$$C_L^{(0)*} = C_{LA1}^* + C_{LA2}^* + C_{LD}^* + C_{LM}^* .$$

$$\text{Expressing } \frac{\hat{v}_1}{U_\infty} = \frac{-k_2 E}{\sqrt{k_1^2 + k_2^2}} \quad , \quad \text{and } \frac{\hat{v}_2}{U_\infty} = \frac{+k_1 E}{\sqrt{k_1^2 + k_2^2}}$$

(derived from the definition of E and the continuity condition), and substituting from equations (6.42) yields the following formula for \mathcal{R} in the notation of the present study:

$$\mathcal{R} = -\frac{k_2}{\sqrt{k_1^2 + k_2^2}} S^*(k_1) + \frac{k_1}{\sqrt{k_1^2 + k_2^2}} S_A^*(k_1, k_2) + \sqrt{k_1^2 + k_2^2} \cdot D^*(k_1, k_2) - \frac{k_2}{\sqrt{k_1^2 + k_2^2}} M^*(k_1) \quad \dots (6.44)$$

A computer program was written to perform the necessary numerical integration for $D(k_1, k_2)$ and to thereby calculate \mathcal{R} via equation (6.44). It is listed in Appendix 11. In figures 41 and 42, two derived curves for \mathcal{R} (for two values of k_2) are presented. These curves were found to be indistinguishable from the corresponding curves presented by Goldstein and Atassi. This suggests that the present analysis is equivalent to the analysis of Goldstein and Atassi.

Also presented in figures 41 and 42 are the parts of \mathcal{R} which arise only from the distortion effect. It can be seen that the distortion effect term becomes a greater part of \mathcal{R} as k_1 and k_2 increase. Goldstein and Atassi stated that their "analysis shows that behaviour of the response function of a lifting aerofoil is determined to a large extent by the gust distortion effect", and implied that the

Morfev response term is less important. Figure 41 shows that, for wavenumbers which are low but which are still of practical interest (e.g. $k_1 = 0.5$, $k_2 = 0.6$), the distortion term is smaller than the other higher order terms. It must also be remembered that the validity of the linearized distortion theory comes into question when k_1 or $k_2 \gg 1$.

Two noteworthy trends of the higher order response, \mathcal{R} , are:

(1) As the frequency, k_1 , tends to ∞ , \mathcal{R} tends to zero.

From a physical viewpoint this is to be expected. On any body of finite size, the nett unsteady lift must be zero in the limit $k_1 = \infty$.

(2) As k_1 tends to zero with k_2 fixed, \mathcal{R} tends to a definite limit, which is different from the quasi-steady limit with both k_1 and $k_2 \rightarrow 0$. The latter limit for \mathcal{R} is -2.0 . The difference is due to the distortion term: for k_1 and $k_2 \rightarrow 0$, it tends to zero (consistent with the reasoning of 6.3.3.1 and general physical reasoning); but for $k_1 \rightarrow 0$ and k_2 fixed, it tends to a definite non-zero limit (refer again to figures 41 and 42). This latter behaviour is also consistent with physical reasoning: one would expect the "steady" gust, $\hat{u}_1 e^{-ik_2 y}$, to be distorted and thus yield an additional steady upwash on the aerofoil. It has not been ascertained whether the solution of Goldstein and Atassi behaves similarly in this limit. They did not discuss this limit, and their response function curves were only plotted as far as $k_1 \approx 0.1$ (in the decreasing k_1 sense).

5.

6.5 Conclusions Regarding the Higher Order Theory for a Frozen,

Two-Dimensional Gust.

The higher order response function, determined with the current

theory is in good agreement with that derived by Goldstein and Atassi via a different approach. This suggests that, within the prescribed assumptions, the present theory is correct to order $(\alpha \epsilon)$.

The current method of analysis has the advantage of enabling a ready comparison of the different types of higher order effect. The effect of distortion is less important than the other higher order effects when k is less than about 1.0; but its relative importance increases with increasing k .

6.6 Extension of Theory to the Non-frozen, Two-Dimensional Gust.

6.6.1 The gust. The gust has components:

$$v_1 = \hat{v}_1 e^{i(\omega t - k_s x - k_2 y)} ; \quad v_2 = \hat{v}_2 e^{i(\omega t - k_s x - k_2 y)}$$

with $\omega = k_f U_\infty$.

Similarly, the gust vorticity is $\gamma_\infty = \hat{\gamma}_\infty e^{i(\omega t - k_s x - k_2 y)}$.

6.6.2 The non-distortion response terms.

The L_p response can be written down immediately:

$$C_{Lp} = 2\pi \cdot S'(k_f, k_s - \alpha k_2) \left\{ \frac{\hat{v}_2}{U_\infty} + \alpha \frac{\hat{v}_1}{U_\infty} \right\} e^{i\omega t} \quad \dots (6.45)$$

This follows because $(k_s - \alpha k_2)$ is the spatial wave-number along the aerofoil chord line, and $k_f = \omega / U_\infty$. Alternatively this result can be derived by a full repeat of the analysis of 6.3.2 with the altered gust input.

C_{Lp} can be sub-divided as before:

$$\left. \begin{aligned} C_{Ls} &= 2\pi S'(k_f, k_s) \cdot \frac{\hat{v}_2}{U_\infty} e^{i\omega t} \\ C_{LA1} &= \alpha 2\pi S'(k_f, k_s) \cdot \frac{\hat{v}_1}{U_\infty} e^{i\omega t} \\ C_{LA2} &= \alpha 2\pi S'_A(k_f, k_s, k_2) \frac{\hat{v}_2}{U_\infty} e^{i\omega t} \end{aligned} \right\} (6.46)$$

$$\text{where } S'_R(k_f, k_s, k_2) = k_2 \left\{ \frac{H_1(k_f) [J_1(k_s) - i J^+(k_s)]}{H_1(k_f) + i H_0(k_f)} + i \frac{k_f}{k_s} \left(J^+(k_s) + \frac{J_1(k_s)}{k_s} \right) \right\}.$$

The L_M response is not altered:

$$C_{LM} = \alpha 2\pi M(k_s) \frac{\hat{v}_1}{U_\infty} e^{i\omega t}.$$

6.6.3 The distortion response term. The analysis for L_D is more significantly altered. Full details are presented in Appendix 5.

The extra complications arise from the altered form of the linearized vorticity transport equation:

$$i U_\infty (k_f - k_s) \hat{J} + U_\infty \frac{\partial \hat{J}}{\partial x} - i k_s V_1' \hat{J}_\infty - i k_2 V_2' \hat{J}_\infty = 0 \quad \dots (6.47)$$

An attempt was made to solve this equation in the manner of the previous analysis. A general solution of the above differential equation was determined, but, when the boundary condition, $\hat{J} = 0$ at $x = -\infty$, was applied, this solution became indeterminate. It was further noticed that this indeterminacy would arise irrespective of the particular mean flow field (V_1', V_2').

However, a determinate solution was possible by applying the upstream boundary condition (the gust undistorted) at a finite distance, B , from the aerofoil; that is, at $x = -B$. This solution for the unsteady lift response due to distortion is outlined fully in the appendix. The response function was calculated for various B , and it was clear that, as B tends towards ∞ , the response tends to a definite finite limit.

For the purposes of comparison, the frozen gust analysis was repeated for the adjusted upstream boundary condition at $x = -B$. It was found that this solution approaches the original solution (of section 6.3.3) as B tends towards ∞ , provided that an additional term, $-\int_{-B}^0 \frac{V_2'(y=0)}{U_\infty} dx'$, is included in the expression for \hat{J} . This term tends to the correct additional term, $-\int_{-\infty}^0 \frac{V_2'(y=0)}{U_\infty} dx'$ of the original analysis (refer to 6.3.3.2) as $B \rightarrow \infty$. A noteworthy feature of the solution for the non-frozen gust is that no such

additional term need be included: for the non-frozen gust, the fact that $V_2' \sim \frac{1}{x}$ as $x \rightarrow -\infty$ does not lead to any phase singularities (as it does for the frozen gust).

Thus, the solution for the non-frozen gust with $B = \infty$ can be estimated (by the current method) to a given accuracy by choosing a large enough finite value of B , e.g., $B = 100$. However the required computation time, governed by a numerical integration with respect to λ , also increases with increase in the value of B . For practical situations in which the gust is "produced" at a finite distance upstream it is relevant to choose the value of B equal to this distance. But it must be stressed that the subsequent calculation of the response due to distortion is then approximate. Although the upstream boundary condition will be exactly correct for the given practical situation, the Biot-Savart integral is applied over the whole field when determining the distorted upwash.

Figure 44 compares the response functions (due to distortion) for a frozen gust and a non-frozen gust ($k_f = 4.0$), for $k_2 = 3.0$ and $B = 1.4$. This value of B is relevant to the case of blade loading in a turbomachine where the gust incident on a blade row is, to a large extent, produced by the row of blades immediately upstream. (The turbomachine application is dealt with in more detail in section 6.7) Also included in the figure is the response function for a frozen gust with $B = \infty$ (that is, the original theory): the frozen gust function for general B will approach this curve as B is increased from 1.4. In general, the difference between the result for a frozen gust and the result for a non-frozen gust is not great. The largest discrepancy occurs as $k_s \rightarrow 0$, where the "non-frozen" result is noticeably less than the "frozen" one. This is consistent with physical reasoning: one expects the distortion to be reduced as k_f/k_s becomes large (refer also to the appendix).

The mathematical result for the distortion response is:

$$C_{LD} = \alpha 2\pi D'(k_f, k_s, k_z, B) \left\{ k_1 \frac{\hat{v}_2}{U_\infty} - k_2 \frac{\hat{v}_1}{U_\infty} \right\} e^{i\omega t}, \quad \dots (6.48)$$

where $D'(k_f, k_s, k_z, B) = \int_0^\infty \left[i J_0(\lambda) B'_E(\lambda) + J_1(\lambda) B'_O(\lambda) \right] d\lambda.$

and the functions B'_E and B'_O are listed in Appendix 5.

6.6.4 Summary for the non-frozen, two-dimensional gust.

To order ($\alpha \epsilon$), the components of the response are:

$$\left. \begin{aligned} C_{LS} &= 2\pi S'(k_f, k_s) \frac{\hat{v}_2}{U_\infty} e^{i\omega t} \\ C_{LA1} &= \alpha 2\pi S'(k_f, k_s) \frac{\hat{v}_1}{U_\infty} e^{i\omega t} \\ C_{LA2} &= \alpha 2\pi S'_A(k_f, k_s, k_z) \frac{\hat{v}_2}{U_\infty} e^{i\omega t} \\ C_{LD} &= \alpha 2\pi D'(k_f, k_s, k_z, B) \left\{ k_s \frac{\hat{v}_2}{U_\infty} - k_z \frac{\hat{v}_1}{U_\infty} \right\} e^{i\omega t} \\ C_{LM} &= \alpha 2\pi M(k_s) \frac{\hat{v}_1}{U_\infty} e^{i\omega t} \end{aligned} \right\} (6.49)$$

and continuity demands that $\frac{\hat{v}_2}{U_\infty} = -\frac{k_s}{k_z} \frac{\hat{v}_1}{U_\infty}.$

6.7 Application of the Higher Order Theory to the Periodic Loading of Turbomachine Blades.

6.7.1 Turbomachine unsteady flow. There are four basic sources of the unsteady velocity encountered by turboblades:

- (1) aerodynamic interference between moving blade rows.
- (2) interference of a moving blade row with the mean viscous wakes from upstream rows.
- (3) the unsteady velocities in the wakes from upstream rows.
- (4) acoustic sources.

Klock (1972) has published measurements of the flow unsteadiness produced by a rotating blade row. This measured unsteadiness could clearly be divided into:

(A) a low frequency periodic component.

(B) general turbulence over a wide frequency range.

Significant power was associated with both components. In the main, component (A) arises from effects (1) and (2) above, while (B) arises from (3) and (4). It is the loading due to the periodic component which is being considered in the present application.

The question of interest is: which components of the sinusoidal gust response (to order (αE)) are important in the blade loading produced by the typical periodic unsteadiness in a turbo-machine? Clearly, knowledge of the typical wavenumbers of the periodic gust is required.

6.7.2 Periodic gust model. The blade rows are assumed to be two-dimensional aerofoil cascades (as usual). The geometry of the flow through a stator/rotor combination is illustrated in figure 45A. The periodic gust is modelled by $\hat{v}_I e^{-iKY}$. (Refer to the figure for the definition of notation). Betz (see Klock), using a simplified cascade model, has shown that the "gust" produced by (1), above, is of this form; and it is expected that the mean profiles of the stator wakes will also approximate to this form. In the co-ordinate system (X', Y') , moving with the rotor blades, the gust is:

$$\hat{v}_I e^{-iK(Y' + |V_B|t)} \quad \text{where } \underline{V}_B \text{ is the rotor blade velocity.}$$

In figure 45B, the flow incident on a single rotor blade is highlighted. In the (x, y) co-ordinate system aligned with the relative mean stream, the gust is of the following non-frozen, two-dimensional form:

$$\hat{\psi}_1 e^{-i(\omega t - k_s x - k_2 y)}$$

where $\omega = K |\underline{V}_B| = k_f |\underline{V}_R|$ (that is, $k_f = K \frac{|\underline{V}_B|}{|\underline{V}_R|}$),
and $k_s = K \sin \delta_A$; $k_2 = K \cos \delta_A$.

\underline{V}_R is the average incident velocity relative to a rotor blade.

δ_A is the angle between \underline{V}_R and the turbomachine axis.

6.7.3 Typical wavenumbers. From the text of Godsey and Young (1949) data for $\frac{|\underline{V}_B|}{|\underline{V}_R|}$ and δ_A was elicited. A blade-spacing to blade-chord ratio of 1.0 was employed (This is a typical machine value). This led to a value of K of π , and enabled the wavenumbers, k_f , k_s , and k_2 , to be estimated for each pair of $\frac{|\underline{V}_B|}{|\underline{V}_R|}$ and δ_A values. The data, which covered a wide range of compressor and turbine blade types, is summarized in table 3.

6.7.4 The calculation. The lift response function was calculated for the following four wave-number combinations which cover the range of data of table 3.

k_s	k_2	k_f
0.1	3.0	3.5
1.0	3.0	5.0
2.0	2.0	3.5
3.0	1.5	2.0

The non-frozen gust theory of section 6.6 was used, with $B = 1.4$; that is, with the gust considered to be produced at the trailing edge of the upstream blade row, and the rows to be separated by a distance, $0.2c$ (typical machine case). The first order (order (ϵ)) response term was included in the calculation; and an angle of incidence of 10°

(between the blade and \underline{V}_R) was assumed: turboblades generally operate at effective angles of attack of this order. In this way, it was possible to compare the order (ϵ) and the order ($\alpha\epsilon$) contributions. It was not expected that the order ($\alpha\epsilon$) term arising from gust distortion would be estimated to greater than "order of magnitude" accuracy. Firstly, the distortion theory for a non-frozen gust with a finite value of B is not an exact theory (refer to 6.6.3). Secondly it is an over-simplification to consider the gust distortion by the mean field of a single blade: clearly the neighbouring blades in the same row will contribute significantly to the distortion of the oncoming gust.

• The response function which was determined in this calculation is defined by:

$$R' = \frac{C_L^*}{2\pi\epsilon} e^{-i\omega t}$$

where C_L^* is the complex conjugate of the total unsteady response.

That is: $R' = R_S + R_A + R_M + R_D$,

$$\left. \begin{aligned} \text{where } R_S &= C_{L_S}^* / 2\pi\epsilon e^{-i\omega t}, \\ R_A &= (C_{LA1}^* + C_{LA2}^*) / 2\pi\epsilon e^{-i\omega t}, \\ R_M &= C_{LM}^* / 2\pi\epsilon e^{-i\omega t}, \\ R_D &= C_{LD}^* / 2\pi\epsilon e^{-i\omega t}. \end{aligned} \right\} (6.50)$$

The response function without distortion, $R'' = R_S + R_A + R_M$, was also determined.

All the calculations were repeated for the corresponding frozen gusts (with the same values of k_1 and k_2).

The computer program employed for the calculation is listed in Appendix 11.

6.7.5 The results. The results for the four wavenumber combinations and for both non-frozen and frozen gusts are presented in table 4. R_S, R_A, R_M and R_D are given as complex numbers, and $|\mathcal{R}'|$ is compared with $|\mathcal{R}''|$.

Features of the results were:

- (1) For the non-frozen gusts (with typical turbomachine wavenumbers):
 - (a) the higher order terms, R_A, R_M and R_D were of similar order in all cases.
 - (b) the combined higher order response ($R_A + R_M + R_D$) was significant. In fact, when k_S was less than k_2 , this response was at least as great as the first order response, R_S .
 - (c) for the four cases considered, neglect of the distortion resulted, respectively, in the following alterations to the modulus of total response: +15%, -2%, -7%, -32%.
- (2) When the gusts were assumed to be frozen, the calculated total responses were markedly different from the above, due to the large effect of the Sears-type responses, R_S and R_A .

6.8 Conclusions Regarding the Application of the Theory to Turboblade Loading.

The theory has been applied to a blade, operating at an effective angle of incidence of 10° , and subjected to a gust which is representative of the periodic unsteadiness in a turbomachine. The calculations have shown that the following two effects need to be included when estimating the unsteady load on such a turboblade:

- (1) The effect of the "non-frozen" nature of the gust.

- (2) The effect of the higher order (order $(\alpha \epsilon)$) response terms arising in the theory.

Of these latter terms, the distortion term, as formulated in the present theory, is the least accurate and the most difficult to calculate. When k_f is greater than k_s and when k_s and k_z are of similar order (a common situation in a turbomachine), the distortion term is relatively small, and it is recommended that it be ignored in this case.

6.9 Theory for the Frozen Three Dimensional Gust

This theory is developed, primarily, as a basis for the higher order turbulent loading theory of the next chapter. However the theory can be applied directly to some problems of practical interest; for example, to the problem of a two-dimensional gust incident upon a swept wing. This latter application is considered further in section 6.9.8.

6.9.1 Additional complications which arise when the gust is three-dimensional.

6.9.1.1 The gust. The gust has three velocity components of the following form:

$$v_i = \hat{v}_i e^{i(\omega t - k_1 x - k_2 y - k_3 z)} \quad \text{with } \omega = k_1 U_\infty.$$

Continuity requires that $k_1 \hat{v}_1 + k_2 \hat{v}_2 + k_3 \hat{v}_3 = 0$.

Associated with this gust velocity, there are three components of vorticity:

$$\hat{j}_{i\infty} = \hat{j}_{i\infty} e^{i(\omega t - k_1 x - k_2 y - k_3 z)}$$

$$\begin{aligned} \text{where } \hat{j}_{1\infty} &= -ik_2 \hat{v}_3 + ik_3 \hat{v}_2 \\ \hat{j}_{2\infty} &= -ik_3 \hat{v}_1 + ik_1 \hat{v}_3 \\ \hat{j}_{3\infty} &= -ik_1 \hat{v}_2 + ik_2 \hat{v}_1. \end{aligned}$$

6.9.1.2 Aerofoil vorticity. The unsteady bound vorticity has, in general, another component in the chordwise direction, which arises because of the upwash variation in the spanwise direction. The shed vorticity in the wake will also have two such components. These vorticity components are subscripted according to the convention described in 6.3.1.1.

The boundary condition for the unsteady upwash is satisfied by the induced velocities of the unsteady vorticity (bound and shed) in two co-ordinate directions. The mean flow is unaltered; that is, the steady bound vorticity is still satisfied by $K(x) = -2U_\infty \alpha \sqrt{\frac{1-x}{1+x}}$.

6.9.2 Problem formulation. The instantaneous velocity to order ($\alpha \epsilon$) is:

$$V_i^T = V_i + V_i' + v_i + v_i' + \tilde{v}_i + \tilde{v}_i' ,$$

as before.

Following the two-dimensional analysis:

(1) On the aerofoil upper surface:

$$V_{\xi U}^T = V_\xi - \frac{K}{2} + v_\xi - \frac{\gamma_3}{2} + \tilde{v}_\xi - \frac{\tilde{\gamma}_3}{2}$$

$$V_\eta^T = 0 \quad : \text{the boundary condition}$$

$$V_{3U}^T = v_3 - \frac{\gamma_\xi}{2} + \tilde{v}_3 - \frac{\tilde{\gamma}_\xi}{2}$$

(2) On the aerofoil lower surface:

$$V_{\xi L}^T = V_\xi + \frac{K}{2} + v_\xi + \frac{\gamma_3}{2} + \tilde{v}_\xi + \frac{\tilde{\gamma}_3}{2}$$

$$V_\eta^T = 0$$

$$V_{3L}^T = v_3 + \frac{\gamma_\xi}{2} + \tilde{v}_3 + \frac{\tilde{\gamma}_\xi}{2}$$

(6.51)

where γ_ξ and γ_3 satisfy the boundary condition for the velocity field, v_i ,

and $\tilde{\gamma}_\xi$ and $\tilde{\gamma}_3$ satisfy the boundary condition for the velocity field, \tilde{v}_i .

The relationship between velocities and pressures is still governed by

equation (6.4):

$$\frac{\partial \underline{V}^T}{\partial t} - \underline{V}^T \times \underline{J}^T = -\nabla \left(\frac{1}{2} |\underline{V}^T|^2 + \frac{p}{\rho} \right) \quad \dots (6.4)$$

In this case, in the (ξ, η, z) reference frame:

$$\underline{V}^T = V_\xi^T \hat{i} + V_\eta^T \hat{j} + V_z^T \hat{k},$$

and $\underline{J}^T = J_\xi^T \hat{i} + J_\eta^T \hat{j} + J_z^T \hat{k}.$

and the equation, integrated with respect to ξ , becomes:

$$\frac{\partial}{\partial t} \int_{-\infty}^{\xi} V_\xi^T d\xi' - \int_{-\infty}^{\xi} [V_\eta^T J_z^T - V_z^T J_\eta^T] d\xi' = -\left(\frac{1}{2} |\underline{V}^T|^2 + \frac{p}{\rho} \right) \quad \dots (6.52)$$

Equation (6.52) is applied to corresponding points on the upper and lower surfaces (using the equations (6.51)). The equations are subtracted, and terms of higher than order $(\alpha \epsilon)$ are ignored. Integration of the pressure difference over the aerofoil chord and removal of the time mean part of the equation yields an expression for the unsteady lift force. The expression is sub-divided and further simplified in the manner of 6.3.1.7, and the resultant components are:

$$(a) \quad \frac{L_D}{\rho} = - \left[i\omega \int_{-1}^1 \int_{-1}^{\xi} \gamma_3(\xi', z) d\xi' d\xi + V_\xi \int_{-1}^1 \gamma_3(\xi, z) d\xi \right] \quad \dots (6.53)$$

where $\gamma_\xi(\xi, z)$ and $\gamma_3(\xi, z)$ satisfy the boundary condition for \tilde{v}_η .

$$(b) \quad \frac{L_D}{\rho} = - \left[i\omega \int_{-1}^1 \int_{-1}^x \tilde{\gamma}_3(x', z) dx' dx + U_\infty \int_{-1}^1 \tilde{\gamma}_3(x, z) dx \right] \quad \dots (6.54)$$

where $\tilde{\gamma}_1(x, z)$ and $\tilde{\gamma}_3(x, z)$ satisfy the boundary condition for \tilde{v}_2 , and \tilde{v}_2 is the additional upwash produced by the distortion of $J_{1\infty}$, $J_{2\infty}$, and $J_{3\infty}$ by the mean field:

$$K(x) = -2 U_\infty \alpha \sqrt{\frac{1-x}{1+x}}.$$

(c)

$$L_{M/p} = - \int_{-1}^1 K(x) \cdot v_1(x, 0, z) dx \quad \dots (6.55)$$

6.9.3 Analysis for L_P . The order (ϵ) result of Graham (refer to 1.2.2) is:

$$C_L = 2\pi \cdot G(k_1, k_3) \cdot \frac{\hat{v}_2}{U_\infty} e^{i(\omega t - k_3 z)}$$

When Graham's analysis is repeated for the zero-thickness aerofoil at incidence, α , and equation (6.53) is thereby solved, the response is of the form:

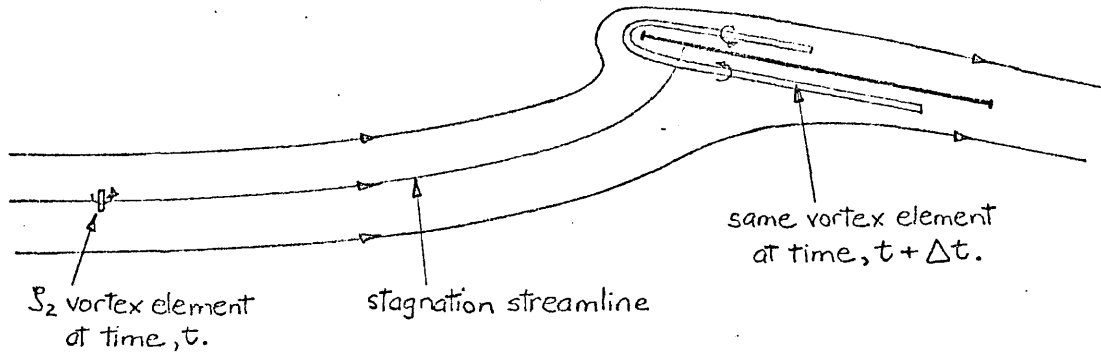
$$C_{L_P} = 2\pi \cdot G'(k_1, k_1 - \alpha k_2, k_3) \cdot \left\{ \frac{\hat{v}_2}{U_\infty} + \alpha \frac{\hat{v}_1}{U_\infty} \right\} e^{i(\omega t - k_3 z)} \dots (6.56)$$

G' is the generalized Graham function, already considered in section 1.2.2 for the case of the order (ϵ) response to a non-frozen three-dimensional gust. Just as for the two-dimensional function, S' , G' will arise whenever the spatial wave-number along the chord line differs from $\frac{\omega}{U_\infty}$. In the above analysis, these wavenumbers are $(k_1 - \alpha k_2)$ and k_1 , respectively. At this point in time, the "exact" response functions, G' and G , can be evaluated only via a complicated numerical route.

6.9.4 Analysis for L_D . This is a linear analysis, paralleling the two-dimensional case: the distorted velocity field is determined first, and then the boundary condition on the aerofoil is satisfied for this field. Appendix 6 gives the full details.

It is relevant to consider how a $\int_{2\infty}$ vortex element, which initially straddles the mean stagnation streamline, is distorted by the mean field. (This component of gust vorticity was not present in the two-dimensional problem). Such a vortex element will be stretched tremendously as it approaches the stagnation point. With the inviscid flow idealization it will be stretched an infinite amount when it reaches

the body (although this will require an infinite time). Furthermore, there will be a "pile-up" of these greatly stretched vortex elements on the body surface.



This "stagnation streamline singularity" has been considered in detail in the theories of Lighthill (1956) and Hunt (1973) (both for the particular case of a circular cylinder). They have demonstrated that the "infinitely-stretched" vortex element induces an infinite velocity on the body surface in the z direction; but the induced velocity perpendicular to the surface (before the surface boundary condition is satisfied) remains finite.

In the present analysis, attention is focussed on the calculation of the upwash velocity perpendicular to the aerofoil surface. The distortion theory does not predict any singularities in this component of velocity.

As before, the exact inviscid vorticity transport equation is:

$$\frac{\partial \underline{\zeta}^T}{\partial t} + (\underline{V}^T \cdot \nabla) \underline{\zeta}^T = (\underline{\zeta}^T \cdot \nabla) \underline{V}^T \quad \dots (6.27)$$

Or, for the i th component:

$$\frac{\partial \zeta_i^T}{\partial t} + V_1^T \frac{\partial \zeta_i^T}{\partial x} + V_2^T \frac{\partial \zeta_i^T}{\partial y} + V_3^T \frac{\partial \zeta_i^T}{\partial z} = \zeta_1^T \frac{\partial V_i^T}{\partial x} + \zeta_2^T \frac{\partial V_i^T}{\partial y} + \zeta_3^T \frac{\partial V_i^T}{\partial z} \dots (6.57)$$

In the determination of the distorted upwash, \tilde{v}_2 , only those components of vorticity that contribute to it, namely ζ_1 and ζ_3 , need be considered.

If the gust distortion system is linear, then, as demonstrated

in 6.3.3.1:

$$\frac{\partial \hat{S}_i}{\partial x} = (-ik_1 \hat{S}_i + \frac{\partial \hat{S}_i}{\partial x}) e^{i(\omega t - k_1 x - k_2 y - k_3 z)},$$

where \hat{S}_i and $\frac{\partial \hat{S}_i}{\partial x}$ are of order $(\alpha \epsilon, k \alpha \epsilon)$.

The derivatives, $\frac{\partial \hat{S}_i}{\partial y}$ and $\frac{\partial \hat{S}_i}{\partial z}$, are of a similar form.

The expansions for \hat{S}_i^T and V_i^T are substituted into equation (6.57), and terms of order $(k^2 \alpha \epsilon)$, $(k \alpha \epsilon)$ and $(\alpha \epsilon)$ are retained. The resultant equations for $i = 1$ and $i = 3$ are:

$$\left. \begin{aligned} U_\infty \frac{\partial \hat{S}_1}{\partial x} - ik_1 V_1' \hat{S}_{1\infty} - ik_2 V_2' \hat{S}_{1\infty} &= \hat{S}_{1\infty} \frac{\partial V_1'}{\partial x} + \hat{S}_{2\infty} \frac{\partial V_1'}{\partial y} \\ O(\alpha \epsilon, k \alpha \epsilon) \quad O(k^2 \alpha \epsilon) \quad O(k^2 \alpha \epsilon) \quad O(k \alpha \epsilon) \quad O(k \alpha \epsilon) & \\ U_\infty \frac{\partial \hat{S}_3}{\partial x} - ik_1 V_1' \hat{S}_{3\infty} - ik_2 V_2' \hat{S}_{3\infty} &= 0 \end{aligned} \right\} (6.58)$$

Following the reasoning of the two-dimensional analysis, these linearized vorticity transport equations will not be valid when k is much greater than 1.

Integrating equations (6.58) with respect to x and using the fact that $\frac{\partial V_1'}{\partial y} - \frac{\partial V_2'}{\partial x} = 0$ (Irrotationality of the mean disturbance field) yields:

$$\left. \begin{aligned} \hat{S}_1 &= \left\{ ik_1 \int_{-\infty}^x \frac{V_1'}{U_\infty} dx' + ik_2 \int_{-\infty}^x \frac{V_2'}{U_\infty} dx' + \frac{V_1'}{U_\infty} \right\} \hat{S}_{1\infty} + \frac{V_2'}{U_\infty} \hat{S}_{2\infty} \\ \hat{S}_3 &= \left\{ ik_1 \int_{-\infty}^x \frac{V_1'}{U_\infty} dx' + ik_2 \int_{-\infty}^x \frac{V_2'}{U_\infty} dx' \right\} \hat{S}_{3\infty} \end{aligned} \right\} (6.59)$$

The lift response, C'_{LD} , for a sinusoidal distribution of mean vorticity, $K'(x) = e^{-i\lambda x}$, is determined first. The integral, $\int_{-\infty}^x \frac{V_2'}{U_\infty} dx'$, is calculated as $\int_0^x \frac{V_2'}{U_\infty} dx' + \int_{-\infty}^0 [V_2' - V_2'(y=0)]/U_\infty dx'$, as before. Analytical expressions for this integral and for $\int_{-\infty}^x \frac{V_1'}{U_\infty} dx'$, V_1' , and V_2' have been derived in the two-dimensional analysis. \hat{S}_1 and \hat{S}_2 are determined by substitution of these expressions into equations (6.59).

The extra upwash produced by distortion, $\tilde{v}_2(x, 0, z)$, is evaluated by application of the Biot-Savart Law in its full three-dimensional form:

$$\tilde{v}_2(x, 0, z) = \frac{1}{4\pi} \iiint_{-\infty}^{\infty} \frac{J_3(x', y', z') (x-x') dx' dy' dz'}{[(x-x')^2 + y'^2 + (z-z')^2]^{\frac{3}{2}}} - \frac{1}{4\pi} \iiint_{-\infty}^{\infty} \frac{J_1(x', y', z') (z-z') dx' dy' dz'}{[(x-x')^2 + y'^2 + (z-z')^2]^{\frac{3}{2}}} \quad (6.60)$$

Again the algebra involved in the evaluation of the integrals is complicated though the method is straightforward. Terms in the resultant

$\tilde{v}_2(x, 0, z)$ expression are of two basic forms:

- (1) $\hat{\tilde{v}}_2 e^{i(\omega t - k_1 x - k_3 z)}$
- (2) $\hat{\tilde{v}}_2 e^{i(\omega t - [k_1 + \lambda] x - k_3 z)}$

where $\hat{\tilde{v}}_2$ is a function of k_1, k_2, k_3 , and λ .

The lift response, C'_{LD} , corresponding to $\tilde{v}_2(x, 0, z)$ is determined with equation (6.54). The solution of this equation for an upwash of the form (1) is provided by the theory of Graham:

$$C'_{LD} = 2\pi G(k_1, k_3) \frac{\hat{\tilde{v}}_2}{U_\infty} e^{i(\omega t - k_3 z)}$$

while the generalized theory for a non-frozen gust (refer to 1.2.2) provides the solution for the case of upwash (2):

$$C'_{LD} = 2\pi G'(k_1, k_1 + \lambda, k_3) \frac{\hat{\tilde{v}}_2}{U_\infty} e^{i(\omega t - k_3 z)}$$

Thus the C'_{LD} expression corresponding to $\tilde{v}_2(x, 0, z)$ can be written down, and finally:

$$C_{LD} = U_\infty \alpha \int_{-\infty}^{\infty} [-J_0(\lambda) + iJ_1(\lambda)] C'_{LD}(\lambda) d\lambda \quad \text{for } K(x) = -2U_\infty \alpha \sqrt{\frac{1-x}{1+x}}.$$

The result is:

$$C_{LD} = \alpha 2\pi \left\{ F_1(k_1, k_2, k_3) \frac{\hat{\tilde{v}}_2}{U_\infty} + F_2(k_1, k_2, k_3) \frac{\hat{\tilde{v}}_2}{U_\infty} + F_3(k_1, k_2, k_3) \frac{\hat{\tilde{v}}_2}{U_\infty} \right\} e^{i(\omega t - k_3 z)} \quad (6.61)$$

where the transfer functions, F_i , can be evaluated numerically via formulae of the following form:

$$F_i(k_1, k_2, k_3) = \int_0^{\infty} [iJ_0(\lambda) \cdot E_i(\lambda) + J_1(\lambda) O_i(\lambda)] d\lambda \quad (6.62)$$

The expressions for E_i and O_i involve the response functions G and G' . They are derived in detail and listed in Appendix 6.

6.9.5 Analysis for L_M

This is identical to the two-dimensional analysis for L_M . The result is:

$$C_{LM} = \alpha 2\pi \cdot M(k_i) \frac{\hat{v}_1}{U_\infty} e^{i(\omega t - k_3 z)}$$

6.9.6 Summary for the frozen, three-dimensional gust.

$$C_L = C_{LP} + C_{LD} + C_{LM} \text{ to order } (\alpha E),$$

where

$$\left. \begin{aligned} C_{LP} &= 2\pi \cdot G'(k_1, k_1 - \alpha k_2, k_3) \left\{ \frac{\hat{v}_1}{U_\infty} + \alpha \frac{\hat{v}_1}{U_\infty} \right\} e^{i(\omega t - k_3 z)} \\ C_{LD} &= \alpha 2\pi \left\{ F_1(k) \frac{\hat{v}_1}{U_\infty} + F_2(k) \frac{\hat{v}_2}{U_\infty} + F_3(k) \frac{\hat{v}_3}{U_\infty} \right\} e^{i(\omega t - k_3 z)} \\ C_{LM} &= \alpha 2\pi \cdot M(k_i) \frac{\hat{v}_1}{U_\infty} e^{i(\omega t - k_3 z)}, \end{aligned} \right\} (6.63)$$

and continuity demands that:

$$k_1 \hat{v}_1 + k_2 \hat{v}_2 + k_3 \hat{v}_3 = 0.$$

When $k_3 = 0$, $G' \equiv S'$ and $G \equiv S$, and the two-dimensional gust result, presented in 6.3.5, is recovered. (Appendix 6 should be referred to for details of the reduction of the distortion term, C_{LD} , when $k_3 = 0$).

6.9.7 Use of the Mugridge approximation to G' and G for the higher order terms. In the numerical computation of C_{LD} , the response functions G' and G must be evaluated many times. As these functions themselves require numerical computation, the calculation of C_{LD} , as above, is rather lengthy. The Mugridge-type approximations to G' and G are fully analytic (refer to section 1.2.2 for the formulae derived in this study); and thus their use enables the computation to be completed in a reasonable time.

In many practical situations, the Mugridge approximation will provide a good estimate of the response function. An example is provided by the current first order turbulent loading study (Chapter 5) where the use of the Mugridge approximation yielded a reasonable theoretical prediction of the admittance. When the approximation is applied only to the higher order terms, the discrepancies so introduced will be relatively smaller.

When the Mugridge formula, G'_M replaces G , the primary response, C_{LP} , can be subdivided in the manner of the two-dimensional analysis (refer to 6.3.2.4):

$$C_{LP} = C_{LS} + C_{LA1} + C_{LA2} ,$$

$$\text{where } C_{LS} = 2\pi \cdot G_M(k_1, k_3) \cdot \frac{\hat{v}_2}{U_\infty} e^{i(\omega t - k_3 z)} ,$$

$$C_{LA1} = \alpha 2\pi G_M(k_1, k_3) \cdot \frac{\hat{v}_1}{U_\infty} e^{i(\omega t - k_3 z)} ,$$

$$C_{LA2} = \alpha 2\pi G_{MA}(k_1, k_2, k_3) \frac{\hat{v}_2}{U_\infty} e^{i(\omega t - k_3 z)} ,$$

and

$$G_{MA}(k_1, k_2, k_3) = k_2 \left\{ L(k_1, k_3) [J_1(k_1) - i J_1^\dagger(k_1)] + i [J_1^\dagger(k_1) + \frac{J_1(k_1)}{k_1}] \right\} .$$

(For $L(k_1, k_3)$, see eqn.(1.4) ; for $J_1^\dagger(k_1)$, see eqn(6.25))

Thus, with the Mugridge approximation for the higher order terms, the total response is:

$$C_L = C_{LS} + C_{LA1} + C_{LA2} + C_{LD} + C_{LM} ,$$

$$\text{where } C_{LS} = 2\pi \cdot G(k_1, k_3) \frac{\hat{v}_2}{U_\infty} e^{i(\omega t - k_3 z)} ,$$

$$C_{LA1} = \alpha 2\pi \cdot G_M(k_1, k_3) \frac{\hat{v}_1}{U_\infty} e^{i(\omega t - k_3 z)} , \quad \text{equations (6.64)}$$

$$C_{LA2} = \alpha 2\pi \cdot G_{MA}(k_1, k_2, k_3) \frac{\hat{v}_2}{U_\infty} e^{i(\omega t - k_3 z)} ,$$

$$C_{LD} = \alpha 2\pi \left\{ F_1(k) \frac{\hat{v}_1}{U_\infty} + F_2(k) \frac{\hat{v}_2}{U_\infty} + F_3(k) \frac{\hat{v}_3}{U_\infty} \right\} e^{i(\omega t - k_3 z)} ,$$

(cont. over)

where the functions, F_i , are evaluated with the Hugriddle approximation, and

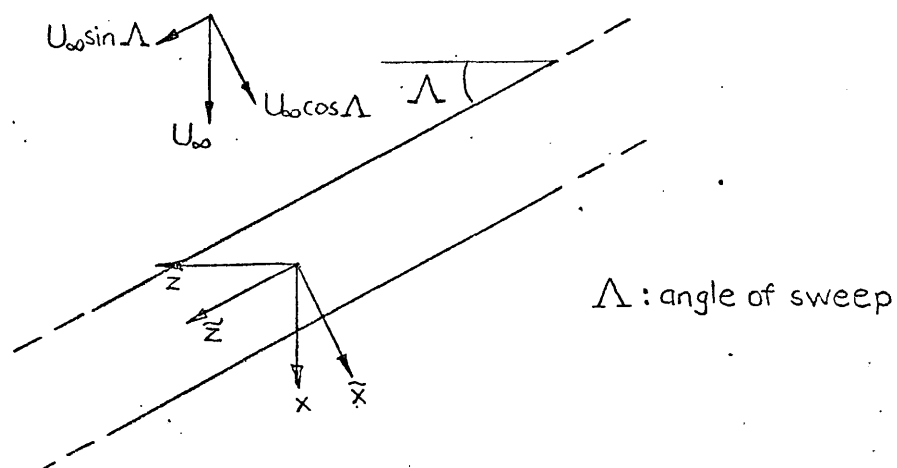
$$C_{LM} = \alpha 2\pi M(k_1) \hat{v}_1 / U_\infty e^{i(\omega t - k_3 z)}.$$

C_{LS} is the order (ϵ) response to the upwash, v_2 . C_{LA1} is of order ($\alpha\epsilon$), and is the response to the component of v_1 which is perpendicular to the chord. C_{LA2} is of order ($\alpha\epsilon$), and arises because the spatial wavenumber of the gust along the chord-line has a component of the wavenumber, k_2 . C_{LD} is the order ($\alpha\epsilon$) response arising from the gust distortion effect; and C_{LM} is the order ($\alpha\epsilon$) "cross-term" between the mean velocity field and the gust velocity field.

These response formulae are employed, in the next chapter, for the theoretical calculation of the turbulence admittance to higher order.

6.9.8 Application to the swept wing/two-dimensional gust problem.

The geometry of the problem is indicated in the following plan view:



The two-dimensional sinusoidal gust has components:

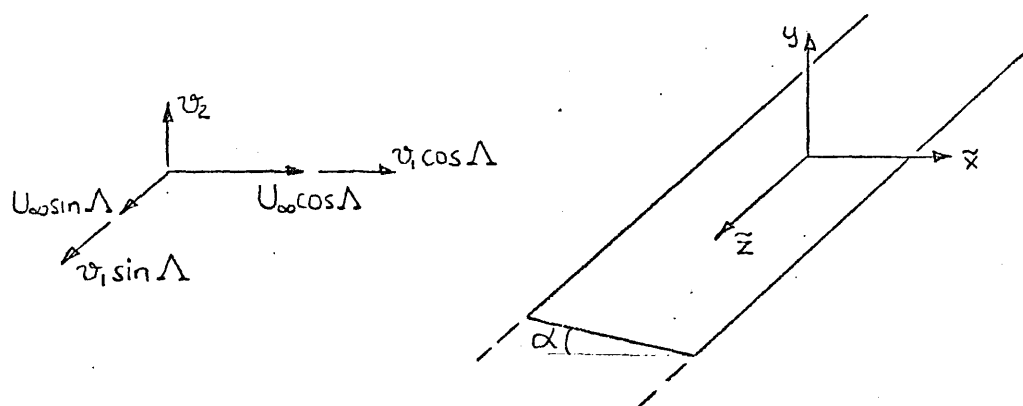
$$\hat{v}_1 e^{i(\omega t - k_1 x - k_2 y)} ; \hat{v}_2 e^{i(\omega t - k_1 x - k_2 y)} \quad \text{with } \omega = k_1 U_\infty$$

In the co-ordinate frame, \tilde{x} , y , \tilde{z} (see above), the gust components

are:

$$\begin{aligned} & \hat{v}_1 \cos \Lambda e^{i(\omega t - k_1 \cos \Lambda \tilde{x} - k_2 y - k_1 \sin \Lambda \tilde{z})} \\ & \hat{v}_2 e^{i(\omega t - k_1 \cos \Lambda \tilde{x} - k_2 y - k_1 \sin \Lambda \tilde{z})} \\ & \hat{v}_1 \sin \Lambda e^{i(\omega t - k_1 \cos \Lambda \tilde{x} - k_2 y - k_1 \sin \Lambda \tilde{z})} . \end{aligned}$$

The equivalent unswept problem is sketched below (three-dimensional view):



The analysis can be greatly simplified, at this stage, by ignoring the mean velocity component, $U_\infty \sin \Lambda$; that is, the gust, frozen in space, is considered to be convected onto the aerofoil by the component, $U_\infty \cos \Lambda$, alone. (The frequency sensed by the aerofoil is still $k_1 U_\infty$). The validity of this simplification for the aerofoil at zero incidence has been rigorously demonstrated by Edwards (1972). The author, by initially retaining the $U_\infty \sin \Lambda$ in the analysis, has found that the simplification remains valid for non-zero α .

With this simplification, the lift response can be written down directly from the result for the frozen three-dimensional gust (equations (6.63)). The swept wing lift coefficient is here defined in terms of the component of the mean stream perpendicular to the leading edge; namely, $U_\infty \cos \Lambda$. Thus:

$$C_L = \frac{L}{\rho (U_\infty \cos \Lambda)^2}$$

The result for C_L , to order $(\alpha \epsilon)$, is:

$$C_L = C_{LP} + C_{LD} + C_{LM},$$

$$\text{where } C_{LP} = 2\pi G'(k_1 \cos \Lambda, k_1 \cos \Lambda - \alpha k_2, k_1 \sin \Lambda) \left\{ \frac{\hat{v}_2}{U_\infty \cos \Lambda} + \alpha \frac{\hat{v}_1}{U_\infty} \right\} e^{i(\omega t - k_1 \sin \Lambda \bar{z})},$$

$$C_{LD} = \alpha 2\pi \left\{ F_1 \frac{\hat{v}_1}{U_\infty} + F_2 \frac{\hat{v}_2}{U_\infty \cos \Lambda} + F_3 \frac{\hat{v}_1 \tan \Lambda}{U_\infty} \right\} e^{i(\omega t - k_1 \sin \Lambda \bar{z})},$$

where $F_i = F_i(k_1 \cos \Lambda, k_2, k_1 \sin \Lambda)$, and

$$C_{LM} = \alpha 2\pi M(k_1 \cos \Lambda) \frac{\hat{v}_1}{U_\infty} e^{i(\omega t - k_1 \sin \Lambda \bar{z})},$$

... equations (6.65)

with $\omega = k_1 U_\infty$ and $k_1 \hat{v}_1 + k_2 \hat{v}_2 = 0$.

CHAPTER 7. Higher Order Turbulent Loading

In this chapter, a higher order admittance theory is developed; and a comparison is then made between the theoretical admittance and the experimentally measured admittance of an aerofoil at incidence, α .

7.1 Higher Order Theory

7.1.1 Basic formulae. In section 1.2.5, a formula for the admittance of lift of an aerofoil subjected to an isotropic turbulent gust has been derived. In tensor notation it is:

$$|A(k_i)|^2 = \left(\frac{U_\infty}{2\pi}\right)^2 \cdot \left(\frac{2}{c}\right)^2 \iint_{-\infty}^{\infty} \Omega_i^* \Omega_j T_{ij}(k_1, k_2, k_3) dk_2 dk_3 \quad \dots (1.11)$$

Ω_i is the response function for the i th component of the frozen sinusoidal gust. It is defined by:

$$C_L = \Omega_i \hat{v}_i e^{i\omega t} \quad \text{where } C_L \text{ is the sinusoidal response,}$$

and \hat{v}_i is the amplitude of the i th component.

The theoretical higher order response to a general, three-dimensional sinusoidal gust is required. In the previous chapter this response has been derived in the form:

$$C_L(t, z) = \hat{C}_L e^{i(\omega t - k_3 z)}$$

The nett lift response for a section of span $2b$ is given by:

$$C_L(t) = \hat{C}_L e^{i\omega t} \frac{1}{2b} \int_{-b}^{+b} e^{-ik_3 z} d\bar{z}$$

$$= \hat{C}_L \frac{\sin k_3 a}{k_3 a} e^{i\omega t} \quad \text{where } a = \frac{2b}{c}, \text{ the aspect ratio.}$$

In this theory, the sinusoidal response employed is that with the

Mugridge approximation for the higher order terms (to enable a feasible computation of the theoretical admittance). This response has been detailed in section 6.9.7. Comparing these equations with those above yields the following formulae for Ω_i :

$$\Omega_i = \frac{2\pi}{U_\infty} \cdot \frac{\sin k_3 a}{k_3 a} \cdot R_i ,$$

$$\left. \begin{aligned} \text{where } R_1 &= \alpha G_M(k_1, k_3) + \alpha F_1(k_1, k_2, k_3) + \alpha M(k_1) \\ R_2 &= G(k_1, k_3) + \alpha G_{MA}(k_1, k_2, k_3) + \alpha F_2(k_1, k_2, k_3) \\ R_3 &= \alpha F_3(k_1, k_2, k_3) . \end{aligned} \right\} (7.1)$$

$T_{ij}(k_1, k_2, k_3)$ is the normalized three-dimensional spectrum of the isotropic turbulence, defined in section 1.2.5. In this study, the formula used for T_{ij} is that which is derived from the Von Karman semi-empirical formula for the one-dimensional spectrum, $\phi_{11}(\bar{K}_1)$. (refer to section 5.2 for a fuller discussion). The T_{ij} formula is (in tensor notation):

$$T_{ij}(k_1, k_2, k_3) = \frac{55}{6\pi} \left\{ \frac{\Gamma(\frac{1}{3})}{\Gamma(\frac{1}{2})\Gamma(\frac{5}{6})} \right\}^2 L_1^2 \frac{(1+k_i^{*2})^{\frac{11}{6}}}{(3+8k_i^{*2})} \cdot \frac{k^{*2}}{(1+k^{*2})^{\frac{7}{6}}} \left\{ \delta_{ij} - \frac{k_i^* k_j^*}{k^{*2}} \right\} \cdot (5.4)$$

$$\text{where } k^{*2} = k_1^{*2} + k_2^{*2} + k_3^{*2} ; \quad k_i^* = \left\{ \frac{\Gamma(\frac{1}{3})}{\Gamma(\frac{1}{2})\Gamma(\frac{5}{6})} \right\}^2 \left(\frac{L_1}{c} \right) k_i .$$

Substitution for Ω_i and T_{ij} in equation (1.11) yields:

$$|A(k_i)|^2 = \frac{55}{6\pi} \cdot \frac{1}{\delta^2} \frac{(1+k_i^{*2})^{\frac{11}{6}}}{(3+8k_i^{*2})} \iint_{-\infty}^{\infty} \frac{\sin^2 k_3 a}{(k_3 a)^2} R_i^* R_j^* \frac{k^{*2}}{(1+k^{*2})^{\frac{7}{6}}} \left\{ \delta_{ij} - \frac{k_i^* k_j^*}{k^{*2}} \right\} \cdot (7.2)$$

$$\text{where } \delta = \left\{ \frac{\Gamma(\frac{1}{2})\Gamma(\frac{5}{6})}{\Gamma(\frac{1}{3})} \right\} \cdot \frac{c}{2} \cdot \frac{1}{L_1} ; \quad k_i^* = k_i / \delta .$$

7.1.2 Substitution for R_i . The equations (7.1) express the functions, R_i in terms of other known functions. The admittance becomes determinate when these expressions are substituted into equation (7.2). It should be noted that the rapid distortion theory of turbulence is effectively being employed in the evaluation of those admittance terms

which involve the response functions, F_i ; and thus the validity of these terms is conditional upon:

$$(\text{ReNo.})^{-1} \lll \ll \min\left(\frac{L_1}{c}, 1\right) \text{ and } (\text{ReNo.})^{\frac{1}{2}} \gg \max\left(\frac{c}{L_1}, 1\right).$$

(refer 1.2.4.2)

The algebra involved in the substitution for R_i is complicated and full details are left to Appendix 7. The resultant integrand in equation (7.2) has a term of order (1) (the term which arises in the first order theory) and terms of order (α) and order (α^2). Some of the terms in the integrand do not contribute to the integral because they are odd functions of the wavenumber, k_2 . In fact it is found that none of the order (α) terms contribute to the integral (being odd in k_2); while all the order (α^2) terms do contribute (being even in both k_2 and k_3).

From this finding follows the major theoretical conclusion of this study; namely that, in isotropic turbulence, the theoretical admittance of lift is not affected, by changes in incidence α , to first order in α . The results of the current experiment, in which the turbulence was approximately isotropic, were in accordance with this conclusion: the measured effect of incidence on the admittance was only moderate (see 7.22, later). It should be stressed that, when the turbulence is non-isotropic, it is likely that the admittance will be affected to first order in α .

It is not entirely surprising that in isotropic turbulence, the admittance does not depend on the first power of α . Isotropic turbulence has no preferred direction, and so the admittance of lift, a "mean squared" property, is clearly the same for $+\alpha$ and for $-\alpha$. In other words, the higher order admittance would have to depend on $|\alpha|$ rather than α . Yet an examination of the present analysis reveals no mechanism by which the modulus sign on α could arise.

In contrast to the present results, Graham (1975) has found that the admittance of drag of a porous plate is affected by the mean

flow field parameter K , to first order. Yet, in this case, the admittance will be different when K , the resistance coefficient, is negative (for example, with the porous plate replaced by some thrust-producing device). It is tentatively suggested that, when the mean field is asymmetric with respect to a plane parallel to the stream (for example, the aerofoil at incidence) there will be no first order effect of the mean field on the admittance (in isotropic turbulence); but that, when the mean field is plane-symmetric (for example, the two-dimensional porous plate) or axisymmetric, there will be a first order effect.

It should be noted, in the aerofoil case, that other statistical properties of the unsteady lift in isotropic turbulence, such as the probability of achieving a certain level of lift, may depend on α to first order.

7.1.3 Evaluation of the order (α^2) contribution. It was felt that this contribution to the theoretical admittance could account for the moderate increase in the measured admittance, resulting from the increase in incidence, α . (The experimental results are discussed in more detail in section 7.2.2).

It was realized that, to evaluate the order (α^2) contribution fully, the sinusoidal gust response must be determined correct to order ($\alpha^2\epsilon$). This is necessary because a crossterm between an order ($\alpha^2\epsilon$) term and an order (ϵ) term is of the order of interest; viz ($\alpha^2\epsilon^2$) (which leads to an admittance of order (α^2)). It is questionable whether the linear analysis can be extended to incorporate such non-linear terms: in fact, a detailed analysis of the convergence of the series in α would be required to verify the validity.

The feasibility of determining the sinusoidal response to order ($\alpha^2\epsilon$) was explored. It was found that some, but not all, of the extra terms could be evaluated; the difficult terms being those

which involve a higher order (non-linear in α) distorted velocity. This velocity clearly cannot be determined with the linearized vorticity transport equations (equations (6.53)) derived previously. An attempt to derive a vorticity transport equation, correct to order ($\alpha^2 \epsilon$), but more tractable than the complete equation (equation (6.27)), was not successful. The evaluation of the tractable ($\alpha^2 \epsilon$) terms was undertaken in part, the complete analysis being a tedious task. This part-evaluation was sufficient to show that some, at least, of these order ($\alpha^2 \epsilon$) terms would result in an integrand even in both k_2 and k_3 ; that is, they would contribute to the theoretical admittance to order (α^2).

However it was considered that a full derivation of all possible ($\alpha^2 \epsilon$) sinusoidal response terms was not worthwhile in view of the facts that:

- (1) the theory would be still incomplete to order ($\alpha^2 \epsilon$),
- (2) the extension of the linear sinusoidal gust theory to incorporate non-linear terms was questionable from a fundamental mathematical viewpoint.

Nonetheless it was decided that those (α^2) admittance terms arising from the order ($\alpha \epsilon$) sinusoidal gust theory should be computed, in the hope that they would provide some measure of the increment in admittance due to incidence. The sum of those order (α^2) admittance terms can be expressed mathematically as:

$$|A(k_1)|_{\alpha^2}^2 = \alpha^2 \cdot \frac{110}{3\pi} \frac{1}{\delta^2 (3 + 8k_1^{*2})} \int_0^\infty \frac{\sin^2 k_3 a}{(k_3 a)^2} \cdot I(k_1, k_2, k_3, L/c) dk_2 dk_3 \quad \dots (7.3)$$

The function, $I(k_1, k_2, k_3, L/c)$ is listed in Appendix 7. It consists of 21 terms and involves various combinations of all the response functions arising in the order ($\alpha \epsilon$) sinusoidal gust theory.

7.1.4 Computation details. The order (α^2) admittance, for each k_1 value, was determined via a double numerical integration of the integral contained in the right-hand-side of equation (7.3). However, imbedded in the function $I(k_1, k_2, k_3, L_1/c)$ are the response functions, F_i , which have, themselves, to be determined with a numerical integration (refer to 6.9.4). Thus the computation was effectively a triple numerical integration and was fairly lengthy: about 300 seconds of CDC 6400 time were required for each value of k_1 .

In the current experiment, detailed measurements were made of the turbulence generated by the 6 inch grid. For this turbulence, the value of $L_1/c = 0.40$ was employed in the calculation of the order (α^2) theoretical admittance. This is the value recommended in section 5.2.1, following examination of the various measured turbulence spectra.

The admittance was calculated for a range of incidence, α , from 10° to 12° . In the experiment, the set incidence of the aerofoil was 10° , but the aerofoil support system produced an additional mean flow incidence in the range 0° to $+2^\circ$ (as determined in section 4.2.5)

The program written for the computation is described and listed in Appendix 11.

7.1.5 Asymptotic admittance formulae for $k_1 \rightarrow 0, L_1/c \rightarrow \infty$

Formulae, corresponding to the previous higher order theory, are derived in order to provide some information on the nature of the turbulent loading when the length scale of the gust is much larger than the aerofoil chord.

To transform equation (7.2) to a form suitable for the application of the limits, the following substitution (after Graham (1975)) is employed:

$$\tilde{k}_i = k_i/\beta \quad \text{where} \quad \beta = \sqrt{\delta^2 + k_1^2}.$$

With this substitution, equation (7.2) becomes:

$$|A(k_1)|^2 = \frac{55}{6\pi} \frac{1}{3+5\tilde{k}_1^2} \iint_{-\infty}^{\infty} \frac{\sin^2 \beta \tilde{k}_3 a}{(\beta \tilde{k}_3 a)^2} R_i^* R_j(\beta \tilde{k}) \frac{\tilde{k}^2}{(1+\tilde{k}_2^2+\tilde{k}_3^2)^{1/2}} \left\{ \delta_{ij} - \frac{\tilde{k}_i \tilde{k}_j}{\tilde{k}^2} \right\} d\tilde{k}_2 d\tilde{k}_3. \quad \dots (7.4)$$

In the transformed variables, the limits $k_1 \rightarrow 0$ and $L/c \rightarrow \infty$, become:

$$\tilde{k}_1 \rightarrow 1 \quad \text{and} \quad \beta \rightarrow 0.$$

Thus,

$$\frac{\sin^2 \beta \tilde{k}_3 a}{(\beta \tilde{k}_3 a)^2} \rightarrow 1.$$

The functions, R_i , have been given in equations (7.1)

(In fact, the Mugridge approximation is not necessary: the same asymptotic formulae are derived if the exact response functions are retained). In the limit, $\beta \rightarrow 0$, the response functions behave as follows:

$$G(\beta \tilde{k}_1, \beta \tilde{k}_3) \rightarrow G_M(\beta \tilde{k}_1, \beta \tilde{k}_3) \rightarrow 1$$

$$G_{MA}(\beta \tilde{k}_1, \beta \tilde{k}_2, \beta \tilde{k}_3) \rightarrow 0$$

$$F_i(\beta \tilde{k}_1, \beta \tilde{k}_2, \beta \tilde{k}_3) \rightarrow 0$$

$$M(\beta \tilde{k}_1) \rightarrow 1$$

Thus $R_1 \rightarrow 2\alpha$, $R_2 \rightarrow 1$, and $R_3 \rightarrow 0$.

These limiting forms are substituted into equation (7.4), and the resulting expression for $|A(0)|^2$ can be divided into two terms; one of order (1) and the other of order (α^2). (Another term, of order (α), has an integrand which is odd in k_2 and so it does not contribute to $|A(0)|^2$. This is consistent with the full theory of section 7.1.2).

The order (1) term is:

$$|A(0)|_1^2 = \frac{55}{48\pi} \iint_{-\infty}^{\infty} \frac{1+\tilde{k}_3^2}{(1+\tilde{k}_2^2+\tilde{k}_3^2)^{1/2}} d\tilde{k}_2 d\tilde{k}_3.$$

This integral can be evaluated analytically (Appendix 8), and the result is:

$$|A(0)|_1^2 = 1.$$

This is the expected quasi-steady admittance for an aerofoil at zero incidence. (refer to the admittance definition, equation (1.8)).

The order (α^2) term is:

$$|A(0)|_{\alpha^2}^2 = \frac{55}{48\pi} \cdot 4\alpha^2 \iint_{-\infty}^{\infty} \frac{\tilde{k}_2^2 + \tilde{k}_3^2}{(1 + \tilde{k}_2^2 + \tilde{k}_3^2)^{3/2}} d\tilde{k}_2 d\tilde{k}_3.$$

Again the integral can be evaluated analytically (Appendix 8), and the result is

$$|A(0)|_{\alpha^2}^2 = 3\alpha^2.$$

This higher order asymptotic admittance contribution has its origins in two of the sinusoidal gust response terms:

- (1) The response to the component of \mathcal{V}_1 perpendicular to the chord: C_{LA1} .
- (2) The Morfey-type response: C_{LM} .

For the same reasons discussed in 7.1.3, this higher order admittance is not completely correct to order (α^2). Nonetheless, it does indicate that, while the effect of distortion tends to zero as $k_1 \rightarrow 0$ and $L_1/c \rightarrow \infty$, other higher order effects remain significant in this limit.

7.2 Comparison of Experiment and Theory

7.2.1 Method of comparison. Because of discrepancies existing between the theory and experiment at zero incidence (refer 5.1.2), it was decided to compare the measured increment of admittance with the theoretical admittance increment. Two forms of graphical presentation are used:

- (1) In figures 46, 47, and 49, the admittance increment is plotted on a linear scale against frequency on a log scale. This presentation emphasizes the absolute magnitude of the increment,

knowledge of which is important in those practical situations in which the overall level of loading power is of interest.

(2) In figure 48, the results for the series 3, 6 inch grid case (which gave the best agreement between theory and experiment) are plotted as log of the total admittance vs. log of the frequency. The total theoretical admittance was here derived by adding the theoretical increment to the zero incidence experimental admittance. This presentation emphasizes the magnitude of the admittance increment relative to the first order admittance.

In each case, two different estimates of the theoretical increment are provided:

- (1) The increment comprised of all of the order (α^2) admittance terms which arise from the order ($\alpha \epsilon$) sinusoidal gust response.
- (2) The increment, as in (1), but with the effect of distortion ignored.

7.2.2 The experimental increment. The experiment has been described in Chapter 4, and the method of data reduction in section 5.1.1.

Figure 46 plots the experimental results of the series 1 and the series 3 tests for the case of the 6 inch grid turbulence. There is a significant discrepancy between the results of the two series; a discrepancy that clearly has the same (as yet undiscovered) source as the difference between the zero-incidence experimental admittances for the two series of tests, discussed in detail in section 5.1.2. The measured admittance increment due to incidence decreases with increasing frequency; and, even at the lowest frequency, as figure 48 indicates, it is only of moderate magnitude.

The less definitive data of the 3 inch grid test is plotted in figure 49.

7.2.3 The theoretical increment. This increment, determined both with and without distortion, is plotted in figures 46 to 49 for the band of values: $\alpha = 10^\circ$ to $\alpha = 12^\circ$. The sensitivity of the result to the value of α (expected because the increment depends on α^2) is clearly demonstrated in the figures.

Comparison of the increments, with and without distortion, provides the following information on the theoretical role of distortion:

- (1) At lower frequencies, the distortion contribution is less than that of the other higher order effects, and leads to a small reduction in the increment.
- (2) At higher frequencies, the distortion effect dominates, and causes the increment to be greater.

7.2.4 Sources of discrepancy between theory and experiment

(a) Incomplete theory. As discussed in 7.1.3, the higher order admittance theory is not exact to order (α^2). This is possibly the greatest source of discrepancy between theory and experiment in the present investigation.

(b) Use of Mugridge approximation. Inspection of the zero-incidence admittance prediction obtained with the Mugridge approximation (figure 38) suggests that the errors introduced into the increment estimate will, in the main, be restricted to a small overestimation at the higher frequencies.

(c) Viscosity. The present theory has been developed with an assumption of completely inviscid flow. As already indicated in 6.3.3.1 the assumption is most questionable when the transport of vorticity is being considered (that is, when the distortion effect is being determined). Bearman (1972), when investigating the distortion of turbulence approaching a bluff body, found, in some measured spectra near the body, that the power at the highest frequencies was less than

the corresponding power in the undistorted turbulence. This he attributed to viscous decay.

(d) Limited validity of linearization. In 6.3.3.1 and 6.9.4, it was argued that the linearized distortion theory is not valid for $k \gg 1$. However, it is felt that the linearization should be valid for the admittances considered in this investigation: $L_1/C = 0.40$ and the maximum value of $k_1 = 5.0$.

(e) Effective incidence of the supports. This potentially significant error has been allowed for in the theoretical calculation. The effective flow incidence should be contained in the range $\alpha = 10^\circ$ to $\alpha = 12^\circ$.

(f) Turbulence description. There are two sources of error: (1) Anisotropy of the turbulence in the experiment. Excursions from isotropy were small but measurable (refer 5.2.1). (2) The value of L_1/C . Different measured spectra suggested different values of L_1/C in the range 0.36 to 0.44. In figure 46, some theoretical results for this wider range of L_1/C have been plotted. It is evident that the theoretical increment is only moderately sensitive to the value of L_1/C .

(g) Aerofoil thickness/non-linear terms in ϵ . These two effects were deemed to be potentially large for the zero-incidence admittance (refer to 5.4.2). However, both effects will be approximately independent of incidence, and thus will have little influence on the admittance increment.

(h) Lift curve slope. As discussed in section 4.2.5, the effective mean lift curve at $\alpha = 10^\circ$ may have been less than the value at $\alpha = 0^\circ$, which, in turn, was less than the theoretical value of 2π used in the theory. For the zero-incidence admittance a maximum possible correction of -15% to the theoretical prediction was suggested (refer to 5.4.2). For the increment in admittance, the required percentage correction will be somewhat greater.

(i) Absolute spectral power. The magnitude of the increment

could be measured accurately relative to the zero-incidence admittance. Thus the estimated relative error in the former is the same as that in the latter; namely $\pm 10\%$ maximum (refer 5.4.2).

(j) Drag. This error arises from the sensitivity of the load balance to some transverse load. Repeating the quasi-steady analysis of section 5.4.2, this time for $\alpha = 10^\circ$, yields: $\frac{\Delta \text{DRAG}}{\Delta \text{LIFT}} \approx 0.064$, a value ten times larger than that for $\alpha = 0^\circ$. Nonetheless, the resultant quasi-steady error on the admittance of lift is still negligible: $\pm 1\%$.

(k) Buffet load. Although it was ascertained that there was no significant flow separation at the highest set incidence (refer 4.2.5), there was still a possibility that the thickened boundary layer and wake would contribute to the unsteady load. A load spectrum for the aerofoil at 10° incidence in smooth flow was measured, and is presented in figure 50. The level of this spectrum is higher than that of the corresponding zero incidence spectrum, particularly at higher frequencies; but it is still more than an order of magnitude less than the typical level of a turbulent load spectrum. An estimate of the possible error on the admittance was made although, strictly, one cannot directly relate boundary layer effects in differing levels of free stream turbulence. A maximum error due to "buffet load" of $\pm 5\%$ for $k_1 > 3.0$ was estimated.

Although not directly related to the aims of the present study, buffet load measurements in smooth flow at higher incidences approaching the stall were made, and are also presented in figure 50. As the angle of incidence increases from 10° to 13° , the level of buffet load increases significantly, indicating separation of flow on the aerofoil. At $\alpha = 14^\circ$, the aerofoil is completely stalled, and the level of buffet load at the low frequencies is of the order of the level of a typical turbulent load spectrum of the current experiment. In turbulent flow at the same angles of incidence, the buffet loads

will be less, as a result of the delay of flow separation (This effect has been considered in detail in the current mean load study: Chapters 2 and 3). Further details of the buffet test are given in Appendix 9.

7.2.5 Comparison of the theoretical and experimental increments.

For the 6 inch grid turbulence, the graphical comparison is presented in figures 46, 47, and 48. These graphs indicate that:

(1) the higher order theory, although not exact to order (α^2) does predict the correct order of magnitude of the admittance increment.

(2) at the lower frequencies where the increment is greatest both the "theory with distortion" and the "theory without distortion" provide a reasonable prediction of the increment; the prediction of the former theory being marginally better. The agreement between theory and experiment would be further improved if a correction for the lift curve slope error (error source (h) above) were included.

(3) at the higher frequencies, the theory without distortion provides a reasonable estimate; while the theory with distortion tends to overestimate the admittance. This overestimation of the distortion effect at the higher frequencies could have its origins in one or more of the following error sources:

- (a) incomplete theory,
- (b) use of Mugridge approximation,
- (c) viscosity.

These have been outlined in the previous section. It should be noted that errors arising from (b) and (c) will lead to, specifically, an overestimation of the distortion effect.

An additional, but not rigorous, comparison of theory and experiment was afforded by the results for the 3 inch grid turbulence, with $\sqrt{v_2^2}/U_\infty = 0.037$ and $L_1/C = 0.38$ (refer section 5.5). As figure 49 shows, the agreement between theory and experiment is

reasonable; the theory without distortion providing a better estimate. It should be noted that the measured increment for the 3 inch grid case is a little larger than the 6 inch grid increment, whereas the theory predicts the opposite trend.

7.3 Conclusions Regarding the Higher Order Turbulent Loading.

- (1) For approximately isotropic turbulence, the increment, due to incidence, in the admittance of lift is only of moderate magnitude. The higher order theory developed in this study predicts that, in isotropic turbulence, the admittance does not depend on the incidence, α , to first order; and so the theory is consistent with the experimental observation.
- (2) The correct order of magnitude of the increment is predicted by the order (α^2) admittance terms which arise in the higher order theory (although the theory is not completely correct to this order).
- (3) When the length scale of turbulence is of order (c , the aerofoil chord) or much greater than c , it is recommended that the increment be determined by the order (α^2) theory which does not include the effect of distortion. The reasons are:
 - (a) There is no evidence that the theory with distortion gives a better overall prediction of the increment.
 - (b) The theory with distortion requires a much greater computation time.
 - (c) The increment is not large compared with the first order admittance; and discrepancies between the first order theory and experiment can be of the same order as the increment.
 - (d) In many practical situations, the length scale of the gust, L_1 , is much greater than c . As L_1/c increases from 0.40 (its value in the current experiment), the distortion contribution will become a still smaller part of the nett

order (α^2) increment. This trend has been verified by an asymptotic analysis of the higher order theory.

(4) When the length scale of the turbulence is much less than c , the measured distortion effect will be greater; but, unless ϵ is much less than L_1/c , the current distortion theory cannot be applied validly to predict it (the "rapid distortion" assumptions breakdown). The distortion effect due to thickness will also become significant when L_1/c is much less than 1. Thus it is not expected that the present order (α^2) theory (with or without distortion) will predict the increment correctly when L_1 is much less than c .

CHAPTER 8. Concluding Comments

This thesis has considered several different aspects of the loading of two-dimensional aerofoils in unsteady streams. Conclusions and recommendations relevant to each have been detailed in the foregoing text. The reader is invited to revise these with the aid of the following index.

Index to Conclusions

Effects of turbulence on mean loading: Section 3.7 , p. 76 .

Higher order sinusoidal gust loading theory.

- (a) the two dimensional frozen gust: Section 6.5, p. 135.
- (b) application to turbo-blade loading: Section 6.8, p. 143.

Turbulent gust loading: theory and experiment.

- (a) aerofoil at zero incidence: Section 5.6, p. 109.
- (b) aerofoil at incidence: Section 7.3, p. 169.

Two overall comments regarding the gust loading of aerofoils can be made:

(1) The first priority for a satisfactory prediction of the admittance of lift of an aerofoil is a correct description of the turbulence over most of the frequency range of interest (This study has emphasized the difficulty of obtaining a sufficiently accurate description at the lowest frequencies of interest). With this realized, the first order theory can provide a reasonable estimate of the admittance; an estimate which can further be adjusted for any incidence effect with the higher order theory developed in this study.

(2) For a thin aerofoil at mean incidence, α , and subjected to a gust, the length scale of which is not much smaller than the aerofoil chord, the effect of gust distortion on the unsteady load is often less

than the other effects which depend on α .

Two suggestions for future work in this area are:

- (1) An extension of the higher order sinusoidal gust theory to the case of the two dimensional cascade. This theory would be relevant to the turboblade loading problem.
- (2) An experimental study of the effect of distortion when the length scale of the gust is much smaller than the aerofoil chord. This study could assist in the understanding of the effect of small scale turbulence on aerofoil mean flow behaviour, in particular, the stall.

LIST OF NOTATION

$ A(k_1) ^2$	admittance of lift, defined in 1.2.5.
$ A(k_1) _1^2$	first order admittance.
$ A(k_1) _{\alpha^2}^2$	order (α^2) admittance.
B	upstream reference distance. See 6.6.3.
B_E, B_O	terms in integrand for $D(k_1, k_2)$. See Appendix 4.
B'_E, B'_O	terms in integrand for $D'(k_f, k_s, k_1, B)$. See Appendix 5.
BF	"best fit" formulae, defined in 5.2
C_L	lift coefficient; locally $= \frac{L}{\frac{1}{2} \rho U_{\infty}^2 c}$; overall $= \frac{\text{overall } L}{\frac{1}{2} \rho U_{\infty}^2 s c}$.
$C_{L_{\max}}$	maximum lift coefficient.
$C_{L_{bb}}$	lift coefficient at "bubble bursting".
$C_{L_D}, C_{L_{A1}}, C_{L_{A2}}, C_{L_D}, C_{L_M}$	various terms in C_L , discussed in 6.3.1 and 6.3.2.
C'_{L_D}	C_{L_D} for sinusoidal mean flow input.
C'_{L_E}, C'_{L_O}	even and odd parts of C'_{L_D} .
C_D	drag coefficient.
$C_{D_{\min}}$	minimum drag coefficient.
$C_{M_{\frac{1}{4}}}$	moment coefficient about the quarter-chord point.
C_f	coefficient of skin friction.
$C_1 \rightarrow C_5$	constants in the BF formulae. See 5.2.
D	sphere diameter.
$D(k_1, k_2)$	2D distortion response function. See 6.3.3.
$D'(k_f, k_s, k_1, B)$	distortion response function; non-frozen gust. See 6.6.3
E_i, E'_i	terms in integrand for $F_i(k_1, k_2, k_3)$. See Appendix 6.
F	upwards force/span.
$F_i(k_1, k_2, k_3)$	3D distortion response functions.
FST	free stream turbulence.
$G(k_1, k_3)$	Graham's response function. See 1.2.2.
$G'(k_f, k_s, k_3)$	Graham's response function; non-frozen gust. See 1.2.2.
$G_M(k_1, k_3)$	Mugridge's response function. See 1.2.2.
$G'_M(k_f, k_s, k_3)$	Mugridge's response function; non-frozen gust. See 1.2.2.
$G_{MA}(k_1, k_2, k_3)$	"additional" Mugridge function. See 6.9.7.
$G_F(k_1, k_3)$	Filotas's asymptotic response function. See 1.2.2.
H	turbulent boundary layer shape parameter.
H_n	Haenkel functions of the second kind.
$I(k_1, k_2, k_3, L/c)$	integrand term for $ A(k_1) _{\alpha^2}^2$.
J_n	Bessel functions.
J^+	$= [J_2 - J_0] / 2$
K	(i) as parameter: resistance coefficient of a porous plate. (ii) as wavenumber: that of turbomachine gust. See figure 45A.

K_n	modified Bessel functions of the second kind.
$K(x)$	mean aerofoil bound vorticity.
$K'(x)$	sinusoidal component of $K(x)$. $K'(x) = e^{-ix}$.
$\bar{K}(\lambda)$	a Fourier transform of $K(x)$. See 6.3.3.
L	lift force/span.
$L(k_1, k_3)$	function within $G_M(k_1, k_3)$. See 1.2.2.
L_1	longitudinal integral length scale = $U_\infty \int_0^\infty (\overline{v_1(t) v_1(t+\tau)}) / \overline{v_1^2} d\tau$
L_P, L_M, L_D	various parts of L , discussed in 6.3.1.
$M(k_1)$	Morfev response function. See 1.2.2.
$N(k_1, k_3)$	function within $L(k_1, k_3)$. See 1.2.2.
O	order of magnitude symbol.
O_i, O'_i	terms in integrand for $F_i(k_1, k_2, k_3)$. See Appendix 6.
P	mean pressure.
R_i	general sinusoidal response function for φ_i . See 7.1.1.
\mathcal{R}	2D higher order sinusoidal response function. See 6.4.2
\mathcal{R}'	\mathcal{R} for non-frozen gust. See 6.7.4.
$\mathcal{R}'_S, \mathcal{R}'_A, \mathcal{R}'_M, \mathcal{R}'_D$	various parts of \mathcal{R}' , as defined in 6.7.4.
Re No.	Reynolds Number based on typical body dimension.
$Re_{\text{bubble bursting}}$	Re.No. corresponding to "bubble bursting". See 2.8.
Re_{crit}	critical Re.No. for a sphere.
Re_δ	Reynolds Number based on boundary layer thickness, δ .
$Re_{\delta \text{crit}}$	critical Re_δ for transition.
$S_{11}(k_1, z)$	normalized φ_1 cross spectrum.
$S_{22}(k_1, z)$	normalized φ_2 cross spectrum. See 1.2.5.
$\overline{S}_{22}(k_1, k_3)$	a Fourier transform of $S_{22}(k_1, z)$. See 1.2.5.
$S(k_1)$	Sears' response function. See 1.2.2.
$S'(k_f, k_s)$	Sears' response function; non-frozen gust. See 1,2.2.
$S_A(k_1, k_2)$	"additional" Sears' function. See 6.3.2.
$S'_A(k_f, k_s, k_2)$	"additional" Sears' function; non-frozen gust. See 6.6.2.
$T_{ij}(k_1, k_2, k_3)$	normalized three dimensional spectrum = $\Phi_{ij}(\mathbf{K}) / \phi_{22}(\bar{K})$.
U_∞	mean free stream velocity.
U	mean velocity external to the boundary layer.
\underline{V}^T	instantaneous velocity: vector.
\underline{V}_i^T	i th component of instantaneous velocity.
\underline{V}	velocity vector = $\underline{U}_\infty + \underline{V}'$.
\underline{V}_i	i th component of mean undisturbed velocity.
\underline{V}'	mean disturbance velocity.
\underline{V}'_i	i th component of \underline{V}' .
$V_\eta, V'_\eta, \text{etc.}$	components in η direction.
$V_\xi, V'_\xi, \text{etc.}$	components in ξ direction.
$\underline{V}_B, \underline{V}_I, \underline{V}_R$	blade velocity, incident velocity, relative velocity in turbomachine calculation. See figure 45A.

VK	"von Karman" formulae, defined in 5.2.
(X,Y), (X',Y')	co-ordinate systems in the turbomachine calculation.
	See figure 45A.
Y	phase change introduced into distortion analysis.
	See 6.3.3.
Y _n	Bessel functions of the second kind.
a	aspect ratio of test element.
b	half span ($\hat{s}/2$) of test element.
c	aerofoil chord length.
i	$= \sqrt{-1}$
$\hat{i}, \hat{j}, \hat{k}$	unit vectors in the three co-ordinate directions.
\bar{k}_i	wave-numbers carrying normal dimensions.
k _i	dimensionless wavenumbers. $k_i = \bar{k}_i c / 2$ In particular, when the gust is frozen, $k_i = \omega c / 2U_\infty$, the reduced frequency.
k	$= \sqrt{k_1^2 + k_2^2 + k_3^2}$
k _s	spatial wavenumber in the x direction: non-frozen gust.
k _f	$= \frac{\omega}{U_\infty}$: non-frozen gust.
k _i *	$= k_i / \delta$
k*	$= \sqrt{k_1^{*2} + k_2^{*2} + k_3^{*2}}$
\bar{k}_i	$= k_i / \beta$
\bar{k}	$= \sqrt{\bar{k}_1^2 + \bar{k}_2^2 + \bar{k}_3^2}$
k ₃ [†]	$= k_3 / (\delta \sqrt{1 + k_1^{*2}})$
k ₃ '	$= \bar{k}_3 / C_5$
k ₁ ', k ₂ '	gust wavenumbers in the ξ and η directions. See 6.3.1.
ℓ	length of separation bubble.
n	frequency.
p	instantaneous pressure.
p'	unsteady component of the pressure.
s	span of test element.
\bar{t}	time with normal dimensions.
t	$= \bar{t} 2 / c$
v _i	i th component of unsteady undisturbed velocity.
\hat{v}_i	amplitude of v _i (when v _i is sinusoidal).
v _i '	i th component of unsteady disturbance velocity. (for v _i).
\tilde{v}_i	additional v _i due to gust distortion.
\tilde{v}_i'	disturbance velocity for \tilde{v}_i .

\hat{v}_2	amplitude of upwash component of \tilde{v}_i .
$v_{\eta}, v'_{\eta}, \text{etc.}$	components in the η direction.
$v_{\xi}, v'_{\xi}, \text{etc.}$	components in the ξ direction.
\hat{v}_T	amplitude of gust in turbomachine calculation. See figure 45A.
\bar{x}	distance in streamwise direction.
x	$= \bar{x}^2/c$ (In Chapters 2 & 3, x carries normal dimensions).
\bar{y}	distance in upwash direction.
y	$= \bar{y}^2/c$
\bar{z}	distance in spanwise direction.
z	$= \bar{z}^2/c$
z^*	$= z \cdot \delta \sqrt{1 + k_1^{*2}}$
z'	$= \bar{z} \cdot C_5$
α	angle of incidence.
$\alpha_{\text{bubble bursting}}$	α corresponding to "bubble bursting." See 2.8.
α_{set}	α set up in experiment.
α_e	effective angle of incidence of a turboblade.
β	$= \sqrt{b^2 + k_1^2}$.
γ_1, γ_3	components of unsteady aerofoil bound vorticity, corresponding to v'_i (In 2D analysis, $\gamma = \gamma_3$ only)
$\tilde{\gamma}_1, \tilde{\gamma}_3$	unsteady bound vorticity corresponding to \tilde{v}'_i (In 2D analysis, $\tilde{\gamma} = \tilde{\gamma}_3$ only)
$\gamma_{\xi}, \tilde{\gamma}_{\xi}, \text{etc.}$	components in the ξ direction.
$\gamma_{1w}, \gamma_{3w}, \text{etc.}$	vorticity shed into wake.
$\hat{\gamma}_1, \hat{\gamma}_3, \text{etc.}$	vorticity amplitudes.
δ	boundary layer thickness.
δ_2	boundary layer momentum thickness.
δ_{2s}	δ_2 at separation.
δ_{ij}	unit diagonal tensor.
$\delta(x)$	Dirac delta function.
δ_A	angle defined in figure 45A.
ξ	dimensionless distance along chord-line. See 1.2.1.
η	dimensionless distance perpendicular to the chord plane.
λ	wavenumber of $K'(x)$.
μ	viscosity.
ζ	$= \left[\left\{ \Gamma\left(\frac{1}{2}\right) \Gamma\left(\frac{2}{3}\right) / \Gamma\left(\frac{1}{3}\right) \right\} \cdot c / 2L_1 \right]$
ρ	density.
$\underline{\gamma}^T$	instantaneous vorticity: vector.
γ_i^T	i th component of $\underline{\gamma}^T$.

$\zeta_{i\infty}$	i th component of undistorted vorticity (In 2D analysis, $\zeta_{\infty} = \zeta_{z\infty}$).
$\hat{\zeta}_{i\infty}$	amplitude of $\zeta_{i\infty}$ (sinusoidal gust).
ζ_i	i th component of additional vorticity due to distortion (In 2D analysis, $\zeta = \zeta_z$).
$\hat{\zeta}_i$	amplitude of ζ_i .
$\zeta_{\xi\infty}, \zeta_{\xi}$	components in ξ direction.
$\zeta_{\eta\infty}, \zeta_{\eta}$	components in η direction.
τ	(i) aerofoil section thickness. (ii) in correlation functions, the time delay $= \mu/\rho$.
ν	$= \mu/\rho$.
$\phi_{11}(\bar{k}_1)$	spectrum of v_1 .
$\phi_{22}(\bar{k}_1)$	spectrum of v_2 .
$\phi(n)$	a spectrum in terms of n ; $\phi(n) = 4\pi/U_{\infty} \phi(\bar{k}_1)$.
$\hat{\phi}(n)$	a normalized spectrum; e.g. $\hat{\phi}_{11}(n) = \phi_{11}(n)/\bar{v}_1^2$.
$\bar{\Phi}_{22}(\bar{k}_1, \bar{k}_3)$	two dimensional upwash spectrum.
$\bar{\Phi}_{ij}(\bar{k}_1, \bar{k}_2, \bar{k}_3)$	three dimensional spectrum (tensor).
$\phi_{C_L}(\bar{k}_1)$	spectrum of C_L .
$\bar{\omega}$	angular frequency with normal dimensions.
ω	$= \bar{\omega} c/2$
$\Gamma(\text{number})$	gamma function.
Γ	unsteady aerofoil circulation.
$\hat{\Gamma}$	amplitude of Γ .
ϵ	(i) sinusoidal gust: amplitude $= \epsilon U_{\infty}$. (ii) turbulent gust: $\sqrt{\bar{v}_1^2} = \epsilon U_{\infty}$.
Λ	angle of sweep.
$\underline{\Lambda}$	pressure gradient parameter: laminar boundary layer. See 2.7.1.
Λ_{ij}, Λ_z	non-linear gust response functions. See Appendix 10.
Ω_i	general sinusoidal response function for v_i . See 1.2.5

Superscripts

—	(i) for time-dependent properties: time mean. (ii) for functions of wavenumber: Fourier transform. (iii) for x, y, z, k_i, ω, t : quantities carry normal dimensions.
*	complex conjugate.
^	amplitude.

Subscripts

$i = 1, 2, 3$	components in the $x, y,$ and z directions respectively.
---------------	--

—

vector.

 ij

tensor.

 ξ, η components in the ξ and η directions respectively.

REFERENCES

- Abbott, I. H.,
von Doenhoff, A. E.,
and Stivers, L. S. Summary of airfoil data. NACA Report 824 (1945)
- Allen, G. H.,
and Vincenti, W. G. Wall interference in a two-dimensional flow
wind tunnel with consideration of the effect
of compressibility. NACA Report 782 (1944)
- Baines, W. D.,
and Peterson, E. G. An investigation of flow through screens.
Trans ASME, 73, 467 - 480 (1951)
- Batchelor, G. K. The theory of homogeneous turbulence.
Cambridge Univ. Press (1953)
- Batchelor, G. K. An introduction to fluid dynamics. Cambridge
Univ. Press (1967).
- Batchelor, G. K.,
and Proudman, I. The effect of rapid distortion of a fluid in
a turbulent motion. Quart. J. Mech. App. Math.
1, 83 (1954) .
- Bearman, P. W. Some effects of turbulence on the flow around
bluff bodies. NPL Aero Report 1264 (1968).
- Bearman, P. W. An investigation of the forces on flat plates
in a turbulent flow. NPL Aero Report 1296 (1969).
- Bearman, P. W. Some measurements of the distortion of
turbulence approaching a two-dimensional bluff
body. J. Fluid Mech, 53, 451 - 467 (1972)
- Bechert, D,
and Pfizenmaier, E. On the Kutta condition at the trailing edge of
a nozzle in a weakly non-stationary jet flow.
Deutsche L & R fahrt, 71 - 09 (1971)
- Bendat, J. S.,
and Piersol, A. G. Measurement and analysis of random data. Wiley
(1966)
- Bisplinghoff, R. L.,
et. al. Aeroelasticity. Addison-Wesley Series in Mech. (1955)

- Bradshaw, P. Digital magtape data logging system. Imperial College. Aero TN 72 - 101 (rev. 1975)
- Braslow, A. L. A review of factors affecting boundary layer transition. NASA TN D-3384 (1966)
- Crabtree, L. F. Effects of leading-edge separation on thin wings in two dimensional incompressible flow J. Aero. Sci., 24, 597-604 (1957)
- Davies, M. E. Wakes of oscillating bluff bodies. PhD thesis Imperial College (1975)
- Dryden, H. L. Reduction of turbulence in wind tunnels. NACA Report 392 (1931)
- Dryden, H. L.,
et. al. Measurements of intensity and scale of wind-tunnel turbulence and their relationship to the critical Reynolds number of spheres. NACA Report 581 (1937)
- Edwards, P. E. The aerodynamic loading on a yawed wing in a sinusoidal gust. Imperial College M.Sc project (1972)
- Evans, B. J. Effects of free stream turbulence on blade performance in a compressor cascade. PhD thesis Cambridge University. (1971)
- Evans, W. T.
and Mort, K. W. Analysis of computed flow parameters for a set of sudden stalls in low speed two-dimensional flow. NASA TN D-85 (1959)
- Filotas, W. I. Theory of aerofoil response in a gusty atmosphere. 1 Aerodynamic transfer function. UTIAS Report 139 (1969)
- Gault, D. E. An experimental investigation of regions of separated laminar flow. NACA TN 3505 (1955)

- Giesing, J. P. Non-linear two dimensional unsteady potential flow with lift. *J. Aircraft*, 5, 2, 135-143 (1968)
- Godsey, F. W. Gas turbines for aircraft. McGraw-Hill (1949)
and Young, L. A.
- Goldstein, M., A complete second order theory for the unsteady
and Atassi, H. flow about an airfoil due to a periodic gust.
To be published in *J. Fluid Mech.* (1975)
- Goldstein, S., Modern developments in fluid mechanics. Vol 2
editor. Clarendon Press (1938)
- Graham, J. M. R. The structure of the turbulent boundary layer
artificially produced by roughness. PhD thesis
Imperial College (1968)
- Graham, J. M. R. Lifting surface theory for the problem of an
arbitrarily yawed sinusoidal gust incident on
a thin aerofoil in incompressible flow.
Aero. Quart. 21, 2, 182-198 (1970)
- Graham, J. M. R. The unsteady forces on porous plates in a
turbulent stream. To be published in *J. Fluid
Mech* (1976)
- Green, J. E. On the influence of free stream turbulence on
a turbulent boundary layer, as it relates to
wind tunnel testing at subsonic speeds.
AGARD Report 602 (1973)
- Gregory, N., Progress report on observations of three
et. al. dimensional flow patterns obtained during stall
development on aerofoils, and on the problem
of measuring two dimensional characteristics.
ARC CP 1146 (1971)
- Hakkinen, R. J., Theoretical and experimental investigation of
and Richardson, A. S. random gust loads. NACA TN 387B (1957)

- Harris, R. J. The nature of the wind. Paper 3 in the CIRIA seminar on the modern design of wind sensitive structures. Institution of Civil Engineers (1970)
- Hinze, J. O. Turbulence. McGraw-Hill (1959)
- Holmes, D.W. Experimental pressure distributions on aerofoils in transverse and streamwise gusts. CUED/A-Turbo/TR 21 (1971)
- Horlock, J. H. Fluctuating lift forces on aerofoils moving through transverse and chordwise gusts. ASME. J. Basic. Eng. FE-28 (1968)
- Horton, H. P. A semi-empirical theory for the growth and bursting of laminar separation bubbles. ARC CP 1073 (1969).
- Hunt, J. C. R. A theory of turbulent flow round two-dimensional bluff bodies. J. Fluid Mech., 61, 4 (1973)
- Huffman, G. D.,
et. al. The effect of free stream turbulence level on turbulent boundary layer behaviour. Agardograph 164 (1972)
- Jackson, R. The loading of rectangular wings in unsteady flows. PhD thesis. Cambridge Univ. (1970)
- Jackson, R,
Graham, J. M. R.
and Maull, D. J. The lift on a wing in a turbulent flow. Aero. Quart, 24, 3 (1973)
- Jacobs, E. N.,
and Sherman, A. Airfoil section characteristics as affected by variations of Reynolds number, NACA Report 586 (1937).
- Jones, B. M. An experimental study of the stalling of wings. ARC R&M. 1588 (1933)

- Kemp, N. H. 183.
On the lift and circulation of aerofoils in
some unsteady flow problems. J. Aero Sci,
19, 713-714, (1952)
- Kemp, N. H.,
and Sears, W. R. Aerodynamic interference between moving blade
rows. J. Aero. Sci. 20, 9, 585 (1953)
- Kemp, N. H.,
and Sears, W. R. The unsteady forces due to viscous wakes in
turbomachines. J. Aero. Sci., 22, 478 (1955)
- Kiock, R. Influence of the degree of turbulence on the
aerodynamic coefficients of cascades.
Agardograph 164 (1972)
- Klebanoff, P. S.,
and Kiehl, Z. W. Some features of artificially thickened fully
developed turbulent boundary layers. NACA TN
2475 (1951)
- Liepmann, H. W. Extension of the statistical approach to
buffeting and gust response of wings of finite
span. J. Aero. Sci., 22, 3 197-200 (1955)
- Lighthill, M. J. The response of laminar skin friction and heat
transfer to fluctuations in stream velocity.
Proc. Roy. Soc., A224, 1-23 (1954)
- Lighthill, M. J. Drift. J. Fluid Mech., 1, 31 (1956)
- Lighthill, M. J. Fourier analysis and generalized functions.
Cambridge Univ. Press (1958)
- M^cCullough, G.B.
and Gault, D. E. Examples of three representative types of air-
foil section stall at low speed. NACA TN2502(1951)
- M^cCullough, G.B. The effect of Reynolds number on the stalling
characteristics and pressure distributions of
four moderately thin airfoil sections. NACA
TN 3524 (1955)
- Millikan, C. B. Further experiments on the variation of
maximum lift coefficient with turbulence and
Reynolds number. Trans. ASME, 56, 815-825(1934)

- Morfey, C. L. Lift fluctuations associated with unsteady chordwise flow past an aerofoil. ASME. J. Basic Eng. Sept. (1970)
- Mugridge, B. D. Gust loading on a thin aerofoil. Aero. Quart. 22, 3, 301 (1971)
- Owen, P. R. and Klanfer, L. On the laminar boundary layer separation from the leading edge of a thin aerofoil. ARC. CP. 220 (1955)
- Petty, D. G. The distortion of turbulence by a circular cylinder. Paper in the symposium on external flows. Univ. of Bristol (1972)
- Relf, E. I. Results from the compressed air tunnel. J. Roy. Aero Soc., 39, 1-30 (1935)
- Ribner, H. S. Spectral theory of buffeting and gust response unification and extension. J. Aero Sci., 23, 12, 1075 (1956)
- Ribner, H. S., and Tucker, M. Spectrum of turbulence in a contracting stream, NACA TN 2606, (1953)
- Roberts, J. B. A linear theory for the fluctuating drag of simple structures in turbulent flow. NPL Aero Report 1329 (1971)
- Sears, W. R. Some aspects of non-stationary aerofoil theory and its practical applications. J. Aero Sci., 8, 3, 104 (1941)
- Stack, J. Tests in the variable density wind tunnel to investigate the effects of scale and turbulence on airfoil characteristics. NACA TN 364(1931)
- Surry, D. The effect of high intensity turbulence on the aerodynamics of a rigid circular cylinder at subcritical Reynolds number. UTIAS Report 142 (1969)

- Tani, I. Note on the interplay between the laminar separation and the transition from laminar to turbulent flow of the boundary layer. J. Soc. Aero Sci., Japan, 6, 122-134 (1939)
- Tani, I. Low-speed flows involving bubble separation. Progress in Aero. Sci. Vol 5 (1964)
- Taylor, C. R. The need for high-Reynolds-number transonic tunnels. AGARD Report 602 (1973)
- Taylor, G. I. Statistical theory of turbulence. Part V. Proc. Roy. Soc., A, 156, 307-317 (1936)
- Titchmarsh, E. C. Introduction to the theory of Fourier integrals Oxford Univ. Press (1937)
- Vickery, B. J. On the flow behind a coarse grid and its use as a model of atmospheric turbulence in studies related to the wind loads on buildings. NPL Aero. Report 1143 (1965)
- Von Karman, T. and Millikan, C. B. A theoretical investigation of the maximum lift coefficient. J. Applied Mechs., 2, 21-27 (1935)
- Wallis, R. A. Experiments with air jets to control the nose stall on a 3 ft chord NACA 64A006 aerofoil. Aero Res. Lab. (Aust). Aero Note 139 (1954)

TABLE 1. Observed Stall Types

SECTION	Smooth LR	Smooth HR	Grid S,1	Grid L
0015	COM > $\frac{1}{2}$ c	COM > $\frac{1}{2}$ c	COM > $\frac{1}{2}$ c INT/MOV	COM > $\frac{1}{2}$ c INT
0012	LE	COM < $\frac{1}{2}$ c	COM $\frac{1}{3}$ c INT/MOV	COM $\frac{1}{3}$ c INT/MOV
0009	TA 7.85°, FS	TA 8.75°, PS	TA 11.25°, PS	TA 9.5°, FS

LEGEND: COM : combined leading edge/trailing edge stall.

LE : leading edge stall.

TA : thin aerofoil stall

For the COM stall, the approximate chordwise extent of trailing edge separation prior to the nose stall is indicated by the "fraction c" below the heading. "INT" indicates intermittency of nose stall, while "INT/MOV" indicates the more complicated moving stall.

For the TA stall, some details of the long bubble formation are included, The "angle in degrees" is the angle of incidence associated with the initial formation of the bubble. "FS" and "PS" indicate, respectively, full span and part span initial bubbles.

Refer to table 2 for details of various flows.

TABLE 2. C_{Lmax} and C_{Dmin} data; Re.No. = $0.26 \cdot 10^6$

	Smooth LR	Grid S,1	Grid S,2	Grid S,3	Grid S,4	Grid S,5	Grid S,6	Grid I
$\sqrt{v_0^2}/U_\infty$	0.001	0.049	0.036*	0.023*	0.015*	0.011*	0.009	0.059
L/c	-	0.020	0.021*	0.025*	0.031*	0.036*	0.045	0.10
$\{\sqrt{v_0^2}/U_\infty\} \cdot \{c/L\}^{1/2}$	-	0.107	0.078	0.048	0.030	0.021	0.017	0.094
$C_{Lmax}, 0009^\dagger$	0.85	1.025	0.975	0.935	0.905	-	0.89	0.955
$C_{Lmax}, 0012^\dagger$	0.925	1.35	1.23	1.125	1.06	1.02	0.995	1.165
$C_{Lmax}, 0015^\dagger$	1.04	1.36	1.295	1.22	1.17	-	1.09	1.30
$C_{Dmin}, 0009$	0.0182	0.0245	0.0230	0.0190	0.0185	-	0.0187	0.0215
$C_{Dmin}, 0012$	0.0203	0.0277	0.0249	0.0229	0.0215	0.0215	0.0207	0.0241
$C_{Dmin}, 0015$	0.0216	0.0287	0.0260	0.0227	0.0221	-	0.0217	0.0247

* interpolated values; † corrected for wall interference effects

Refer to page 61 in the main test for details of grids.

TABLE 3. Typical Turbomachine Data

EXAMPLE ↓	$ V_B / V_R $	δ_A	k_s	k_z	k_f
<u>COMPRESSOR</u>					
50% Reaction	1.1	45°	2.2	2.2	3.5
10% Reaction: Rotor	0.9	60°	2.7	1.6	2.8
Stator	1.6	25°	1.3	2.8	5.0
Vortex-type : Rotor	0.7	65°	2.8	1.3	2.2
Stator	1.6	25°	1.3	2.8	5.0
<u>TURBINE</u>					
50% Reaction . (A)	1.7	35°	1.8	2.6	5.3
50% Reaction . (B) Root	1.15	25°	1.3	2.8	3.6
Tip	1.5	20°	1.1	3.0	4.7
Impulse-type: Rotor	0.7	55°	2.6	1.8	2.2
Stator	1.1	10°	0.5	3.1	3.5

NOTES: The data for $|V_B|/|V_R|$ and δ_A (refer figure 45) was elicited from the text of Godsey and Young (1949). A blade spacing to blade chord ratio of 1.0 was assumed. With the model presented in figure 45, the wavenumbers, k_s , k_z , and k_f were then given by:

$$k_s = \pi \sin \delta_A ,$$

$$k_z = \pi \cos \delta_A ,$$

$$k_f = \pi \frac{|V_B|}{|V_R|} .$$

TABLE 4 Results of the Turbomachine Calculation

$$\alpha = 10^\circ, \quad B = 1.4$$

k_s	k_z	k_f	$\text{Re}(R_g)$	$\text{Im}(R_g)$	$\text{Re}(R_A)$	$\text{Im}(R_A)$	$\text{Re}(R_M)$	$\text{Im}(R_M)$	$\text{Re}(R_D)$	$\text{Im}(R_D)$	$ R' $	$ R'' $
0.1	3.0	3.5	.017	-.056	-.086	.288	-.173	.009	.144	.038	.296	.342
1.0	3.0	5.0	.118	-.620	-.024	.203	-.126	.073	.130	.006	.351	.345
2.0	2.0	3.5	.066	-.502	.060	-.052	-.028	.071	.051	-.023	.528	.493
3.0	1.5	2.0	-.137	-.060	.047	-.021	.020	.026	-.018	-.041	.130	.088
0.1	3.0	0.1	.027	.005	-.140	-.036	-.173	.009	.188	.097	.124	.288
1.0	3.0	1.0	.117	-.040	-.016	-.020	-.126	.073	.144	.010	.121	.029
2.0	2.0	2.0	.058	-.189	.061	-.037	-.028	.071	.060	-.029	.240	.181
3.0	1.5	3.0	-.130	-.159	.048	-.052	.020	.026	-.014	-.028	.226	.195

A

TYPICAL

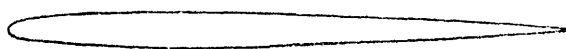
TURBOMACHINE

GUSTS

A

FROZEN

GUSTS

FIGURES

NACA 0006

o free tunnel

* with grid : estimated $\frac{\sqrt{v_1^2}}{U_\infty} = 0.06$; $\frac{L_1}{c} = 0.12$

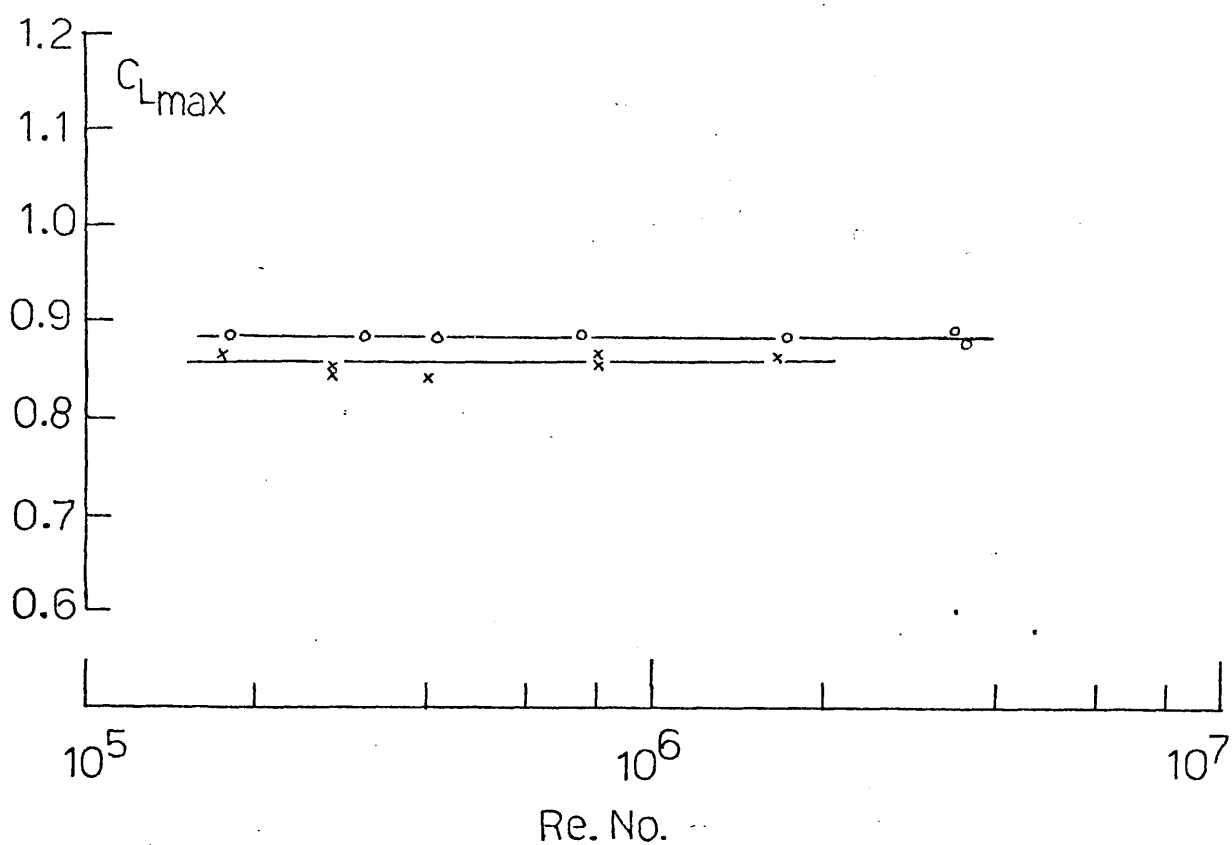
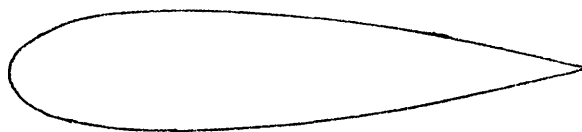


FIGURE 1. EXPERIMENTAL RESULTS OF STACK ; A.



NACA 0021

o free tunnel

x with grid : estimated $\frac{\sqrt{v_i^2}}{U_\infty} = 0.06$; $\frac{L_i}{c} = 0.12$

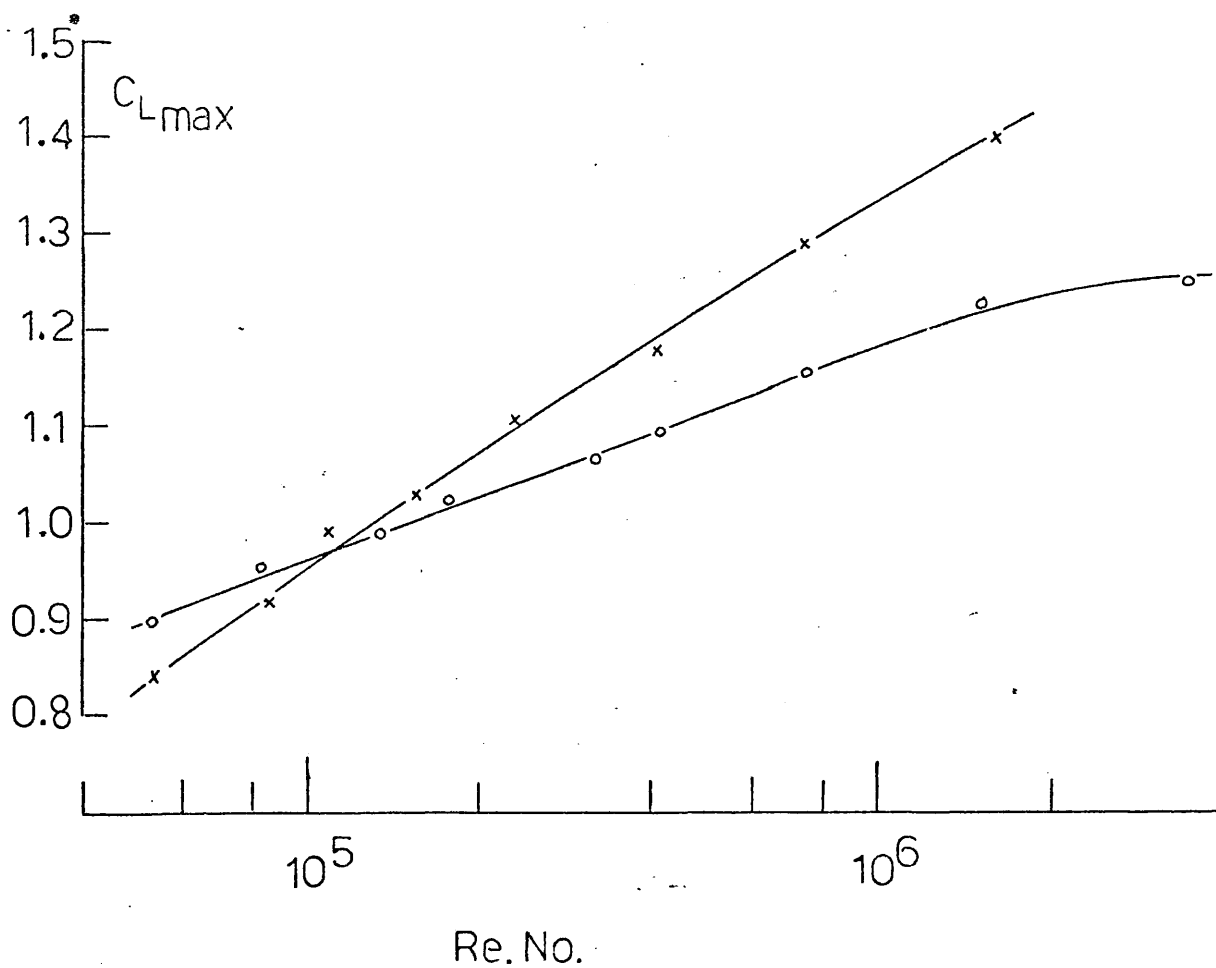
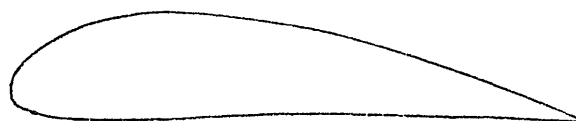


FIGURE 2. EXPERIMENTAL RESULTS OF STACK ; B.



USA 35A

• free tunnel

x with grid : estimated $\frac{\sqrt{v_i^2}}{U_\infty} = 0.06$; $\frac{L_1}{c} = 0.12$

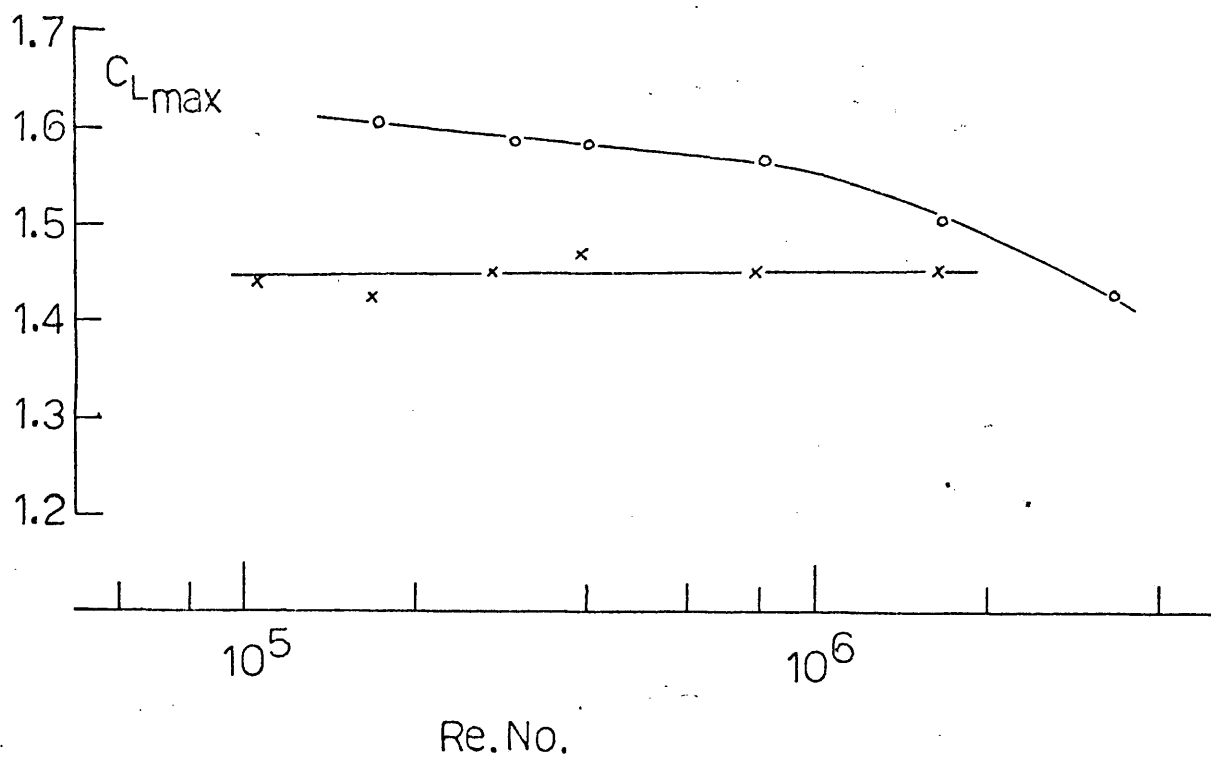


FIGURE 3. EXPERIMENTAL RESULTS OF STACK ;C.

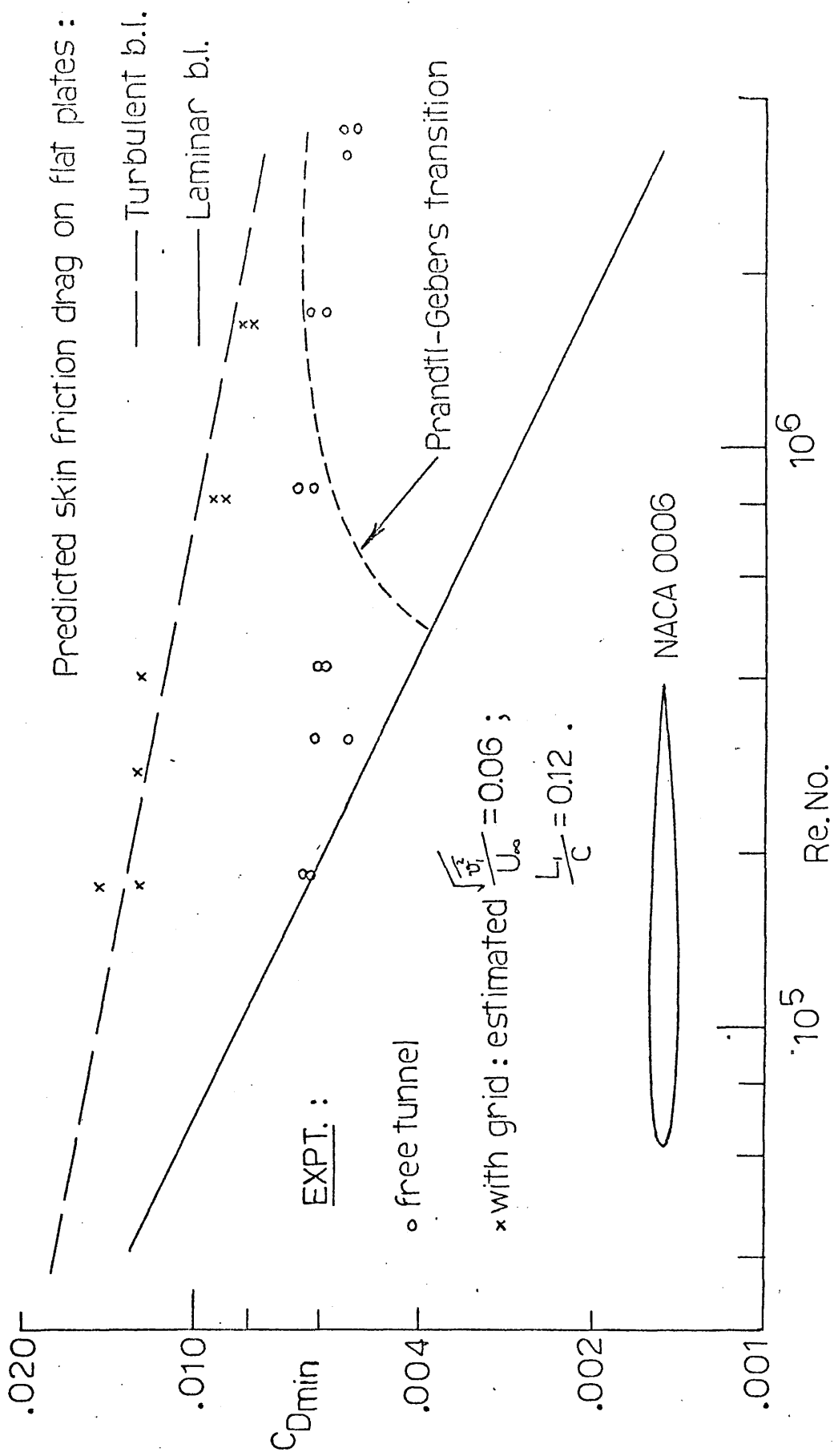


FIGURE 4. EXPERIMENTAL RESULTS OF STACK ; D.

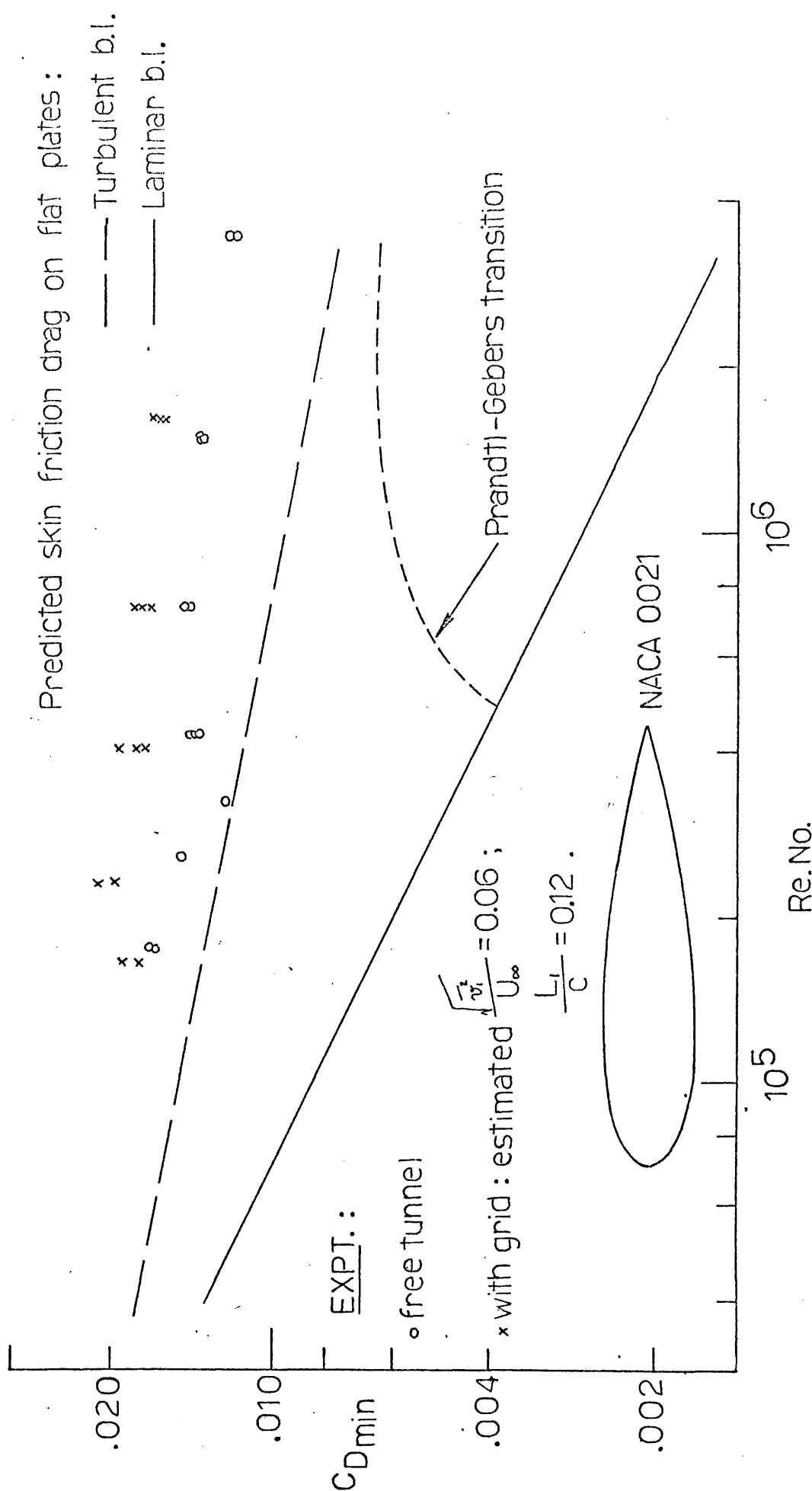


FIGURE 5. EXPERIMENTAL RESULTS OF STACK ; E.

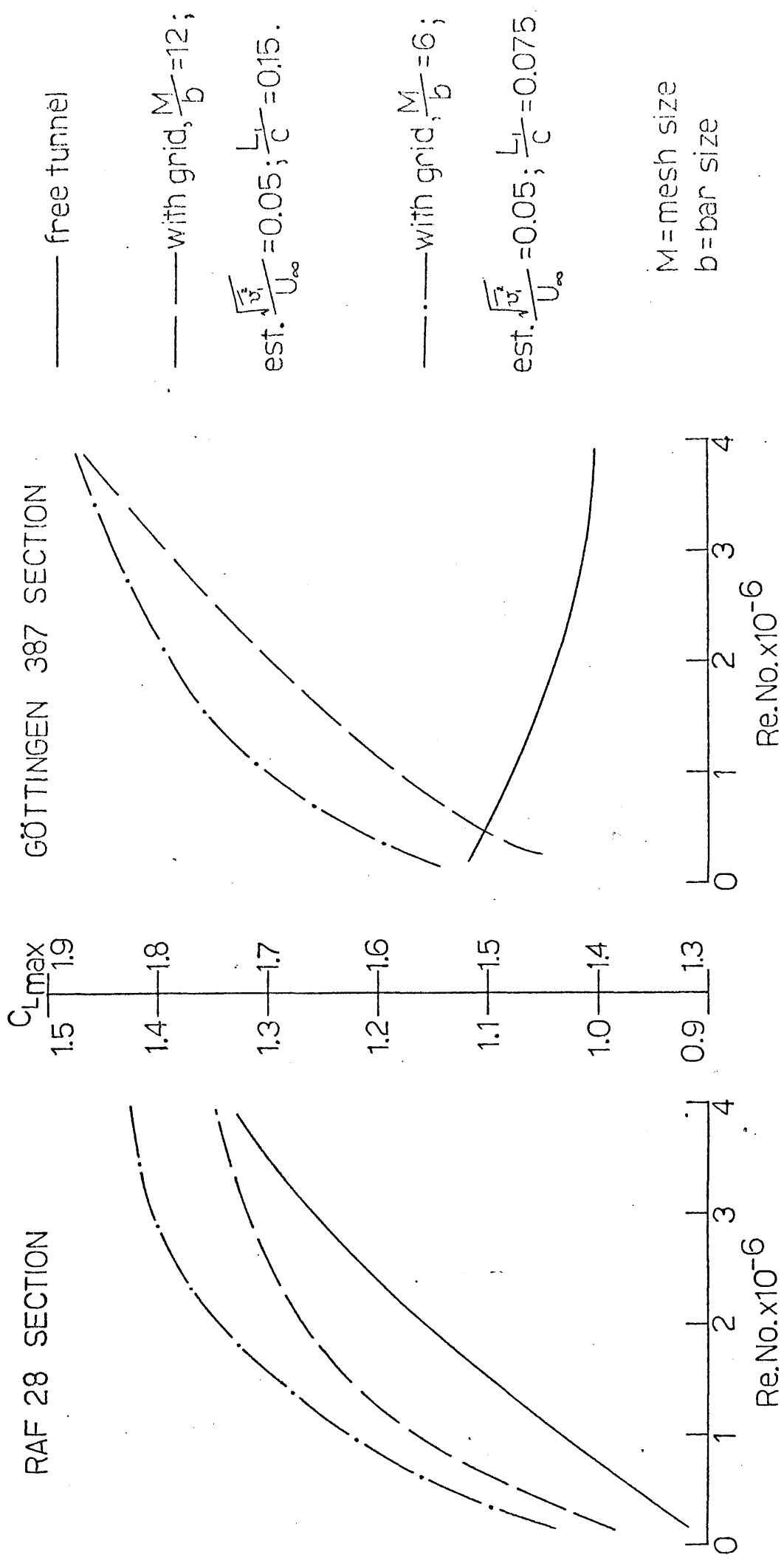
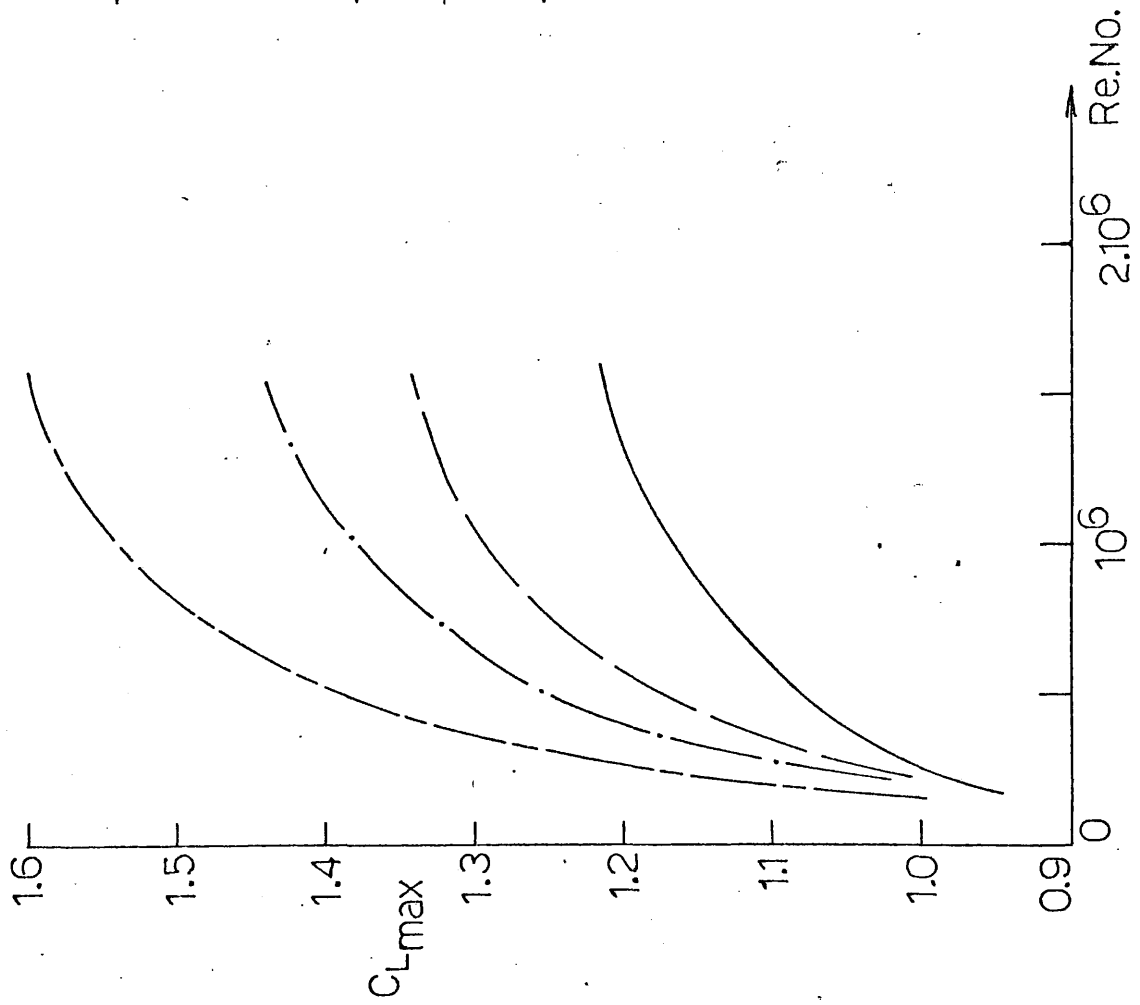


FIGURE 6. EXPERIMENTAL RESULTS OF RELF



For all cases, est. $\frac{L}{c} = 0.03$.

NACA 2412 SECTION

FIGURE 7. EXPERIMENTAL RESULTS OF MILLIKAN.

SPECTRAL ANALYSIS

EXPT 4 3 GRID

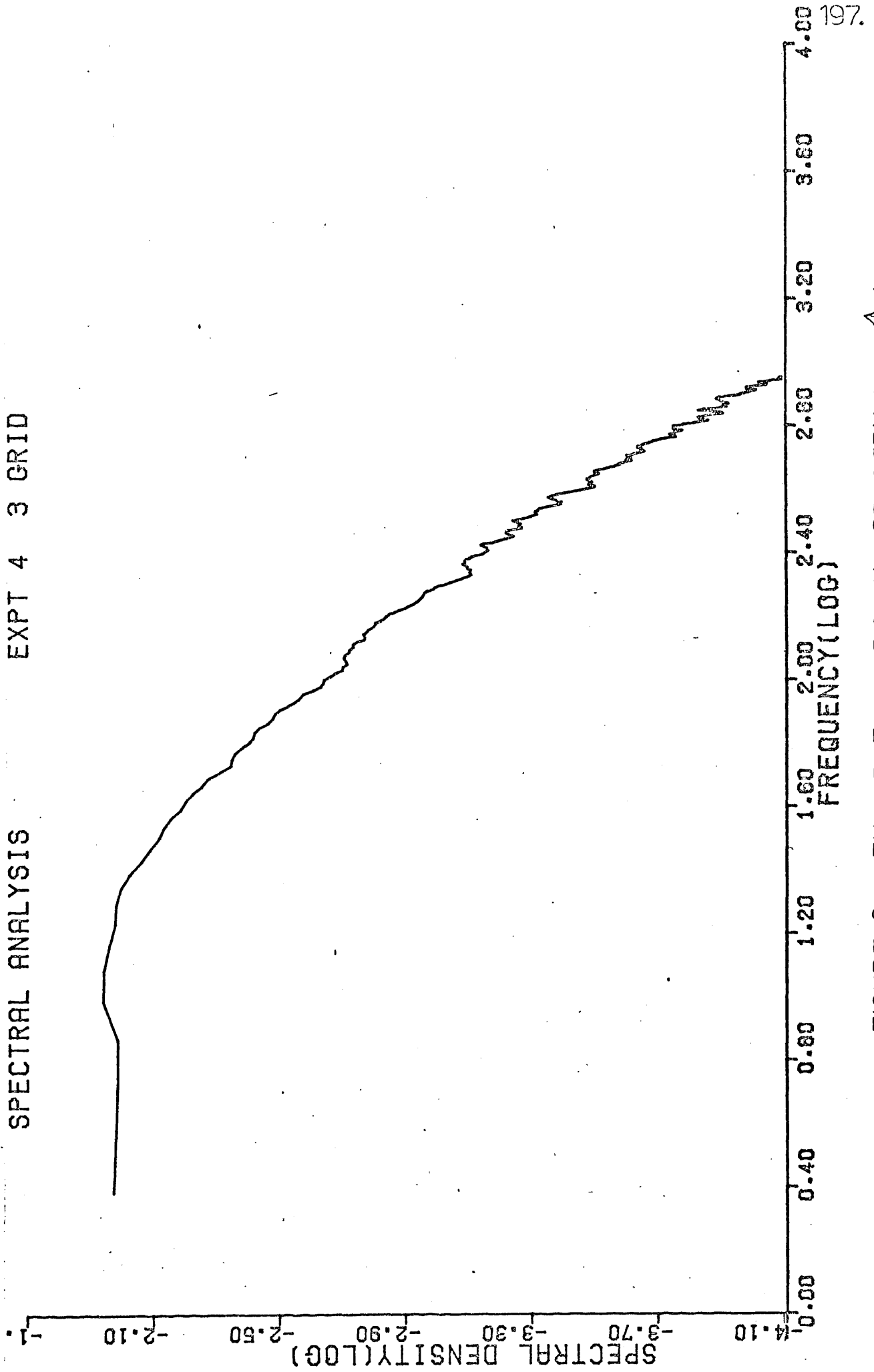


FIGURE 8. EXAMPLE OF DIGITAL SPECTRUM : $\hat{\Phi}_{11}(m)$

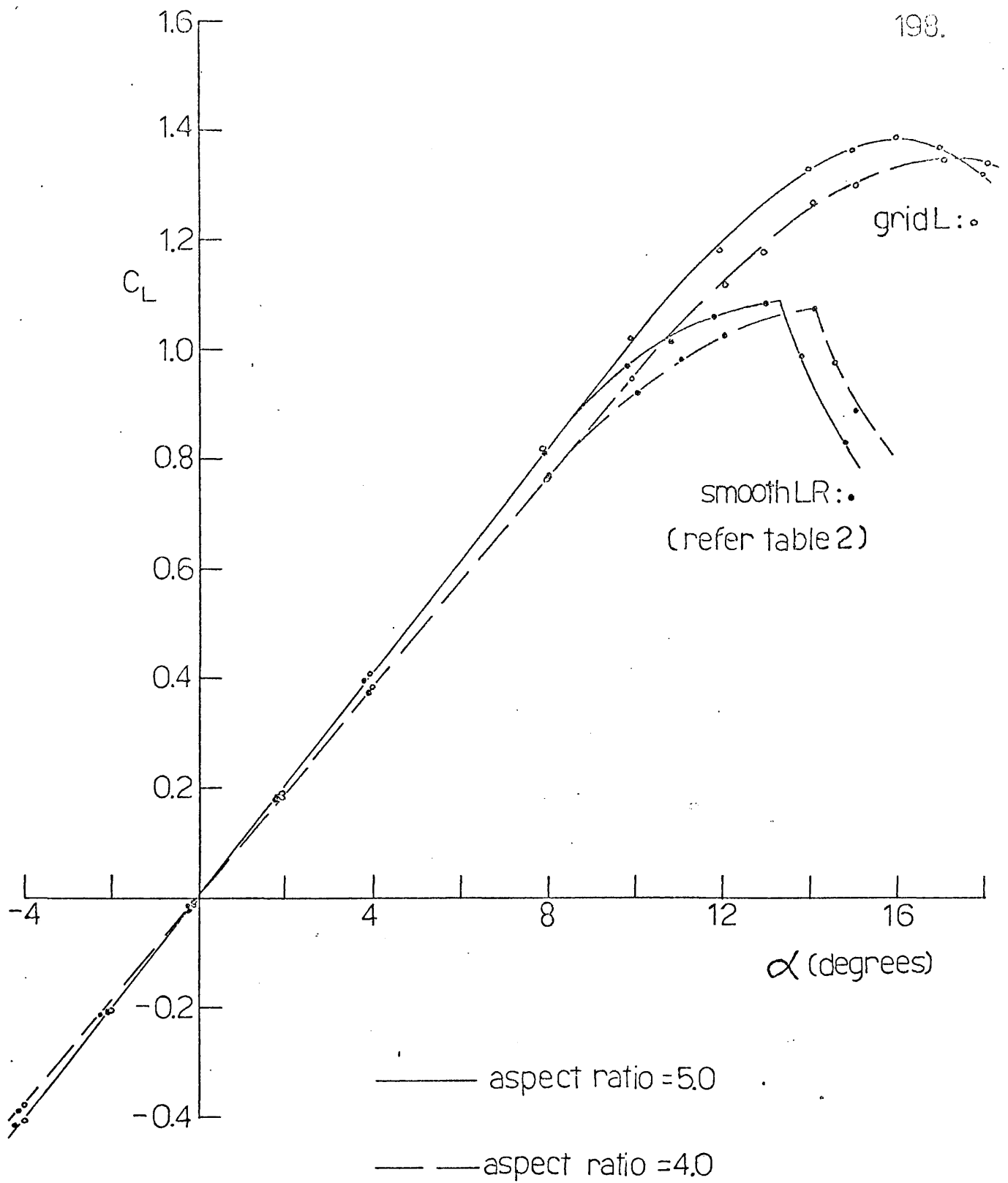


FIGURE 9. COMPARISON OF DIFFERENT SPAN MODELS;
NACA 0015.

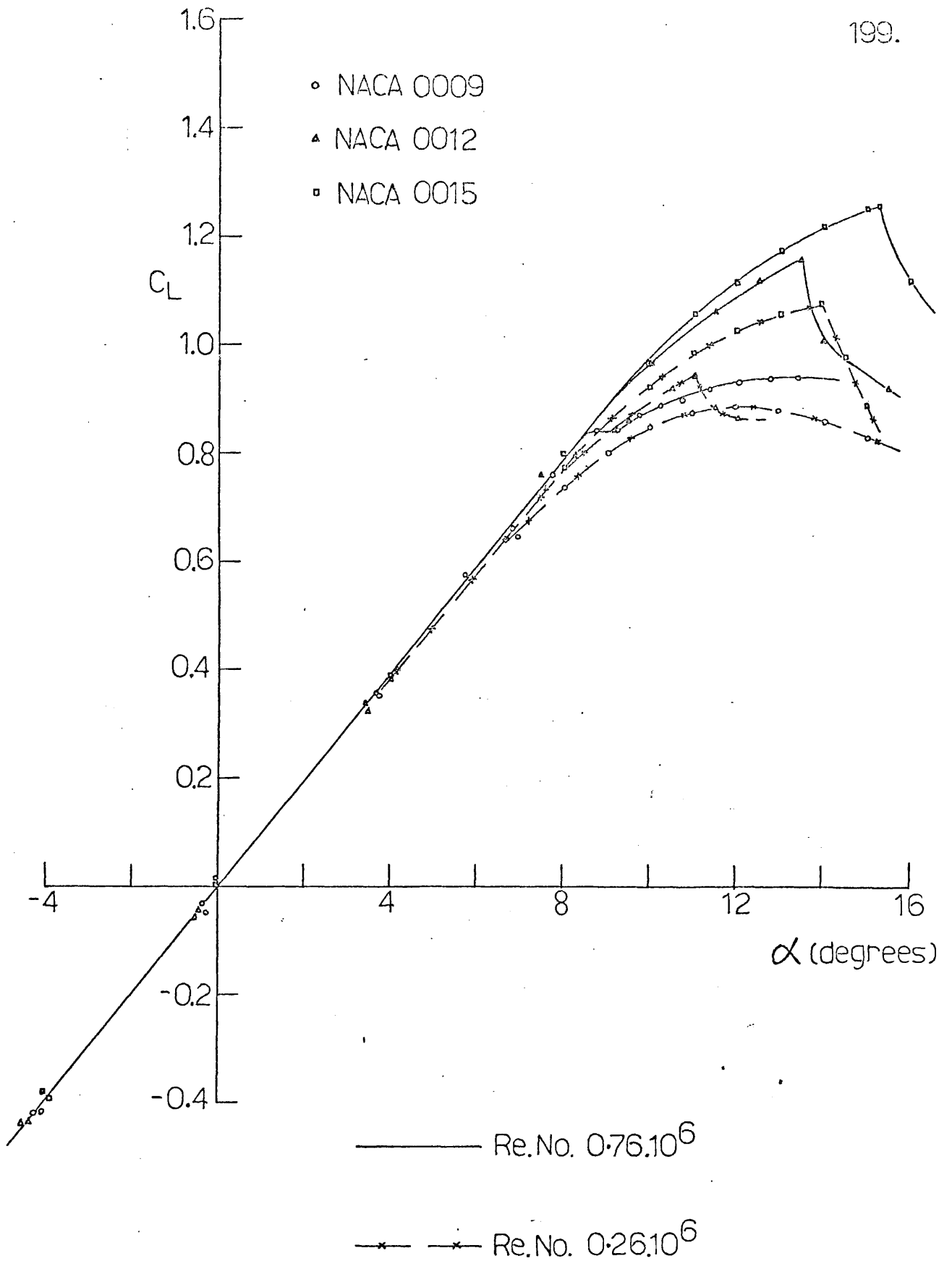


FIGURE 10. EFFECT OF REYNOLDS NUMBER ON LIFT ; SMOOTH FLOW.

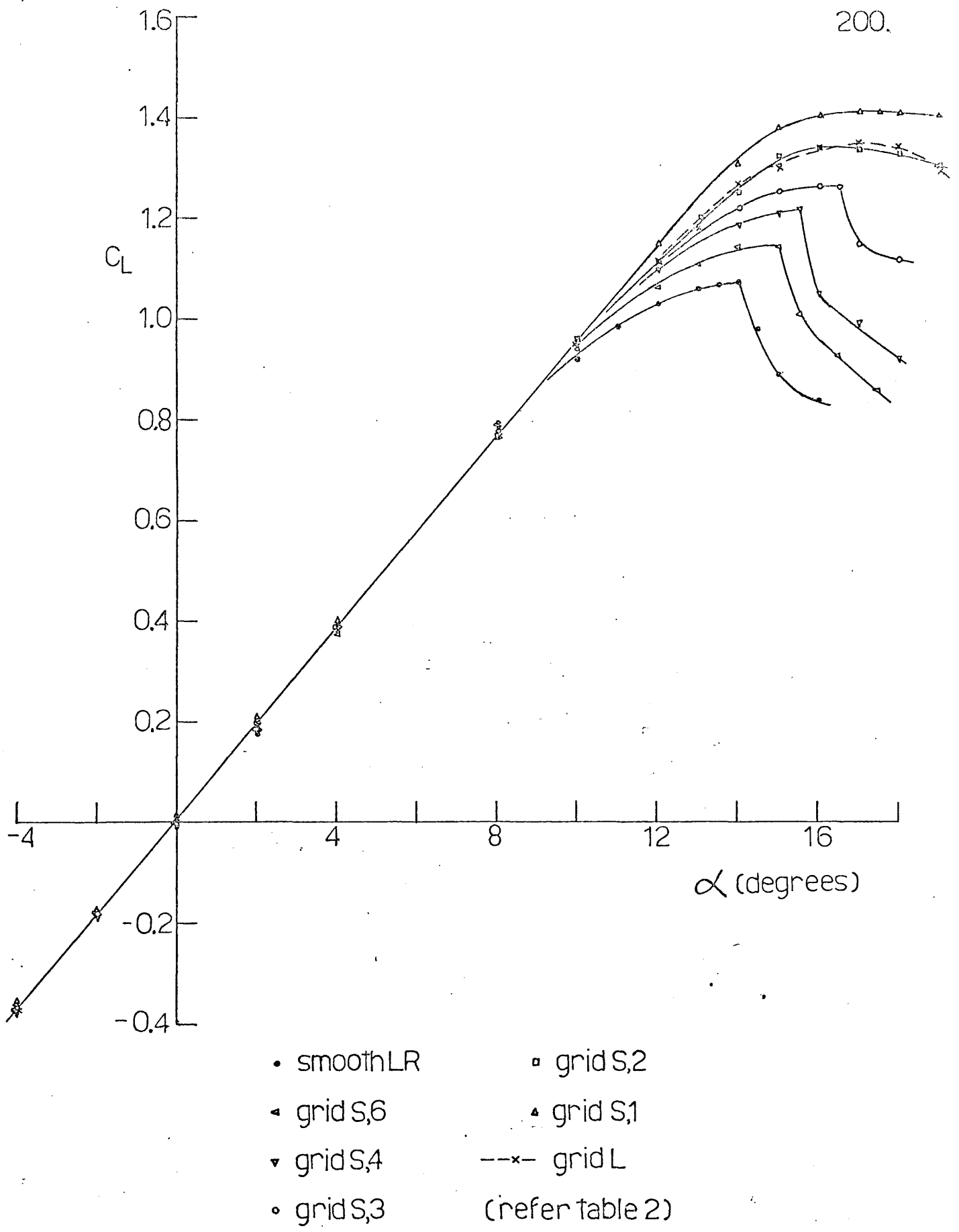


FIGURE 11. C_L vs. α ; NACA 0015 ; Re.No. = $0.26 \cdot 10^6$

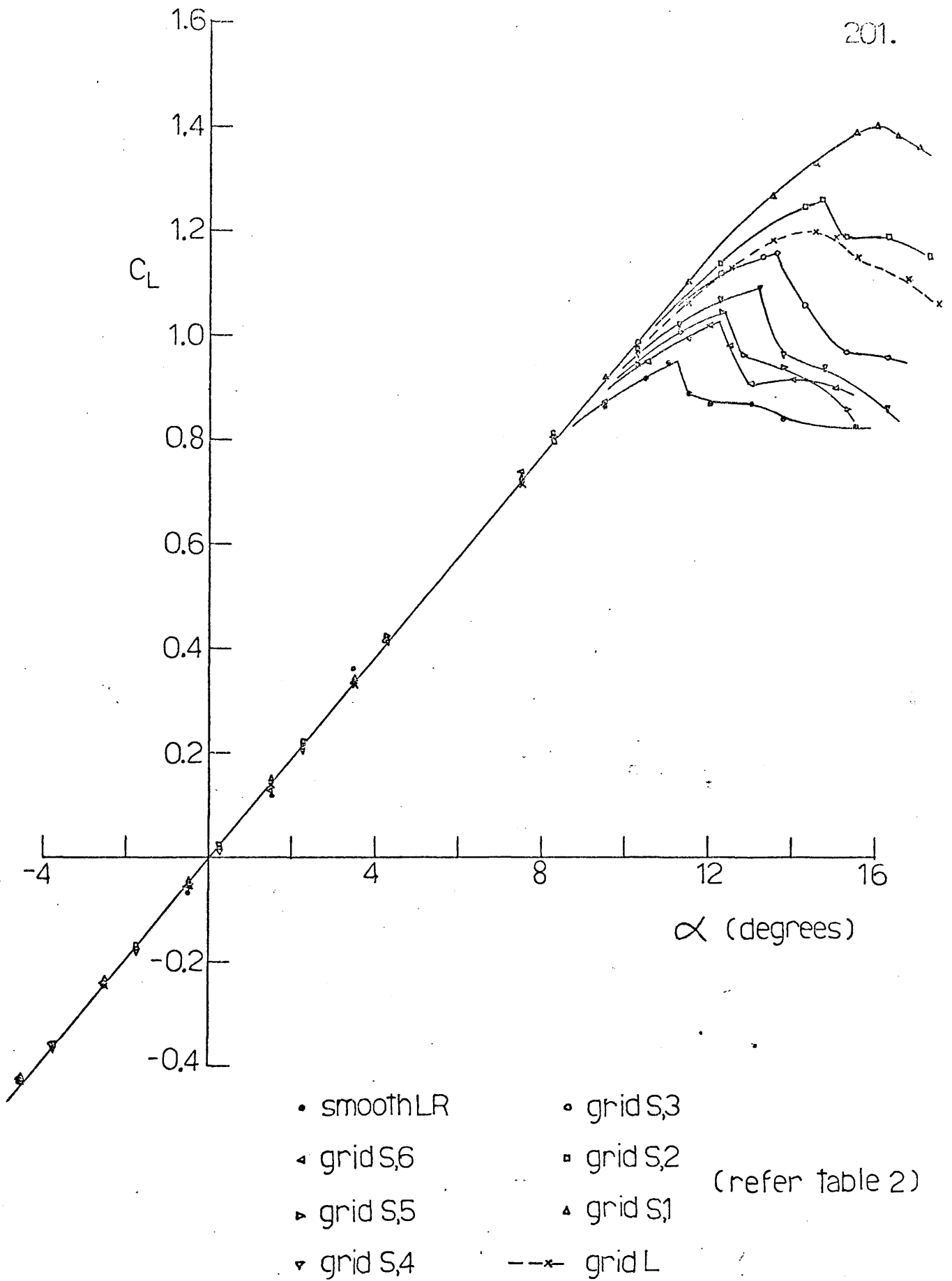


FIGURE 12. C_L vs. α ; NACA 0012 ; Re.No. = $0.26 \cdot 10^6$

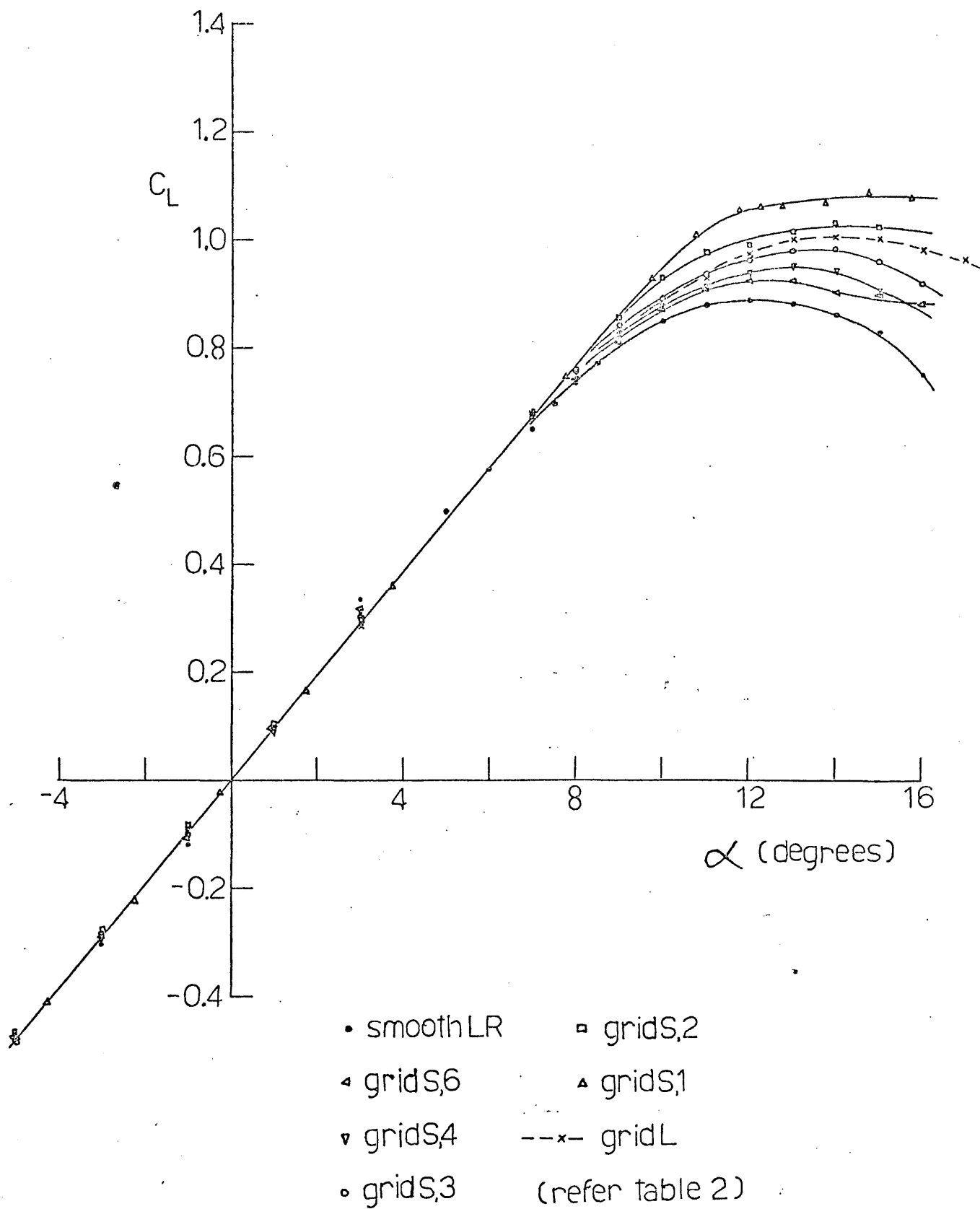


FIGURE 13. C_L vs. α ; NACA 0009 ; Re.No. = $0.26 \cdot 10^6$

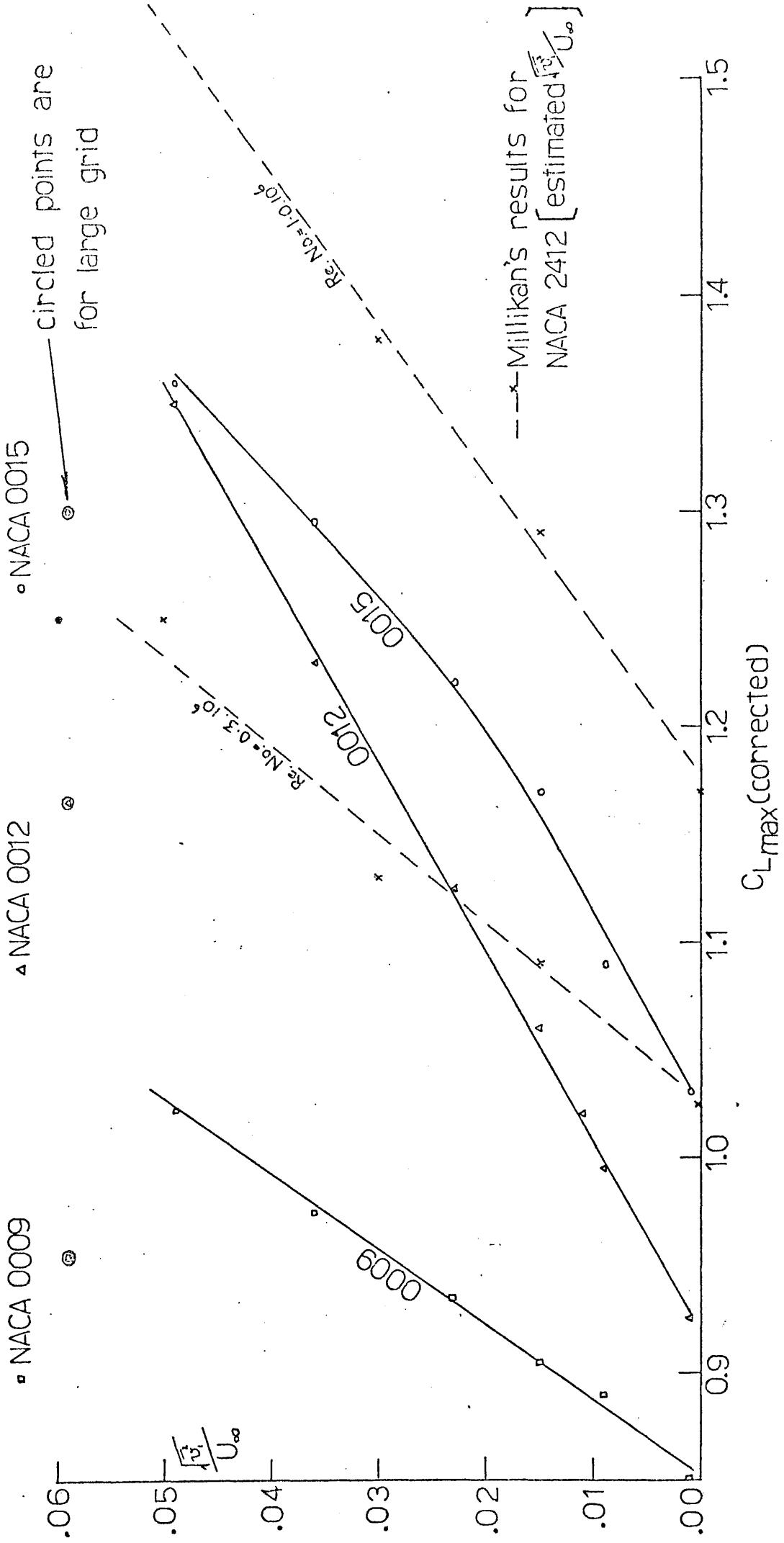


FIGURE 14. C_{Lmax} vs INTENSITY, $\frac{\sqrt{x}}{U_\infty}$. Re. No. = $0.26 \cdot 10^6$

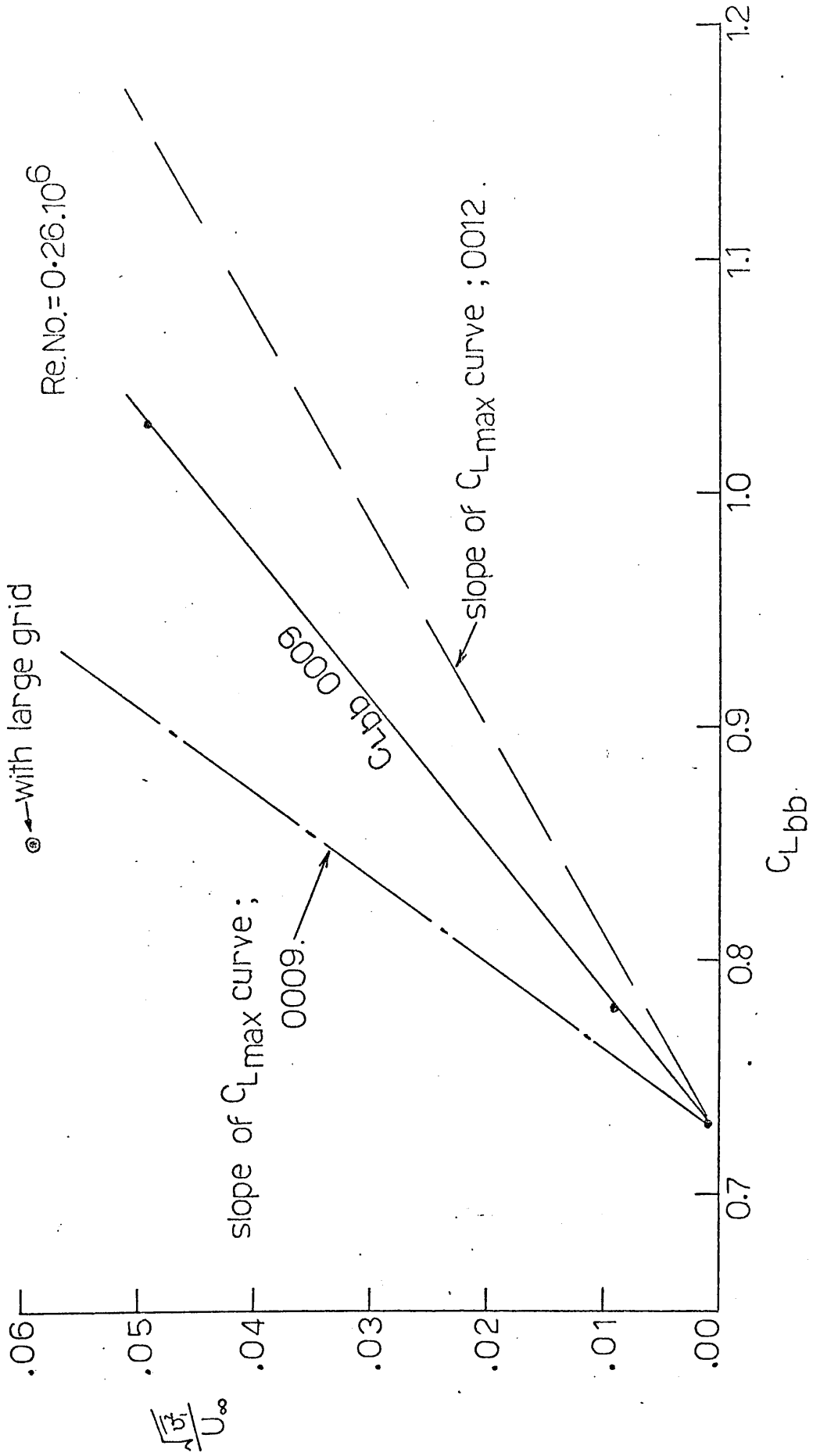


FIGURE 15 "BUBBLE-BURSTING" C_L vs. $\frac{\sqrt{x}}{U_\infty}$; NACA 0009.

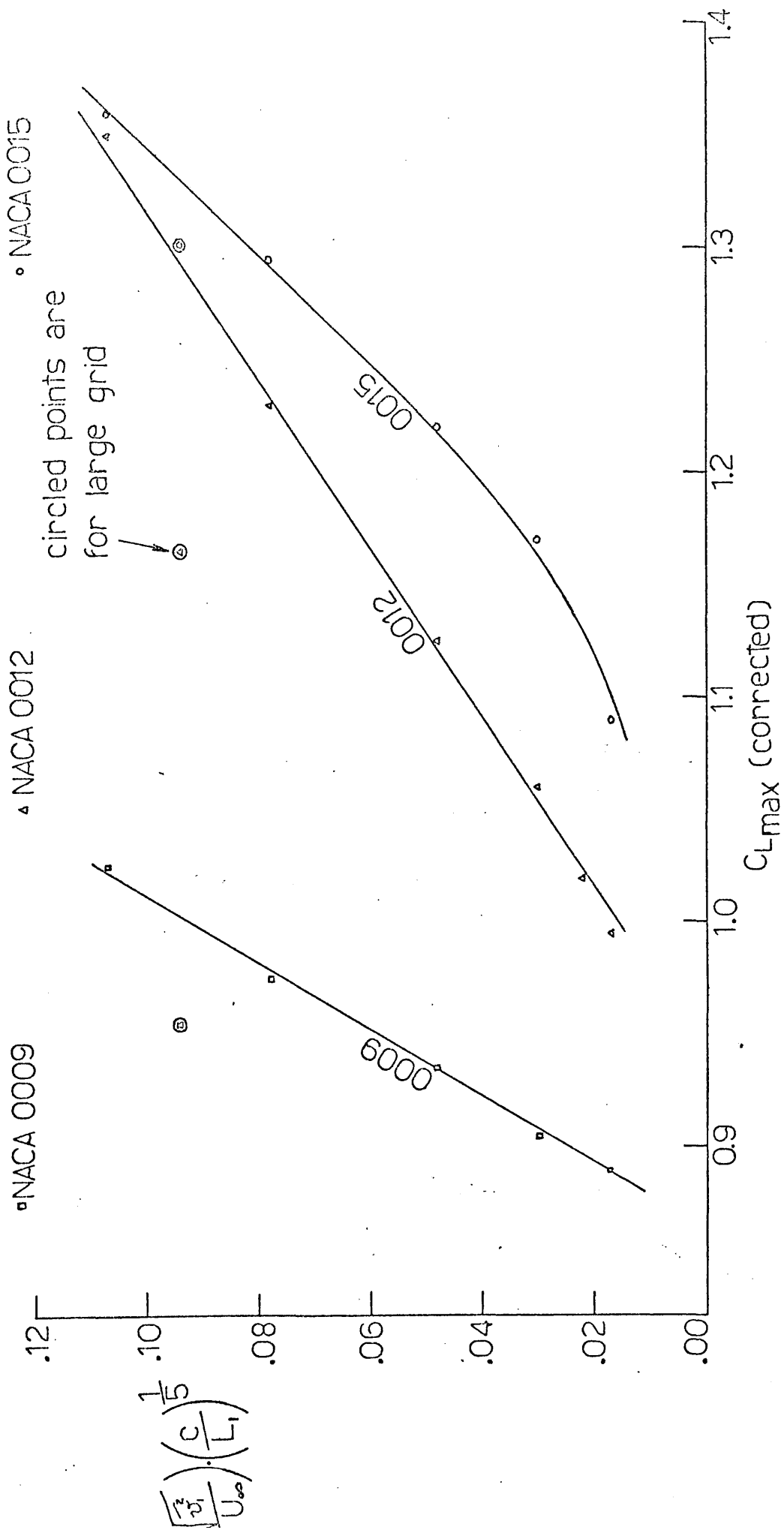


FIGURE 16. C_{Lmax} vs. TAYLOR'S PARAMETER. $Re.No. = 0.26 \cdot 10^6$.

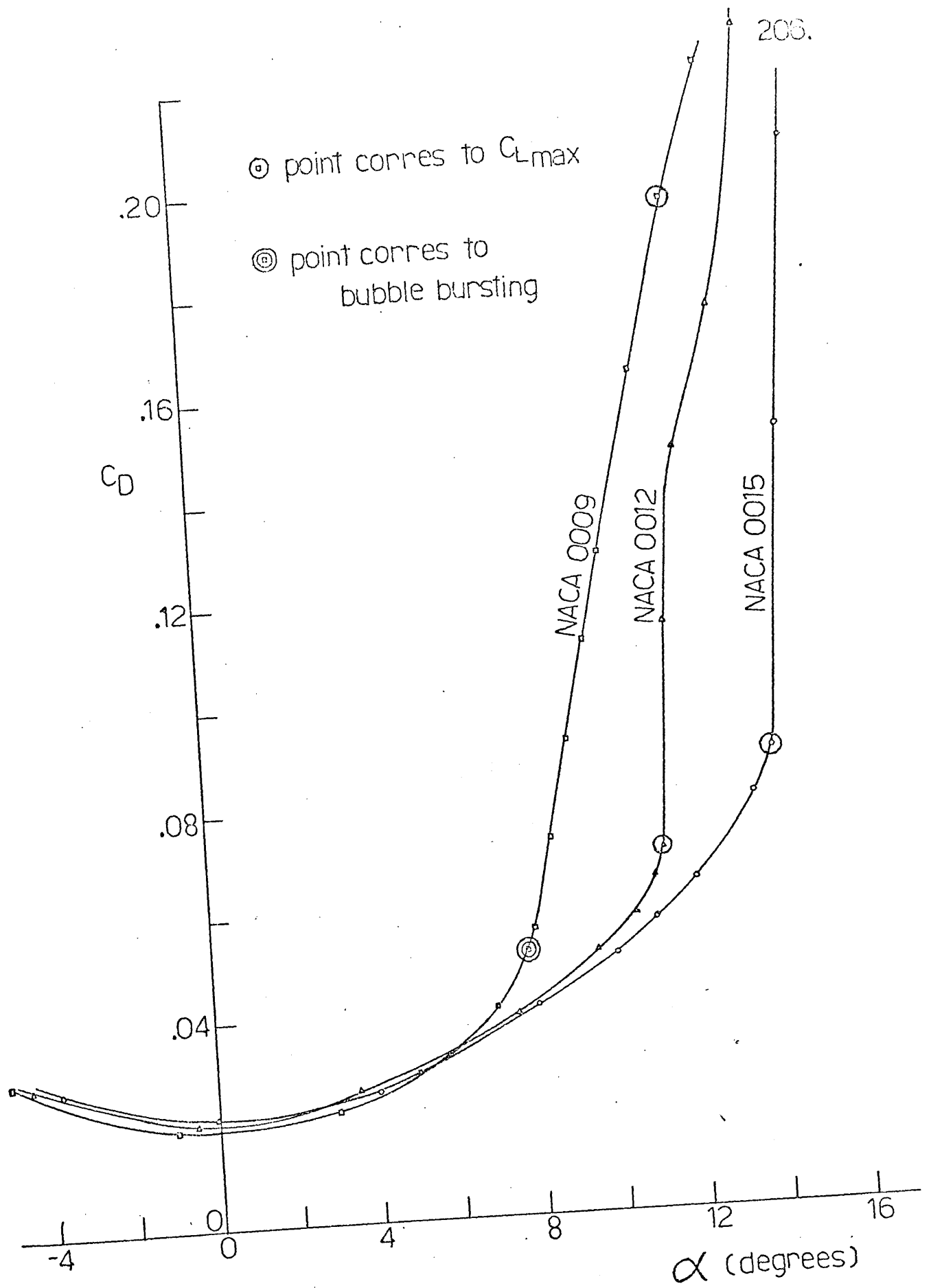


FIGURE 17. EFFECT OF THICKNESS ON DRAG ;
 SMOOTH FLOW ; $Re.No. = 0.26 \cdot 10^6$.

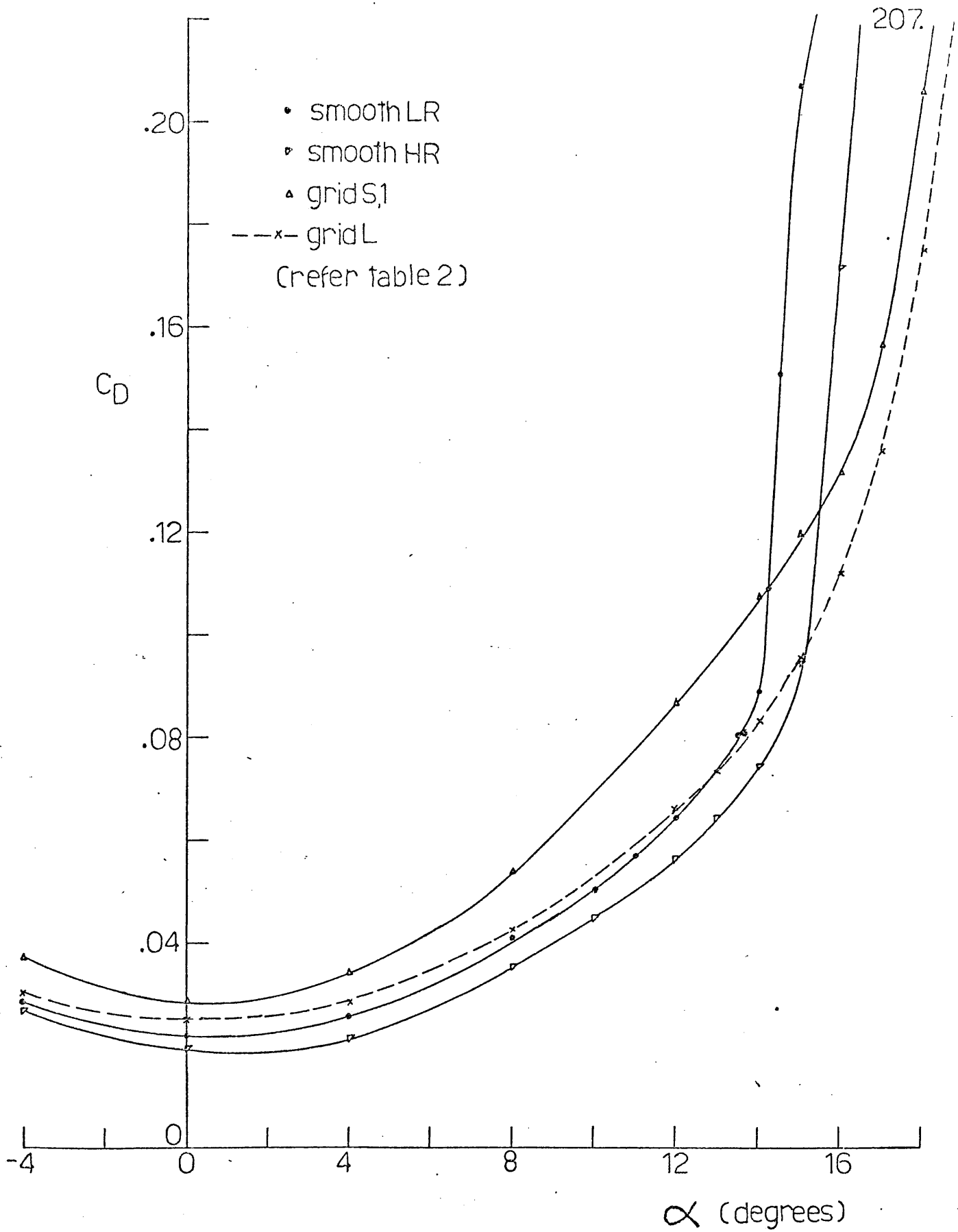


FIGURE 18 . C_D vs. α ; NACA 0015 .

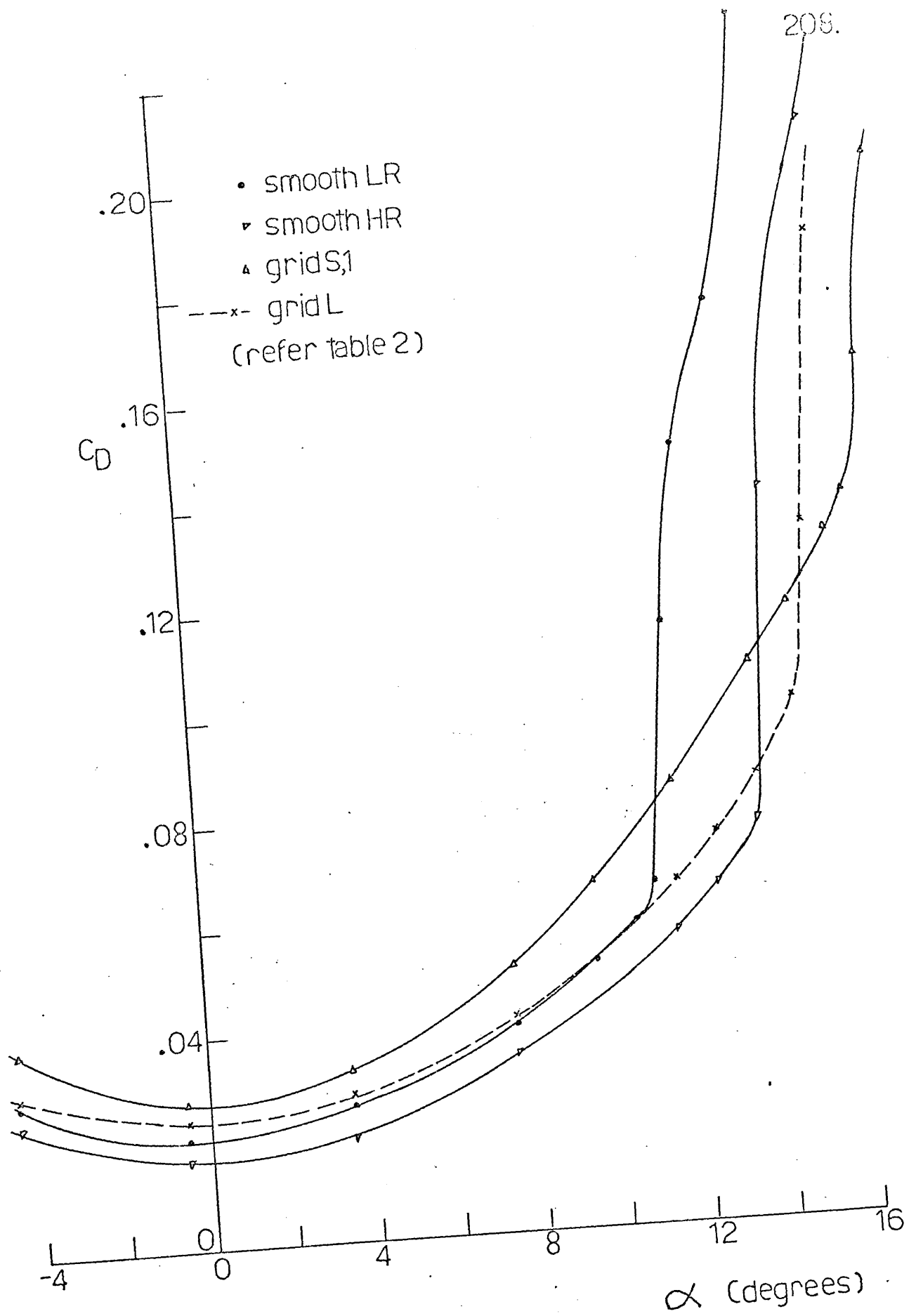


FIGURE 19. C_D vs. α ; NACA 0012

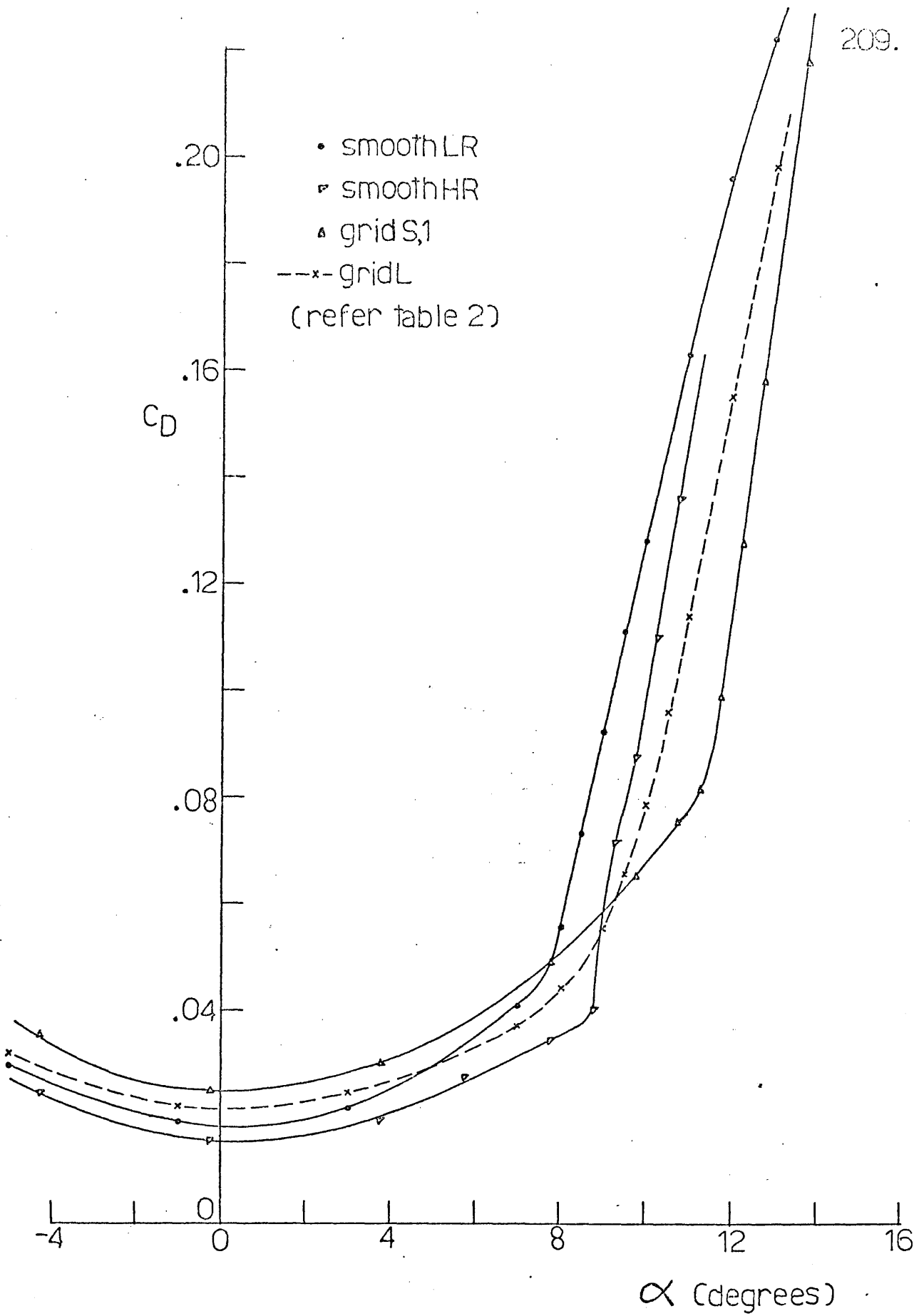


FIGURE 20. C_D vs. α ; NACA 0009 .

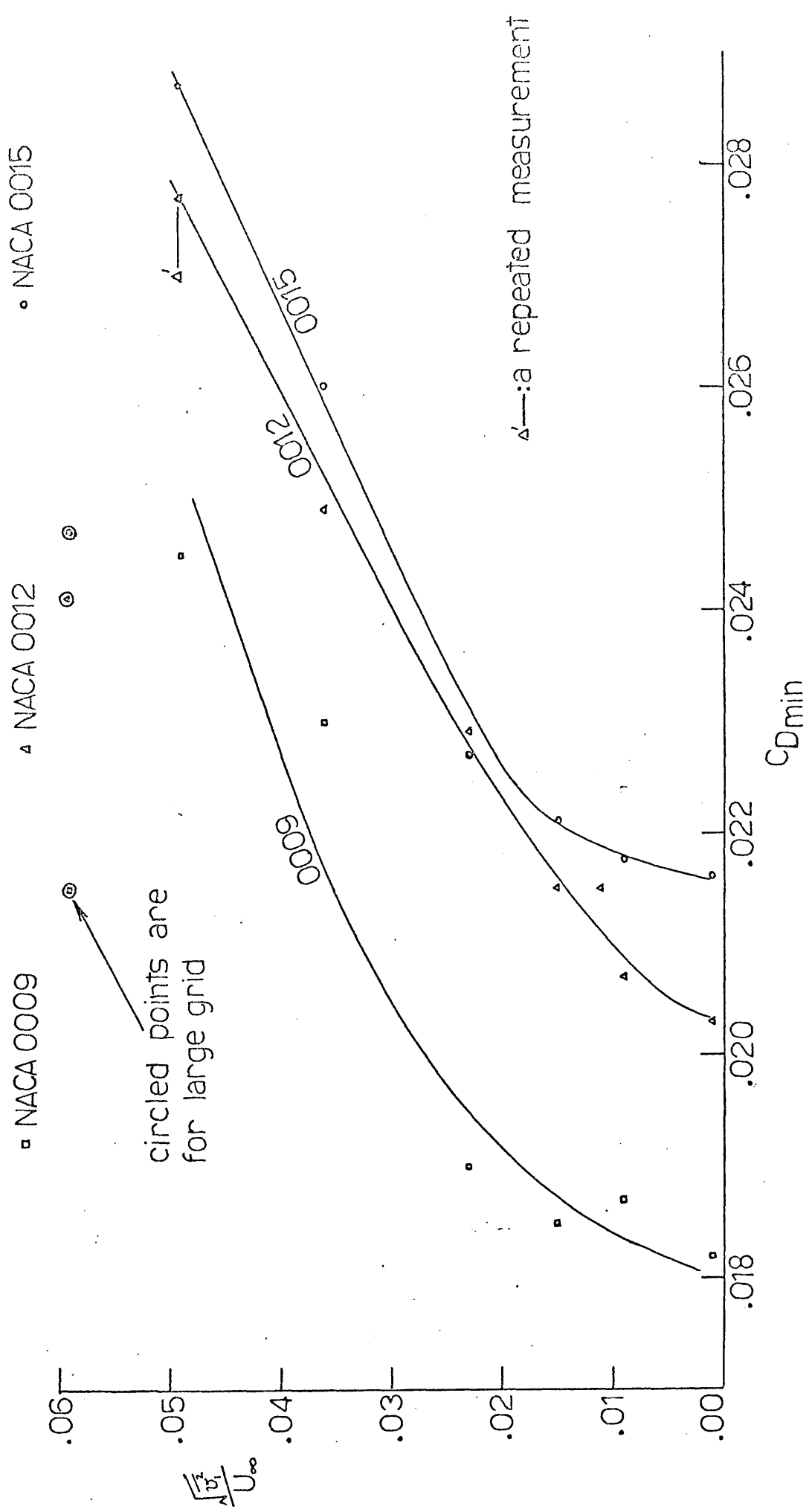


FIGURE 21. C_{Dmin} vs. INTENSITY, $\frac{\sqrt{v}}{U_\infty}$. Re. No. = $0.26 \cdot 10^6$.

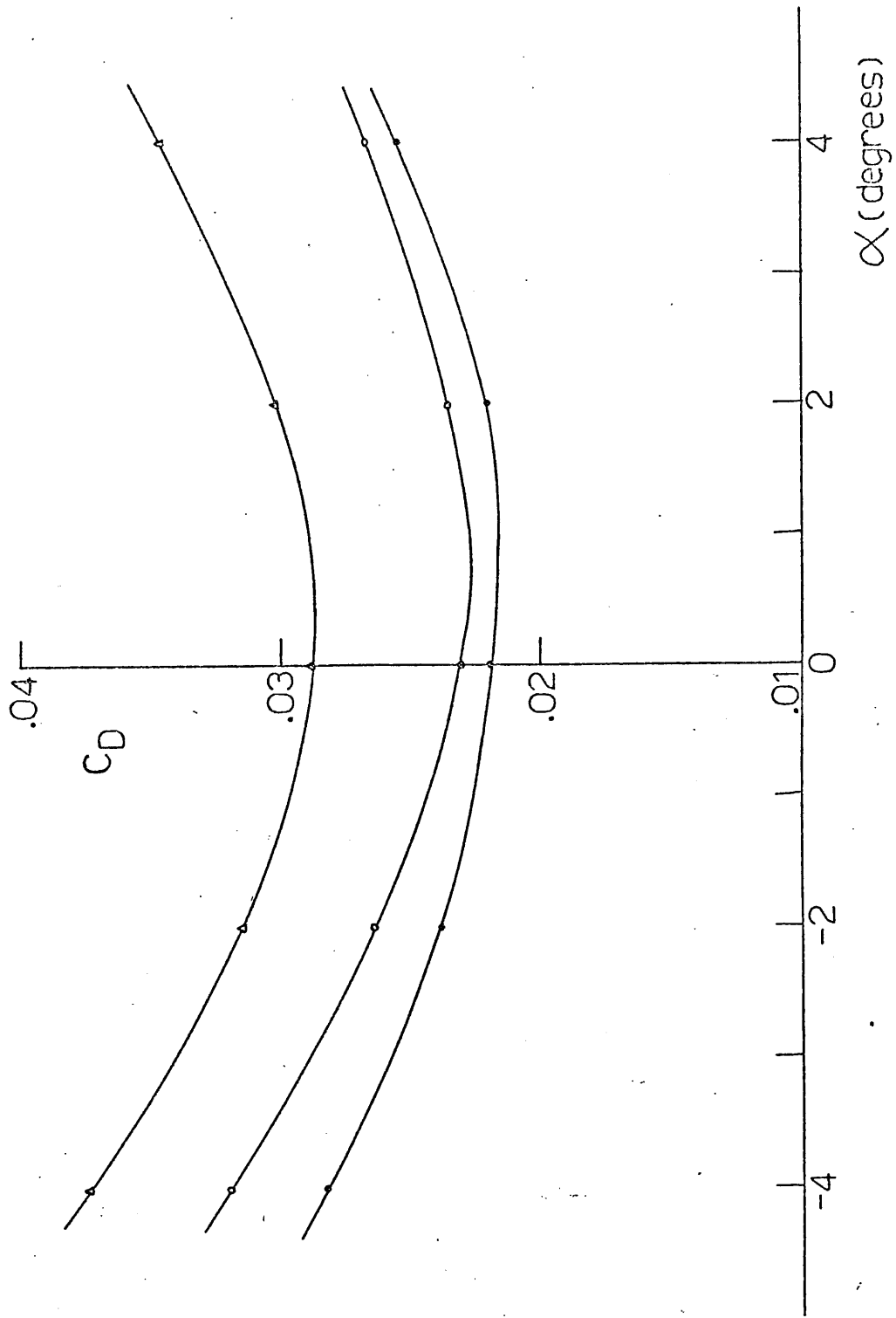


FIGURE 22. EXAMPLE CURVES USED FOR C_{Dmin} DETERMINATION.

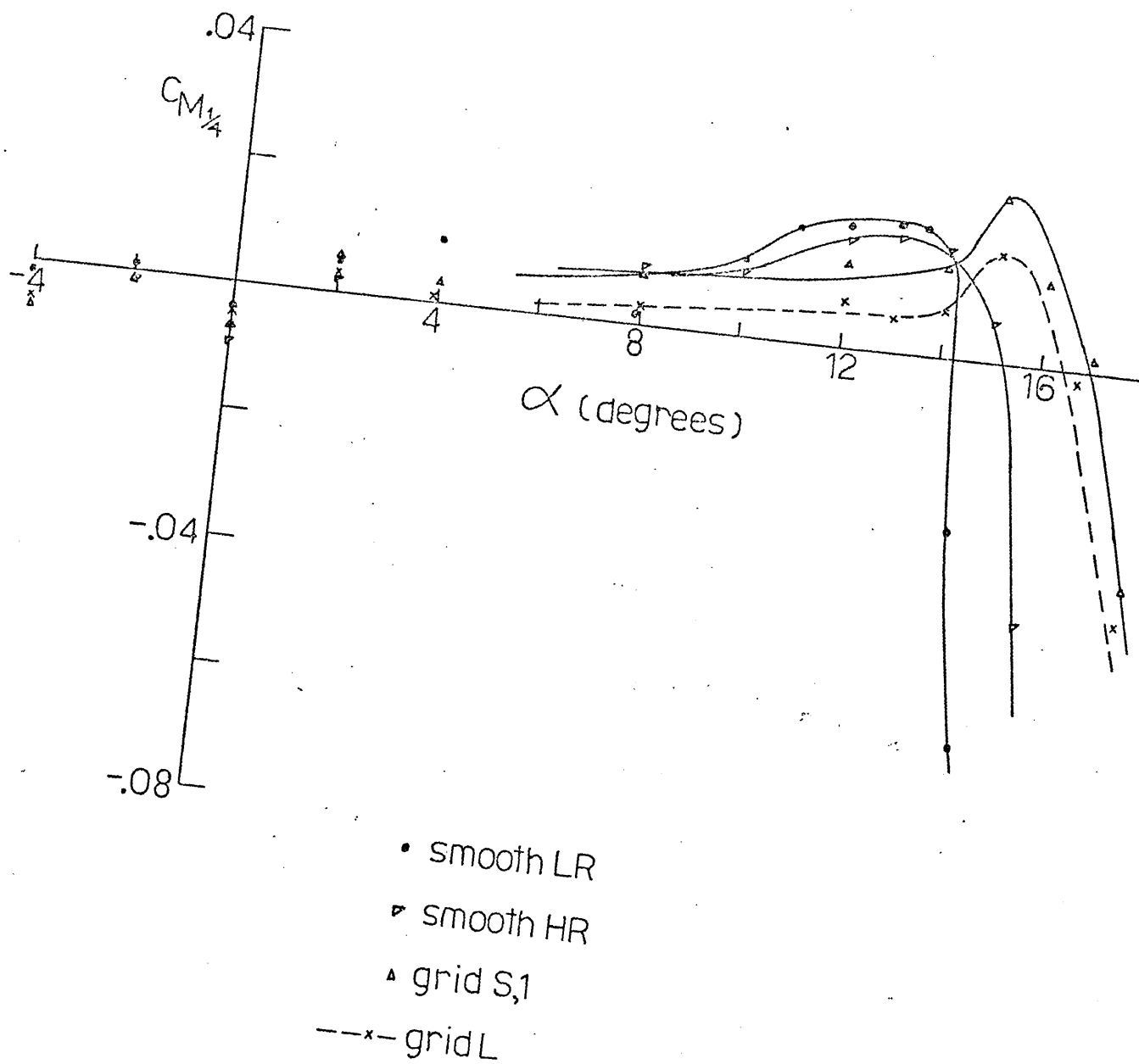


FIGURE 23. $C_{M_{1/4}}$ vs. α ; NACA 0015.

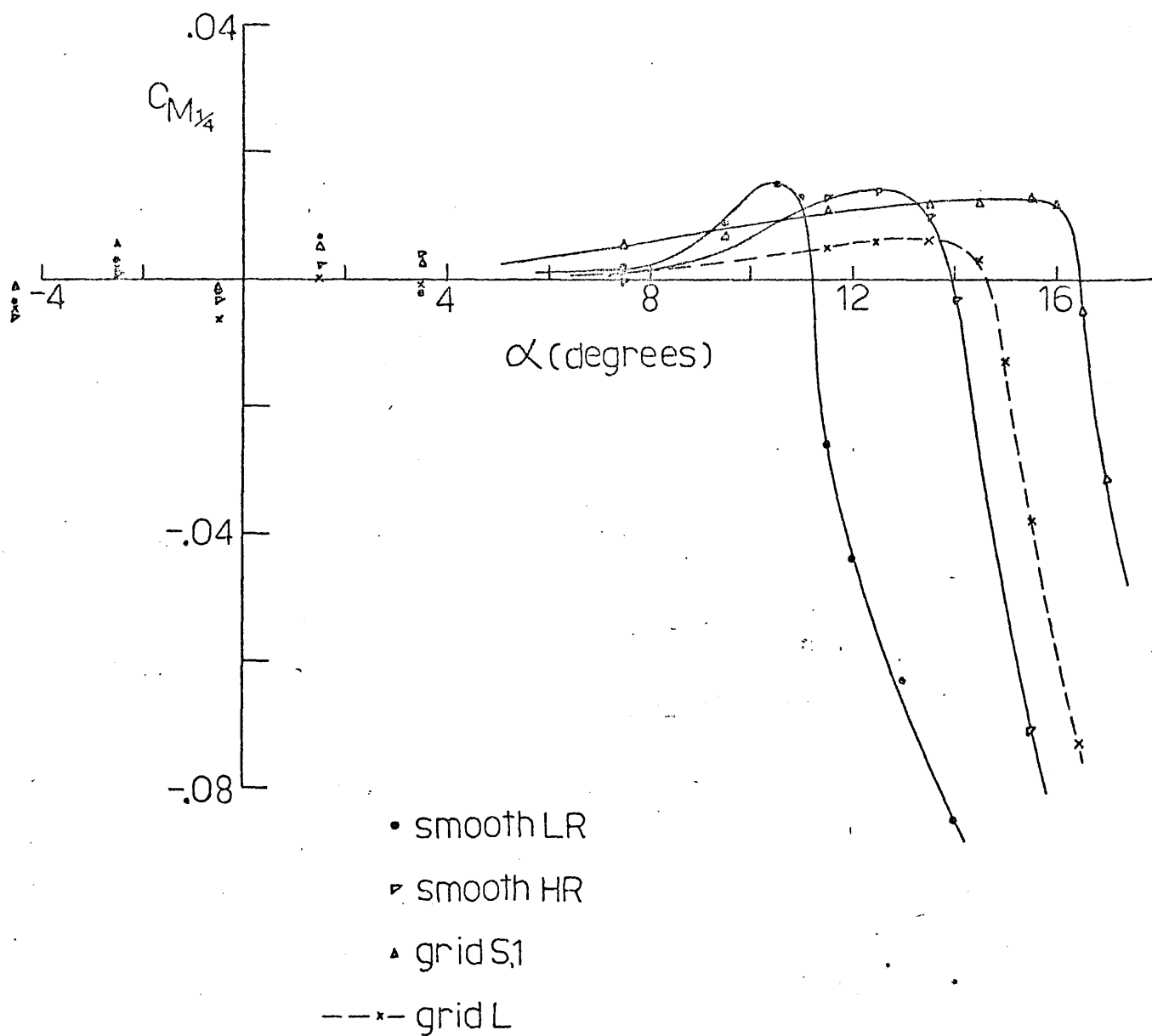


FIGURE 24. $C_{M_{1/4}}$ vs. α ; NACA 0012.

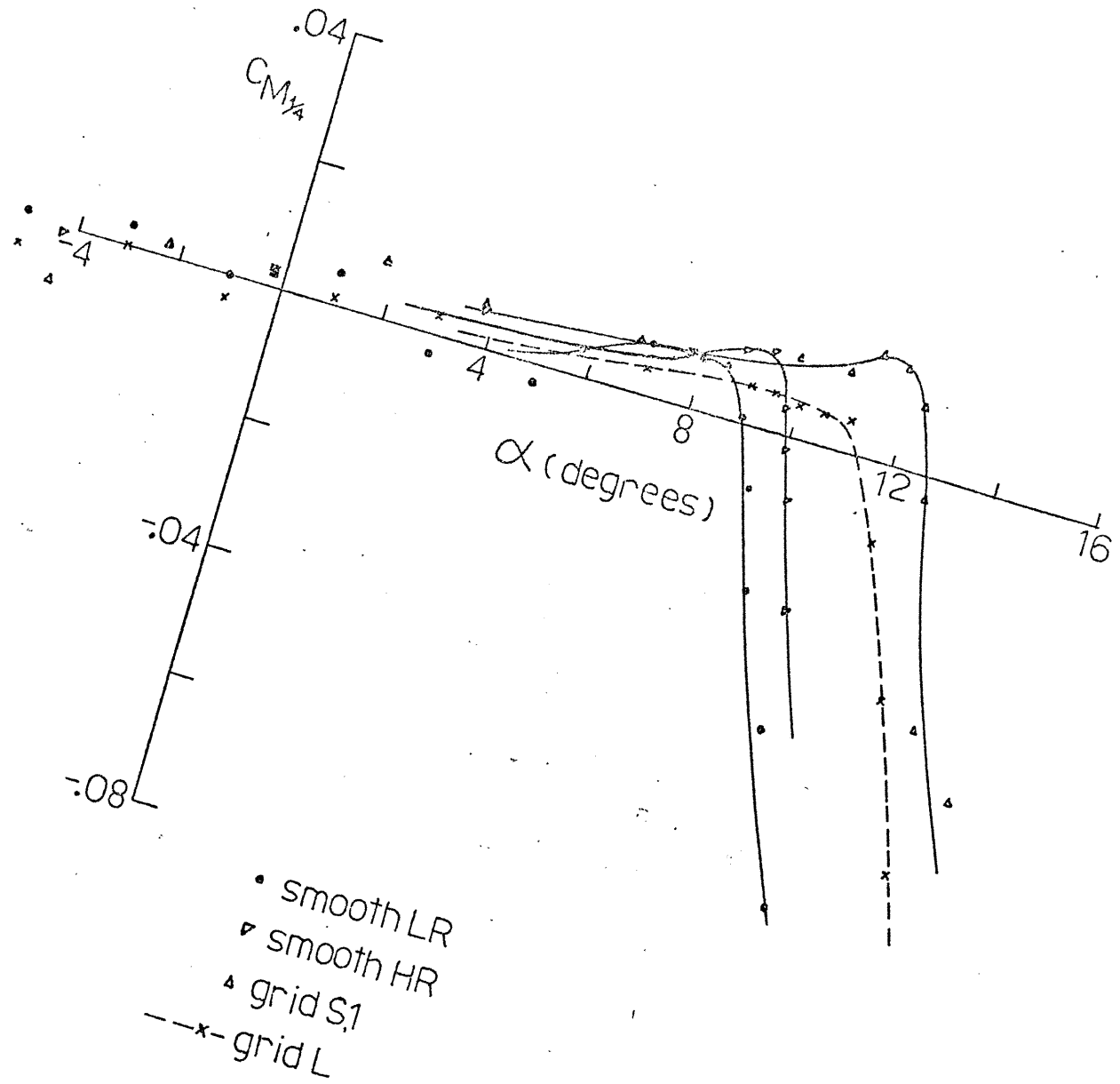
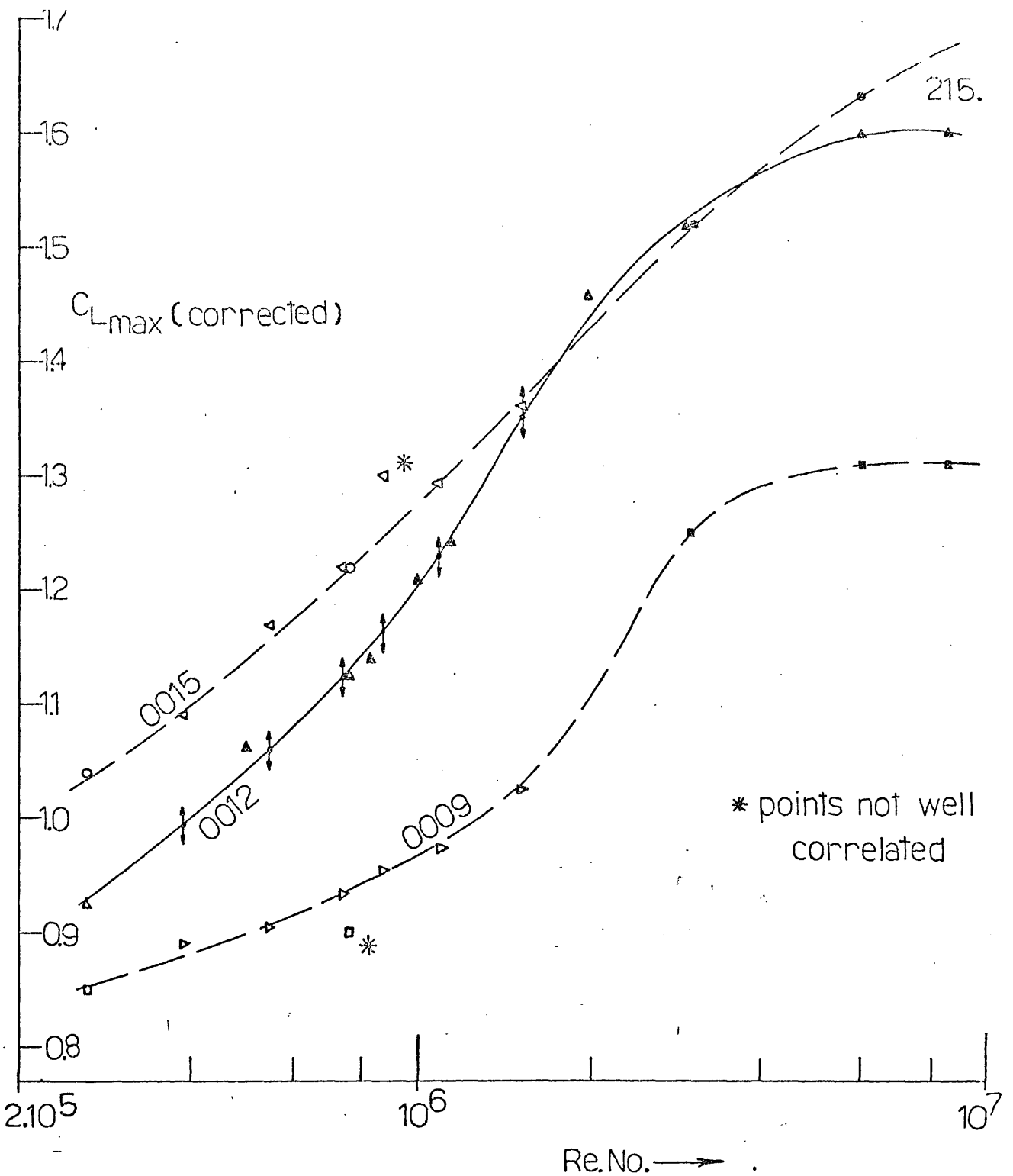


FIGURE 25. $C_{M_{1/4}}$ vs. α ; NACA 0009.



	<u>Smooth flow data</u>		<u>Turbulent flow data</u>
	this expt.	other workers	
NACA 0015 :	○	●	◁
NACA 0012 :	△	▲	↕ (the datum)
NACA 0009 :	□	■	▷

FIGURE 26. $C_{L_{max}}$ vs. EFFECTIVE REYNOLDS NUMBER

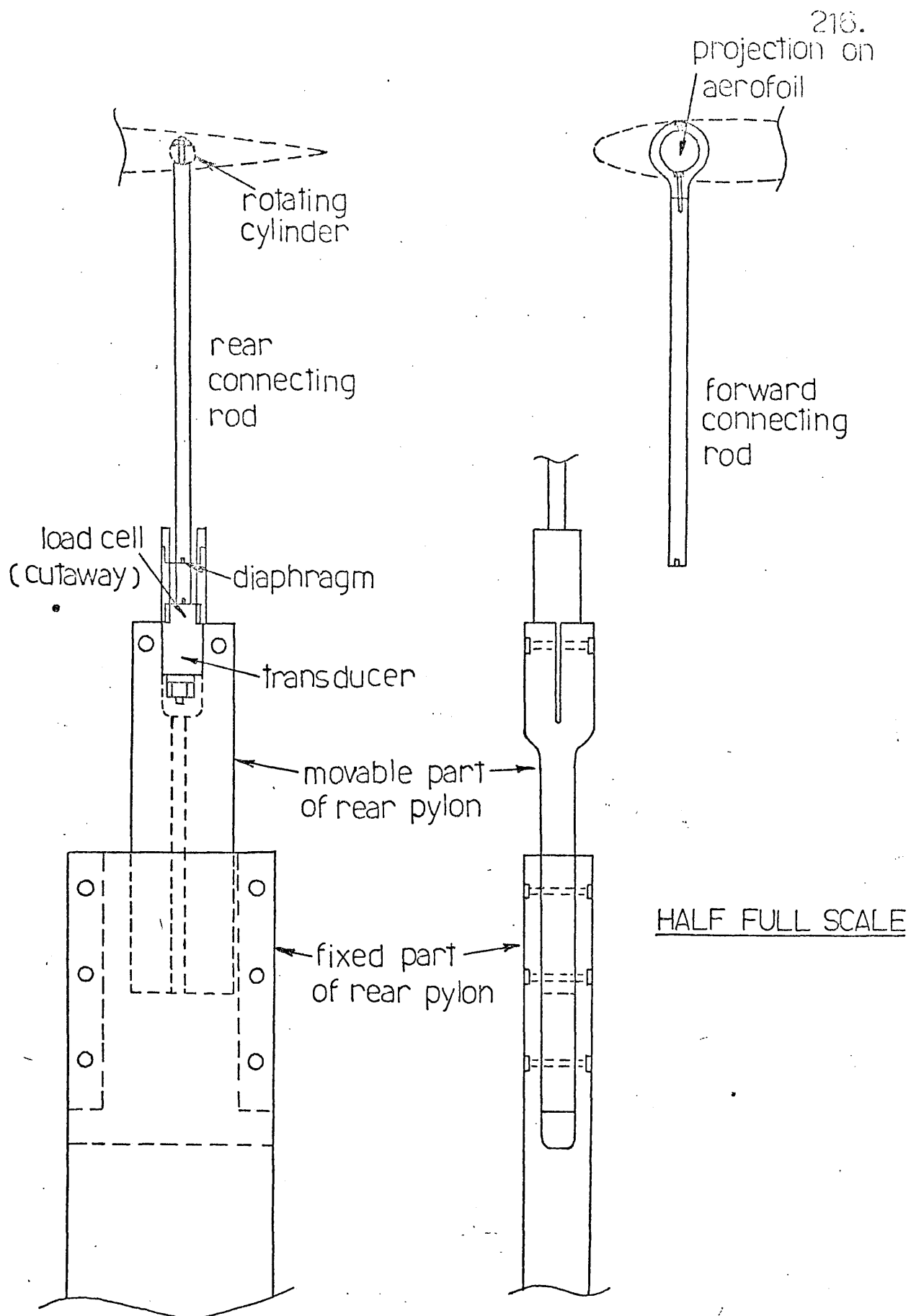
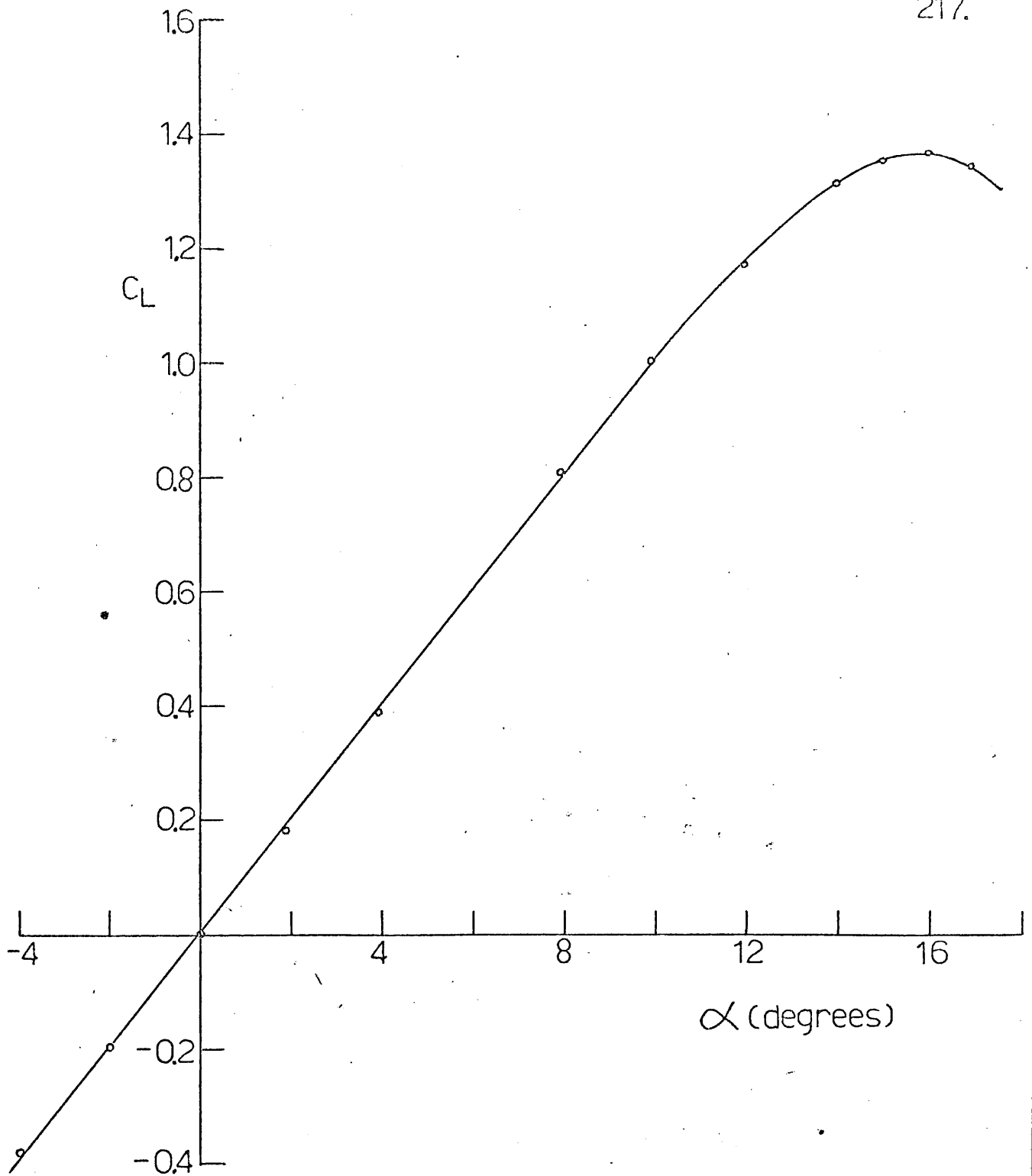


FIGURE 27. REAR PYLON , LOAD CELL , AND
CONNECTING RODS.



Re.No. = $0.26 \cdot 10^6$

$\frac{\sqrt{c_f}}{U_\infty} \doteq 0.06$

ASPECT RATIO = 5.0

FIGURE 28. MEAN LIFT CURVE ; NACA 0015

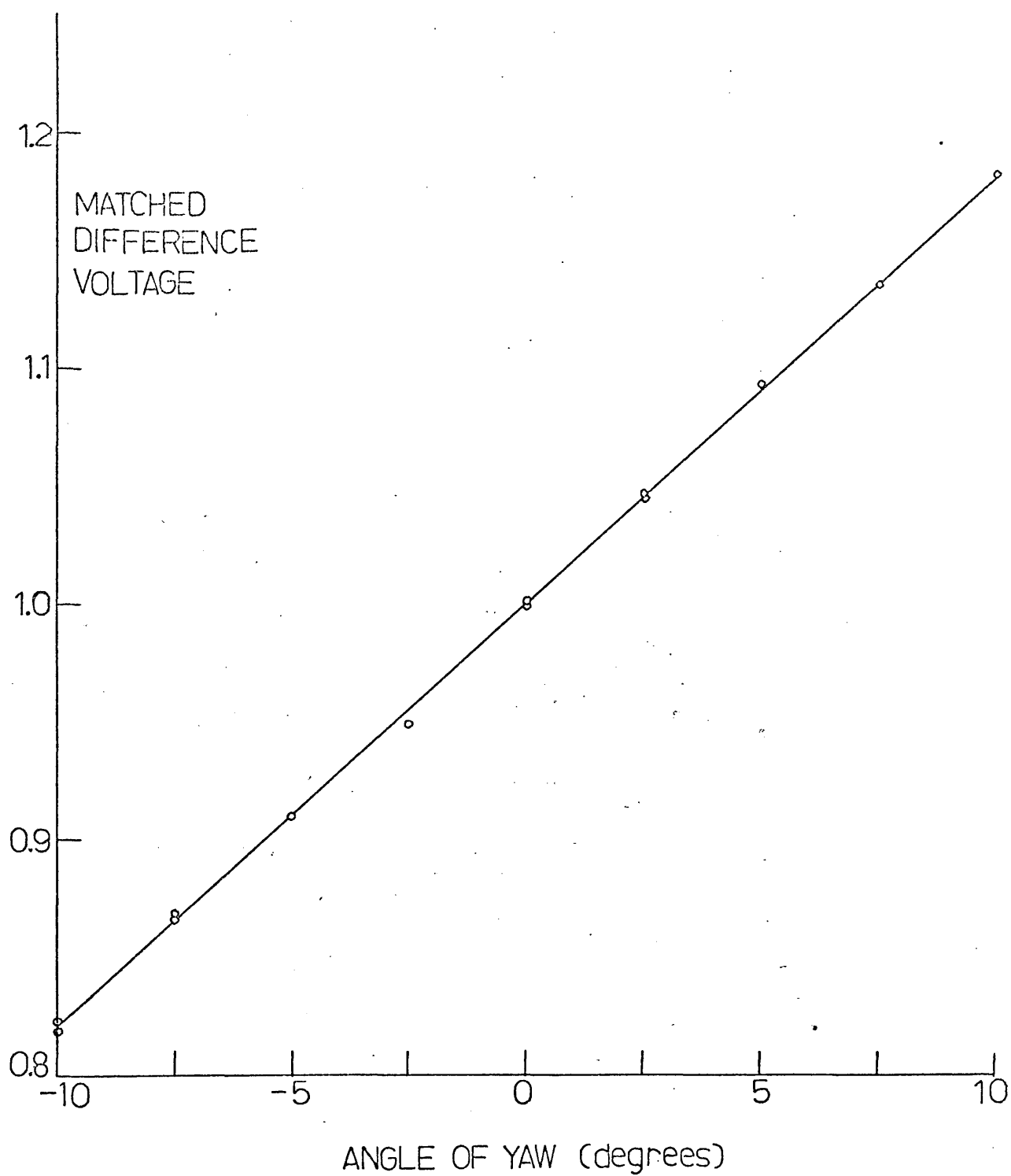


FIGURE 29. EXAMPLE OF X-WIRE CALIBRATION

SPECTRAL ANALYSIS EXPT 3 LOAD 10DEG 6GRID1

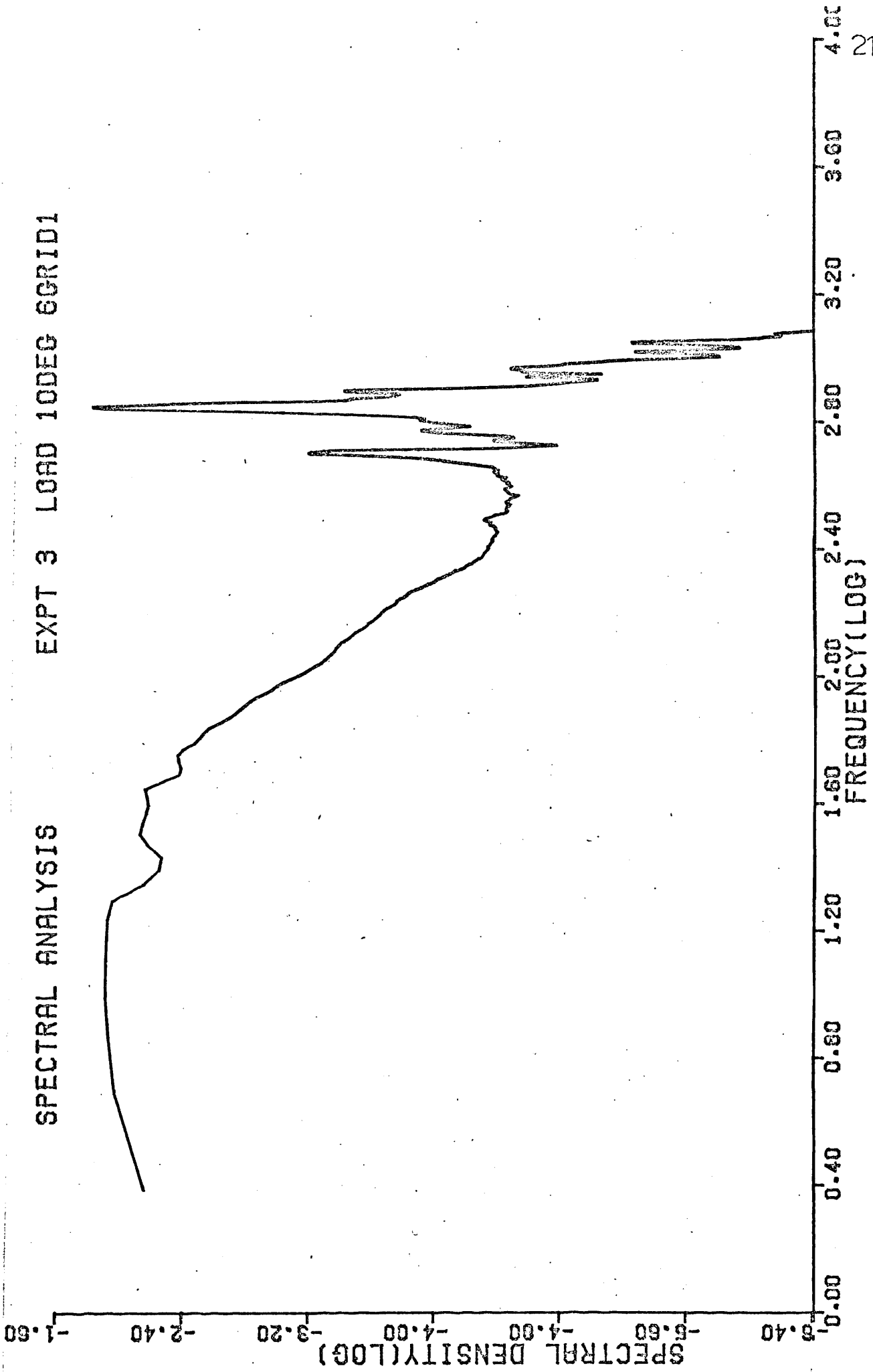


FIGURE 30. EXAMPLE OF DIGITAL SPECTRUM : $\hat{\Phi}_{CL}(\omega)$.

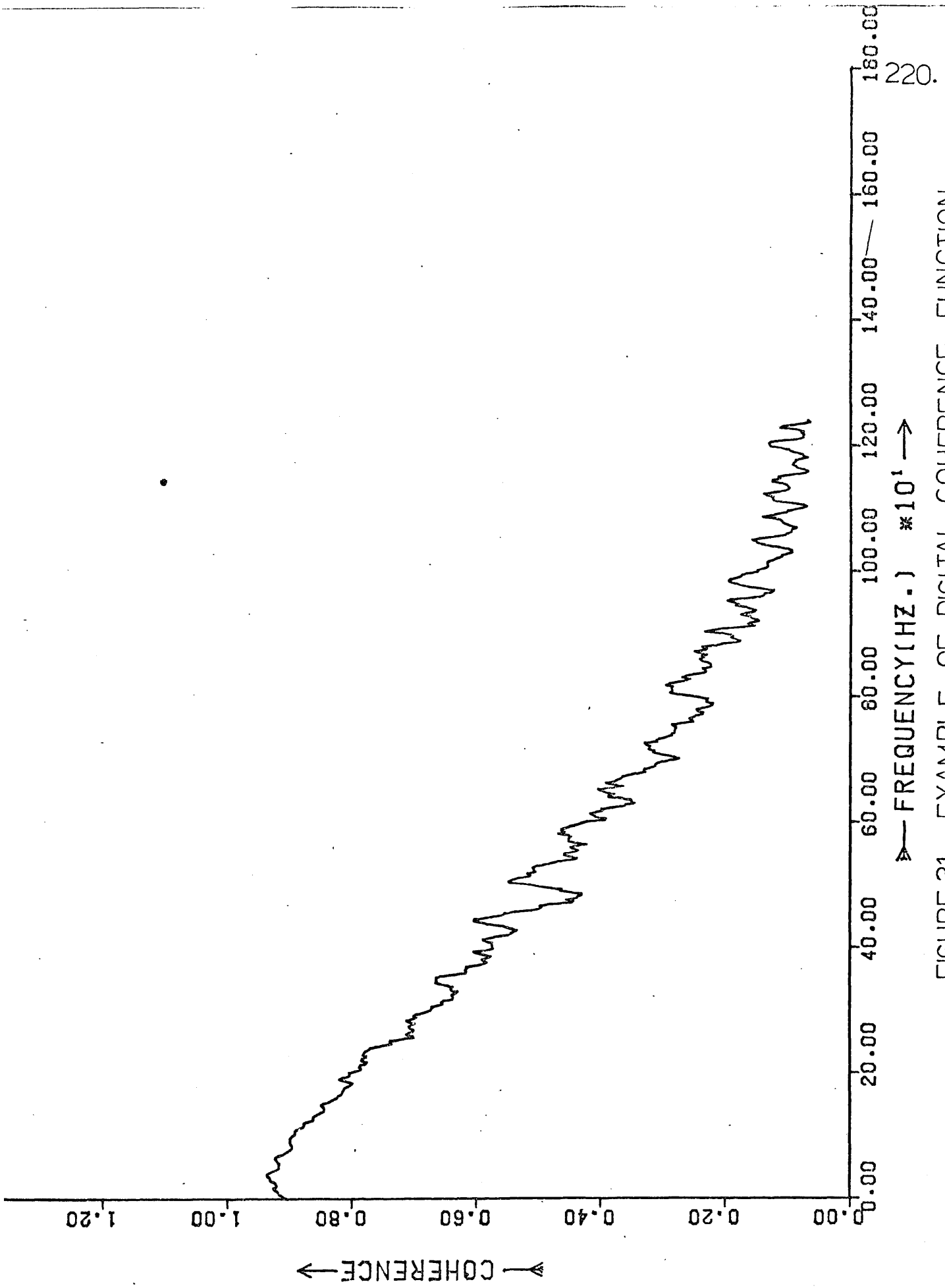
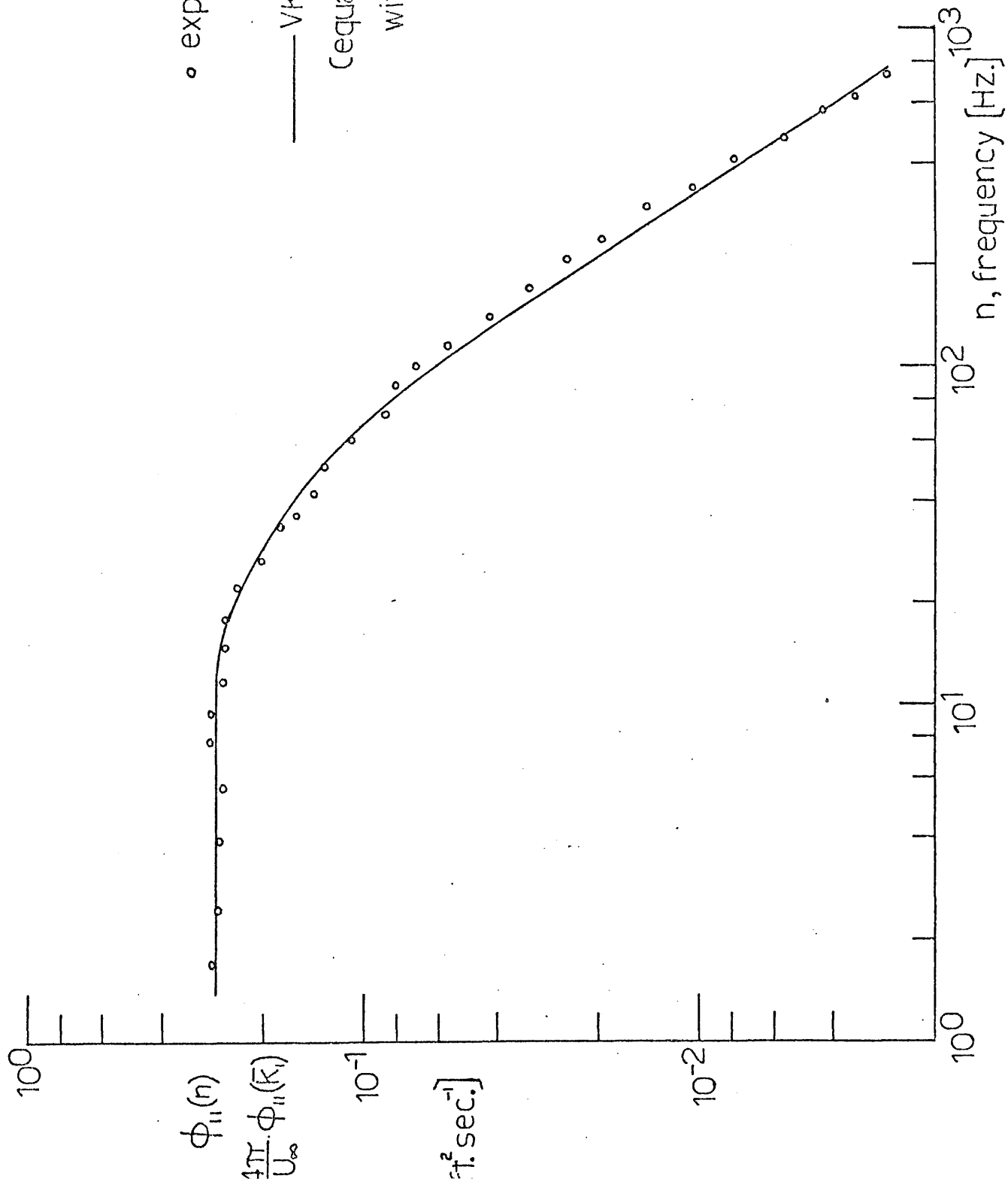


FIGURE 31. EXAMPLE OF DIGITAL COHERENCE FUNCTION



◦ exptl. data

— VK formula for ϕ_{11}
 (equation 5.1 in main text)
 with $L/\zeta = 0.44$.

FIGURE 32. SPECTRUM OF ϕ_{11} ; 6 INCH GRID.

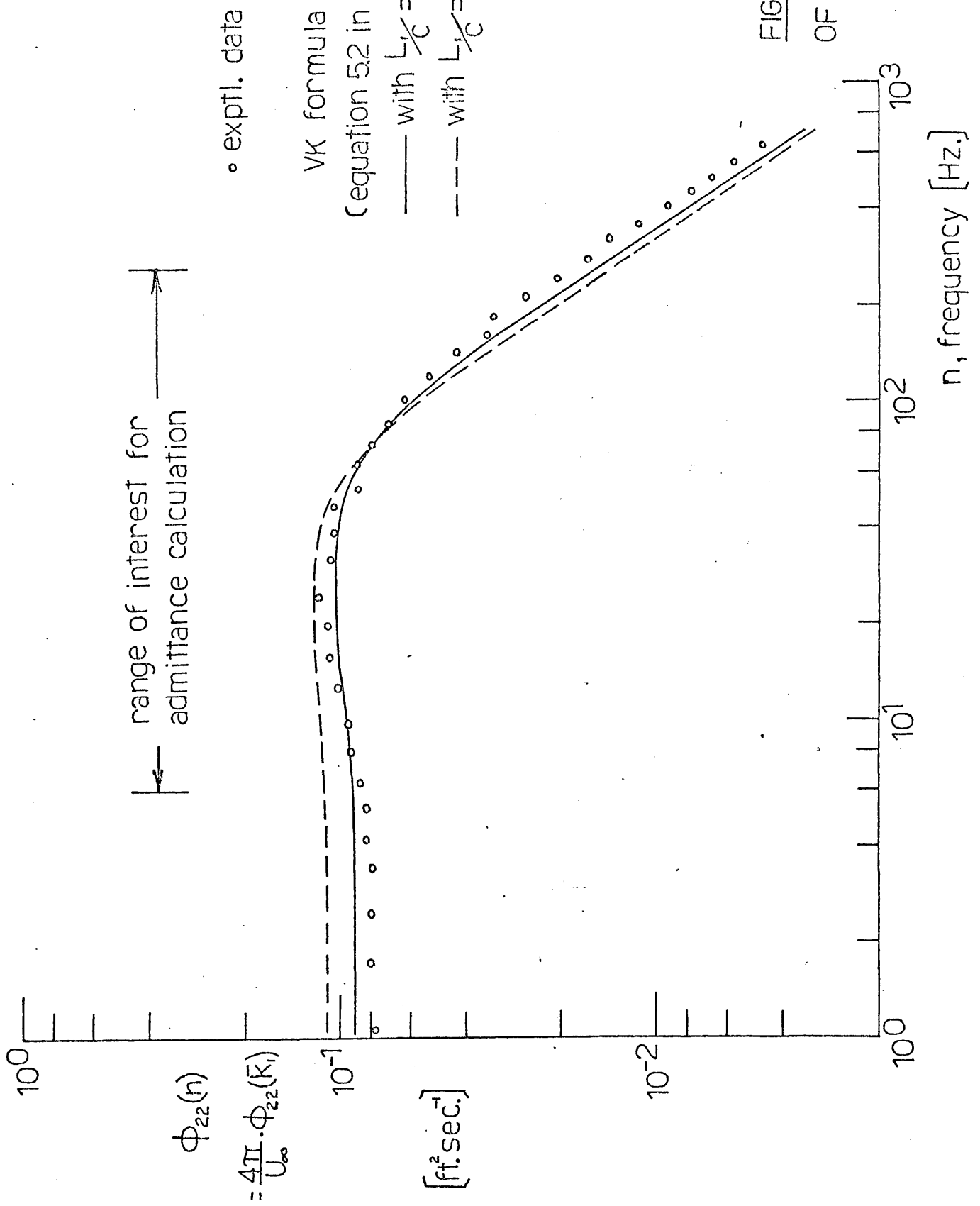


FIGURE 33. SPECTRUM OF v_{22} ; 6 INCH GRID

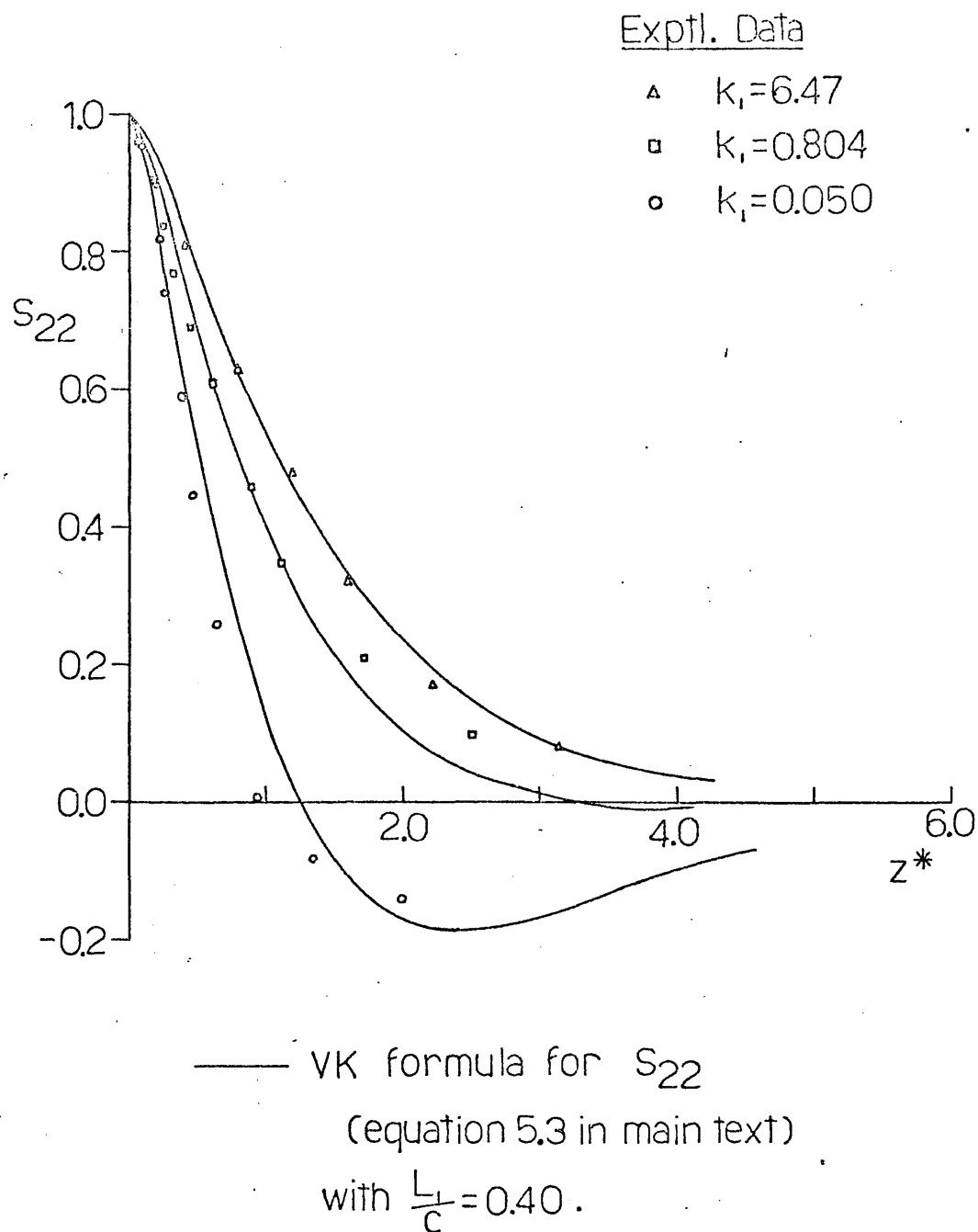


FIGURE 34. CURVE FIT TO EXPERIMENTAL S_{22} DATA ; A.

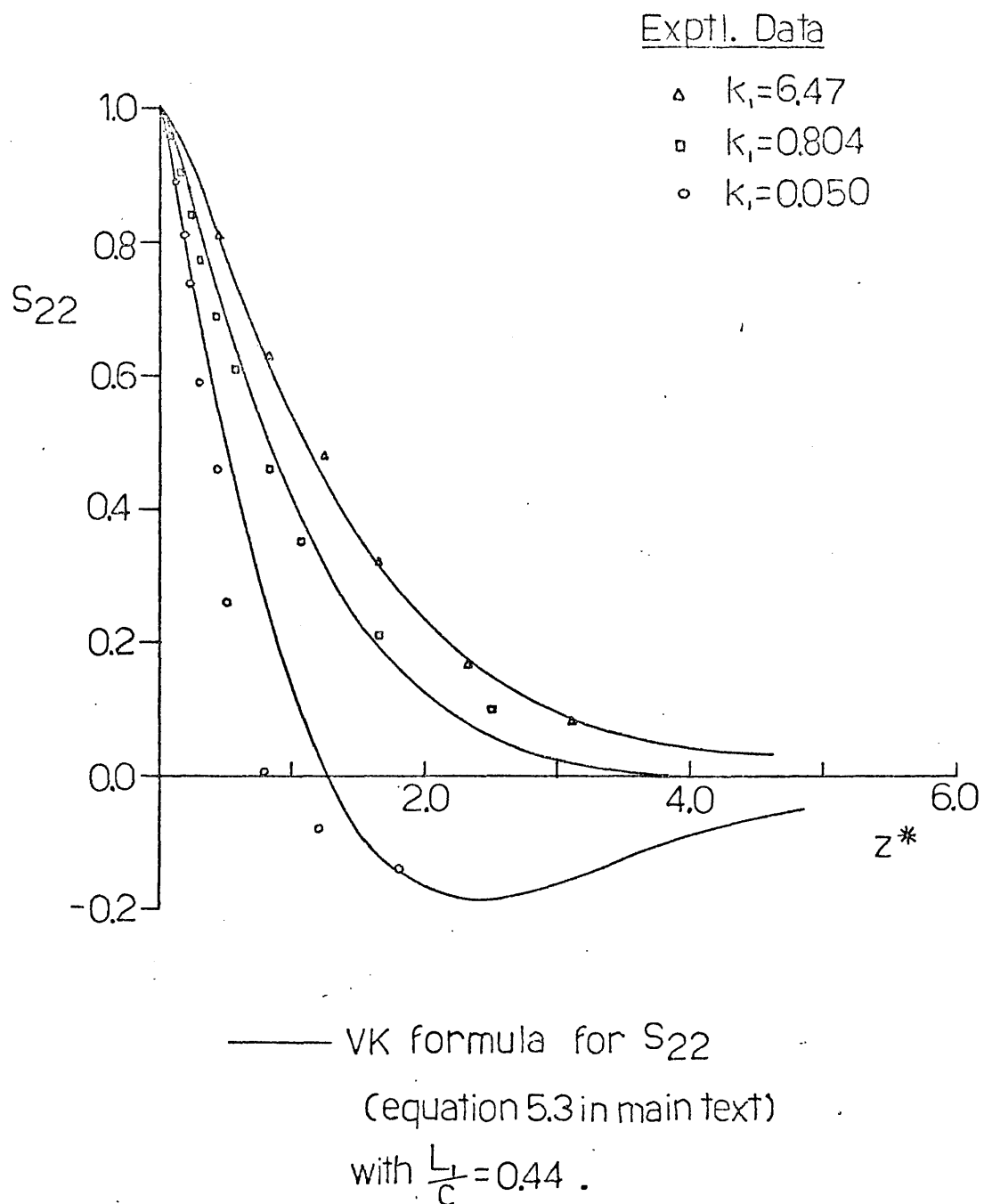
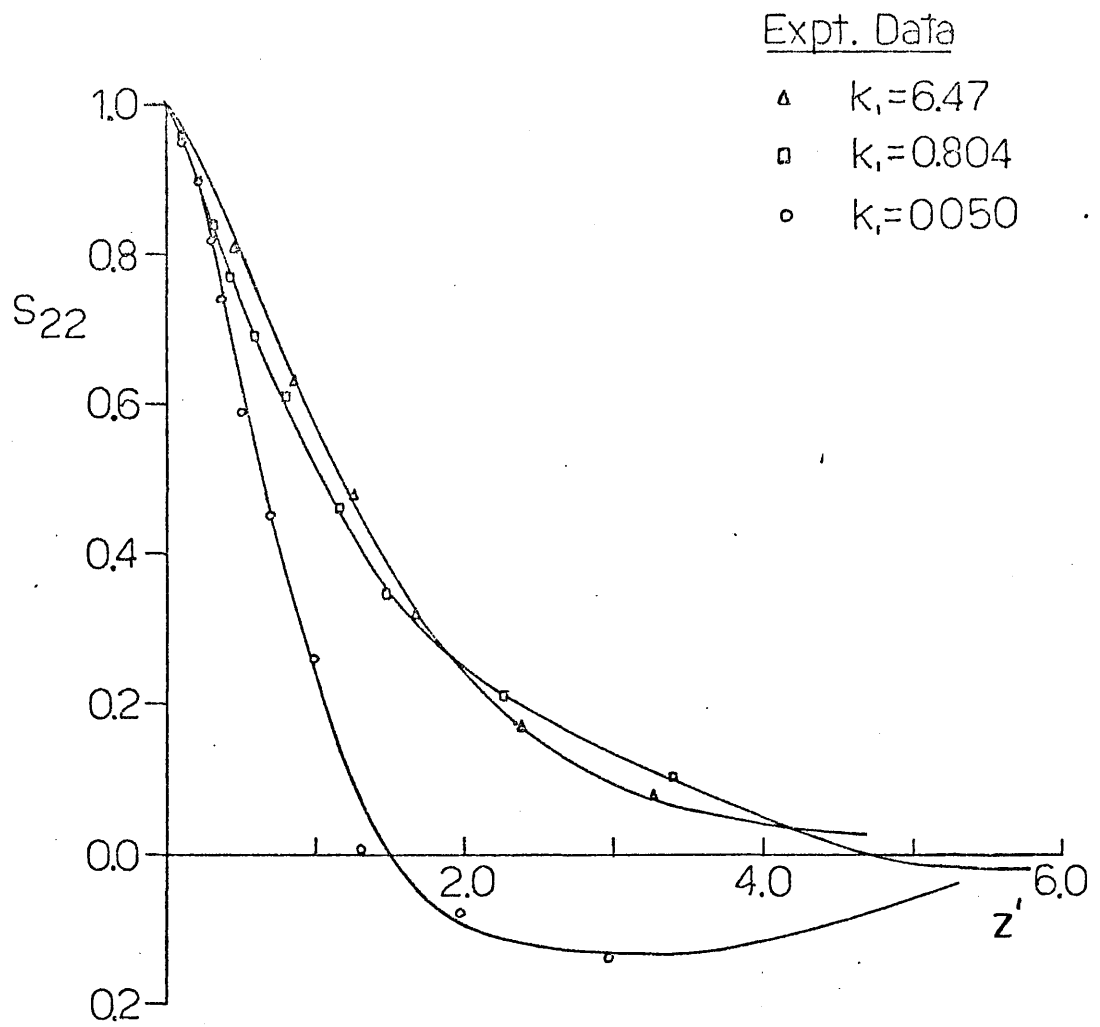


FIGURE 35. CURVE FIT TO EXPERIMENTAL S_{22} DATA ; B.



Expt. Data

- △ $k_1=6.47$
- $k_1=0.804$
- $k_1=0.050$

— BF formula for S_{22}

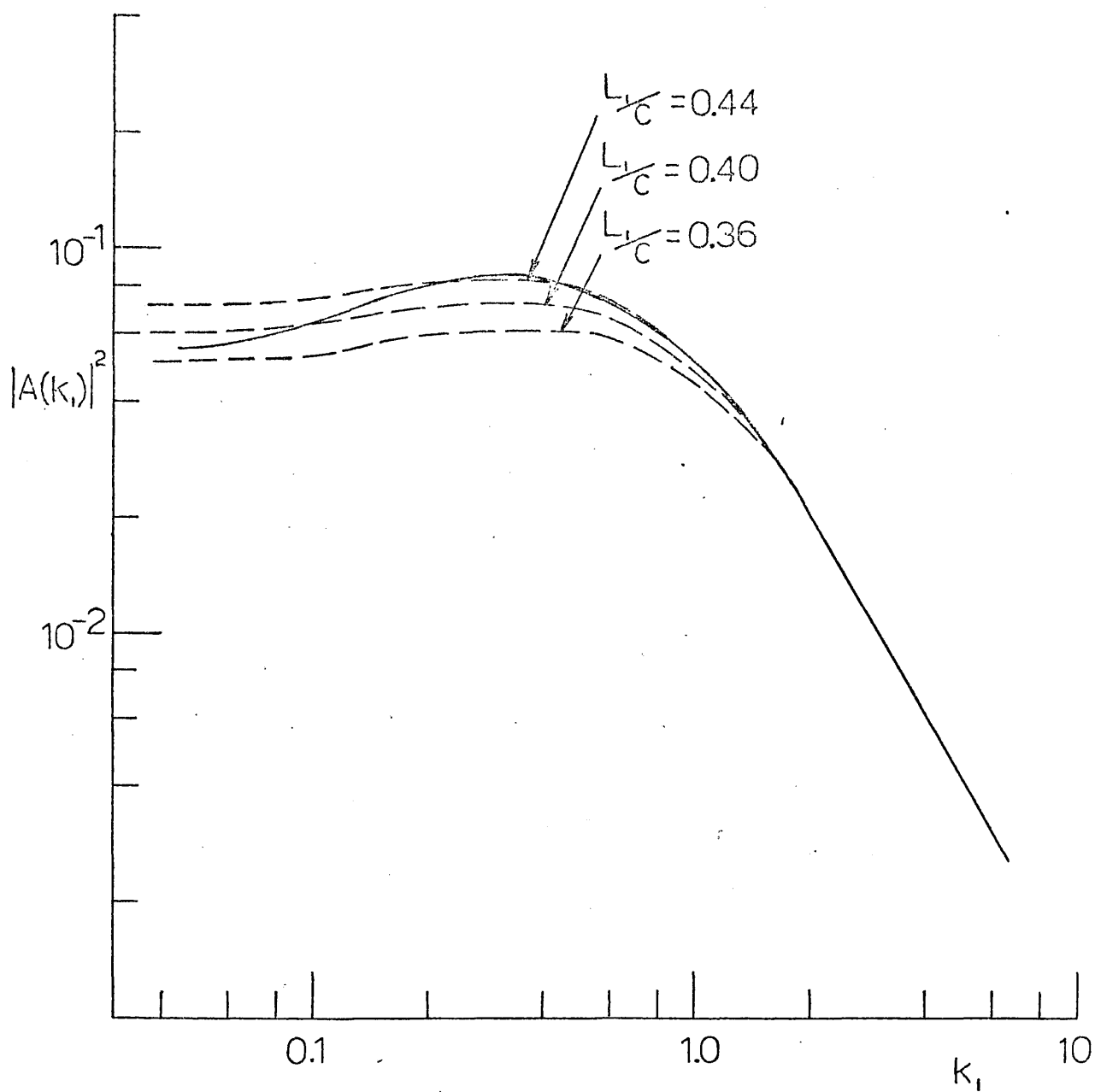
(equation 5.5 in the main text)

with the following constant values :

k_1	C_1	C_2	C_3	C_4	C_5
6.47	10.0	0.0	—	—	26.5
0.804	2.50	0.16	$\frac{\pi}{4}$	0.5	6.43
0.050	1.07	0.12	$\frac{\pi}{3}$	1.0	5.56

FIGURE 36.

CURVE FIT FOR EXPERIMENTAL S_{22} DATA ; C.

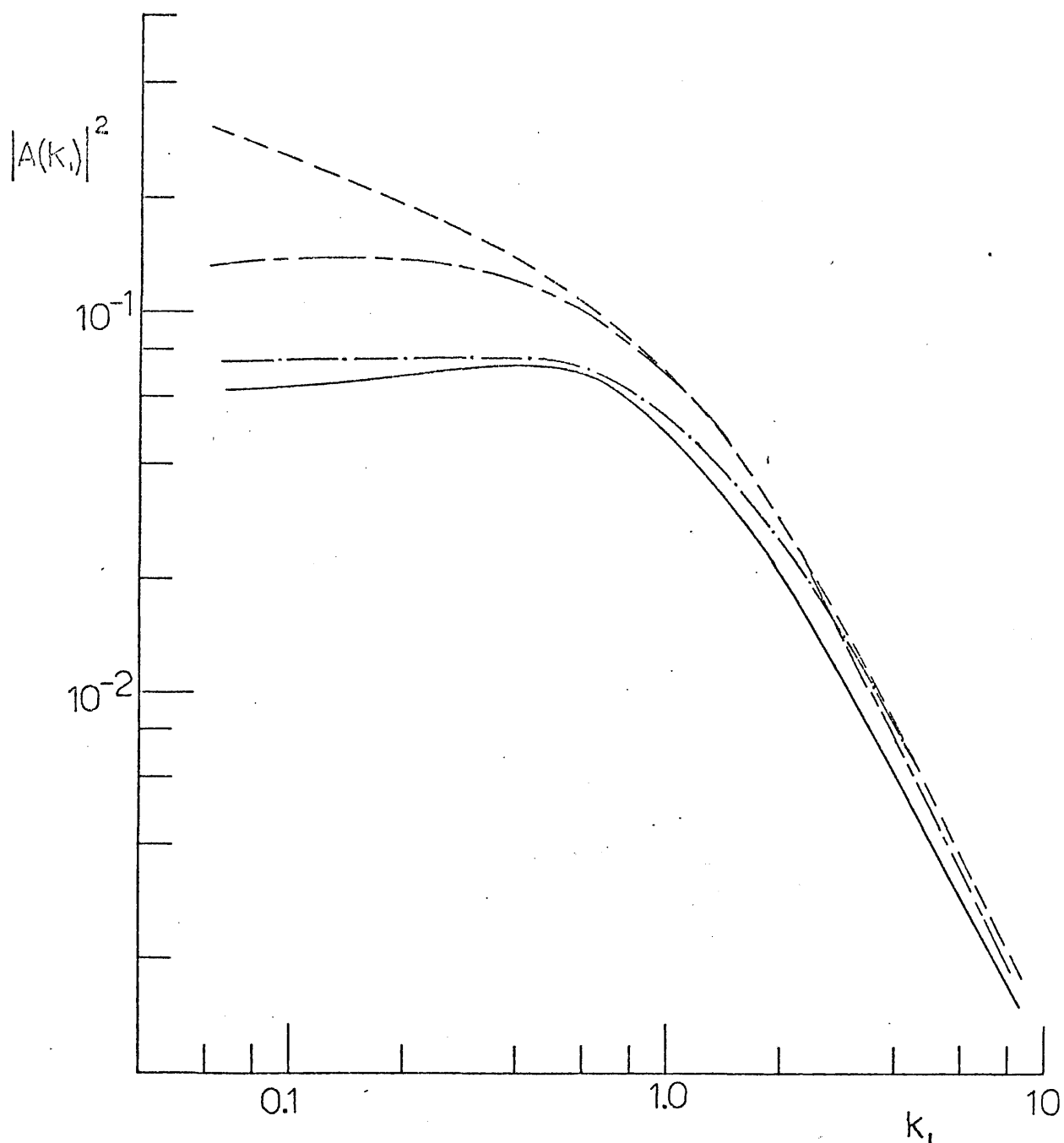


— with BF formula for $\bar{S}_{22}(k_1, k_3)$

- - - with VK formula for $\bar{S}_{22}(k_1, k_3)$

FIGURE 37. THEORETICAL ADMITTANCE ; $\alpha = 0$;

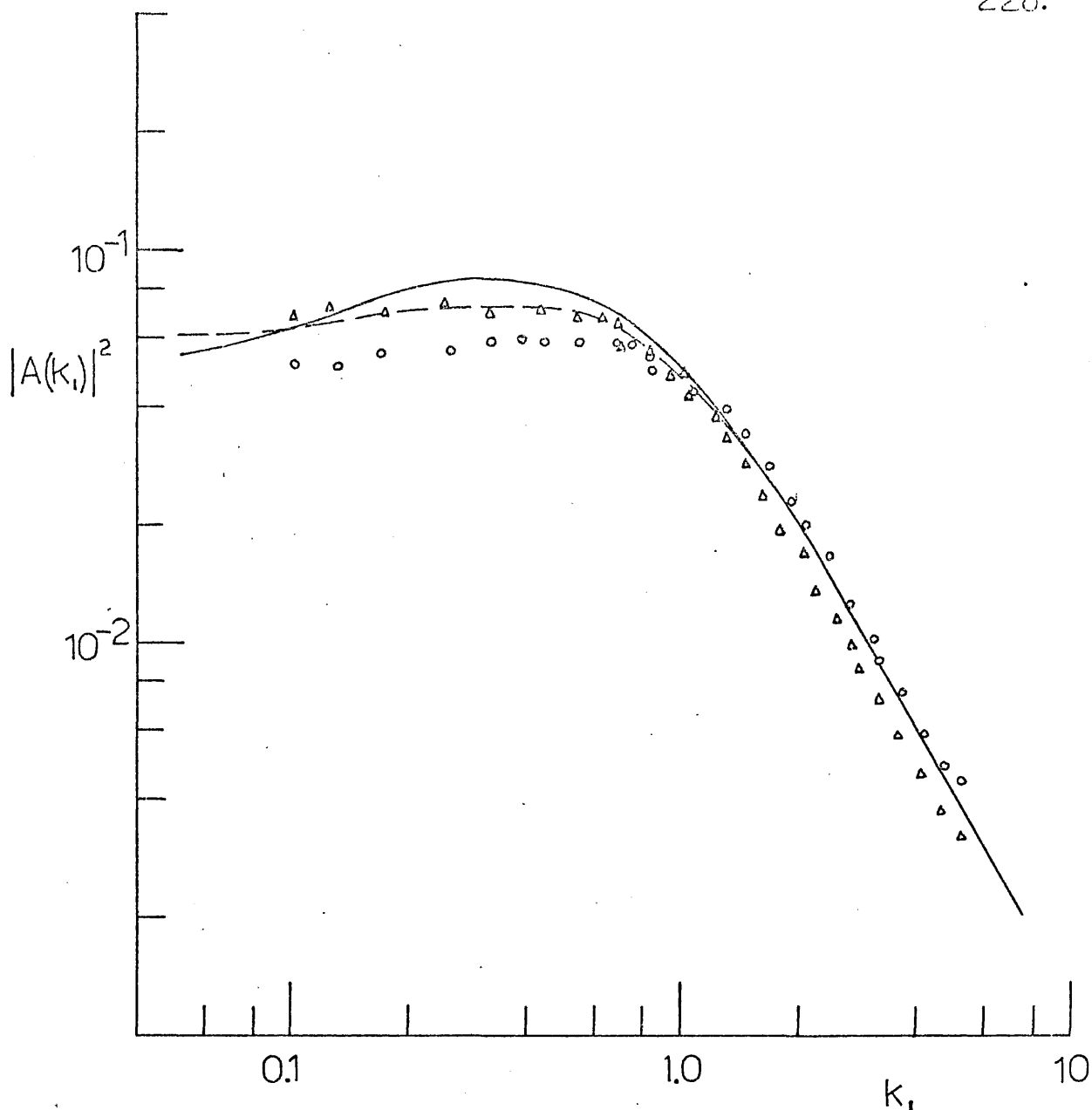
EXACT $G(k_1, k_3)$; 6 INCH GRID .



RESPONSE FUNCTIONS

- $G(k_i, k_3)$: exact (Graham)
- · - · - $G_M(k_i, k_3)$: Mugridge
- $G_F(k_i, k_3)$: Filotas
- $S(k_i)$: strip (Sears)

FIGURE 38. THEORETICAL ADMITTANCE ; $\alpha=0$;
 $VK \bar{S}_{22}(k_i, k_3)$ with $L/\rho = 0.40$; 6 INCH GRID .



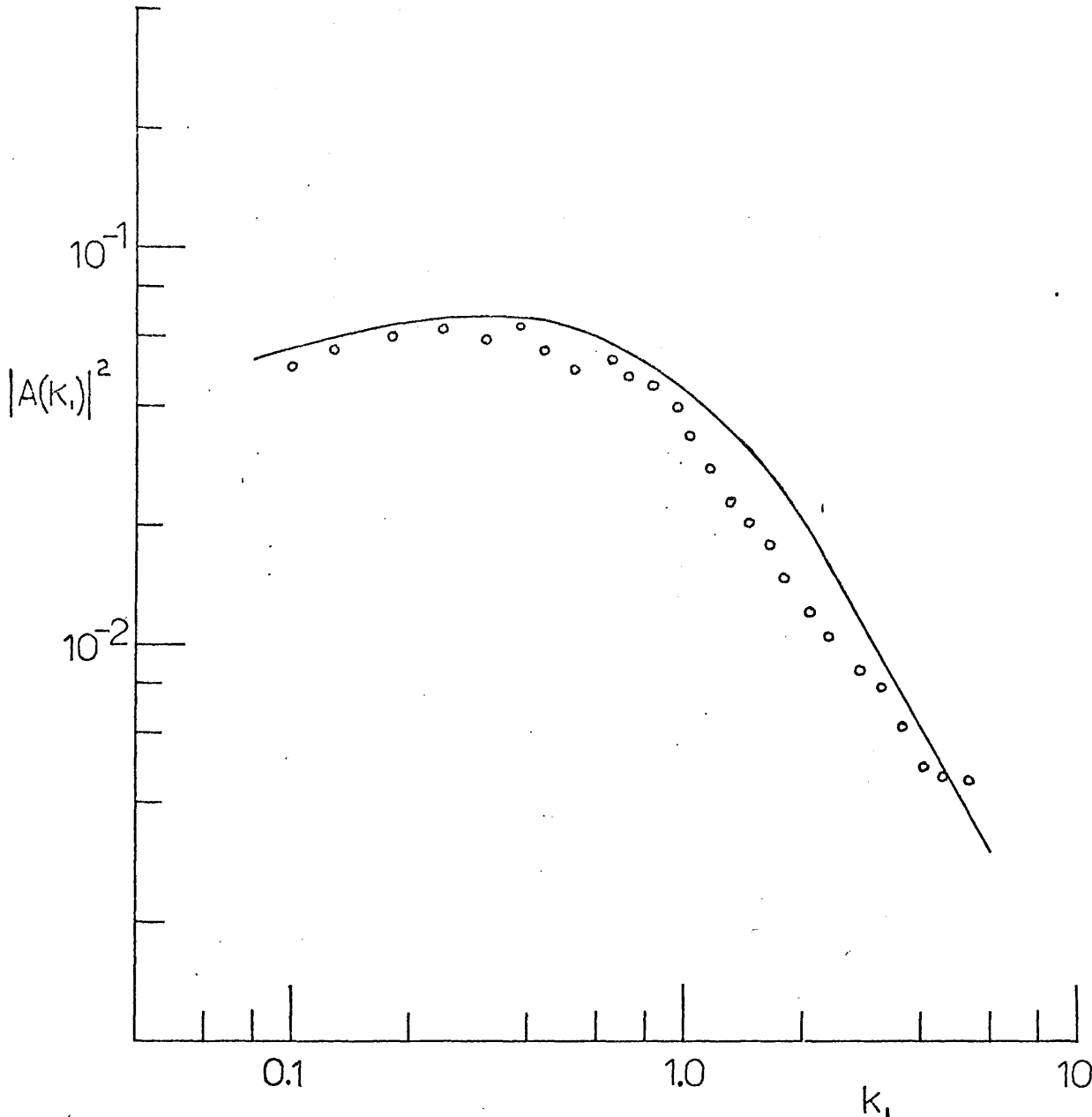
Exptl. data : \circ Series 1 ; \triangle Series 3 .

Theory with exact $G(k_1, k_3)$ and

———— BF formula for \bar{S}_{22} ,

----- VK formula for \bar{S}_{22} : $L_1/c = 0.40$.

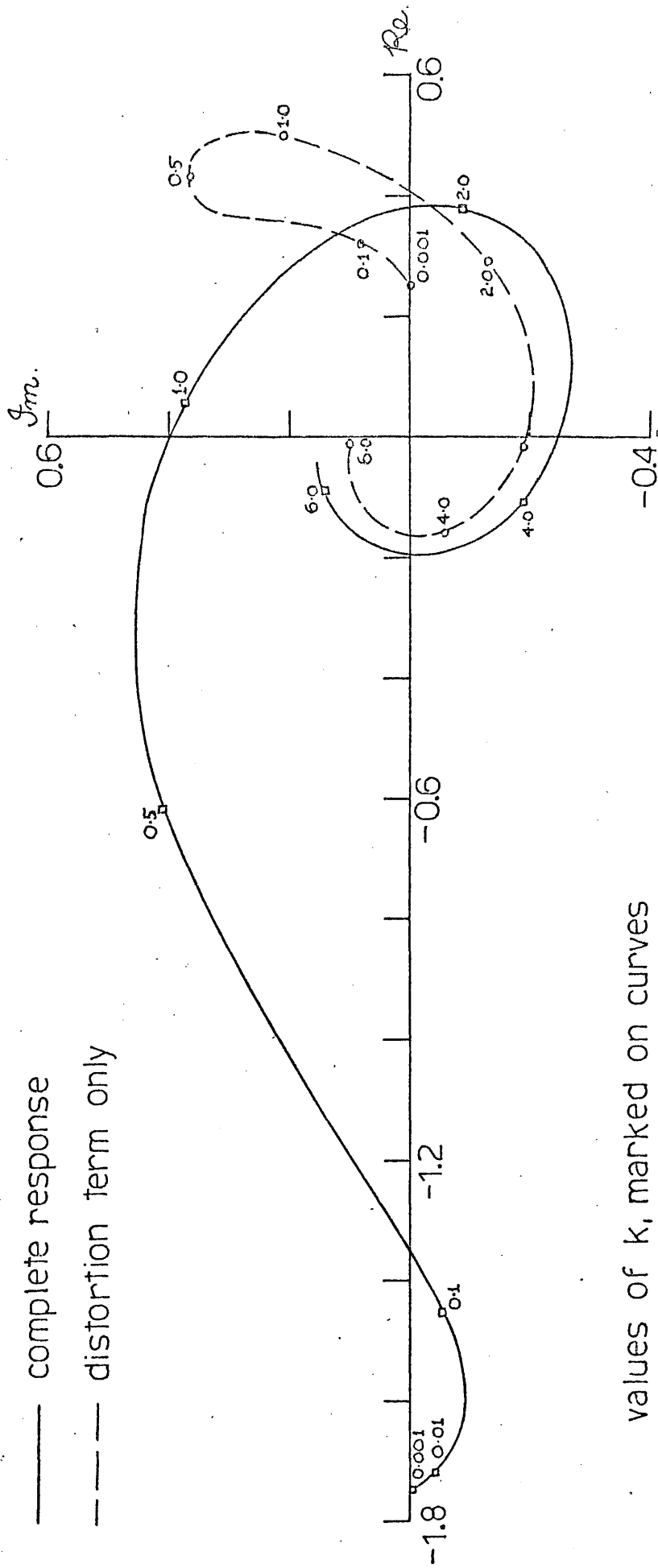
FIGURE 39. ADMITTANCE : THEORY AND EXPERIMENT ;
 $\alpha = 0$; 6 INCH GRID .



Exptl. data : ◦ (Series 3)
 with VK formula for $\phi_{22} : \frac{\sqrt{v_2^2}}{U_\infty} = 0.037$
 $L_1/c = 0.38$

— Theory with exact $G(k_1, k_3)$ and with
 VK formula for $\bar{S}_{22} : L_1/c = 0.38.$

FIGURE 40. ADMITTANCE : THEORY AND EXPERIMENT ;
 $\alpha = 0$; 3 INCH GRID.



values of k , marked on curves

FIGURE 41 SECOND ORDER RESPONSE, $k_2 = 0.6$.

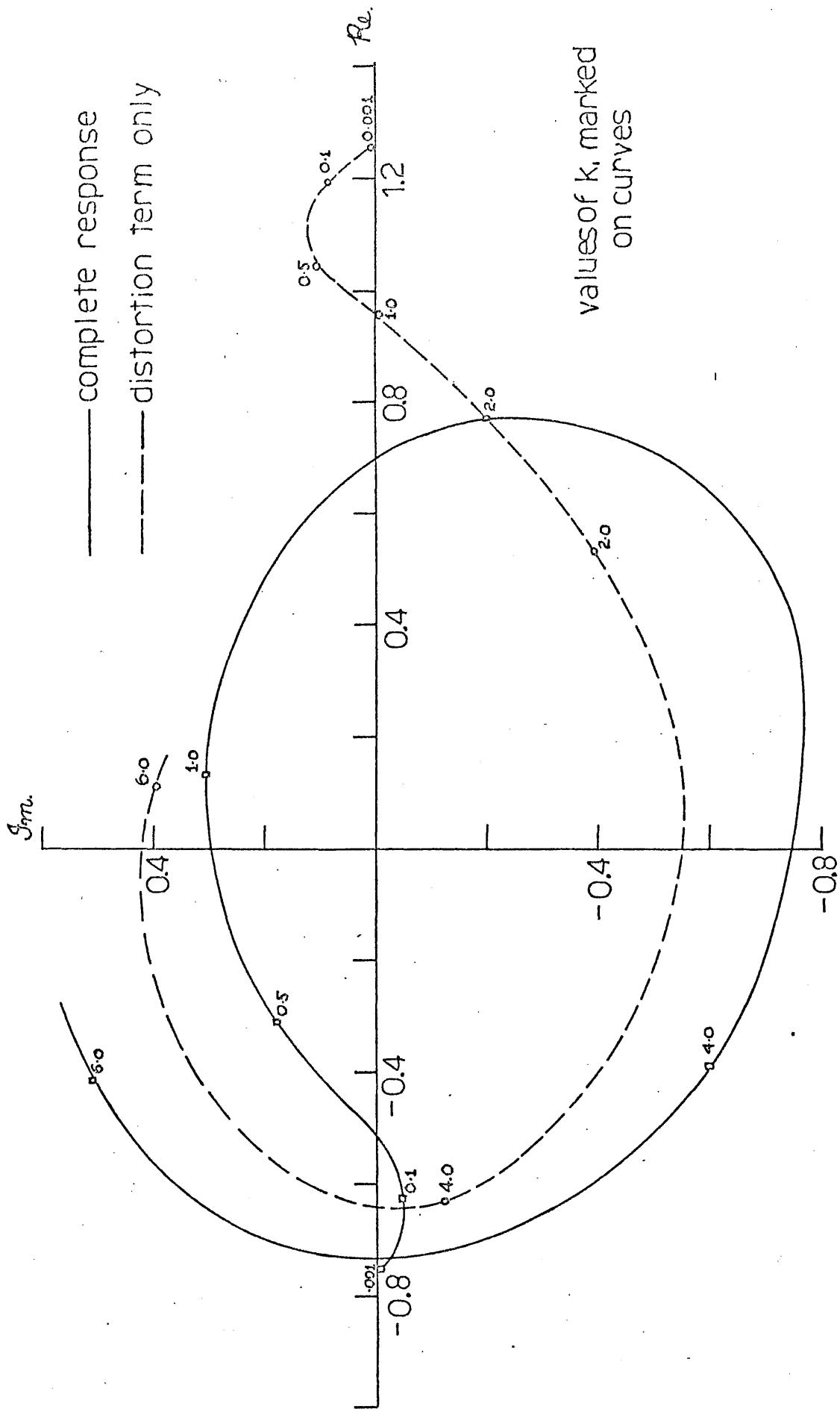


FIGURE 42. SECOND ORDER RESPONSE, $R : K_2 = 3.0$

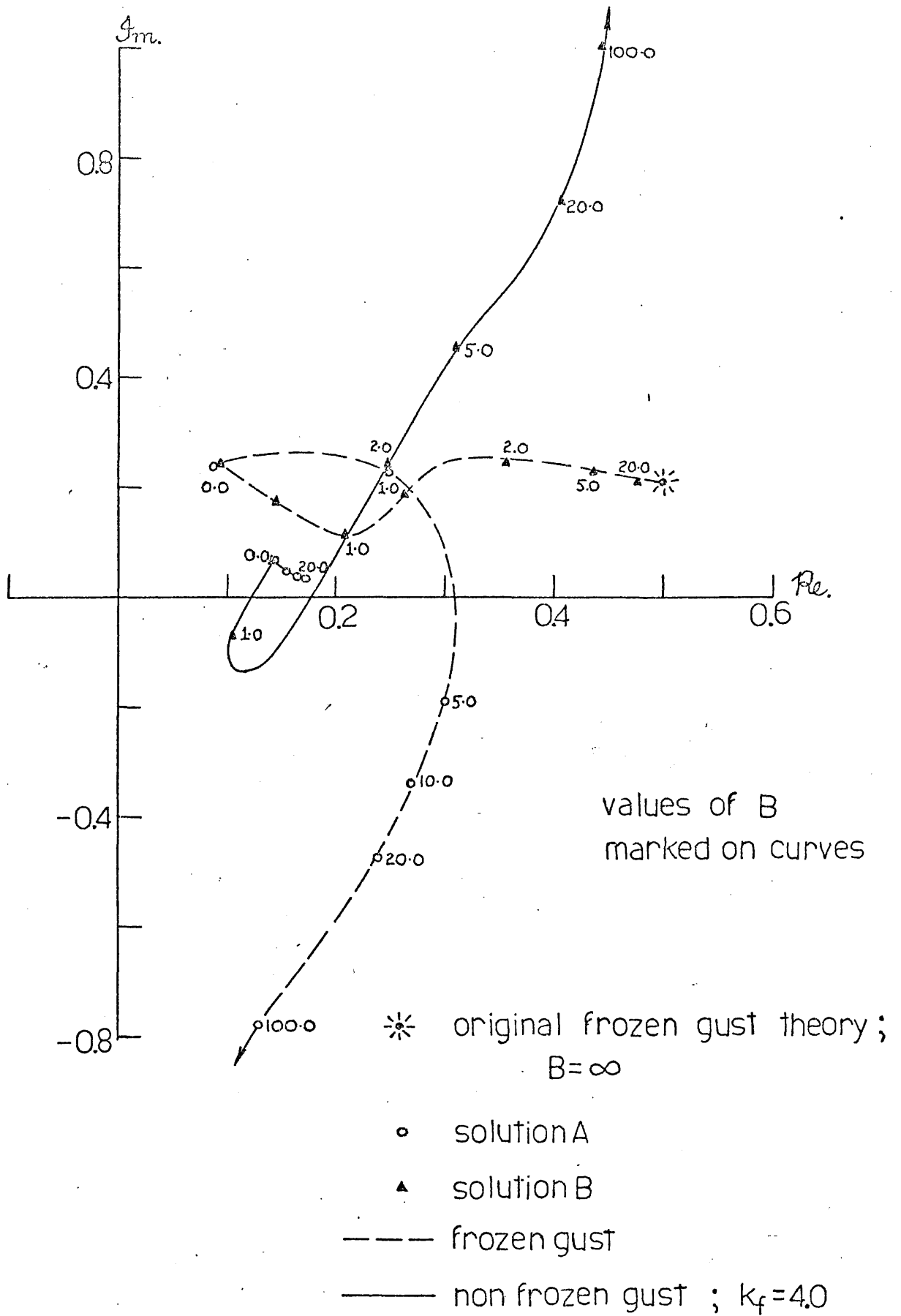
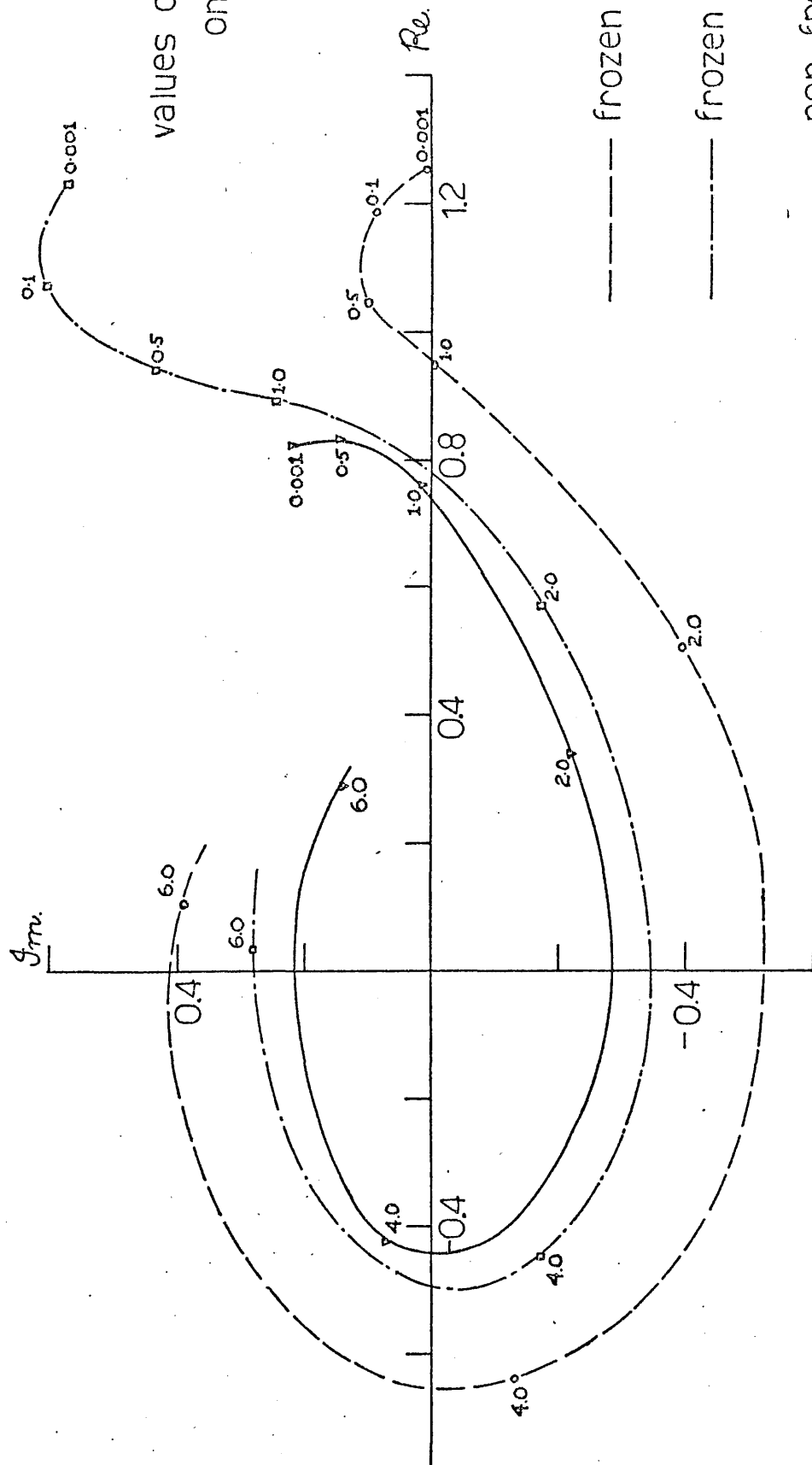


FIGURE 43. RESPONSE DUE TO DISTORTION ;
 $k_s = 1.0$; $k_2 = 0.6$.



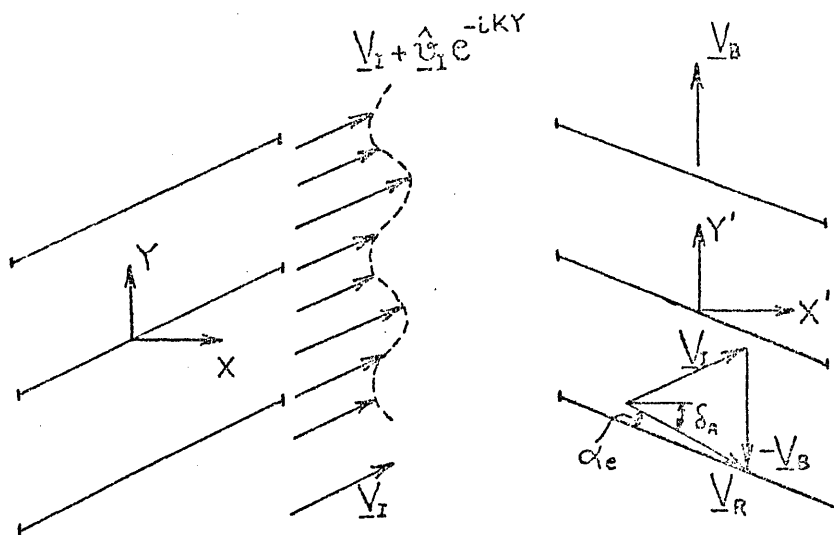
values of k_s marked
on curves

----- frozen gust ; $B = \infty$.

----- frozen gust ; $B = 1.4$.

----- non-frozen gust ;
 $B = 1.4$; $K_f = 4.0$.

FIGURE 44. RESPONSE DUE TO DISTORTION ; $K_2 = 3.0$.



\underline{V}_I : average incident velocity

\underline{V}_R : average incident velocity relative to rotor blade

\underline{V}_B : rotor blade velocity

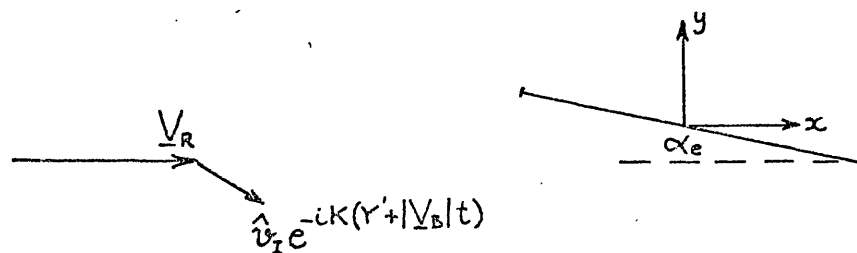
α_e : angle of incidence of rotor blade to \underline{V}_R

δ_A : angle between \underline{V}_R and the machine axis

In co-ordinate system (X', Y') moving with the rotor blade, the instantaneous incident velocity relative to the rotor is:

$$\underline{V}_R + \hat{v}_I e^{-iK(Y' + |V_B|t)}$$

FIGURE 45A. TURBOMACHINE MODEL.



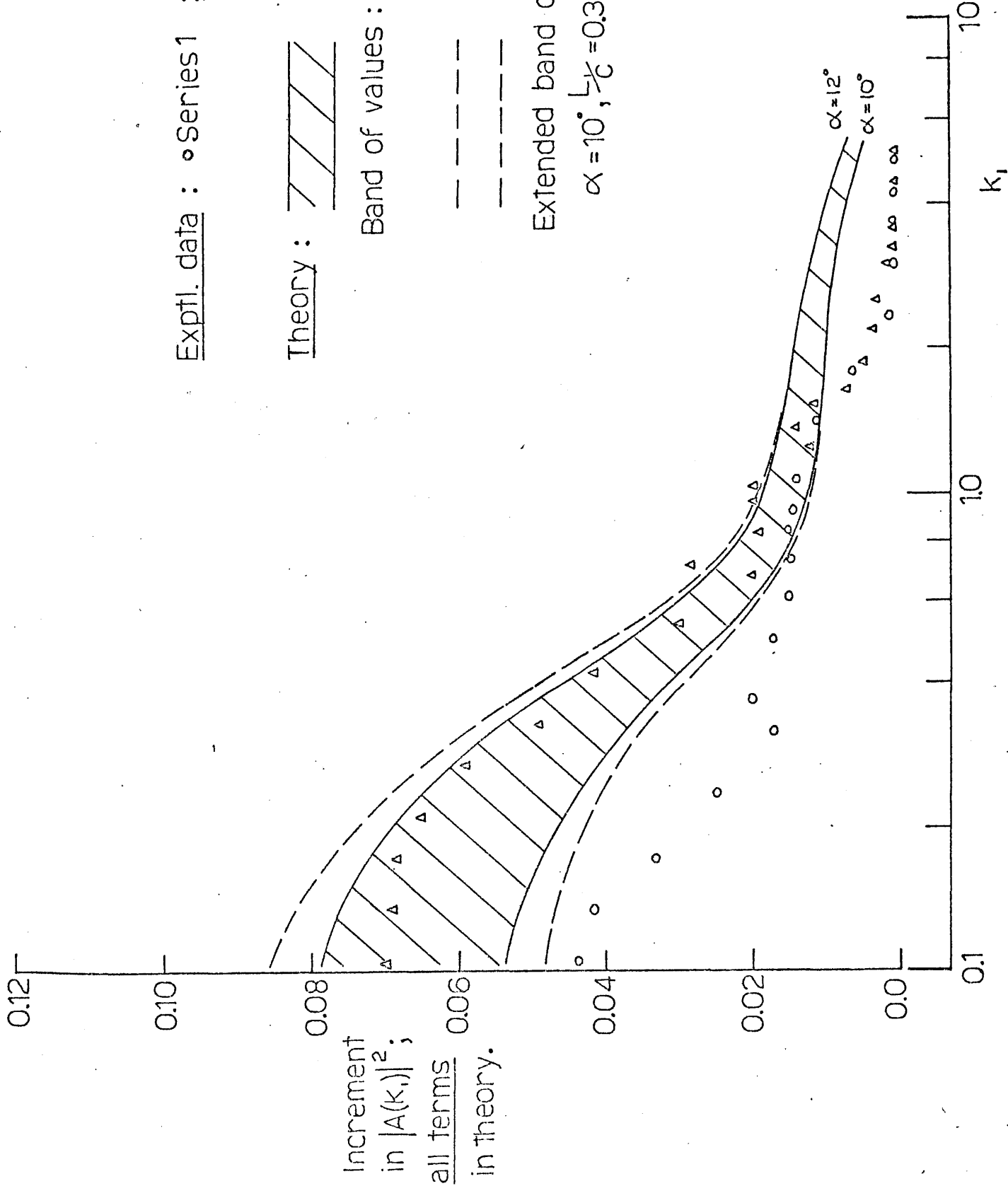
In co-ordinate system (x, y) , the gust is : $\hat{v}_I e^{-i(\omega t - k_s x - k_2 y)}$,

where, $\omega = K|V_B| = k_f|V_R|$,

$k_s = K \sin \delta_A$,

$k_2 = K \cos \delta_A$.

FIGURE 45B. FLOW ON SINGLE BLADE



Exptl. data : • Series 1 ; ▲ Series 3 .

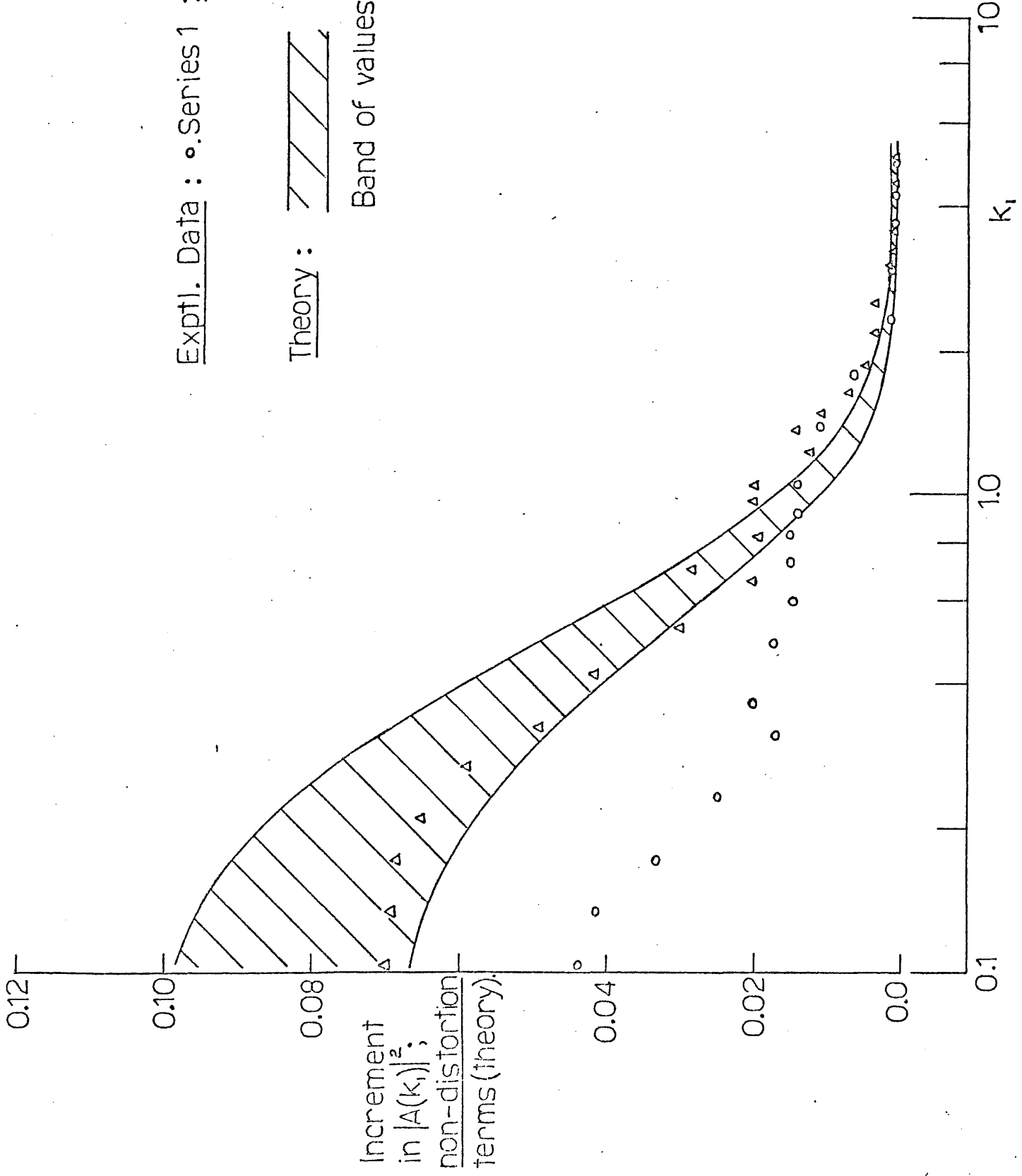
Theory :  $L/C = 0.40$

Band of values : $\alpha = 10^\circ \rightarrow 12^\circ$.

Extended band of values :

$\alpha = 10^\circ, L/C = 0.36 \rightarrow \alpha = 12^\circ, L/C = 0.44$.

FIGURE 46.
INCREMENT IN
ADMITTANCE ;
ALL TERMS IN THEORY
6 INCH GRID.

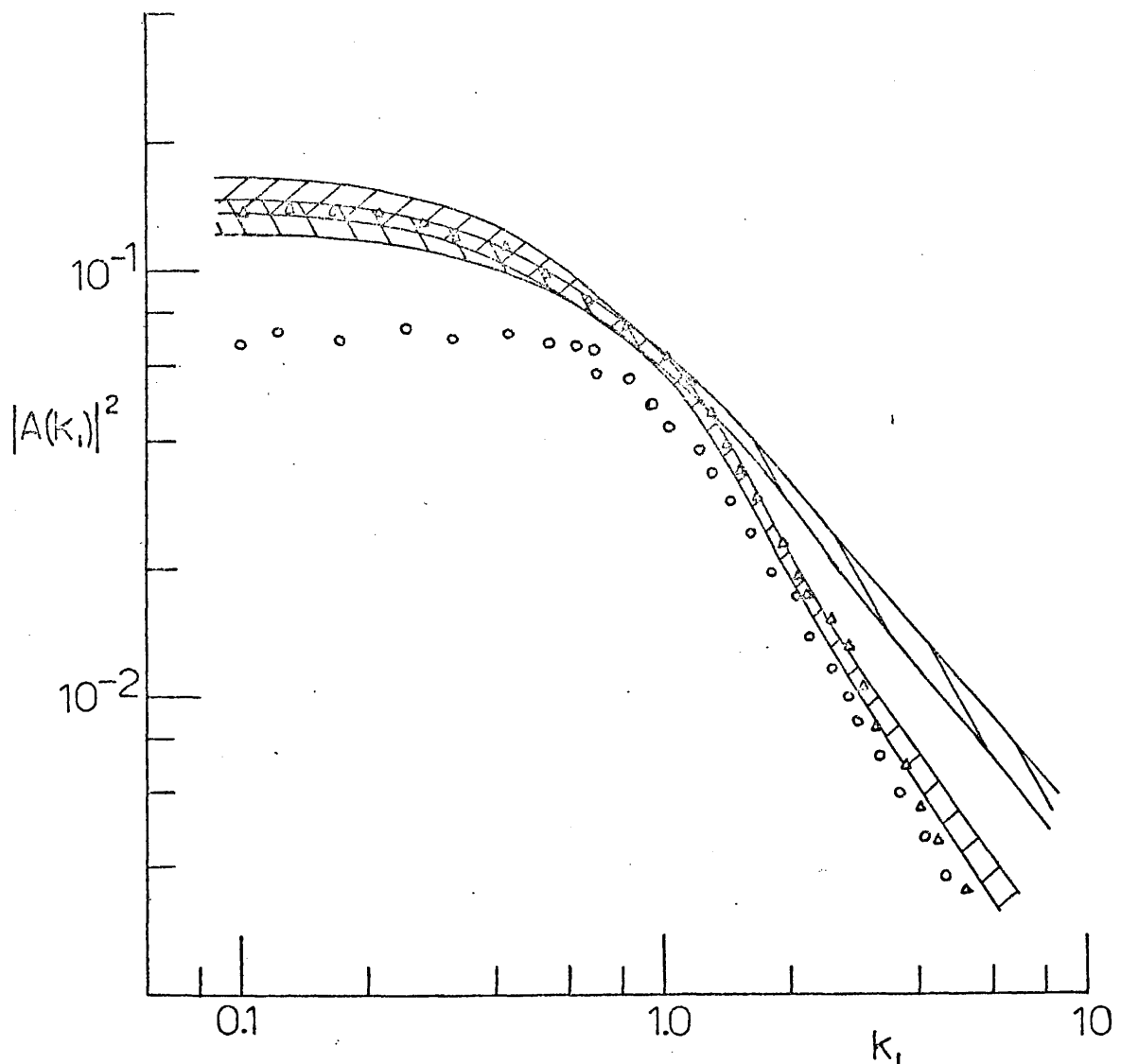


Exptl. Data : \circ . Series 1 ; \blacktriangle Series 3

Theory :  $L/C = 0.40$

Band of values : $\alpha = 10^\circ \rightarrow 12^\circ$

FIGURE 47.
INCREMENT IN
ADMITTANCE ;
NON-DISTORTION
TERMS IN THEORY ;
6 INCH GRID. 236.

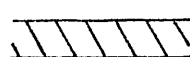


Exptl. data : Series 3 ; \circ $\alpha_{\text{set}} = 0^\circ$, Δ $\alpha_{\text{set}} = 10^\circ$.

Theoretical admittance

\equiv Exptl. admittance ($\alpha = 0^\circ$) + theoretical increment.

$L/c = 0.40$; band of values : $\alpha = 10^\circ \rightarrow 12^\circ$;

 all terms.

 non-distortion terms only.

FIGURE 48 . INCREMENT IN ADMITTANCE ; 6 INCH GRID.
ALTERNATIVE PRESENTATION.

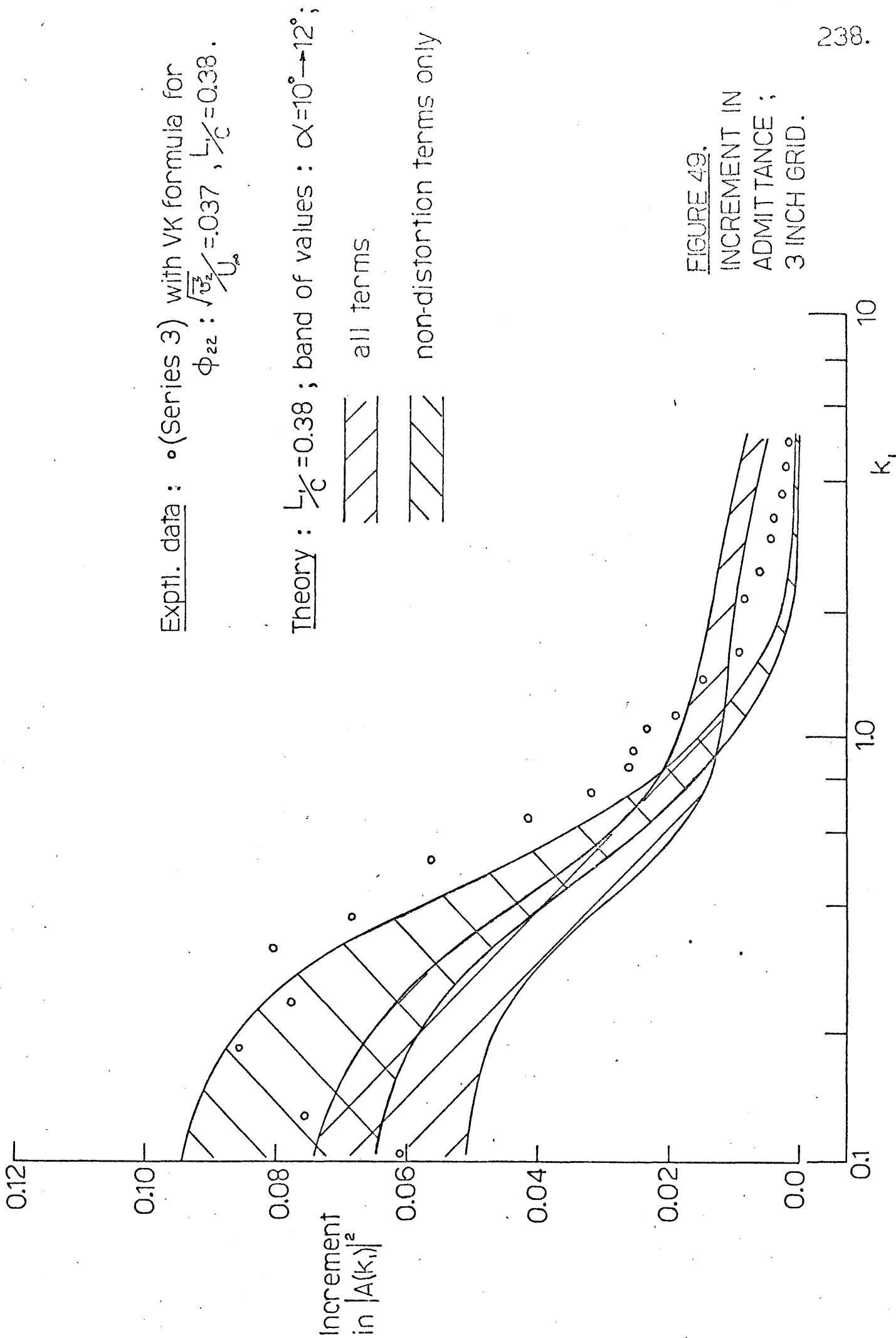
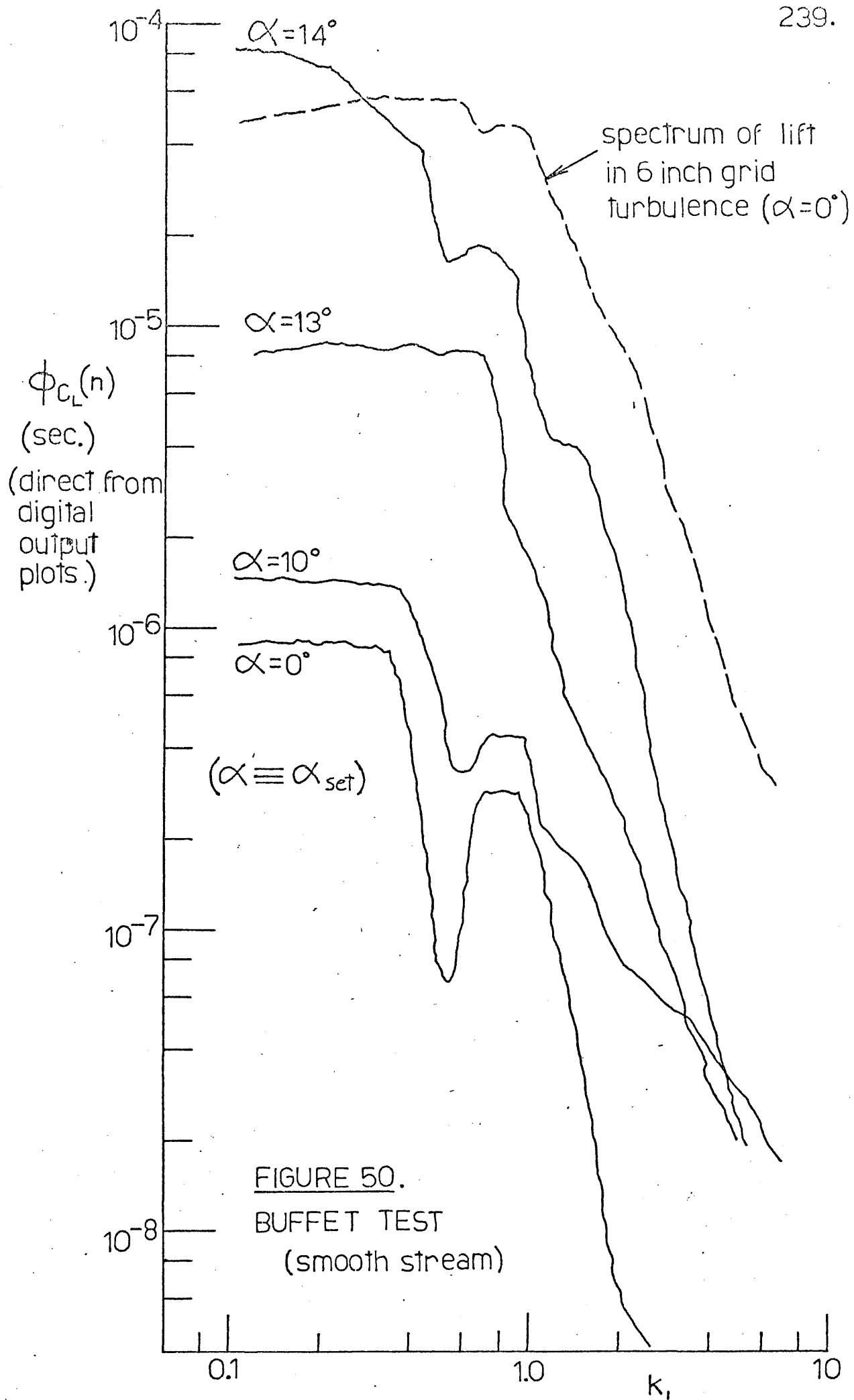


FIGURE 49.
INCREMENT IN
ADMITTANCE ;
3 INCH GRID.



PLATES

DETAILS OF PLATES 1→10 (TUFT VISUALIZATION) :

- Photograph exposure time : 2 secs .
- Suction surface of aerofoil.
- Leading edge at top.
- Approximate regions of separation indicated by: ————
- Refer to table 2 for details of the flows .

PLATE 1. Attached flow:

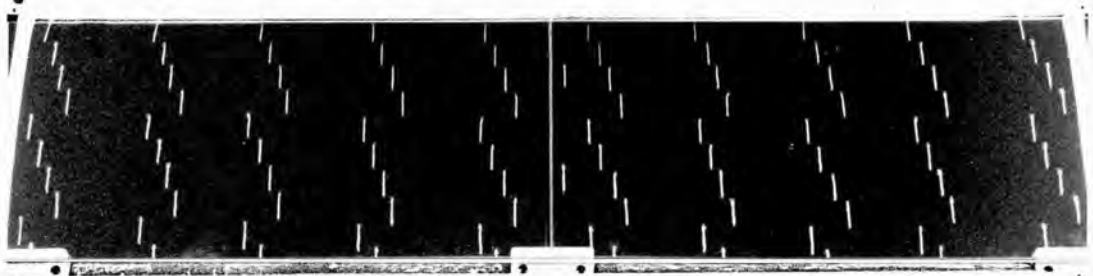


PLATE 1. NACA0015 ; SMOOTH LR ; $\alpha=0.0^\circ$

PLATES 2&3. Combined l.e./t.e. stall:

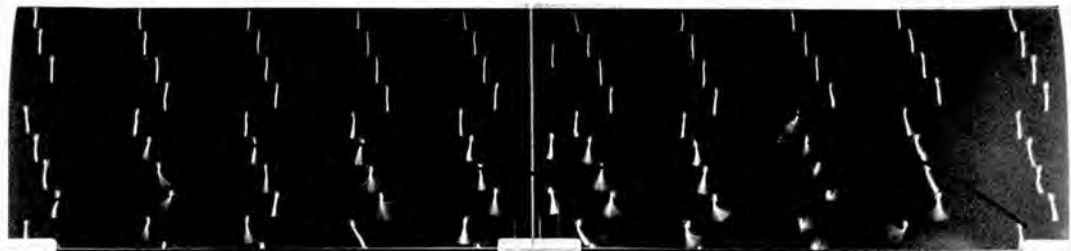


PLATE 2. NACA0015 ; SMOOTH LR ; $\alpha=14.0^\circ$

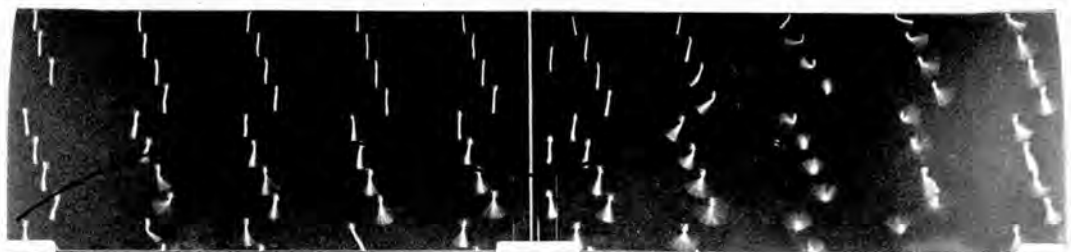
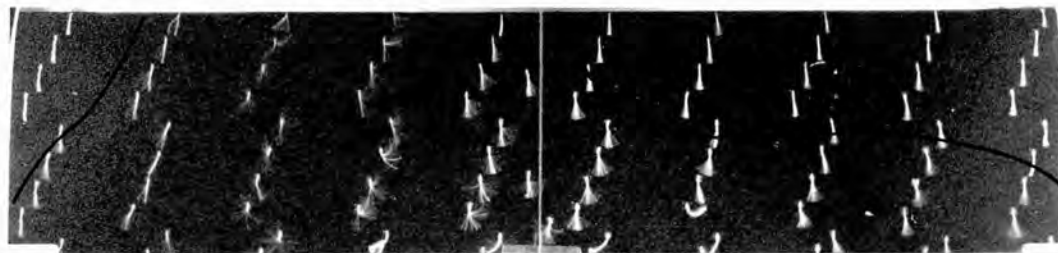
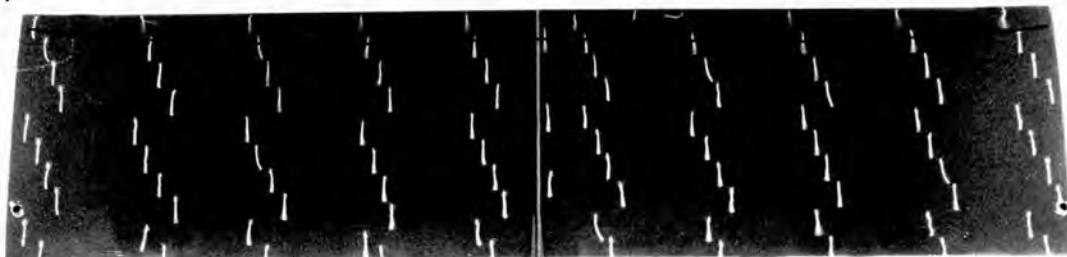


PLATE 3. NACA0015 ; SMOOTH LR ; $\alpha=14.5^\circ$

PLATES 4&5. Moving stall :PLATE 4. NACA0012 ; GRID L ; $\alpha = 15^\circ$; A.

- PLATE 5. NACA0012 ; GRID L ; $\alpha = 15^\circ$; B.

PLATES 6&7. Leading edge stall :PLATE 6. NACA0012 ; SMOOTH LR ; $\alpha = 11.0^\circ$ PLATE 7. NACA0012 ; SMOOTH LR ; $\alpha = 11.5^\circ$ PLATES 8&9. Thin-aerofoil stall ; 2D:PLATE 8. NACA0009 ; SMOOTH LR ; $\alpha = 8.0^\circ$

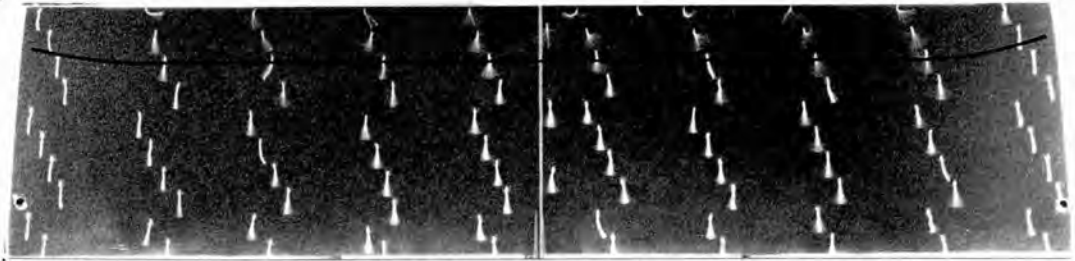


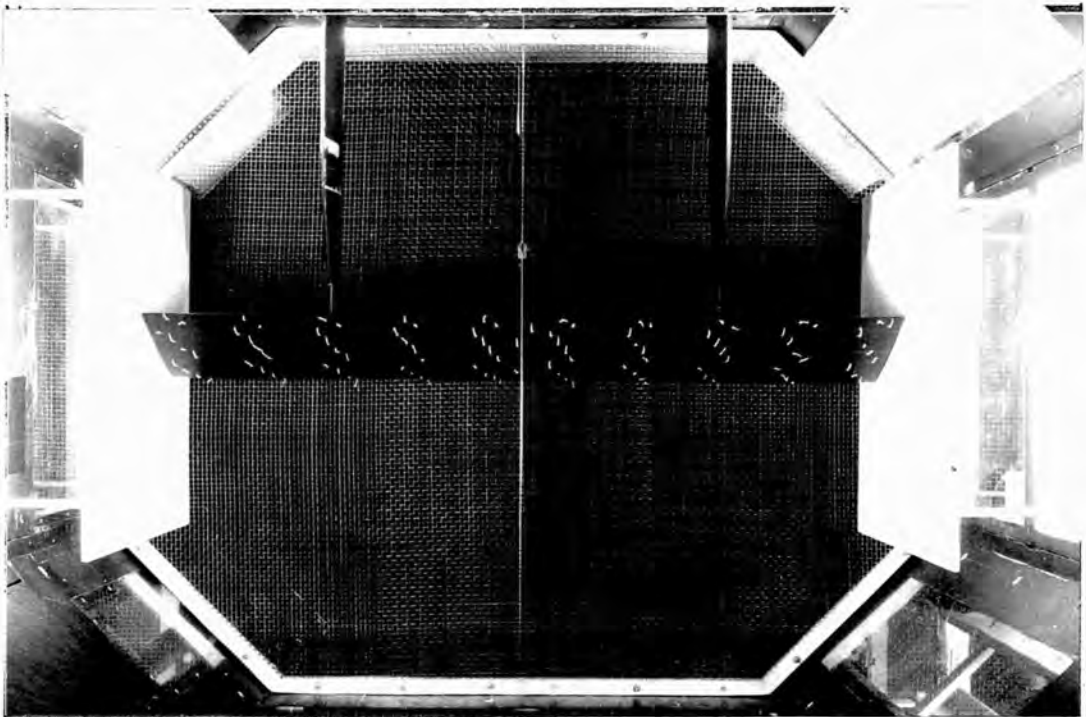
PLATE 9. NACA0009 ; SMOOTH LR ; $\alpha = 8.5^\circ$.

PLATE 10. Thin-aerofoil stall ; 3D :



PLATE 10. NACA0009 ; GRID S,1 ; $\alpha = 11.75^\circ$

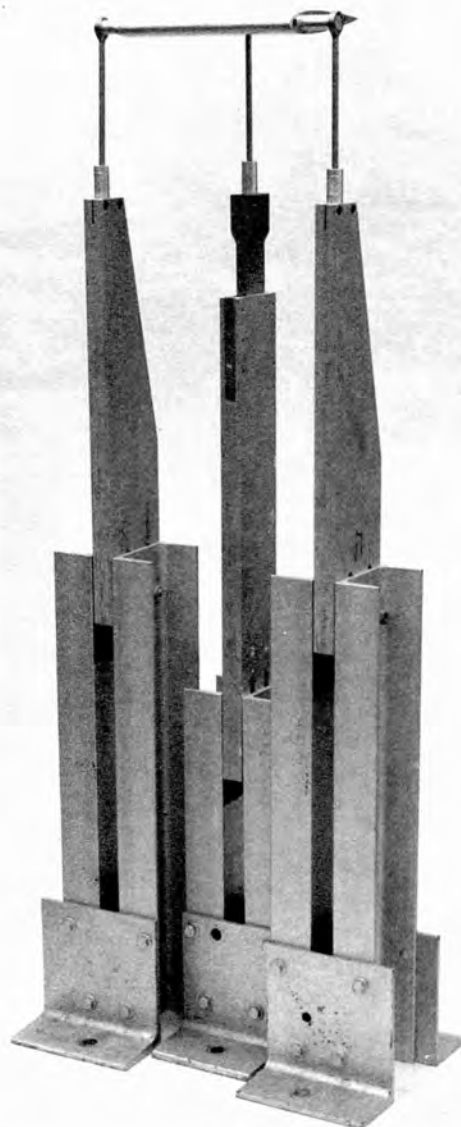
PLATE 11. Overall view of mean-load model in tunnel.





ABOVE : PLATE 12.

The measuring element;
unsteady lift balance.



AT LEFT : PLATE 13.

The measuring element,
mounted on supporting
rods and pylons.

The Mugridge-type Approximations to $G(k_1, k_2)$ and $G'(k_f, k_s, k_3)$

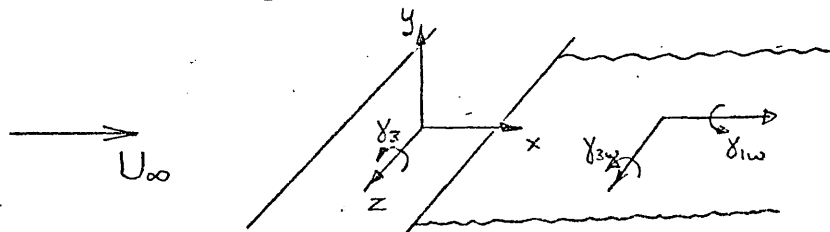
In this appendix, the formula of Mugridge (1971) is rederived, and then extended to encompass the case of a non-frozen gust. Mugridge's theory effectively adjusts the theory of Sears (1941) for the effect of an additional streamwise component of wake vorticity; that is, it provides a "lifting-line theory" adjustment to Sears theory. The analysis follows the form of that presented in section 6.3.2 of the main text.

(A) Frozen gust

In this order (ϵ) theory, the aerofoil is of zero-thickness and at zero incidence; and the gust is of the form:

$$v_2(x, 0, z) = \hat{v}_2 e^{i(\omega t - k_1 x - k_3 z)} \quad (\text{refer 1.2.2})$$

It is assumed that only one component of unsteady bound vorticity exists; viz, the component γ_3 in the z direction. However, the vortex sheet wake is assumed to have two components: γ_{3w} and γ_{1w} , the latter arising (as in lifting line theory) from the spanwise variation of the upwash.



γ_3 will be of the form:

$$\gamma_3(x, z) = \hat{\gamma}_3(x) e^{i(\omega t - k_3 z)}$$

The following three equations are used to express the wake vorticity, γ_{1w} and γ_{3w} , in terms of the aerofoil circulation,

$$\Gamma = \hat{\Gamma} e^{i(\omega t - k_3 z)} = \int_{-1}^1 \gamma_3 dx :$$

$$\frac{\partial \Gamma}{\partial t} = -U_\infty \gamma_{3w}(1, z) \quad , \quad \left(\begin{array}{l} \text{arising from Kelvin's} \\ \text{Circulation Theorem and the} \\ \text{Kutta condition} \end{array} \right)$$

$$\frac{\partial \gamma_{3w}}{\partial t} + U_\infty \frac{\partial \gamma_{3w}}{\partial x} = 0 \quad , \quad \left(\text{simple wake convection at } U_\infty \right)$$

$$\frac{\partial \gamma_{1w}}{\partial x} + \frac{\partial \gamma_{3w}}{\partial z} = 0 \quad . \quad \left(\text{continuity of wake vorticity} \right)$$

The solution is:

$$\gamma_{3w} = -ik_1 e^{ik_1 x} \hat{\Gamma} e^{i(\omega t - k_1 x - k_3 z)} \quad ,$$

$$\gamma_{1w} = +ik_3 e^{ik_1 x} \hat{\Gamma} e^{i(\omega t - k_1 x - k_3 z)}$$

The upwash resulting from γ_3 , γ_{3w} , and γ_{1w} can be determined from the Biot-Savart Law:

$$v_2'(x, 0, z) = \frac{1}{4\pi} \iint_{-\infty}^{\infty} \frac{(\gamma_3(x', z')(x-x') - \gamma_1(x', z')(z-z')) dx' dz'}{[(x-x')^2 + (z-z')^2]^{3/2}}$$

Mugridge makes two further assumptions:

- (1) The contribution from γ_3 (and γ_{3w}) is evaluated as if the gust were two-dimensional, that is, for this component, the Biot-Savart Law becomes:

$$\frac{1}{2\pi} \int_{-\infty}^{\infty} \frac{\gamma_3(x', z)}{(x-x')} dx' .$$

- (2) The contribution from γ_{1w} is evaluated as if the aerofoil were a lifting line; that is, the wake is assumed to originate at $x = 0$.

Thus, the induced upwash is determined as:

$$v_2'(x,0,z) = \frac{1}{2\pi} \int_{-1}^1 \frac{\gamma_3(x',z)}{(x-x')} dx' + \frac{1}{2\pi} \int_{-1}^{\infty} \frac{\gamma_{3\omega}(x',z)}{(x-x')} dx' - \frac{1}{4\pi} \int_{-\infty}^{\infty} \int_{-\infty}^{\infty} \frac{\gamma_{1\omega}(x',z')(z-z')}{[(x-x')^2 + (z-z')^2]^{\frac{3}{2}}} dx' dz'$$

The first two terms arise in Sears' theory; the third term is Muiridge's adjustment.

Applying the boundary condition, $v_2(x,0,z) + v_2'(x,0,z) = 0$, and substituting for $\gamma_{3\omega}$ and $\gamma_{1\omega}$ leads to:

$$\hat{v}_2 e^{-ik_1 x} = -\frac{1}{2\pi} \int_{-1}^1 \frac{\hat{\gamma}_3 dx'}{(x-x')} + \frac{ik_1 e^{ik_1 \hat{\Gamma}}}{2\pi} \int_{-1}^{\infty} \frac{e^{-ik_1 x'}}{(x-x')} dx' + \frac{ik_3 e^{ik_1 \hat{\Gamma}}}{e^{-ik_3 z} 4\pi} \int_{-\infty}^{\infty} \int_{-\infty}^{\infty} \frac{e^{-ik_1 x'}(z-z') e^{-ik_3 z'}}{[(x-x')^2 + (z-z')^2]^{\frac{3}{2}}} dx' dz'$$

The double integral in the last term can be evaluated analytically as follows:

Let the integral be I. Substituting $X = x - x'$ and $Z = z - z'$

$$I = -e^{-ik_1 x} e^{-ik_3 z} \int_{-\infty}^{\infty} \int_{-\infty}^{\infty} \frac{e^{ik_1 X} e^{ik_3 Z} Z}{(X^2 + Z^2)^{\frac{3}{2}}} dz dx$$

Using $\int_0^{\infty} \frac{\sin k_3 Z \cdot Z}{(X^2 + Z^2)^{\frac{3}{2}}} dz = k_3 K_0(k_3 X)$, (K is the modified Bessel function)

$$I = -2ik_3 e^{-ik_1 x} e^{-ik_3 z} \int_0^{\infty} K_0(k_3 X) e^{ik_1 X} dx.$$

Using the results:

$$\int_0^{\infty} K_0(k_3 X) \sin k_1 X dx = \frac{1}{\sqrt{k_3^2 + k_1^2}} \log \left\{ \frac{k_1 + \sqrt{k_1^2 + k_3^2}}{k_3} \right\}$$

and:

$$\int_0^{\infty} K_0(k_3 X) \cos k_1 X dx = \frac{1}{\sqrt{k_3^2 + k_1^2}} \cdot \frac{\pi}{2}$$

the integral becomes:

$$I = i e^{-ik_1 x} e^{-ik_3 z} \pi \frac{k_1}{k_3} N(k_1, k_3),$$

$$\text{where } N(k_1, k_3) = \frac{k_3^2}{k_1 \sqrt{k_1^2 + k_3^2}} \left(1 - i \frac{2}{\pi} \log \left\{ \frac{k_1 + \sqrt{k_1^2 + k_3^2}}{k_3} \right\} \right).$$

The boundary condition equation becomes:

$$\hat{v}_2 \left(1 + \frac{k_1 e^{ik_1} N(k_1, k_3)}{4} \frac{\hat{\Gamma}}{\hat{v}_2} \right) e^{-ik_1 x} = -\frac{1}{2\pi} \int_{-1}^1 \frac{\hat{\gamma}_3 dx'}{(x-x')} + \frac{ik_1 e^{ik_1} \hat{\Gamma}}{2\pi} \int_1^{\infty} \frac{e^{-ik_1 x'}}{(x-x')} dx'.$$

The analysis now parallels the normal two-dimensional Sears analysis (similar to that of section 6.3.2) with \hat{v}_2 replaced by $\hat{v}_2 \left(1 + \frac{k_1 e^{ik_1} N(k_1, k_3)}{4} \frac{\hat{\Gamma}}{\hat{v}_2} \right)$ = say, $\hat{v}_2 (1+T)$.

The above equation is inverted, and integrated w.r. t. x to yield the following expression for $\hat{\Gamma}$:

$$\frac{k_1 e^{ik_1} \hat{\Gamma}}{4 \hat{v}_2} = \frac{J_0(k_1) - i J_1(k_1)}{i [(1+N(k_1, k_3))(J_1(k_1) + i J_0(k_1)) + Y_0(k_1) - i Y_1(k_1)]}$$

The equation for the lift in the Sears theory is:

$$\frac{L}{\rho} = -U_{\infty} \left[ik_1 \hat{\Gamma} - ik_1 \int_{-1}^1 \hat{\gamma}_3 x dx + \hat{\Gamma} \right] e^{i\omega t},$$

and the solution is:

$$C_L = 2\pi S(k_1) \frac{\hat{v}_2}{U_{\infty}} e^{i\omega t}.$$

Thus the present solution is:

$$C_L = 2\pi S(k_1) [1+T] \frac{\hat{v}_2}{U_{\infty}} e^{i(\omega t - k_3 z)}$$

where

$$T = \frac{k_1 e^{ik_1} N(k_1, k_3) \hat{\Gamma}}{4 \hat{v}_2} = \frac{N(k_1, k_3) [J_0(k_1) - i J_1(k_1)]}{i [(1+N(k_1, k_3))(J_1(k_1) + i J_0(k_1)) + Y_0(k_1) - i Y_1(k_1)]}$$

Equivalently, the result can be written:

$$C_L = 2\pi G_M(k_1, k_3) \frac{\hat{v}_2}{U_{\infty}} e^{i(\omega t - k_3 z)},$$

where $G_M(k_1, k_3) = L(k_1, k_3) [J_0(k_1) - i J_1(k_1)] + i J_1(k_1)$;

$$L(k_1, k_3) = \frac{(1+N(k_1, k_3)) J_1(k_1) - i Y_1(k_1)}{(1+N(k_1, k_3))(J_1(k_1) + i J_0(k_1)) + Y_0(k_1) - i Y_1(k_1)}$$

and $N(k_1, k_3)$ has been defined above.

(B) Non-frozen gust.

The gust is:

$$\hat{v}_2 e^{i(\omega t - k_s x - k_3 z)} \quad , \quad \text{where } \omega = k_f U_\infty .$$

The analysis follows that of the frozen gust case, except that functions arising from wake terms will depend on k_f , while those arising from gust terms will depend on k_s .

The wake vorticity is:

$$\gamma_{3w} = -ik_f e^{ik_f \hat{\Gamma}} e^{i(\omega t - k_f x - k_3 z)} \quad ; \quad \gamma_{1w} = +ik_3 e^{ik_f \hat{\Gamma}} e^{i(\omega t - k_f x - k_3 z)} .$$

The boundary condition equation becomes:

$$\hat{v}_2 e^{-ik_s x} + \frac{k_f e^{ik_f} N(k_f, k_s) \hat{\Gamma} e^{-ik_f x}}{4} = -\frac{1}{2\pi} \int_{-1}^1 \frac{\hat{\gamma}_3 dx'}{(x-x')} + \frac{ik_f e^{ik_f} \hat{\Gamma}}{2\pi} \int_1^\infty \frac{e^{-ik_f x'}}{(x-x')} dx' ,$$

and the circulation expression:

$$\frac{k_f e^{ik_f} \hat{\Gamma}}{4} \frac{\hat{\Gamma}}{\hat{v}_2} = \frac{J_0(k_s) - iJ_1(k_s)}{i[(1+N(k_f, k_s))(J_1(k_f) + iJ_0(k_f)) + Y_0(k_f) - iY_1(k_f)]} .$$

The equation for the lift is:

$$\frac{L}{\rho} = - \left[i\omega \hat{\Gamma} - i\omega \int_{-1}^1 \hat{\gamma}_3 x dx + U_\infty \hat{\Gamma} \right] e^{i(\omega t - k_3 z)} \quad (\text{see 6.3.2})$$

$$= -U_\infty \left[ik_f \hat{\Gamma} - ik_f \int_{-1}^1 \hat{\gamma}_3 x dx + \hat{\Gamma} \right] e^{i(\omega t - k_3 z)} ,$$

since $\omega = k_f U_\infty$.

In this case:

$$\int_{-1}^1 \hat{\gamma}_3 x dx = 2\pi \hat{v}_2 \frac{J_1(k_s)}{k_s} + \frac{\pi}{2} e^{ik_f} \hat{\Gamma} N(k_f, k_s) J_1(k_f) - i \frac{(+ik_f) \hat{\Gamma}}{k_f} + e^{ik_f} \frac{\pi}{2} H_1(k_f) \hat{\Gamma} .$$

The resultant lift response is:

$$C_L = 2\pi G'_M(k_f, k_s, k_3) \frac{\hat{v}_2}{U_\infty} e^{i(\omega t - k_3 z)}$$

$$\text{where } G'_M(k_f, k_s, k_3) = L(k_f, k_3) [J_0(k_s) - iJ_1(k_s)] + i \frac{k_f}{k_s} J_1(k_s) ,$$

and where the function, L , has been defined in the frozen gust analysis.

The response function, $G'_M(k_f, k_s, k_3)$, reduces to $G(k_1, k_3)$ when $k_f = k_s = k_1$, and to the generalized Sears function, $S'(k_f, k_s)$, (see 1.2.2) when $k_3 = 0$.

APPENDIX 2

A Derivation of $\phi_{C_L}(\bar{k}_1) = \iint_{-\infty}^{\infty} \Omega_i^* \Omega_j \Phi_{ij}(\bar{k}) d\bar{k}_1 d\bar{k}_2 d\bar{k}_3$

Tensor notation is used in this analysis.

In this report, the lift response to a general sinusoidal gust is of the form:

$$C_L(\bar{t}) = \Omega_i \hat{v}_i e^{i\bar{\omega}'\bar{t}} \quad \text{where } \bar{\omega}' = \bar{k}_1 U_\infty.$$

If the frequency, $\bar{\omega}'$, is of opposite sign, the response is:

$$C_L(\bar{t}) = \Omega_i^* \hat{v}_i e^{-i\bar{\omega}'\bar{t}}$$

This form is used in the following analysis.

The turbulence is considered to be composed of Fourier components. Let $d\hat{v}$ be the amplitude (complex in general) of the Fourier component of wavenumber, \underline{k} . (The spatial components of $d\hat{v}$ and \underline{k} are $d\hat{v}_i$ and k_i , respectively). The lift response to this Fourier component is:

$$dC_L(\bar{t}) = \Omega_i^* d\hat{v}_i e^{-i\bar{\omega}'\bar{t}}.$$

The auto-correlation function of this Fourier component is (by definition):

$$\overline{dC_L(\bar{t}) dC_L^*(\bar{t}+\bar{\tau})} = \Omega_i^* \Omega_j \overline{d\hat{v}_i d\hat{v}_j^*} e^{i\bar{\omega}'\bar{\tau}} \quad \text{where the overbar denotes a time mean.}$$

In homogeneous, stationary turbulence, the three dimensional spectrum, $\Phi_{ij}(\bar{k})$, is defined by (see for example, Batchelor (1953)):

$$\overline{d\hat{v}_i d\hat{v}_j^*} = \Phi_{ij}(\bar{k}) d\bar{k}_1 d\bar{k}_2 d\bar{k}_3.$$

Therefore: $\overline{dC_L(\bar{t}) dC_L^*(\bar{t}+\bar{\tau})} = \Omega_i^* \Omega_j \Phi_{ij}(\bar{k}) e^{i\bar{\omega}'\bar{\tau}} d\bar{k}_1 d\bar{k}_2 d\bar{k}_3.$

For the turbulence, as a whole, the auto-correlation function will be:

$$\begin{aligned} C_L(\bar{t}) C_L(\bar{t} + \bar{\tau}) &= \sum_{\text{all } \bar{k}} \left[dC_L(\bar{t}) \cdot dC_L^*(\bar{t} + \bar{\tau}) \right] \\ &= \iiint_{-\infty}^{\infty} \Omega_i^* \Omega_j \Phi_{ij}(\bar{k}) e^{i\bar{\omega}'\bar{\tau}} d\bar{k}_1 d\bar{k}_2 d\bar{k}_3 . \end{aligned}$$

The spectrum, $\phi_{C_L}(\bar{k}_1)$, is related to the auto-correlation function by:

$$\begin{aligned} \phi_{C_L}(\bar{k}_1) &= \frac{U_\infty}{2\pi} \int_{-\infty}^{\infty} C_L(\bar{t}) \cdot C_L(\bar{t} + \bar{\tau}) e^{-i\bar{\omega}\bar{\tau}} d\bar{\tau}, \quad (\omega = k_1 U_\infty) \\ &= \frac{U_\infty}{2\pi} \iiint_{-\infty}^{\infty} \Omega_i^* \Omega_j \Phi_{ij}(\bar{k}) e^{-i[\bar{\omega} - \bar{\omega}']\bar{\tau}} d\bar{\tau} d\bar{k}_1 d\bar{k}_2 d\bar{k}_3 \\ &= \iiint_{-\infty}^{\infty} \Omega_i^* \Omega_j \Phi_{ij}(\bar{k}) \delta(\bar{\omega} - \bar{\omega}') d\bar{\omega}' d\bar{k}_2 d\bar{k}_3 , \end{aligned}$$

since $\frac{1}{2\pi} \int_{-\infty}^{\infty} e^{-i\bar{\omega}\bar{\tau}} d\bar{\tau} = \delta(\bar{\omega})$, and $\bar{\omega}' = \bar{k}_1 U_\infty$.

Finally, integrating with respect to $\bar{\omega}'$ yields:

$$\phi_{C_L}(\bar{k}_1) = \iint_{-\infty}^{\infty} \Omega_i^* \Omega_j \Phi_{ij}(\bar{k}) d\bar{k}_2 d\bar{k}_3 . .$$

APPENDIX 3

Expansion of $S'(k_1, k_1 - \alpha k_2)$ to First Order in α .

$$S'(k_1, k_1 - \alpha k_2) = \frac{H_1(k_1) [J_0(k_1 - \alpha k_2) - i J_1(k_1 - \alpha k_2)]}{H_1(k_1) + i H_0(k_1)} + \frac{i k_1 J_1(k_1 - \alpha k_2)}{k_1 - \alpha k_2} \quad (\text{refer 6.3.2})$$

Using Taylor's expansion about k_1 , and retaining only the first two terms of the series yields:

$$J_0(k_1 - \alpha k_2) \approx J_0(k_1) - \alpha k_2 J_0'(k_1) \quad (\text{where the superscript indicates } \frac{\partial}{\partial k_1})$$

$$J_1(k_1 - \alpha k_2) \approx J_1(k_1) - \alpha k_2 J_1'(k_1)$$

$$\frac{k_1}{k_1 - \alpha k_2} = \left(1 - \alpha \frac{k_2}{k_1}\right)^{-1} \approx 1 + \alpha \frac{k_2}{k_1}$$

From the properties of Bessel Functions:

$$J_0'(k_1) = -J_1(k_1)$$

$$J_1'(k_1) = \frac{1}{2} [J_0(k_1) - J_2(k_1)]$$

Thus, as $\alpha \rightarrow 0$,

$$J_0(k_1 - \alpha k_2) \rightarrow J_0(k_1) + \alpha k_2 J_1(k_1)$$

$$J_1(k_1 - \alpha k_2) \rightarrow J_1(k_1) + \alpha k_2 J^+(k_1) \quad \text{where } J^+(k_1) = \frac{1}{2} (J_2(k_1) - J_0(k_1))$$

and

$$\frac{k_1}{k_1 - \alpha k_2} J_1(k_1 - \alpha k_2) \rightarrow J_1(k_1) + \alpha \frac{k_2}{k_1} J_1(k_1) + \alpha k_2 J^+(k_1)$$

Substituting these equations into the equation for $S'(k_1, k_1 - \alpha k_2)$ yields the result:

$$\text{As } \alpha \rightarrow 0, \quad S'(k_1, k_1 - \alpha k_2) \rightarrow S(k_1) + \alpha S_A(k_1, k_2)$$

where

$$S_A(k_1, k_2) = k_2 \left\{ \frac{H_1(k_1) [J_1(k_1) - i J^+(k_1)]}{H_1(k_1) + i H_0(k_1)} + i \left[J^+(k_1) + \frac{J_1(k_1)}{k_1} \right] \right\}$$

APPENDIX 4

The Detailed Analysis for L-D : Two Dimensional Gust Theory.

The integrated form of the linearized vorticity transport equation is used to evaluate the distortion effect:

$$\hat{S}(x,y) = \left\{ ik_1 \int_{-\infty}^x \frac{V_1'}{U_\infty} dx' + ik_2 \int_0^x \frac{V_2'}{U_\infty} dx' + ik_2 \int_{-\infty}^0 \frac{V_2' - V_2'(y=0)}{U_\infty} dx' \right\} \hat{S}_\infty.$$

Initially, the mean flow field due to $K'(x) = e^{-i\lambda x}$ is considered.

The velocities in this field can be determined by an application of the Biot-Savart Law:

$$V_1' = -\frac{y}{2\pi} \int_{-\infty}^{\infty} \frac{e^{-i\lambda x'} dx'}{(x-x')^2 + y^2} \quad ; \quad V_2' = \frac{1}{2\pi} \int_{-\infty}^{\infty} \frac{e^{-i\lambda x}(x-x') dx'}{(x-x')^2 + y^2}$$

These integrals can be evaluated analytically by substituting

$X = x - x'$, and using the standard integral results:

$$\int_0^{\infty} \frac{\sin \lambda X \cdot X dx}{X^2 + y^2} = \frac{\pi}{2} e^{-\lambda y} \quad ; \quad \int_0^{\infty} \frac{\cos \lambda X \cdot dx}{X^2 + y^2} = \frac{\pi}{2y} e^{-\lambda y} \quad ; \quad \text{if } \lambda > 0, y > 0.$$

The results are:

$$V_1' = \begin{cases} \pm \frac{1}{2} e^{-i\lambda x} e^{\pm \lambda y}, & \lambda > 0 \\ \pm \frac{1}{2} e^{-i\lambda x} e^{\mp \lambda y}, & \lambda < 0 \end{cases} \quad V_2' = \begin{cases} \frac{i}{2} e^{-i\lambda x} e^{\pm \lambda y}, & \lambda > 0 \\ -\frac{i}{2} e^{-i\lambda x} e^{\mp \lambda y}, & \lambda < 0 \end{cases}$$

where the top signs in the dual sign combinations refer to $y < 0$, and the bottom signs to $y > 0$.

The integrals $\int_{-\infty}^x \frac{V_1'}{U_\infty} dx'$ etc. are evaluated next. The following mathematical result is employed:

$$\int_{-\infty}^0 e^{-i\lambda x} dx = \pi \delta(\lambda) + \frac{i}{\lambda}.$$

In the classical theory of integration, this integral is not determinate.

The above assigned value was obtained from Lighthill's (1958) theory of generalized functions.

Thus:

$$\int_{-\infty}^x \frac{V_1'}{U_\infty} dx' = \begin{cases} \pm \frac{i}{2\lambda U_\infty} e^{-i\lambda x} e^{\pm\lambda y} \pm \frac{\pi}{2U_\infty} \delta(\lambda) & , \lambda > 0 \\ \pm \frac{i}{2\lambda U_\infty} e^{-i\lambda x} e^{\mp\lambda y} \pm \frac{\pi}{2U_\infty} \delta(\lambda) & , \lambda < 0 \end{cases}$$

$$\int_0^x \frac{V_2'}{U_\infty} dx' + \int_{-\infty}^0 \frac{V_2' - V_2'(y=0)}{U_\infty} dx' = \begin{cases} -\frac{1}{2\lambda U_\infty} (e^{-i\lambda x} e^{\pm\lambda y} - 1) & , \lambda > 0 \\ \frac{1}{2\lambda U_\infty} (e^{-i\lambda x} e^{\mp\lambda y} - 1) & , \lambda < 0 \end{cases}$$

Substitution yields:

$$\frac{\hat{J}(x,y)}{\int_{-\infty}^{\infty} \frac{\hat{J}(x,y)}{2\lambda U_\infty}} = \begin{cases} \mp k_1 e^{\pm\lambda y} e^{-i\lambda x} \pm \lambda i k_1 \pi \delta(\lambda) - i k_2 e^{\pm\lambda y} e^{-i\lambda x} + i k_2 & , \lambda > 0 \\ \mp k_1 e^{\mp\lambda y} e^{-i\lambda x} \pm \lambda i k_1 \pi \delta(\lambda) + i k_2 e^{\mp\lambda y} e^{-i\lambda x} - i k_2 & , \lambda < 0 \end{cases}$$

The extra upwash due to distortion, $\tilde{v}_2(x,0)$, is determined with the Biot-Savart Law:

$$\tilde{v}_2(x,0) = \frac{1}{2\pi} \iint_{-\infty}^{\infty} \frac{\hat{J}(x',y') e^{i(\omega t - k_1 x' - k_2 y')} (x-x')}{(x-x')^2 + y'^2} dx' dy'$$

Upon substituting for $\hat{J}(x',y')$, the terms in $\tilde{v}_2(x,0)$ are all of the form:

$$\frac{e^{i\omega t}}{4\pi U_\infty} \iint_{-\infty}^{\infty} \frac{C(y') e^{-ik_2 y'} e^{-ik_1 x'} (x-x')}{(x-x')^2 + y'^2} dx' dy'.$$

K has the value $k_1 + \lambda$ or k_1

$$\text{The integral, } \int_{-\infty}^{\infty} \frac{e^{-iKx'} (x-x')}{(x-x')^2 + y'^2} dx'$$

has already been considered in the evaluation of V_2' . Its values are

$$\begin{cases} i\pi e^{-iKx} e^{\pm Ky'} & , K > 0 \\ -i\pi e^{-iKx} e^{\mp Ky'} & , K < 0 \end{cases}$$

The $C(y')$ terms in the integrand are already different for $\lambda > 0$ and $\lambda < 0$. Thus, when $K = k_1 + \lambda$, the number of different solutions is further increased. For $k_1 > 0$ (the case of practical interest), the following three ranges of λ yield different analytical solutions:

$$(1) \quad -\infty \quad \text{to} \quad -k_1$$

$$(2) \quad -k_1 \quad \text{to} \quad 0$$

$$(3) \quad 0 \quad \text{to} \quad +\infty$$

When the integration w.r.t. x has been carried out, the terms in \tilde{v}_2 reduce to the form:

$$\frac{i e^{i\omega t} e^{-iKx}}{4U_\infty} \int_{-\infty}^{\infty} D e^{\pm Ey'} e^{-ik_2 y'} dy', \quad \text{where } E > 0 \text{ in each case.}$$

The following standard integral results are employed:

$$\int_0^{\infty} e^{-Ey'} \sin k_2 y' dy' = \frac{k_2}{E^2 + k_2^2} ; \quad \int_0^{\infty} e^{-Ey'} \cos k_2 y' dy' = \frac{E}{E^2 + k_2^2} ; \quad \text{if } E > 0.$$

With these results, the above integral becomes:

$$2i|D| \cdot \frac{k_2}{E^2 + k_2^2} ; \quad \text{if the sign of } D \text{ is } \pm.$$

$$2|D| \cdot \frac{E}{E^2 + k_2^2} . \quad \text{if the sign of } D \text{ is } +.$$

Thus a complete, analytical evaluation of $\tilde{v}_2(x, 0)$ is obtained. The full result is given in the following table:

λ range	$\tilde{v}_2(x, 0) / \frac{1}{2} \int_{-\infty}^{\infty} e^{i(\omega t - k_1 x)} U_\infty$
$-\infty$ to $-k_1$	$-\frac{1}{\lambda} \frac{k_1 k_2 e^{-i\lambda x}}{[(k_1 + 2\lambda)^2 + k_2^2]} - i\pi \delta(\lambda) \frac{k_1 k_2}{[k_1^2 + k_2^2]} - \frac{1}{\lambda} \frac{(k_1 + 2\lambda) k_2 e^{-i\lambda x}}{[(k_1 + 2\lambda)^2 + k_2^2]} + \frac{1}{\lambda} \frac{k_1 k_2}{[k_1^2 + k_2^2]}$
$-k_1$ to 0	$+\frac{1}{\lambda} \frac{k_1 k_2 e^{-i\lambda x}}{[k_1^2 + k_2^2]} - i\pi \delta(\lambda) \frac{k_1 k_2}{[k_1^2 + k_2^2]} - \frac{1}{\lambda} \frac{k_1 k_2 e^{-i\lambda x}}{[k_1^2 + k_2^2]} + \frac{1}{\lambda} \frac{k_1 k_2}{[k_1^2 + k_2^2]}$
0 to $+\infty$	$+\frac{1}{\lambda} \frac{k_1 k_2 e^{-i\lambda x}}{[(k_1 + 2\lambda)^2 + k_2^2]} - i\pi \delta(\lambda) \frac{k_1 k_2}{[k_1^2 + k_2^2]} + \frac{1}{\lambda} \frac{(k_1 + 2\lambda) k_2 e^{-i\lambda x}}{[(k_1 + 2\lambda)^2 + k_2^2]} - \frac{1}{\lambda} \frac{k_1 k_2}{[k_1^2 + k_2^2]}$

The terms in $\tilde{v}_2(x, 0)$ are of two basic forms:

$$(1) \hat{\tilde{v}}_2 e^{i(\omega t - k_1 x)} ; \quad (2) \hat{\tilde{v}}_2 e^{i(\omega t - [k_1 + \lambda]x)}$$

The lift responses to the two upwashes are, respectively:

$$(1) C'_{LD} = 2\pi S(k_1) \frac{\hat{v}_2}{U_0} e^{i\omega t} \quad (2) C'_{LD} = 2\pi S'(k_1, k_1 + \lambda) \frac{\hat{v}_2}{U_0} e^{i\omega t} \text{ (refer 1.2.2)}$$

Thus the complete C'_{LD} response can be written down directly from the above table. For convenience in later calculation, C'_{LD} is divided into its even and odd parts as a function of λ , denoted by C'_{LE} and C'_{LO} respectively. The result is:

λ range	$B_E(\lambda) = \frac{C'_{LE}}{\pi} \frac{\hat{v}_2}{U_0} e^{i\omega t}$
0 to $+k_1$	$+\frac{1}{\lambda} \frac{(k_1 + \lambda) k_2 S'(k_1, k_1 + \lambda)}{[(k_1 + 2\lambda)^2 + k_2^2]} - \frac{1}{\lambda} \frac{k_1 k_2 S(k_1)}{[k_1^2 + k_2^2]} - i\pi \delta(\lambda) \frac{k_1 k_2 S(k_1)}{[k_1^2 + k_2^2]}$
$+k_1$ to $+\infty$	$+\frac{1}{\lambda} \frac{(k_1 + \lambda) k_2 S'(k_1, k_1 + \lambda)}{[(k_1 + 2\lambda)^2 + k_2^2]} + \frac{1}{\lambda} \frac{(k_1 - \lambda) k_2 S'(k_1, k_1 - \lambda)}{[(k_1 - 2\lambda)^2 + k_2^2]} - \frac{1}{\lambda} \frac{k_1 k_2 S(k_1)}{[k_1^2 + k_2^2]} - i\pi \delta(\lambda) \frac{k_1 k_2 S(k_1)}{[k_1^2 + k_2^2]}$

λ range	$B_O(\lambda) = \frac{C'_{LO}}{\pi} \frac{\hat{v}_2}{U_0} e^{i\omega t}$
0 to $+k_1$	$+\frac{1}{\lambda} \frac{(k_1 + \lambda) k_2 S'(k_1, k_1 + \lambda)}{[(k_1 + 2\lambda)^2 + k_2^2]}$
$+k_1$ to $+\infty$	$+\frac{1}{\lambda} \frac{(k_1 + \lambda) k_2 S'(k_1, k_1 + \lambda)}{[(k_1 + 2\lambda)^2 + k_2^2]} - \frac{1}{\lambda} \frac{(k_1 - \lambda) k_2 S'(k_1, k_1 - \lambda)}{[(k_1 - 2\lambda)^2 + k_2^2]}$

C'_{LD} is the lift response for $K(x) = e^{-i\lambda x}$. The lift response, C_{LD} , to a general input, $K(x)$, is given by:

$$C_{LD} = \frac{1}{\sqrt{2\pi}} \int_{-\infty}^{\infty} \bar{K}(\lambda) C'_{LD}(\lambda) d\lambda$$

where

$$\bar{K}(\lambda) = \frac{1}{\sqrt{2\pi}} \int_{-\infty}^{\infty} K(x) e^{i\lambda x} dx$$

This is proved as follows:

Let $r(x_0)$ be the response of a linear system to the indicial input, $K(x) = \delta(x+x_0)$.

For a general input, $K(x)$:

$$K(x) = \int_{-\infty}^{\infty} \delta(x+x_0) K(-x_0) dx_0 \quad \begin{array}{l} \text{(from the definition} \\ \text{of } \delta(x)) \end{array}$$

By linear superposition, the general response, R , to this input is:

$$R = \int_{-\infty}^{\infty} r(x_0) K(-x_0) dx_0$$

From the properties of Fourier transforms (see Titchmarsh (1937)):

$$R = \int_{-\infty}^{\infty} r(x_0) K(-x_0) dx_0 = \int_{-\infty}^{\infty} \bar{r}(\lambda) \bar{K}(\lambda) d\lambda$$

$$\text{where } \bar{r}(\lambda) = \frac{1}{\sqrt{2\pi}} \int_{-\infty}^{\infty} r(x_0) e^{i\lambda x_0} dx_0; \quad \bar{K}(\lambda) = \frac{1}{\sqrt{2\pi}} \int_{-\infty}^{\infty} K(x_0) e^{i\lambda x_0} dx_0$$

Consider, now, the sinusoidal input,

$$K'(x_0) = e^{-i\lambda_0 x_0}$$

Corresponding to this,

$$\bar{K}'(\lambda) = \frac{1}{\sqrt{2\pi}} \int_{-\infty}^{\infty} e^{-i\lambda_0 x_0} e^{i\lambda x_0} dx_0 = \sqrt{2\pi} \delta(\lambda - \lambda_0)$$

Thus the sinusoidal response,

$$\begin{aligned} R'(\lambda_0) &= \sqrt{2\pi} \int_{-\infty}^{\infty} \delta(\lambda - \lambda_0) \bar{r}(\lambda) d\lambda \\ &= \sqrt{2\pi} \cdot \bar{r}(\lambda_0) \end{aligned}$$

That is,

$$\bar{r}(\lambda) = \frac{1}{\sqrt{2\pi}} \cdot R'(\lambda)$$

Substituting for $\bar{r}(\lambda)$ in the equation for R gives the required result:

$$R = \frac{1}{\sqrt{2\pi}} \int_{-\infty}^{\infty} \bar{K}(\lambda) \cdot R'(\lambda) d\lambda$$

Or, in this case:

$$C_{LD} = \frac{1}{\sqrt{2\pi}} \int_{-\infty}^{\infty} K(\lambda) C'_{LD}(\lambda) d\lambda$$

For the zero-thickness aerofoil at incidence, α :

$$K(x) = -2U_\infty \alpha \sqrt{\frac{1-x}{1+x}} = -2U_\infty \alpha \frac{1-x}{\sqrt{1-x^2}} \text{ for } |x| \leq 1 \text{ (0, otherwise)}$$

Using the following standard Fourier transforms:

$$\int_0^\infty J_0(\lambda) \cos \lambda x d\lambda = \frac{1}{\sqrt{1-x^2}} \text{ for } x \leq 1 \text{ (0, otherwise)}$$

$$\int_0^\infty J_1(\lambda) \sin \lambda x d\lambda = \frac{x}{\sqrt{1-x^2}} \text{ for } x \leq 1 \text{ (0, otherwise),}$$

it can be shown that:

$$\bar{K}(x) = -\sqrt{2\pi} \cdot U_\infty \cdot \alpha [J_0(\lambda) - i J_1(\lambda)] .$$

Thus:

$$C_{LD} = U_\infty \alpha \int_{-\infty}^\infty [-J_0(\lambda) + i J_1(\lambda)] C_{LD}'(\lambda) d\lambda .$$

Substituting for $C_{LD}' = \pi \hat{J}_\infty / U_\infty e^{i\omega t} \{B_E(\lambda) + B_O(\lambda)\}$

and for $\hat{J}_\infty = ik_2 \hat{v}_1 - ik_1 \hat{v}_2$,

yields the final result:

$$C_{LD} = \alpha 2\pi D(k_1, k_2) \left\{ k_1 \frac{\hat{v}_2}{U_\infty} - k_2 \frac{\hat{v}_1}{U_\infty} \right\} e^{i\omega t} ,$$

where $D(k_1, k_2) = \int_0^\infty [i J_0(\lambda) B_E(\lambda) + J_1(\lambda) B_O(\lambda)] d\lambda .$

[An analytical solution to this integral has only been found for the term of $B_E(\lambda)$ which contains the function, $\delta(\lambda)$ (see previous table).

The value of $D(k_1, k_2)$ for this term is:

$$\frac{\pi}{2} k_1 k_2 / [k_1^2 + k_2^2] \cdot S(k_1) .$$

$\bar{B}_E(\lambda)$ is used to denote the function which is $B_E(\lambda)$ without the $\delta(\lambda)$ term]

APPENDIX 5

Analysis for L_D : Non-frozen Two Dimensional Gust

For this case, the linearized vorticity transport equation is:

$$iU_\infty(k_f - k_s)\hat{\zeta} + U_\infty \frac{\partial \hat{\zeta}}{\partial x} = ik_s V_1' \hat{\zeta}_\infty + ik_2 V_2' \hat{\zeta}_\infty ;$$

that is, a first order linear differential equation in $\hat{\zeta}$.

(1) Analysis with the method of the frozen gust theory (Appendix 4)

By inspection, the complementary function of the solution to the above equation is:

$$\hat{\zeta} = G_1 e^{-i(k_f - k_s)x} \quad \text{where } G_1 \text{ is a constant.}$$

A particular integral can be established when V_1' and V_2' are known. Following the previous analysis, $K'(x) = e^{-i\lambda x}$ is considered first. The corresponding expressions for V_1' and V_2' have been derived in Appendix 4. These expressions suggest the following form for the particular integral:

$$\hat{\zeta} = \begin{cases} G_2 e^{-i\lambda x} e^{\pm\lambda y} & , \lambda > 0 \\ G_2 e^{-i\lambda x} e^{\mp\lambda y} & , \lambda < 0. \end{cases}$$

Substituting these into above differential equation leads to an evaluation of G_2 :

$$G_2 = \begin{cases} \frac{\hat{\zeta}_\infty}{2U_\infty} \left(\frac{\pm k_s + ik_2}{k_f - k_s - \lambda} \right) & , \lambda > 0 \\ \frac{\hat{\zeta}_\infty}{2U_\infty} \left(\frac{\pm k_s - ik_2}{k_f - k_s - \lambda} \right) & , \lambda < 0. \end{cases}$$

The overall solution is

$$\hat{J} = \begin{cases} G_1 e^{-i(k_f - k_s)x} + G_2 e^{-i\lambda x} e^{\pm\lambda y} & , \lambda > 0 \\ G_1 e^{-i(k_f - k_s)x} + G_2 e^{-i\lambda x} e^{\mp\lambda y} & , \lambda < 0. \end{cases}$$

As usual, G_1 is evaluated by applying a boundary condition to \hat{J} . In the previous frozen gust theory, the boundary condition was effectively $\hat{J} = 0$ at $x = -\infty$. However the above general solution for \hat{J} is indeterminate when $x = -\infty$, and so G_1 can not be evaluated. Note that, at $x = -\infty$, the complementary function will be indeterminate, irrespective of the particular integral. In other words, this problem will occur for a non-frozen gust in any flow field to which the above linearized vorticity transport equation can be applied.

(2) Analysis with altered upstream boundary condition

An explicit solution for \hat{J} is readily obtained if the boundary condition is altered to: $\hat{J} = 0$ at $x = -B$ where B is finite. Then:

$$G_1 = -G_2 e^{iB(\lambda - k_f + k_s)} e^{\pm\lambda y} , \lambda > 0. \quad (e^{\mp\lambda y} \text{ when } \lambda < 0)$$

and the solution for \hat{J} is:

$$\frac{\hat{J}(x,y)}{\frac{\hat{J}_0}{2(\lambda - k_f + k_s)U_\infty}} \begin{cases} \mp k_s e^{\pm\lambda y - i\lambda x} \pm k_s e^{\pm\lambda y} e^{iB(\lambda - k_f - k_s)} e^{-i(k_f - k_s)x} - ik_2 e^{\pm\lambda y - i\lambda x} \\ \quad + ik_2 e^{\pm\lambda y} e^{iB(\lambda - k_f - k_s)} e^{-i(k_f - k_s)x} & \lambda > 0 \\ \mp k_s e^{\mp\lambda y - i\lambda x} \pm k_s e^{\mp\lambda y} e^{iB(\lambda - k_f - k_s)} e^{-i(k_f - k_s)x} + ik_2 e^{\mp\lambda y - i\lambda x} \\ \quad - ik_2 e^{\mp\lambda y} e^{iB(\lambda - k_f - k_s)} e^{-i(k_f - k_s)x} & \lambda < 0 \end{cases}$$

The analysis now proceeds exactly along the lines of Appendix 4. The final result is:

$$C_{LD} = \alpha 2\pi D'(k_f, k_s, k_z, B) \left\{ k_1 \frac{\hat{v}_1}{U_\infty} - k_2 \frac{\hat{v}_2}{U_\infty} \right\} e^{i\omega t} ,$$

where $D'(k_f, k_s, k_z, B) = \int_0^{\infty} [i J_0(\lambda) B'_E(\lambda) + J_1(\lambda) B'_O(\lambda)] d\lambda$.

$B'_E(\lambda)$ is given by:

λ range	$B'_E(\lambda)$
0 to $+k_1$	$+ \frac{1}{(\lambda - k_f - k_s)} \frac{(k_s + \lambda) k_z S'(k_f, k_s + \lambda)}{[(k_s + 2\lambda)^2 + k_z^2]} - \frac{S(k_f)}{2} b_E(\lambda)$
$+k_1$ to $+\infty$	$+ \frac{1}{(\lambda - k_f - k_s)} \frac{(k_s + \lambda) k_z S'(k_f, k_s + \lambda)}{[(k_s + 2\lambda)^2 + k_z^2]} - \frac{1}{(-\lambda - k_f + k_s)} \frac{(k_s - \lambda) k_z S'(k_f, k_s - \lambda)}{[(k_s - 2\lambda)^2 + k_z^2]} - \frac{S(k_f)}{2} b_E(\lambda)$

where
$$b_E(\lambda) = \frac{e^{iB(\lambda - k_f + k_s)} k_z (k_f + k_s + \lambda)}{(\lambda - k_f + k_s) [(k_f + \lambda)^2 + k_z^2]} * \frac{e^{iB(-\lambda - k_f + k_s)} k_z (k_f - k_s + \lambda)}{(-\lambda - k_f + k_s) [(k_f + \lambda)^2 + k_z^2]}$$

$B'_O(\lambda)$ differs from $B'_E(\lambda)$ only in that the signs indicated by: * are changed to +.

This solution with $\hat{J} = 0$ at $x = -B$ is denoted as Solution A.

(3) Solution B. In the frozen gust analysis (Appendix 4), $\int_{-\infty}^x \frac{V'_2}{U_{\infty}} dx'$ was calculated as:

$$\int_0^x \frac{V'_2}{U_{\infty}} dx' + \int_{-\infty}^0 \frac{V'_2 - V'_2(y=0)}{U_{\infty}} dx' \quad (\text{refer also to } 6.3.3.2)$$

It was decided to repeat the above analysis with an equivalent change of time origin to $\hat{J}(x, y)$. In the original analysis, the effect of this adjustment was to add the following extra term to the expression for \hat{J} :

$$- \frac{\hat{J}_{\infty}}{2} \frac{ik_z}{\lambda} \int_{-\infty}^0 \frac{V'_2(y=0)}{U_{\infty}} dx'$$

Thus, in the present analysis, an equivalent adjustment to \hat{y} is:

$$-\frac{\hat{y}_{\infty}}{2} \cdot \frac{ik_2}{\lambda} \int_{-B}^0 \frac{V_2'(y=0)}{U_{\infty}} dx'$$

which approaches the former adjustment as $B \rightarrow \infty$. The latter simplifies to:

$$\begin{cases} +\frac{\hat{y}_{\infty}}{2U_{\infty}} \cdot \frac{ik_2}{\lambda} [1 - e^{i\lambda B}] & , \lambda > 0. \\ -\frac{\hat{y}_{\infty}}{2U_{\infty}} \cdot \frac{ik_2}{\lambda} [1 - e^{i\lambda B}] & , \lambda < 0. \end{cases}$$

The resultant additional terms to $B'_E(\lambda)$ and $B'_O(\lambda)$ are respectively:

$$-\left[\frac{1}{\lambda} - \frac{\cos\lambda B}{\lambda}\right] \cdot \frac{k_1 k_2}{[k_1^2 + k_2^2]} S(k_1) \quad ; \quad i \frac{\sin\lambda B}{\lambda} \cdot \frac{k_1 k_2}{[k_1^2 + k_2^2]} S(k_1)$$

This adjusted solution with $\hat{y} = 0$ at $x = -B$ is denoted as Solution B.

(4) Comparison of solutions. Solutions A and B were compared over a wide range of the value, B, for both frozen and non-frozen gusts.

The following response function was computed:

$$R_D = \frac{C_{LD}^*}{2\pi\alpha E} e^{-i\omega t} \quad \text{where } C_{LD}^* \text{ is the complex conjugate of } C_{LD}.$$

The computer program used in the calculation was similar to that employed for the turbomachine application (section 6.7.4), described in Appendix 11.

In figure 43, R_D values corresponding to $k_s = 1.0$ and $k_2 = 0.6$ are plotted. For the non-frozen gust case, a k_f value of 4.0 was employed; while, for the frozen gust, $k_f = k_s = 1.0$.

(a) Frozen gust. As B becomes large, Solution B tends to the correct frozen gust solution for $B = \infty$ (that is, the original solution); while Solution A becomes singular (the imaginary part $\rightarrow -\infty$). This is expected, as Solution B was derived with equivalence to the

original theory in mind.

(b) Non-frozen gust. As B becomes large, Solution A tends to a definite non-zero limit; while solution B becomes singular in the opposite sense to the above case (the imaginary part $\rightarrow +\infty$). Thus it is clear that the time origin change required in the original analysis to avoid the singularity arising from: $V_2' \sim \frac{1}{x}$ as $x \rightarrow -\infty$, is not necessary for the non-frozen gust case (In fact, its use actually introduces a singularity into the solution). In other words, the gust phase change during convection from $y = -\infty$ to the aerofoil is only infinite when $k_f = k_s$. There is a mathematical explanation of this trend. In the frozen gust analysis, the singularity arose at $\lambda = 0$ because the integrand (for the integration with respect to λ) had a factor $\frac{1}{\lambda}$. In the present analysis, the equivalent factor is $\frac{1}{(\lambda - k_f + k_s)}$ and this will only lead to a singularity in the integral when $\lambda = 0$ and $k_f = k_s$. (No integral singularity occurs when $\lambda - k_f + k_s = 0$ but $\lambda \neq 0$).

It should be noted that the time required for a numerical computation of the non-frozen gust response, C_{LD} , increases rapidly with increasing B , as a result of the fact that the required integration step size must be made smaller for larger B .

From figure 43, it is also evident that:

(1) for the frozen gust, the effect of distortion decreases as $B \rightarrow 0$. This is expected as the $\hat{y} = 0$ boundary condition is being applied nearer to the aerofoil.

(2) for the non-frozen gust (with $k_f/k_s = 4.0$) the distortion effect is smaller than for the frozen gust, and it is less dependent on B . This can be explained by using the fact that a non-frozen gust being convected at U_∞ is analogous to a frozen gust being convected at $\frac{k_f}{k_s} \cdot U_\infty$. It is expected that the latter gust will be distorted less by the mean streamlines when it is being convected at a higher velocity than the mean stream; that is, it is expected that the

distortion will be reduced when k_f/k_s is increased from 1.0 to 4.0.

APPENDIX 6

The Detailed Analysis for L_D : Three Dimensional Gust Theory.

This analysis closely follows the form of the two-dimensional analysis presented in Appendix 4, and employs a number of intermediate results derived therein.

The integrated linearized vorticity transport equations, in this case, are:

$$\hat{J}_1 = \left\{ ik_1 \int_{-\infty}^x \frac{V_1'}{U_\infty} dx' + ik_2 \int_{-\infty}^x \frac{V_2'}{U_\infty} dx' + \frac{V_1'}{U_\infty} \right\} \hat{J}_{1\infty} + \frac{V_2'}{U_\infty} \hat{J}_{2\infty}$$

$$\hat{J}_3 = \left\{ ik_1 \int_{-\infty}^x \frac{V_1'}{U_\infty} dx' + ik_2 \int_{-\infty}^x \frac{V_2'}{U_\infty} dx' \right\} \hat{J}_{3\infty} ,$$

$$\text{where } \int_{-\infty}^x \frac{V_2'}{U_\infty} dx' \text{ is again calculated as } \int_0^x \frac{V_2'}{U_\infty} dx' + \int_{-\infty}^0 \frac{V_2' - V_2'(y=0)}{U_\infty} dx' .$$

The mean flow field, $K'(x) = e^{-i\lambda x}$, is considered first.

Corresponding expressions for V_1' , V_2' , $\int_{-\infty}^x \frac{V_1'}{U_\infty} dx'$ and $\int_{-\infty}^x \frac{V_2'}{U_\infty} dx'$ have been derived in Appendix 4. Thus, expressions for \hat{J}_1 and \hat{J}_3 are obtained by simple substitution.

The extra upwash due to distortion, $\tilde{v}_2(x, 0, z)$, is determined by the Biot-Savart Law in the following form:

$$\tilde{v}_2(x, 0, z) = \frac{1}{4\pi} \iiint_{-\infty}^{\infty} \frac{\tilde{J}_3(x', y', z') (x-x') dx' dy' dz'}{[(x-x')^2 + y'^2 + (z-z')^2]^{\frac{3}{2}}} - \frac{1}{4\pi} \iiint_{-\infty}^{\infty} \frac{\tilde{J}_1(x', y', z') (z-z') dx' dy' dz'}{[(x-x')^2 + y'^2 + (z-z')^2]^{\frac{3}{2}}} .$$

Upon substituting for $\tilde{J}_3(x', y', z')$ and $\tilde{J}_1(x', y', z')$, the terms in $\tilde{v}_2(x, 0, z)$ are of the form:

$$\frac{e^{i\omega t}}{8\pi U_\infty} \iiint_{-\infty}^{\infty} \frac{C_3(y') e^{-ik_2 y'} e^{-ik_1 x'} e^{-ik_3 z'} (x-x') dx' dy' dz'}{[(x-x')^2 + y'^2 + (z-z')^2]^{\frac{3}{2}}}$$

or:

$$-\frac{e^{i\omega t}}{8\pi U_\infty} \iiint_{-\infty}^{\infty} \frac{C_1(y') e^{-ik_2 y'} e^{-ik_1 x'} e^{-ik_3 z'} (z-z') dx' dy' dz'}{[(x-x')^2 + y'^2 + (z-z')^2]^{\frac{3}{2}}}$$

The individual values for $C_1(y')$, $C_3(y')$ and the corresponding K are as follows:

K	$C_1(y')$		$C_3(y')$	
	$\lambda > 0$	$\lambda < 0$	$\lambda > 0$	$\lambda < 0$
$k_1 + \lambda$	$\mp k_1 \lambda e^{\pm \lambda y'} \hat{J}_{100}$	$\mp k_1 \lambda e^{\mp \lambda y'} \hat{J}_{100}$	$\mp k_1 \lambda e^{\pm \lambda y'} \hat{J}_{300}$	$\mp k_1 \lambda e^{\mp \lambda y'} \hat{J}_{300}$
k_1	$\pm i k_1 \pi \delta(\lambda) \hat{J}_{100}$	$\pm i k_1 \pi \delta(\lambda) \hat{J}_{100}$	$\pm i k_1 \pi \delta(\lambda) \hat{J}_{300}$	$\pm i k_1 \pi \delta(\lambda) \hat{J}_{300}$
$k_1 + \lambda$	$-i k_2 \lambda e^{\pm \lambda y'} \hat{J}_{100}$	$+i k_2 \lambda e^{\mp \lambda y'} \hat{J}_{100}$	$-i k_2 \lambda e^{\pm \lambda y'} \hat{J}_{300}$	$+i k_2 \lambda e^{\mp \lambda y'} \hat{J}_{300}$
k_1	$+i k_2 \lambda \hat{J}_{100}$	$-i k_2 \lambda \hat{J}_{100}$	$+i k_2 \lambda \hat{J}_{300}$	$-i k_2 \lambda \hat{J}_{300}$
$k_1 + \lambda$	$\pm e^{\pm \lambda y'} \hat{J}_{100}$	$\pm e^{\mp \lambda y'} \hat{J}_{100}$		
$k_1 + \lambda$	$+i e^{\pm \lambda y'} \hat{J}_{200}$	$-i e^{\mp \lambda y'} \hat{J}_{200}$		

The double integrals:

$$I_1 = \iint_{-\infty}^{\infty} \frac{e^{-iKx'} e^{-ik_3 z'} (z-z')}{[(x-x')^2 + y'^2 + (z-z')^2]^{\frac{3}{2}}} dx' dz' ; \quad I_2 = \iint_{-\infty}^{\infty} \frac{e^{-iKx'} e^{-ik_3 z'} (x-x')}{[(x-x')^2 + y'^2 + (z-z')^2]^{\frac{3}{2}}} dx' dz'$$

can be evaluated analytically. In fact, as inspection of the above integrals indicates, I_2 can be obtained directly from the result for I_1 by interchanging k_3 and K . Consider the evaluation of I_1 :

The substitutions $X = x - x'$ and $Z = z - z'$ are made as

usual:

$$I_1 = e^{-iKx} e^{-ik_3 z} \iint_{-\infty}^{\infty} \frac{e^{iKX} e^{ik_3 Z} Z dZ dX}{[X^2 + y'^2 + Z^2]^{\frac{3}{2}}}$$

Using the standard integral result:

$$\int_0^{\infty} \frac{\sin k_3 Z \cdot Z \cdot dZ}{[A^2 + Z^2]^{\frac{3}{2}}} = k_3 K_0(k_3 A)$$

I_1 becomes:

$$I_1 = 2i e^{-iKx} e^{-ik_3 z} k_3 \int_{-\infty}^{\infty} K_0[k_3 \sqrt{X^2 + y'^2}] e^{iKX} dX \quad \text{for all } k_3 .$$

And using the further standard result:

$$\int_0^{\infty} K_0[k_3 \sqrt{X^2 + y'^2}] \cos KX dX = \frac{\pi}{2} \frac{1}{\sqrt{K^2 + k_3^2}} e^{-\sqrt{K^2 + k_3^2} y'} , \quad \text{if } \underline{k_3} > 0, y' > 0. ,$$

yields:

$$I_1 = i 2\pi \frac{k_3}{\sqrt{k_3^2 + K^2}} e^{-iKx} e^{-ik_3 z} e^{\pm \sqrt{k_3^2 + K^2} y'} , \quad \text{for all } k_3 \text{ and } K ,$$

and thus:

$$I_2 = i 2\pi \frac{K}{\sqrt{k_3^2 + K^2}} e^{-iKx} e^{-ik_3 z} e^{\pm \sqrt{k_3^2 + K^2} y'} , \quad \text{for all } k_3 \text{ and } K .$$

Using these results, the terms in $\tilde{v}_2(x,0,z)$ reduce to the form

$$\frac{i e^{i\omega t} e^{-iKx} e^{-ik_3 z}}{4U_\infty} \int_{-\infty}^{\infty} D e^{\pm E y'} e^{-ik_1 y'} dy' \quad \text{where } E > 0.$$

This form was also obtained in the two-dimensional analysis (Appendix 4) where it was shown that the integral has the values:

$$2i |D| \frac{k_2}{E^2 + k_2^2} \quad \text{if the sign of } D \text{ is } \pm .$$

$$2 |D| \frac{E}{E^2 + k_2^2} \quad \text{if the sign of } D \text{ is } + .$$

Thus an analytical formula for $\tilde{v}_2(x,0,z)$ evolves. It is noteworthy that only two different ranges of λ need be considered: $\lambda > 0$ and $\lambda < 0$; whereas the two dimensional case was more complicated. However, in this case, the extra complications are contained within the algebraic expressions by virtue of the involvement of square root terms. For example:

$$\sqrt{k^2 - K} = \begin{cases} 0, & \text{if } K > 0 \\ 2K, & \text{if } K < 0 \end{cases} \quad \text{or: } \frac{K}{\sqrt{k^2 - K}} = \begin{cases} 1, & \text{if } K > 0 \\ -1, & \text{if } K < 0 . \end{cases}$$

In fact, careful inspection of the present analysis reveals that, when $k_3 = 0$, it is equivalent to the two-dimensional analysis of Appendix 4.

The terms of $\tilde{v}_2(x,0,z)$ are given in the following tables in the form:

$$\tilde{v}_2(x,0,z) / \frac{1}{2} \frac{\hat{J}_{i\omega}}{U_\infty} e^{i(\omega t - k_1 x - k_3 z)} , \quad \text{(over)}$$

with $Q = \sqrt{k_3^2 + (k_1 + \lambda)^2}$:

Terms in $\hat{J}_{1\infty}$	
$\lambda > 0$	$\lambda < 0$
$\frac{1}{\lambda} \frac{k_1 k_2 k_3 e^{-i\lambda x}}{Q[(Q+\lambda)^2 + k_2^2]}$	$-\frac{1}{\lambda} \frac{k_1 k_2 k_3 e^{-i\lambda x}}{Q[(Q-\lambda)^2 + k_2^2]}$
$+\frac{i k_1 k_2 k_3 \pi \delta(\lambda)}{\sqrt{k_3^2 + k_1^2} [k_1^2 + k_2^2 + k_3^2]}$	$+\frac{i k_1 k_2 k_3 \pi \delta(\lambda)}{\sqrt{k_3^2 + k_1^2} [k_1^2 + k_2^2 + k_3^2]}$
$\frac{1}{\lambda} \frac{k_2 k_3 (Q+\lambda) e^{-i\lambda x}}{Q[(Q+\lambda)^2 + k_2^2]}$	$+\frac{1}{\lambda} \frac{k_2 k_3 (Q-\lambda) e^{-i\lambda x}}{Q[(Q-\lambda)^2 + k_2^2]}$
$+\frac{1}{\lambda} \frac{k_2 k_3}{[k_1^2 + k_2^2 + k_3^2]}$	$-\frac{1}{\lambda} \frac{k_2 k_3}{[k_1^2 + k_2^2 + k_3^2]}$
$+\frac{k_2 k_3 e^{-i\lambda x}}{Q[(Q+\lambda)^2 + k_2^2]}$	$+\frac{k_2 k_3 e^{-i\lambda x}}{Q[(Q-\lambda)^2 + k_2^2]}$

Term in $\hat{J}_{2\infty}$	
$\lambda > 0$	$\lambda < 0$
$+\frac{k_3 (Q+\lambda) e^{-i\lambda x}}{Q[(Q+\lambda)^2 + k_2^2]}$	$-\frac{k_3 (Q-\lambda) e^{-i\lambda x}}{Q[(Q-\lambda)^2 + k_2^2]}$

Terms in $\hat{J}_{3\infty}$	
$\lambda > 0$	$\lambda < 0$
$+\frac{1}{\lambda} \frac{k_1 (k_1 + \lambda) k_2 e^{-i\lambda x}}{Q[(Q+\lambda)^2 + k_2^2]}$	$+\frac{1}{\lambda} \frac{k_1 (k_1 + \lambda) k_2 e^{-i\lambda x}}{Q[(Q-\lambda)^2 + k_2^2]}$
$\frac{i k_1^2 k_2 \pi \delta(\lambda)}{\sqrt{k_3^2 + k_1^2} [k_1^2 + k_2^2 + k_3^2]}$	$\frac{i k_1^2 k_2 \pi \delta(\lambda)}{\sqrt{k_3^2 + k_1^2} [k_1^2 + k_2^2 + k_3^2]}$
$+\frac{1}{\lambda} \frac{(k_1 + \lambda) k_2 (Q+\lambda) e^{-i\lambda x}}{Q[(Q+\lambda)^2 + k_2^2]}$	$-\frac{1}{\lambda} \frac{(k_1 + \lambda) k_2 (Q-\lambda) e^{-i\lambda x}}{Q[(Q-\lambda)^2 + k_2^2]}$
$-\frac{1}{\lambda} \frac{k_1 k_2}{[k_1^2 + k_2^2 + k_3^2]}$	$+\frac{1}{\lambda} \frac{k_1 k_2}{[k_1^2 + k_2^2 + k_3^2]}$

The terms in $\tilde{v}_2(x, 0, z)$ are of two basic forms:

$$(1) \hat{v}_2 e^{i(\omega t - k_1 x - k_3 z)} \quad ; \quad (2) \hat{v}_2 e^{i(\omega t - [k_1 + \lambda]x - k_3 z)}$$

The lift responses to the two upwashes are, respectively:

$$(1) C_{LD}' = 2\pi G(k_1, k_3) \frac{\hat{v}_2}{U_\infty} e^{i(\omega t - k_3 z)} \quad ; \quad (2) C_{LD}' = 2\pi G'(k_1, k_1 - \lambda, k_3) \frac{\hat{v}_2}{U_\infty} e^{i(\omega t - k_3 z)}$$

(refer 1.2.2)

Thus the complete C_{LD}' response can be written down from the previous tables for $\tilde{v}_2(x, 0, z)$. The final lift response is given by:

$$C_{LD} = U_\infty \alpha \int_{-\infty}^{\infty} [-J_0(\lambda) + iJ_1(\lambda)] C_{LD}'(\lambda) d\lambda \quad . \quad (\text{refer Appendix 4})$$

Again C_{LD} is split into its odd and even parts, and the final result is

$$C_{LD} = \alpha 2\pi \left\{ F_1(k_1, k_2, k_3) \frac{\hat{U}_1}{U_\infty} + F_2(k_1, k_2, k_3) \frac{\hat{U}_2}{U_\infty} + F_3(k_1, k_2, k_3) \frac{\hat{U}_3}{U_\infty} \right\} e^{i\omega t},$$

where each F_i is of the form:

$$\int_0^\infty [\dot{L} J_0(\lambda) E_i(k_1, k_2, k_3, \lambda) + J_1(\lambda) O_i(k_1, k_2, k_3, \lambda)] d\lambda.$$

The terms containing the function, $\delta(\lambda)$, can be evaluated

analytically and the form of F_i becomes

$$F_i = \int_0^\infty [\dot{L} J_0(\lambda) E'_i(k_1, k_2, k_3, \lambda) + J_1(\lambda) O'_i(k_1, k_2, k_3, \lambda)] d\lambda + d_i(k_1, k_2, k_3).$$

where:

$$E'_1(k_1, k_2, k_3, \lambda) = -k_3 V_E(\lambda) + k_2 W_E(\lambda) + k_1 B(\lambda)$$

$$O'_1(k_1, k_2, k_3, \lambda) = -k_3 V_0(\lambda) + k_2 W_0(\lambda)$$

$$E'_2(k_1, k_2, k_3, \lambda) = +k_3 U_E(\lambda) - k_1 W_E(\lambda) + k_2 A(\lambda) - k_1 B(\lambda)$$

$$O'_2(k_1, k_2, k_3, \lambda) = +k_3 U_0(\lambda) - k_1 W_0(\lambda)$$

$$E'_3(k_1, k_2, k_3, \lambda) = -k_2 U_E(\lambda) + k_1 V_E(\lambda) - k_1 A(\lambda)$$

$$O'_3(k_1, k_2, k_3, \lambda) = -k_2 U_0(\lambda) + k_1 V_0(\lambda),$$

and:

$$U_E(\lambda) = \frac{1}{2\lambda} \frac{k_2 k_3 (Q + k_1) G'(k_1, k_1 + \lambda, k_3)}{Q[(Q + \lambda)^2 + k_2^2]} +^* \frac{1}{2\lambda} \frac{k_2 k_3 (Q' - k_1) G'(k_1, k_1 - \lambda, k_3)}{Q'[(Q' + \lambda)^2 + k_2^2]}$$

$$V_E(\lambda) = -\frac{k_3 (Q + \lambda) G'(k_1, k_1 + \lambda, k_3)}{2Q[(Q + \lambda)^2 + k_2^2]} +^* \frac{k_3 (Q' + \lambda) G'(k_1, k_1 - \lambda, k_3)}{2Q'[(Q' + \lambda)^2 + k_2^2]}$$

$$W_E(\lambda) = \frac{1}{2\lambda} \frac{(k_1 + \lambda) k_2 [Q + (k_1 + \lambda)] G'(k_1, k_1 + \lambda, k_3)}{Q[(Q + \lambda)^2 + k_2^2]} +^* \frac{1}{2\lambda} \frac{(k_1 - \lambda) k_2 [Q' - (k_1 + \lambda)] G'(k_1, k_1 - \lambda, k_3)}{Q'[(Q' + \lambda)^2 + k_2^2]}$$

$$\text{where } Q = \sqrt{k_3^2 + (k_1 + \lambda)^2} \quad ; \quad Q' = \sqrt{k_3^2 + (k_1 - \lambda)^2}.$$

$U_0(\lambda)$, $V_0(\lambda)$, and $W_0(\lambda)$ are obtained by changing the signs marked * in the above expressions for $U_E(\lambda)$, $V_E(\lambda)$, and $W_E(\lambda)$ respectively.

$$\text{Also: } A(\lambda) = -\frac{1}{\lambda} \frac{k_2 k_3 G(k_1, k_3)}{[k_1^2 + k_2^2 + k_3^2]} \quad \text{and} \quad B(\lambda) = \frac{1}{\lambda} \frac{k_1 k_2 G(k_1, k_3)}{[k_1^2 + k_2^2 + k_3^2]}$$

$$\text{and } d_1(\lambda) = -\frac{\pi}{2} \frac{k_1^2 k_2^2 G(k_1, k_2)}{\sqrt{k_3^2 + k_1^2} [k_1^2 + k_2^2 + k_3^2]}, \quad d_2(\lambda) = +\frac{\pi}{2} \frac{k_1 k_2 \sqrt{k_2^2 + k_1^2} G(k_1, k_3)}{[k_1^2 + k_2^2 + k_3^2]},$$

$$d_3(\lambda) = -\frac{\pi}{2} \frac{k_2^2 k_1 k_3 G(k_1, k_3)}{\sqrt{k_3^2 + k_1^2} [k_1^2 + k_2^2 + k_3^2]}.$$

This solution for C_{LD} reduces to the two-dimensional result (Appendix 4) when $k_3 = 0$, although this reduction is not immediately obvious (Refer to earlier note in this appendix).

APPENDIX 7

Details of the Theoretical Admittance to Higher Order

The relevant admittance equation is (in tensor notation):

$$|A(k_i)|^2 = \frac{55}{6\pi} \frac{1}{\delta^2 (3+8k_i^{*2})} \int_{-\infty}^{\infty} \frac{\sin^2 k_3 a}{(k_3 a)^2} \cdot R_i^* R_j \frac{k^{*2}}{(1+k^{*2})^{1/2}} \left\{ \delta_{ij} - \frac{k_i^* k_j^*}{k^{*2}} \right\} dk_2 dk_3,$$

$$\text{where } \delta = \frac{\Gamma(\frac{1}{2}) \Gamma(\frac{5}{6})}{\Gamma(\frac{1}{3})} \frac{c}{2} L_1 \quad \text{and} \quad k_i^* = k_i / \delta.$$

R_i are the sinusoidal gust response functions; viz,

$$C_L = 2\pi R_i \hat{w}_i / U_0 e^{i\omega t}.$$

Let:

$$X = R_i^* R_j \frac{k^{*2}}{(1+k^{*2})^{1/2}} \left\{ \delta_{ij} - \frac{k_i^* k_j^*}{k^{*2}} \right\}.$$

Expanding the right hand side, and using the facts that:

$$R_1^* R_2 + R_2^* R_1 = 2 \operatorname{Re}(R_1 R_2^*), \text{ etc.}; \quad R_i^* R_i = |R_i|^2, \text{ etc.}$$

yields:

$$X = |R_1|^2 \frac{k_1^{*2} + k_3^{*2}}{(1+k^{*2})^{1/2}} + |R_2|^2 \frac{k_1^{*2} + k_3^{*2}}{(1+k^{*2})^{1/2}} + |R_3|^2 \frac{k_1^{*2} + k_2^{*2}}{(1+k^{*2})^{1/2}} \\ + 2 \operatorname{Re}(R_1 R_2^*) \frac{-k_1^* k_2^*}{(1+k^{*2})^{1/2}} + 2 \operatorname{Re}(R_2 R_3^*) \frac{-k_2^* k_3^*}{(1+k^{*2})^{1/2}} + 2 \operatorname{Re}(R_1 R_3^*) \frac{-k_1^* k_3^*}{(1+k^{*2})^{1/2}}.$$

Now, to order ($\alpha \epsilon$) and with the Mugridge approximation for the higher order terms, the response functions are:

$$R_1 = \alpha G_M(k_1, k_3) + \alpha F_1(k_1, k_2, k_3) + \alpha M(k_1)$$

$$R_2 = G(k_1, k_3) + \alpha G_{MA}(k_1, k_2, k_3) + \alpha F_2(k_1, k_2, k_3)$$

$$R_3 = \alpha F_3(k_1, k_2, k_3)$$

Thus:

$$|R_1|^2 = \alpha^2 |G_M|^2 + \alpha^2 |F_1|^2 + \alpha^2 |M|^2 + \alpha^2 2 \operatorname{Re}(G_M M^*) + \alpha^2 2 \operatorname{Re}(G_M F_1^*) + \alpha^2 2 \operatorname{Re}(F_1 M^*).$$

$$|R_2|^2 = |G|^2 + \alpha^2 |G_{MA}|^2 + \alpha^2 |F_2|^2 + \alpha^2 2 \operatorname{Re}(G G_{MA}^*) + \alpha^2 2 \operatorname{Re}(G F_2^*) + \alpha^2 2 \operatorname{Re}(G_{MA} F_2^*).$$

$$|R_3|^2 = \alpha^2 |F_3|^2.$$

$$\operatorname{Re}(R_1 R_2^*) = \alpha \operatorname{Re}(G_M G^*) + \alpha^2 \operatorname{Re}(G_M G_{MA}^*) + \alpha^2 \operatorname{Re}(G_M F_2^*) + \alpha \operatorname{Re}(F_1 G^*) + \alpha^2 \operatorname{Re}(F_1 G_{MA}^*) \\ + \alpha^2 \operatorname{Re}(F_1 F_2^*) + \alpha \operatorname{Re}(M G^*) + \alpha^2 \operatorname{Re}(M G_{MA}^*) + \alpha^2 \operatorname{Re}(M F_2^*).$$

$$\operatorname{Re}(R_2 R_3^*) = \alpha \operatorname{Re}(G F_3^*) + \alpha^2 \operatorname{Re}(G_{MA} F_3^*) + \alpha^2 \operatorname{Re}(F_2 F_3^*).$$

$$\operatorname{Re}(R_1 R_3^*) = \alpha^2 \operatorname{Re}(G_M F_3^*) + \alpha^2 \operatorname{Re}(F_1 F_3^*) + \alpha^2 \operatorname{Re}(M F_3^*).$$

Substituting these expressions into the above equation for X and multiplying by $\frac{\sin^2 k_3 a}{(k_3 a)^2}$, yields the required integrand for the admittance calculation. It can be seen that the integrand contains a term of order (1), six terms of order (α), and many others, all of order (α^2). Clearly any terms that are odd functions of either k_2 or k_3 will not contribute to the integral (and thus to $|A(k_1)|^2$).

The symmetry properties of the response functions are as follows:

$G(k_1, k_1)$ and $G_M(k_1, k_3)$ are independent of k_2 , even in k_3 .

$G_{MA}(k_1, k_1, k_3)$ is odd in k_2 , even in k_3 .

$F_1(k_1, k_2, k_3)$ is even in k_2 , even in k_3 .

$F_2(k_1, k_2, k_3)$ is odd in k_2 , even in k_3 .

$F_3(k_1, k_2, k_3)$ is even in k_2 , odd in k_3 .

$M(k_1)$ is independent of k_2 and k_3 .

Using these facts, the symmetry properties of the terms in the integrand,

$\frac{\sin^2 k_3 a}{(k_3 a)^2} \cdot X$, can be determined. It is found that:

(1) the terms of order (1) and order (α^2) are even in both k_2 and k_3 and thus contribute to the admittance.

(2) the terms of order (α) are all odd in k_2 , and thus do not contribute.

The order (α^2) contribution to the admittance can be written:

$$|A(k_1)|_{\alpha^2}^2 = \alpha^2 \frac{110}{3\pi} \cdot \frac{1}{\delta^2} \frac{(1+k_1^{*2})^{1/6}}{(3+8k_1^{*2})} \iint_0^\infty \frac{\sin^2 k_3 a}{(k_3 a)^2} \cdot I(k_1, k_2, k_3, \frac{L}{c}) dk_2 dk_3.$$

$I(k_1, k_2, k_3, \frac{L}{c})$ consists of the following 21 terms:

$$\begin{aligned} & \left[|G_M|^2 + |F_1|^2 + |M|^2 + 2 \operatorname{Re}(G_M M^*) + 2 \operatorname{Re}(G_M F_1^*) + 2 \operatorname{Re}(F_1 M^*) \right] \frac{k_2^{*2} + k_3^{*2}}{(1+k^{*2})^{1/6}} \\ & + \left[|G_{MA}|^2 + |F_2|^2 + 2 \operatorname{Re}(G_{MA} F_2^*) \right] \frac{k_1^{*2} + k_3^{*2}}{(1+k^{*2})^{1/6}} \\ & + \left[|F_3|^2 \right] \frac{k_1^{*2} + k_2^{*2}}{(1+k^{*2})^{1/6}} \end{aligned}$$

(continued over)

$$+ \left[2 \operatorname{Re}(G_M G_{MA}^*) + 2 \operatorname{Re}(G_M F_2^*) + 2 \operatorname{Re}(F_1 G_{MA}^*) + 2 \operatorname{Re}(F_1 F_2^*) \right. \\ \left. + 2 \operatorname{Re}(M G_{MA}^*) + 2 \operatorname{Re}(M F_2^*) \right] \frac{-k_1^* k_2^*}{(1+k^{*2})^{1/6}}$$

$$+ \left[2 \operatorname{Re}(G_{MA} F_3^*) + 2 \operatorname{Re}(F_2 F_3^*) \right] \frac{-k_2^* k_3^*}{(1+k^{*2})^{1/6}}$$

$$+ \left[2 \operatorname{Re}(G_M F_3^*) + 2 \operatorname{Re}(F_1 F_3^*) + 2 \operatorname{Re}(M F_3^*) \right] \frac{-k_1^* k_3^*}{(1+k^{*2})^{1/6}} .$$

Evaluation of the Integrals Arising in the Asymptotic Analysis

$$(1) \quad \iint_{-\infty}^{\infty} \frac{(1+k_3^2)}{(1+k_2^2+k_3^2)^{5/2}} dk_2 dk_3 = I_1, \text{ say.}$$

Substituting $k_2 = \tau \sin \theta$, $k_3 = \tau \cos \theta$ (i.e. changing to a polar co-ordinate system) gives:

$$I_1 = \int_0^{\infty} \int_0^{2\pi} \frac{(1+\tau^2 \cos^2 \theta) \tau}{(1+\tau^2)^{5/2}} d\tau d\theta.$$

Using the result that $\int_0^{2\pi} (1+\tau^2 \cos^2 \theta) d\theta = 2\pi + \tau^2 \pi$, I_1 simplifies to:

$$I_1 = \pi \int_0^{\infty} \frac{(2+\tau^2)}{(1+\tau^2)^{5/2}} \tau d\tau.$$

Putting $z = \tau^2$ gives:

$$I_1 = \frac{\pi}{2} \int_0^{\infty} \frac{2+z}{(1+z)^{5/2}} dz.$$

The following indefinite integral result is employed:

$$\int \frac{z}{Z^n} dz = \frac{1}{b^2} \left[\frac{-1}{(n-2)Z^{n-2}} + \frac{a}{(n-1)Z^{n-1}} \right] \text{ where } Z = a+bz.$$

With this result I_1 can be fully evaluated. The result is

$$I_1 = \pi \frac{48}{55}.$$

$$(2) \quad \iint_{-\infty}^{\infty} \frac{(k_2^2+k_3^2)}{(1+k_2^2+k_3^2)^{5/2}} dk_2 dk_3 = I_2, \text{ say.}$$

The same method as above is employed. Thereby:

$$\begin{aligned} I_2 &= \int_0^{\infty} \int_0^{2\pi} \frac{\tau^3}{(1+\tau^2)^{5/2}} d\tau d\theta = \pi \int_0^{\infty} \frac{z}{(1+z)^{5/2}} dz \\ &= \pi \frac{36}{55}. \end{aligned}$$

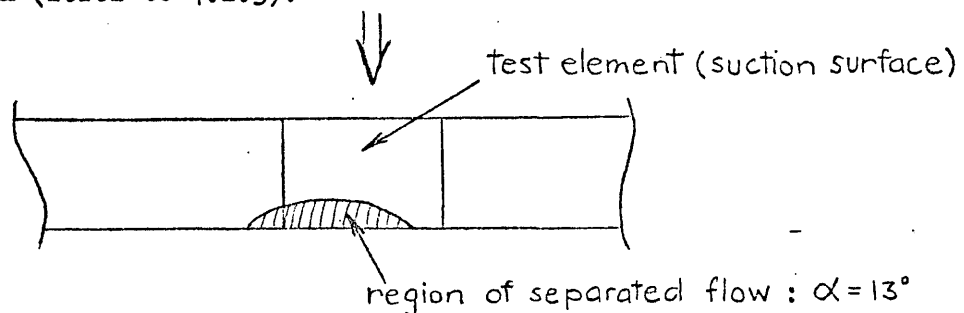
APPENDIX 9

Details of Buffet Test

The unsteady load on the test element (of the aerofoil described fully in Chapter 4) was measured with no grid present. The following set angles of incidence were employed: $\alpha = 0^\circ, 10^\circ, 13^\circ, 14^\circ$. The resultant lift coefficient spectra are presented in figure 50. The load measured was that perpendicular to the stream, but it must be noted that the load balance was, to a certain extent, sensitive to drag forces (refer to 4.2.2), and that these forces were significant at the two higher incidences.

The tests were conducted with a tunnel velocity of 76.0 ft/sec; that is, at a Reynolds Number of $0.23 \cdot 10^6$. The intensity of the background turbulence in the free tunnel was measured at 0.1%

The extent of flow separation at each of the set incidences was assessed by the tuft visualization technique. The stall type was determined to be of the combined leading edge-trailing edge type (refer to 2.2.4). At 0° and 10° there was no discernible flow separation. At 13° there was definite trailing edge separation. However this separation was not uniform across the span of the test element, probably as a result of the variation of effective incidence over the span (refer to 4.2.3):



Thus, for the flow measurement at $\alpha = 13^\circ$, the mean flow was not two dimensional. By $\alpha = 14^\circ$ the flow had separated from the leading edge right across the span.

The resonant loading peak, at about 780 Hz, has not been included in figure 50. The power in this peak was found to increase slightly from $\alpha = 0^\circ$ to $\alpha = 13^\circ$, but to then decrease somewhat with the complete stall ($\alpha = 14^\circ$).

Possible Contribution of Non Linear Terms to the Spectrum of Lift

In the sinusoidal gust theory of Chapter 6, higher order terms of order $(\alpha\epsilon)$ are derived, but the second order non linear terms in ϵ (that is, those of order (ϵ^2)) are ignored. When the order (ϵ^2) terms are retained in the analysis, it can be shown that the resultant lift response is of the form (in tensor notation):

$$C_L = \underbrace{\Omega_i \hat{v}_i e^{i\omega t}}_{O(\epsilon, \alpha\epsilon)} + \underbrace{\Lambda_{ij} \hat{v}_i \hat{v}_j^* e^{i2\omega t}}_{O(\epsilon^2)} \quad \dots (A-1)$$

(An attempt to evaluate the response function, Λ_{ij} , was not successful)

Because this is the response of a non-linear system, it is not possible to derive a simple relationship between the load spectrum and the velocity spectrum for a random turbulence input to this system (Admittance functions are defined only for linear systems). One question raised by the above equation is:

Can a response term at twice the frequency of the input contribute to the output spectrum? This question can be investigated, to some extent, by examination of a system with the following form of sinusoidal response:

$$C_L = \Omega_2 \hat{v}_2 e^{i\omega t} + \Lambda_2 \hat{v}_2 e^{i2\omega t}, \text{ for input } \hat{v}_2 e^{i(\omega t - k_1 x - k_2 y - k_3 z)} \quad \dots (A-2)$$

Such a system is a particular example of a time-varying linear system. The response (A-2) is roughly equivalent to the general non-linear response (A-1) when Ω_2 is of order (1) and Λ_2 is of order (ϵ) .

An input-output spectral relationship for this system has been derived using theory presented by Bendat and Piersol (1966). With their notation, the derivation is as follows:

The frequency response function, $H(f,t)$, for a time-varying

linear system is defined as follows:

For input $e^{i2\pi ft}$, the output is $H(f,t)e^{i2\pi ft}$.

In general, when the input to such a system is a stationary random process, the output will be a non-stationary random process. For non-stationary data, the double frequency spectrum is defined:

$$S_x(f_1, f_2) = \iint_{-\infty}^{\infty} R_x(t_1, t_2) e^{i2\pi(f_1 t_1 - f_2 t_2)} dt_1 dt_2$$

where $R_x(t_1, t_2)$ is the correlation function which, for a non-stationary process, depends on t_1 and t_2 , rather than the simple difference, $t_1 - t_2$.

With this definition, Bendat and Piersol derive the following equation for the output, $S_y(f_3, f_4)$, of a time-varying linear system when the input, $S_x(f_2)$, is that due to a stationary process:

$$S_y(f_3, f_4) = \int_{-\infty}^{\infty} S_x(f_2) \cdot J^*(f_2, f_2 - f_3) \cdot J(f_2, f_2 - f_4) \cdot df_2,$$

$$\text{where } J(f_1, f_2) = \int_{-\infty}^{\infty} H(f_1, t) e^{i2\pi f_2 t} dt.$$

For the particular time varying system which produces response (A - 2), $H(f, t)$ is of the form :

$$H(f, t) = H(f) + A(f) e^{i2\pi ft}$$

Substitution of this into the above input-output spectral equation yields:

$$\begin{aligned} S_y(f_3, f_4) = S_x(f_3) & \left[|H'(f_3)|^2 \cdot \delta(f_3 - f_4) + H' A^*(f_3) \delta(2f_3 - f_4) \right] \\ & + \frac{S_x(f_3)}{2} \left[A^* H'(f_3) \cdot \delta(f_3 - f_4) + |A(f_3)|^2 \delta(f_3 - f_4) \right]. \end{aligned}$$

From the form of this expression, it is clear that, in this particular case, S_y is a function of one frequency only. In other words, for this particular time-varying linear system, the output is a stationary process.

Integrating with respect to f_4 gives the final result:

$$S_y(f) = S_x(f) [|H'(f)|^2 + H'^* A(f)] + S_x\left(\frac{f}{2}\right) \left[\frac{1}{2} |A\left(\frac{f}{2}\right)|^2 + \frac{1}{2} A^* H'\left(\frac{f}{2}\right) \right].$$

Translating this result to the notation of this study and to the specific lift response of equation (A-2) gives:

$$\phi_{C_L}(\bar{k}_1) = \underbrace{\phi_{22}(\bar{k}_1)}_{O(\epsilon^2)} \left[\underbrace{|\Omega_2|^2}_{O(1)} + \underbrace{\Omega_2^* \Lambda_2}_{O(\epsilon)} \right] + \phi_{22}\left(\frac{\bar{k}_1}{2}\right) \left[\underbrace{\frac{1}{2} |\Lambda|^2}_{O(\epsilon^2)} + \underbrace{\frac{1}{2} \Lambda_2^* \Omega_2}_{O(\epsilon)} \right]$$

As may be expected, $\phi_{C_L}(\bar{k}_1)$ depends on ϕ_{22} at \bar{k}_1 and at $\bar{k}_1/2$.

Thus a sinusoidal response term at twice the frequency of the input can contribute to the lift spectrum. In fact, the above equation suggests that a non-linear response term, of order (ϵ^2), may contribute to the spectrum to order (ϵ^3).

APPENDIX 11

Computer Programs

Four programs are listed in this appendix. The programs and their functions are:

- (1) ADMITL. This computes the first order theoretical admittance via the equation:

$$|A(k_1)|^2 = \frac{4}{c} \int_0^{\infty} \frac{\sin^2 k_3 a}{(k_3 a)^2} |G(k_1, k_3)|^2 \bar{S}_{22}(k_1, k_3) dk_3 \quad \dots (1.17)$$

- (2) TORT 2. This computes the higher order, two-dimensional sinusoidal gust response via:

$$R = -\frac{k_2}{\sqrt{k_1^2 + k_2^2}} S^*(k_1) + \frac{k_1}{\sqrt{k_1^2 + k_2^2}} S_A^*(k_1, k_2) + \sqrt{k_1^2 + k_2^2} D^*(k_1, k_2) - \frac{k_2}{\sqrt{k_1^2 + k_2^2}} M^*(k_1) \quad (6.44)$$

where

$$D(k_1, k_2) = \int_0^{\infty} [i J_0(\lambda) B_E(\lambda) + J_1(\lambda) B_0(\lambda)] d\lambda \quad (6.40)$$

- (3) TORT 2I. This computes the non-frozen, two-dimensional sinusoidal gust response to order ($\alpha \epsilon$):

$$R' = R_S + R_A + R_M + R_D \quad \dots (6.50)$$

where

$$R_S = \frac{k_s}{\sqrt{k_s^2 + k_2^2}} S^*(k_f, k_s); \quad R_A = -\frac{k_2}{\sqrt{k_s^2 + k_2^2}} \alpha S^*(k_f, k_s) + \frac{k_s}{\sqrt{k_s^2 + k_2^2}} \alpha S_A^*(k_f, k_s, k_2)$$

$$R_M = -\frac{k_2}{\sqrt{k_s^2 + k_2^2}} \alpha M^*(k_s); \quad R_D = \sqrt{k_s^2 + k_2^2} \alpha D^*(k_f, k_s, k_2, B),$$

and $D'(k_f, k_s, k_2, B) = \int_0^{\infty} [i J_0(\lambda) B'_E(\lambda) + J_1(\lambda) B'_0(\lambda)] d\lambda \quad (6.48)$

- (4) TORTFG. This computes the higher order theoretical admittance via:

$$|A(k_1)|_{\alpha^2}^2 = \alpha^2 \frac{110}{3\pi} \cdot \frac{1}{\delta^2} \cdot \frac{(1 + k_1^{*2})^{1/6}}{(3 + 8k_1^{*2})} \iint_0^{\infty} \frac{\sin^2 k_3 a}{(k_3 a)^2} I(k_1, k_2, k_3, \frac{1}{2}) dk_2 dk_3$$

where $\delta = \frac{\Gamma(\frac{1}{2}) \Gamma(\frac{5}{6})}{\Gamma(\frac{1}{3})} \frac{c}{2} \frac{1}{L_1}$; $k_i^* = k_i / \delta$.

The 21 individual terms of I are listed in Appendix 7. The response functions, F_i , which are imbedded in the function, I , must be determined with an integration:

$$F_i = \int_0^{\infty} [i J_0(\lambda) E'_i + J_1(\lambda) O'_i] d\lambda + d_i. \quad (\text{refer to Appendix 6 for details})$$

Further notes on the programs. (refer to the subsequent listings)

- (1) ADMITL. The main program performs the single integration of equation (1.17). The subroutines (INTEQN2, COEFF, and CMAT) compute the response function, $G(k_1, k_3)$. (These were written by Graham (1970).)

Features of the numerical integration of the main program are:

- (a) Simpson's method is used.
- (b) Two different ranges of integration are dealt with separately. The first range is for k_3 near zero: here SS is the step size and the number of steps is IX (an odd number). Then the integration continues with step size, BS , until the change in the integral value is less than 1%.

As listed in this appendix, the program computes the admittance for 5 inputted values of k_1 . For each value of k_3 , $G(k_1, k_3)$ is determined for the 5 values of k_1 simultaneously. This is significantly more efficient than evaluating $G(k_1, k_3)$ separately for each of the five inputs.

Also as presented, the von Karman-type formula for $\overline{S}_{22}(k_1, k_3)$ is employed (refer 5.3.1).

The inputs to the program are:

$$AR = \frac{g}{2}, XL = L, CH = C(L, \text{ and } c \text{ in the same units})$$

and the five values of $WL = 2k_1$.

The outputs are the corresponding values of WL and $AD = |A(k)|^2$.

Further relationships between the program variables and variables of the present report are:

$SK = k_1^*$, $SU = k_3^*$, $WM = 2k_3$, $PHI = \pi \cdot \overline{S}_{22}(k_1, k_3)$ (Von Karma n)
and $G = G(k_1, k_3)$

Recommended values of the integration parameters are:

$$IX = 11 \text{ , } SS = 0.2 \text{ , } BS = 1.0 .$$

(2) TORT 2. The program evaluates \mathcal{R} ; in the main, by direct substitution into known analytical formulae. The exception is $D(k_1, k_3)$ which is evaluated by numerical integration (via equation (6.40)). Integrand values are provided by subroutine TORT 1 ; while library routines are called for the evaluation of the Bessel functions contained in the formulae.

The numerical integration employs Simpson's method. The step size, SL, and the number of steps, M , are inputs to the program. The other inputs are $W1 = k_1$ and $W2 = k_2$; while the outputs are the real and imaginary parts of \mathcal{R} , RR and RI respectively.

Also: $WL = \lambda$, $SK = S(k_1)$, $BR + i BI = D(k_1, k_2)$,

$$ER + i EI = S_A(k_1, k_2) \text{ , } CJO + i CJ1 = M(k_1) \text{ ,}$$

$$C + D + A = \widetilde{B}_E(\lambda) \text{ , } C - D = B_0(\lambda) .$$

(\widetilde{B}_E and B_0 are presented in detail in Appendix 4)

The integration parameters, SL and M , must be selected carefully to ensure an accurate estimate. In the present calculation, the values $SL = 0.2$ and $M = 99$ were found to be suitable (M must be odd)

(3) TORT 2I. This is a straightforward extension of TORT 2. The inputs are $W1 = k_s$, $W2 = k_2$, $WF = k_f$, $BD = B$, $AP = \alpha$ (radians), SL and M . The outputs are SER , SEI , SSR , SSI , RMR , RMI , DR and DI , where :

$$SER + i SEI = \mathcal{R}_s \text{ , } SSR + i SSI = \mathcal{R}_A \text{ ,}$$

$$RMR + i RMI = \mathcal{R}_M \text{ , } DR + i DI = \mathcal{R}_D \text{ .}$$

and HR and TR , where:

$$TR = |\mathcal{R}'| \text{ ; } HR = |\mathcal{R}''| .$$

Also:

$$C+D+A+B = B'_E(\lambda) \quad \text{and} \quad C-D+A-B = B'_O(\lambda)$$

where B'_E and B'_O are presented in Appendix 5.

(4) TORTFG. The integrand in equation (7.3) is $A(I, J, K)$, and the double numerical integration of it with respect to k_2 and k_3 is done in the main program.

Subroutine TORT 5 evaluates the response functions, F_i , by numerical integration with respect to λ . It is essentially the three dimensional version of program TORT 2 above. The outputs of the subroutine are $FX = F_1$, $FY = F_2$, and $FZ = F_3$. Also: $S(I) = G_M(k_1, k_3)$, $UA + UB = U_E(\lambda)$, $UA - UB = U_O(\lambda)$, etc (refer to Appendix 6), $A = A$, $B = B$, and $D1 = d_1(\lambda)$, etc.

The main program has been written to deal with three values of $XL = L_1/C$ simultaneously. (The lengthy part of the computation, the F_i evaluation, does not depend on L_1/C). For k_2 , the integration step size and number of steps are SK2 and M2; while, for k_3 , they are SK3 and M3. Again these must be chosen with care. In the present calculation it was found necessary to vary these parameters for different values of k_1 . Two examples are:

For $k_1 = 0.1$; SK2 = 0.35, M2 = 21, SK3 = 0.2, M3 = 13.

For $k_1 = 5.0$; SK2 = 1.0, M2 = 21, SK3 = 0.5, M3 = 13.

The integration parameters for the λ integration (subroutine TORT 5), SL and M, were optimized at 0.2 and 49 respectively. These values were written into the program.

Thus, the inputs to the program are $WK1 = k_1$, the three values of $XL = L_1/C$, SK2, SK3, M2, and M3. The outputs are the admittances, AD, corresponding to the three XL values; $AD = |A(k_i)|^2 / \alpha^2$.

Also: $WK2 = k_2$, $WK3 = k_3$, $SP = G_M(k_1, k_3)$, $SE = G_{MA}(k_1, k_2, k_3)$,
 $TM = M(k_1)$, $XF = F_1$, $YF = F_2$, $ZF = F_3$,
 $WW1 = k_1^*$, $WW2 = k_2^*$, $WW3 = k_3^*$,

$$\delta = 1 / (2.6782 \cdot XL) ; \quad \frac{110}{3\pi} \cdot \frac{1}{\delta^2} = 20.9297 \cdot (XL)^2.$$

As the program is listed, the value for the aspect ratio, AR = a = 1.3333, has been written in; but, with a small adjustment, AR can be made an input variable. (Note that M2 and M3 are required to be odd numbers).

The listings

1. ADMITL

```

PROGRAM ADMITL (INPUT,OUTPUT)
DIMENSION V1(10,31),V2(10,100),WL(10),A1(10),A2(10),AD(10),YA(10),
1S(52),J(52),A(21,22)
COMPLEX A
COMMON/A/S,C,A,CML
READ 10,AR,XL,CH,IX,SS,BS
10 FORMAT(3F0.4,12,2F4.2)
11 READ 12,(WL(J),J=1,5)
12 FORMAT(F0.3)
WM=0.001
IF=0
DO 30 MS=1,IX
CML=0.0
J0=20 LS=1,5
SK=2.6789+*WL(LS)*XL/(CH*1.77245*1.2*0.94056)
SU=2.6789+*WL(LS)*XL/(CH*1.77245*1.2*0.94056*((1.+SK**2)**0.5))
PH1=0.*XL*2.6789**2*(SK**2+SU**2+SK**2*SU**2)/(3.*(1.2*0.94056)**
12*(1.+SK**2)**0.5*(1.+SU**2)**(7.0/3.0)*(3.+8.*SK**2))
WLL=WL(LS)
CALL INTLN2(WLL,M1,6)
20 V1(LS,BS)=6**2*PH1*(SIN(WM*AR))**2/(WM*AR)**2
30 WM=WM+SS
WN=WN-SS
DO 35 LS=1,5
ODD=0.0
EVEN=0.0
N1=IX-1
DO 31 I=2,N1,2
31 EVEN=EVEN+V1(LS,I)
N2=IX-2
DO 32 I=3,N2,2

32 ODD=ODD+V1(LS,I)
A1(LS)=SS/3.*(V1(LS,1)+4.*EVEN+2.*ODD+V1(LS,IX))*2./(3.14159*CH)
35 V2(LS,1)=V1(LS,IX)
MSS=2
MJ=1
40 WM=WM+BS
CML=0.0
DO 50 LS=1,5
SK=2.6789+*WL(LS)*XL/(CH*1.77245*1.2*0.94056)
SU=2.6789+*WL(LS)*XL/(CH*1.77245*1.2*0.94056*((1.+SK**2)**0.5))
PH1=0.*XL*2.6789**2*(SK**2+SU**2+SK**2*SU**2)/(3.*(1.2*0.94056)**
12*(1.+SK**2)**0.5*(1.+SU**2)**(7.0/3.0)*(3.+8.*SK**2))
WLL=WL(LS)
CALL INTLN2(WLL,M1,6)
50 V2(LS,MSS)=6**2*PH1*(SIN(WM*AR))**2/(WM*AR)**2
IF (MJ.EQ.1) GO TO 60
DO 57 LS=1,5
ODD=0.0
EVEN=0.0
N1=MSS-1
DO 51 I=2,N1,2
51 EVEN=EVEN+V2(LS,I)
IF (MSS.EQ.3) GO TO 53
N2=MSS-2
DO 52 I=3,N2,2
52 ODD=ODD+V2(LS,I)
53 A2(LS)=SS/3.*(V2(LS,1)+4.*EVEN+2.*ODD+V2(LS,MSS))*2./(3.14159*CH)
AD(LS)=A1(LS)+A2(LS)
IF (MSS.GT.3) GO TO 55
IF (ABS((AD(LS)-A1(LS))/AD(LS)).LE.0.01) IP=IP+1
GO TO 56
55 IF (ABS((AD(LS)-YA(LS))/AD(LS)).LE.0.01) IP=IP+1

```

```

50 YA(LS)=A0(LS)
57 CONTINUE
   IF (IF.EQ.5) GO TO 73
   IF=0
   NJ=1
   GO TO 61
60 NJ=NJ+1
61 MSS=MSS+1
   GO TO 49
70 NF=MSS+MS-1
   PRINT 75,NF
75 FORMAT(1X,I3)
   DO 80 LS=1,5
   PRINT 60,NL(LS),A0(LS)
80 FORMAT(1X,F6.3,8X,E12.5)
90 CONTINUE
   STOP
   END

```

```

SUBROUTINE INTEQR2(CL,CM,RL2)
  DIMENSION S(52),C(52),A(21,22),B4(27),B5(27),AX(2,27),AS(27),
  I(21,21),SM(2,3),SB(2),RJ(1,52),A5(27),DT(51),AI(27),IT(21,3)
  2,Q(1)
  COMPLEX AI,S0,AS,AT,ZT,SN,Q,TT,T,SM,S3,CL1,CL0,RT,B0,A,B5,A5,B,RF,
  1R5
  COMMON/A/S,C,A,CM
  COMMON/S3/N,N1,I
  AI=(0.0,1.0)
  RL=0.5931+7
  P=3.141593
  B4(1)=2*R
  B4(2)=0.5-RL
  N=27
  NC=N+2
  N1=N+1
  DO 16 K=3,N2
10 B4(K)=-2.0/(K*(K-1)*(K-2))
  INT=0

```

- NAME - INT SAME AS STANDARD FUNCTION AND REMOVES FUNCTION FROM USE

```

CN=CM/2
CP=EXP(CM)
B0=-ALOG(CN/2)-0.577216
IF(CM.EQ.CML) GO TO 12
CALL COEFF(S,C,A,CN,P)

```

C
C
C CALCULATE COEFFICIENTS OF BK/H0 (=A5(J)) AND BK/H1 (=B5(J)) FOR H

```

DO 13 J=1,N1
  B5(J)=A(1,J)/2
DO 14 K=2,N1
14 B5(J)=B5(J)+A(K,J)
13 B5(N+2)=(0.0,0.0)
  B=(0.0,0.0)
DO 15 J=2,N1
  A5(J)=CN*(B5(J-1)-B5(J+1))/(2*(J-1))
15 B=B+A5(J)
  A5(1)=2*(B0-B)
  A5(N+2)=0
12 CK=CL/2
  DT(1)=1
22 Z=CL/2
  I=1
25 Q(I)=COS(Z)+AI*SIN(Z)
  CALL BESJ(Z,0,K2,.001,IER)
  RJ(1,52)=0
  RJ(I,51)=1.0 E-10
DO 41 J=1,50
  JJ=51-J
  RJ(1,JJ)=2*JJ*RJ(1,JJ+1)/Z -RJ(1,JJ+2)
  IF(ABS(RJ(1,JJ))-1.0 E10)41,27,27
27 J2=J+2
DO 20 L=1,J2
  JK=53-L
20 RJ(1,JK)=RJ(1,JK)*1.0 E-15
41 DT(J+1)=0
  RY=RJ(1,1)
DO 28 J=1,52
28 RJ(I,J)=RJ(1,J)*RZ/RY

```

C
C
C CALCULATE COEFFICIENTS OF SINH AND COSH OR SIN AND COS.

```

DO 61 K=1,N1
  A(K,N+2)=0

```

```

1 AX(1,K)=-1/2*(C/CN-1/(C*C)))*(-1)**K/(4*N+2)
AX(2,K)=1/(2*N+1)-(C+1/C)*(-1)**K/(4*N+2)
RS=2**N+1
DO 52 J=2,N3
IR=(K-1)*(J-1)/(2*N+1)
RS=(-1)**I*RS*(C*(K-1)*(J-1)-IR*(2*N+1)+1)
J=LAP(CN*(1-C(J)))
AX(1,K)=AX(1,K)+(C/CN-1/(C*C))*RS/(2*N+1)
52 AX(2,K)=AX(2,K)+(C+1/C)*RS/(2*N+1)
51 CONTINUE
AX(1,N+2)=0
AX(2,N+2)=0
R1=C/CN
C1=R1**2
C2=1+C1
C3=C2/C1
RS=SQRT(C2)
JS=-1
S4=JS*R1*ALOG(R1-RS*JS)/RS+AI*R1*P/(2*RS)
DO 53 J=1,N2
53 AT(J)=(0.0,0.0)
AS(1)=(0.0,0.0)
33 ZT=AS(1)
SN=(0.0,0.0)
DO 57 J=1,N2
57 AS(J)=AI*CL/2*(AT(J)-34(J))+A5(J)+2*DT(J)*SQ
IF(CABS(AS(1))-1.0E25)5,6,6
6 PRINT 52,CK,CN
GO TO 18
5 IF(CABS(AS(1)-ZT)-0.002*CABS(ZT))56,56,30
30 DO 51 J=2,N1
AT(J)=(AS(J-1)-AS(J+1))/(2*(J-1))
51 SN=SN+AT(J)
32 AI(1)=-2*SN
INI=INI+1
GO TO 33
56 IT(1,1)=P*(Q(1)*RJ(1,1)+AI*Q(1)*RJ(1,2))
IT(2,1)=-P*Q(1)*(RJ(1,1)+RJ(1,3))/2
IT(1,2)=C1*C3*(AS(1)+AS(2))/2+JS*(A5(1)+A5(2))/(C1*2)+1+RL)*AI
IT(2,2)=-CL*(C3*(AS(1)-AS(3))/4+JS*(A5(1)-A5(3))/(C1*4)-0.25+RL/2)
1*AI

DO 35 J=1,N1
T(1,J)=-CN*(A(J,1)+A(J,2))*S(J)/2+DT(J)
35 T(2,J)=CN*(A(J,1)-A(J,3))*S(J)/4+JT(1+IABS(2-J))
IT(1,3)=JS*CN**2*((A5(1)+A5(2))/2+1+RL)*4
IT(2,3)=CN**2*(A5(1)-A5(3)-1+RL*2)*(-JS)
DO 36 J=3,N1
IT(J,3)=CN**2*(A5(J-1)-A5(J+1)+4.0/((J-2)*J))*(-JS)
IT(J,1)=F*AI**J*Q(1)*(RJ(1,J-1)+RJ(1,J+1))/2
IT(J,2)=-CL*(C3*(AS(J-1)-AS(J+1))/4+JS*(A5(J-1)-A5(J+1))/(C1*4)+1.
10/((J-2)*J))*AI
DO 37 I=1,N1
A(I,N+2)=0
37 T(I,1)=CN*(A(I,J-1)-A(I,J+1))*S(I)/4+DT(1+IABS(J-I))
36 CONTINUE
CALL CMAT(TT,I,N+1,3)
DO 39 I=1,2
DO 40 K=1,3
SM(I,K)=0.125*AX(I,1)*TT(1,K)
DO 45 J=2,N1
45 SM(I,K)=SM(I,K)+AX(I,J)*TT(J,K)/4
43 CONTINUE
39 RT=1-SM(1,3)
DO 46 J=1,2
46 SB(J)=RT*SM(2,J)+SM(2,3)*SM(1,J)+(1-J)*RT/2
RF=-Sb(1)/Sb(2)
RG=(SM(1,1)+RF*SM(1,2))/RT
CL1=-AI*CL*RG+RF
3 CLJ=Q(1)*CUNJG(CL1)*2/P
RL2=CABS(SL0)
52 FURNAL(1HJ,2F12.2,' ITERATION FAILURE AT 5.')
18 GBL=CN
RETURN
END

SUBROUTINE COEFF(S,C,A,CN,P)
DIMENSION S(52),C(52),I(21,21),B2(21,21),A(21,22),B(2)
COMPLEX I, B2,A,A1
COMMON/S/N,N1,I

```

CALCULATE COEFFICIENTS OF DOUBLE CHEBYCHEV SERIES FOR DELTAK/H(2)1.

AI=(0.0,1.0)

```

      B(2)=0
      RZ=1.0
      DO 3 J=1,N1
      S(J)=1
3     C(J)=COS(P*(J-1)/(2*N+1))
      DO 1 J=1,N1
      JN=N+2-J
      KN=J+N+1
      C(KN)=-C(JN)
      S(KN)=1
      S(1)=0.5
      DO 2 K=1,J
      IF (J-K) 5,5,5
6     T(J,K)=(0.0,0.0)
      GO TO 7
5     CJK=(C(J)-C(K))*CN
20    CALL BESK (-CJK,1,S(1),IER)
22    T(J,K)=(-S(1))*RZ-1/CON+AI*(-S(2))*P/2
7     CJK=(C(J)+C(K))*CN
25    CALL BESK (CJK,1,S(1),IER)
29    B2(J,K)=S(1)*RZ-1/CON+AI*B(2)*P/2
      B2(K,J)=B2(J,K)
2     T(K,J)=-T(J,K)
1     CONTINUE
      DO 8 IK=1,N1

```

```

      DO 9 IS=1,IK
      A(IK,IS)=(0.0,0.0)
      IF (IK+IS-2*((IK+IS)/2)) 12,9,12
12    DO 10 J=1,N1
      JN=(IK-1)*(J-1)
      DO 11 K=1,N1
      JN=(IS-1)*(K-1)
      JRS=JN/(2*N+1)+JN/(2*N+1)+2
11    A(IK,IS)=A(IK,IS)+S(J)*S(K)*(T(J,K)-(-1)**IS*B2(J,K))*(-1)**JRS
1     C(JN+1-(2*N+1)*(JN/(2*N+1)))*C(JN+1-(2*N+1)*(JN/(2*N+1)))
10    CONTINUE
      A(IK,IS)=8*A(IK,IS)/(2*N+1)**2
9     A(IS,IK)=-A(IK,IS)
8     CONTINUE
      RETURN
      END

```

SUBROUTINE GNAT (TT,T,N,M)

```

C
C
C SOLVES SET OF COMPLEX LINEAR EQUATIONS WITH MANY RIGHT HAND SIDES
C TT=MATRIX OF RHS. (M*M)
C T=MATRIX OF COEFFS. (N*N)
C REAL PART OF T MUST BE NONSINGULAR
C ANSWER IN TT WHICH IS DESTROYED
C SUBROUTINE REQUIRES SSPBIN ROUTINES
C
      DIMENSION T(21,21), TT(21,3), TTR(21,3), TTI(21,3), TR(21,21), TI(21,21)
      W(21,21), X(21,21), Y(21,21), Z(21,3), K(21), L(21)
      COMPLEX AI,T,TT
      AI=(0.0,1.0)
      DO 1 I=1,N
      DO 2 J=1,N
1     TTR(I,J)=REAL(TT(I,J))
2     TTI(I,J)=AIMAG(TT(I,J))
      DO 1 J=1,N
      TR(I,J)=REAL(T(I,J))
      TI(I,J)=AIMAG(T(I,J))
1     W(I,J)=TR(I,J)
      CALL MIMV (W,N,N,D,K,L)
      CALL GMPRO (T1,N,A,L,N,N)
      CALL GMPRO (X,TTI,Z,N,N,M)
      DO 3 I=1,N
      DO 3 J=1,N
3     TTR(I,J)=TTR(I,J)+Z(I,J)
      CALL GMPRO (X,TTI,Y,N,N,N)
      DO 4 I=1,N
      DO 4 J=1,N
4     TR(I,J)=TR(I,J)+Y(I,J)
      CALL BELG (TTR,TR,N,N,1.0E-7,IES)
      CALL GMPRO (W,TTI,Z,N,N,M)
      CALL GMPRO (W,TTI,X,L,N,N)
      CALL GMPRO (X,TTR,TTI,N,N,M)
      DO 5 I=1,N
      DO 5 J=1,N
5     TTI(I,J)=TTR(I,J)+AI*(Z(I,J)-TTI(I,J))
      RETURN
      END

```

2. TORT 2

```

PROGRAM TORT2(INPUT,OUTPUT)
DIMENSION T(200),U(200)
COMPLEX DD,SK
READ 10,W1,W2,SL,M
10  FORMAT(3F6.4,I3)
    WL=.001
    WX=W1
    CALL BESJ(W1,0,CJ0,.000001,IER)
    CALL BESJ(W1,1,CJ1,.000001,IER)
    CALL BESY(W1,0,CY0,IER)
    CALL BESY(W1,1,CY1,IER)
    DO 20 J=1,M
20  CALL TORT1(WX,W2,WL,CJ0,CJ1,CY0,CY1,T(J),U(J),SK)
    WL=WL+SL
    N=M-1
    K=M-2
    ODD=0.0
    EVEN=0.0
    DO 30 J=2,N,2
30  EVEN=EVEN+T(J)
    DO 40 J=3,K,2
40  ODD=ODD+T(J)
    AR=SL/3.*(T(1)+4.*EVEN+2.*ODD+T(M))
    ODD=0.0
    EVEN=0.0
    DO 50 J=2,N,2
50  EVEN=EVEN+U(J)
    DO 60 J=3,K,2
60  ODD=ODD+U(J)
    AI=-SL/3.*(U(1)+4.*EVEN+2.*ODD+U(M))
    DD=SK*3.14159*W1*W2/(2.*(W1**2+W2**2))
    DR=REAL(DD)
    DI=AIMAG(DD)
    BR=AR+DR
    BI=AI-DI
    P=SQRT(W1**2+W2**2)
    Q=-W2/SQRT(W1**2+W2**2)
    T=W1/SQRT(W1**2+W2**2)
    SR=REAL(SK)
    SI=AIMAG(SK)
    EE=CJ1+CY0
    FE=CJ0-CY1
    CALL BESJ(W1,2,CJ2,.000001,IER)
    CE=(CJ2-CJ0)/2.
    GE=CJ1*CJ1-CE*CY1
    HE=CJ1*CY1+CE*CJ1
    ER=W2*(EE*GE-FE*HE)/(EE**2+FE**2)
    EI=W2*((CE+CJ1/W1)-(FE*GE+EE*HE)/(EE**2+FE**2))
    RR=P*BR+Q*CJ0+Q*SR+T*ER
    RI=P*BI-Q*CJ1-Q*SI-T*EI
70  PRINT 70,W1,W2,RR,RI
    FORMAT(2(2X,F10.6))
    STOP
END
SUBROUTINE TORT1(RK1,RK2,RL,BJ0,BJ1,BY0,BY1,V,W,SA)
DIMENSION S(3),B0(3),B1(3),R(3)
COMPLEX S,x,C,D,A,SA
R(1)=RK1+RL
R(2)=RK1-RL
R(3)=RK1
WLL=RL
R1=R(1)

```

```

R2=ARS(R(2))
CALL BESJ(R1,0,B0(1),.000001,IER)
CALL BESJ(R1,1,B1(1),.000001,IER)
CALL BESJ(WLL,0,BL0,.000001,IER)
CALL BESJ(WLL,1,BL1,.000001,IER)
B0(3)=RJO
B1(3)=RJI
E=BJ1+BY0
F=BJ0-BY1
IF(RL.LE.RK1) GO TO 20
CALL BESJ(R2,0,B0(2),.000001,IER)
CALL BESJ(R2,1,B1(2),.000001,IER)
IF(R(2).LT.0.0) B1(2)=-B1(2)
J=1
GO TO 30
20  S(2)=(0.0,0.0)
    J=2
30  DO 40 I=1,3,J
    G=BJ1*B0(I)-B1(I)*BY1
    H=B0(I)*BY1+B1(I)*BJ1
40  S(I)=(E*G-F*H)/(E**2+F**2)+(0.0,1.0)*(RK1*B1(I)/R(I)-(F*G+E*H)/(E*
    I**2+F**2))
    C=S(1)*R(1)*RK2/(RL*((RK1+2.*RL)**2+RK2**2))
    D=S(2)*R(2)*RK2/(RL*((RK1-2.*RL)**2+RK2**2))
    A=-S(3)*RK1*RK2/(RL*(RK1**2+RK2**2))
    X=(0.0,1.0)*BL0*(C+D+A)+BL1*(C-D)
    V=REAL(X)
    W=AIMAG(X)
    SA=S(3)
    RETURN
    END

```

3. TORT 2I

```

PROGRAM TORT2I(INPUT,OUTPUT)
DIMENSION T(500),U(500),G0(3),G1(3),H(3),SA(3)
COMPLEX SA,SK
10  READ 10,W1,W2,WF,BD,AP,SL,M
    FORMAT(6F6.4,I3)
    WL=.001
    WX=W1
    CALL BESJ(W1,0,CJ0,.000001,IER)
    CALL BESJ(W1,1,CJ1,.000001,IER)
    CALL BESJ(W1,2,CJ2,.000001,IER)
    CALL BESJ(WF,0,FJ0,.000001,IER)
    CALL BESJ(WF,1,FJ1,.000001,IER)
    CALL BESY(WF,0,FY0,IER)
    CALL BESY(WF,1,FY1,IER)
    AE=FJ1+FY0
    AF=FJ0-FY1
    AD=AE**2+AF**2
    G0(1)=FJ0
    G1(1)=FJ1
    G0(2)=CJ0
    G1(2)=CJ1
    G0(3)=CJ1
    G1(3)=(CJ2-CJ0)/2.
    H(1)=FJ1
    H(2)=CJ1*WF/W1
    H(3)=(G1(3)+CJ1/W1)*WF/W1
    DO 15 I=1,3
    AG=FJ1*G0(I)-G1(I)*FY1
    AH=G0(I)*FY1+G1(I)*FJ1
15  SA(I)=(AE*AG-AF*AH)/AD+(0.0,1.0)*(H(I)-(AF*AG+AE*AH)/AD)

```

```

SK=SA(1)
DO 20 J=1,M
CALL TORT1(WX,W2,WF,WL,FJ0,FJ1,FY0,FY1,T(J),U(J),BD,SK)
20 WL=WL+SL
N=N-1
K=M-2
ODD=0.0
EVEN=0.0
DO 30 J=2,N,2
30 EVEN=EVEN+T(J)
DO 40 J=3,K,2
40 ODD=ODD+T(J)
AR=SL/3.*(T(1)+4.*EVEN+2.*ODD+T(M))
ODD=0.0
EVEN=0.0
DO 50 J=2,N,2
50 EVEN=EVEN+T(J)
DO 60 J=3,K,2
60 ODD=ODD+U(J)
AI=-SL/3.*(U(1)+4.*EVEN+2.*ODD+U(M))
P=SQRT(W1**2+W2**2)
Q=-W2/SQRT(W1**2+W2**2)
T=W1/SQRT(W1**2+W2**2)
SR=REAL(SA(2))
SI=AIMAG(SA(2))
ER=W2*(REAL(SA(3)))
EI=W2*(AIMAG(SA(3)))
SER=T*SR
SEI=-T*SI
SSR=(Q*SR+T*ER)*AP

```

```

SSI=-(Q*SI+T*EI)*AP
RMR=Q*CJ0*AP
RMI=-Q*CJ1*AP
DR=P*AR*AP
DI=P*AI*AP
ETR=SER+SSR+RMR
ETI=SEI+SSI+RMI
RR=ETR+DR
RI=ETI+DI
TR=SQRT(RR**2+RI**2)
HR=SQRT(ETR**2+ETI**2)
70 PRINT 70,W1,W2,SER,SEI,SSR,SSI,RMR,RMI,DR,DI
FORMAT(2(2X,F10.6))
PRINT 71,HR,TR
71 FORMAT(5X,F12.5)
STOP
END
SUBROUTINE TORT1(RK1,RK2,RKF,RL,BJ0,BJ1,BY0,BY1,V,W,DS,SF)
DIMENSION S(2),B0(2),B1(2),R(2)
COMPLEX S,X,C,D,A,B,E1,E2,SF
RN=RL-RKF+RK1
RM=-(-RL-RKF+RK1)
R(1)=RK1+RL
R(2)=RK1-RL
WLL=RL
R1=R(1)
R2=ABS(R(2))
CALL BESJ(R1,0,B0(1),.000001,IER)
CALL BESJ(R1,1,B1(1),.000001,IER)
CALL BESJ(WLL,0,BL0,.000001,IER)
CALL BESJ(WLL,1,BL1,.000001,IER)

```

```

E=BJ1+RY0
F=BJ0-RY1
IF(RL.LE.RK1) GO TO 20
CALL BESJ(R2,0,R0(2),.000001,IER)
CALL BESJ(R2,1,R1(2),.000001,IER)
IF(R(2).LT.0.0) B1(2)=-B1(2)
J=2
GO TO 30
20 S(2)=(0.0,0.0)
J=1
30 DO 40 I=1,J
G=RJ1*R0(I)-B1(I)*BY1
H=R0(I)*BY1+B1(I)*BJ1
40 S(I)=(E*G-F*H)/(E**2+F**2)+(0.0,1.0)*(RKF*B1(I)/R(I)-(F*G+E*H)/(E*
I**2+F**2))
C=S(1)*R(1)*RK2/(RN*((RK1+2.*RL)**2+RK2**2))
D=S(2)*R(2)*RK2/(RN*((RK1-2.*RL)**2+RK2**2))
E1=CMPLX(COS(RN*DS),SIN(RN*DS))
E2=CMPLX(COS(RM*DS),-SIN(RM*DS))
A=-SF*E1*(RKF+RK1+RL)*RK2/(2.*RN*((RKF+RL)**2+RK2**2))
B=-SF*E2*RK2/(2.*((RKF+RL)**2+RK2**2))
X=(0.0,1.0)*RL0*(C+D+A+B)+BL1*(C-D+A-B)
V=REAL(X)
W=AIMAG(X)
RETURN
END

```

4. TORTFG

```

PROGRAM TORTFG(INPUT,OUTPUT)
DIMENSION A(25,25,3),B(25,3),XL(3),AD(3)
COMPLEX SP,TM,SPC,TMC,SE,XF,YF,ZF,XFC,YFC,ZFC,RN,L
10 READ 10,WK1,XL(1),XL(2),XL(3),SK2,SK3,M2,M3
FORMAT(6F6.4,2I2)
PRINT 11,WK1
11 FORMAT(2X,F6.4)
A=1.3333
CALL BESJ(WK1,1,EJ0,.000001,IER)
CALL BESJ(WK1,1,EJ1,.000001,IER)
CALL BESJ(WK1,2,EJ2,.000001,IER)
CALL BESY(WK1,0,EY0,IER)
CALL BESY(WK1,1,EY1,IER)
CE=(EJ2-EJ0)/2.
TM=EJ1+(0.0,1.0)*TJ1
TMC=CONJG(TM)
TMA=(CABS(TM))**2
WK2=0.001
DO 50 I=1,M2
WK3=0.001
DO 20 J=1,M3
TY=SQR(1-WK1**2+WK3**2)
RN=(WK3**2/(WK1+TY))*(1.-(0.0,1.0)*2./3.14159*ALOG((WK1+TY)/WK3))
L=((1.+RN)*EJ1+(0.0,-1.0)*EY1)/((1.+RN)*(EJ1+(0.0,1.0)*EJ0)+EY0+(0
1.0,-1.0)*EY1)
SP=L*(EJ2+(0.0,-1.0)*EJ1)+(0.0,1.0)*EJ1
SE=WK2*(L*(EJ1+(0.0,-1.0)*CE)+(0.0,1.0)*(CE+EJ1/WK1))
SPA=(CABS(SP))**2
SPC=CONJG(SP)
SMA=REAL(SP*TMC)

SEA=(CABS(SE))**2
E1A=REAL(SE*TMC)
E2A=REAL(SE*SPC)
CALL TORTB(WK1,WK2,WK3,EJ2,EJ1,EY0,EY1,L,XF,YF,ZF)
XFC=CONJG(XF)
YFC=CONJG(YF)
ZFC=CONJG(ZF)
XFA=(CABS(XF))**2
YFA=(CABS(YF))**2
ZFA=(CABS(ZF))**2
SXA=REAL(SP*XFC)
XMA=REAL(XF*TMC)
EYA=REAL(SE*YFC)
EXA=REAL(SE*XFC)
YSA=REAL(YF*SPC)

```



```

YXA=REAL(YF*XF/C)
YNA=REAL(YF*TC/C)
EZA=REAL(CE*ZFC)
YZA=REAL(YF*ZFC)
SZA=REAL(SP*ZFC)
XZA=REAL(XF*ZFC)
ZMA=REAL(TM*ZFC)
DO 14 K=1,3
  WW1=2.6782*XL(K)*WK1
  WW2=2.6782*XL(K)*WK2
  WW3=2.6782*XL(K)*WK3
  CN=(1.+WW1**2+WW2**2+WW3**2)**(17./6.)
  TF=(SIN(WK3*AK)/(WK3*AK))**2
  A1=(SFA+XFA+TMA+2.*SMA+2.*SXA+2.*XMA)*TF*(WW2**2+WW3**2)/CN
  A2=(YFA+SFA+2.*LYA)*TF*(WW1**2+WW3**2)/CN
  A3=ZFA*TF*(WW1**2+WW2**2)/CN
  A4=(2SA+EXA+EMA+YSA+YXA+YMA)*TF*(-WW1*WW2)/CN
  A5=(EZA+YZA)*TF*(-WW2*WW3)/CN
  A6=(SZA+XZA+ZMA)*TF*(-WW1*WW3)/CN
14  A(I,J,K)=A1+A2+A3+2.*A4+2.*A5+2.*A6
20  WK3=WK3+SK3
  DO 48 K=1,3
  N3=M3-1
  K3=M3-2
  ODD=0.0
  EVEN=0.0
  DO 30 J=2,N3,2
  EVEN=EVEN+A(I,J,K)
  DO 40 J=3,K3,2
  ODD=ODD+A(I,J,K)
  B(I,K)=2.*SK3/3.*(A(I,1,K)+4.*EVEN+2.*ODD+A(I,M3,K))
  WK2=WK2+SK2
  DO 95 K=1,3
  N2=M2-1
  K2=M2-2
  EVEN=0.0
  ODD=0.0
  DO 60 I=2,N2,2
  EVEN=EVEN+B(I,K)
  DO 70 I=3,K2,2
  ODD=ODD+B(I,K)
  RA=2.*SK2/3.*(B(1,K)+4.*EVEN+2.*ODD+B(M2,K))
  WW1=2.6782*XL(K)*WK1
  F=((1.+WW1**2)**(11./6.))/(3.+8.*(WW1**2))
  AD(K)=20.9297*(XL(K)**2)*F*RA
  PRINT 80, XL(K), AD(K)
30  FORMAT(2X,F6.4,3X,E12.5)
95  CONTINUE
  STOP
  END

```

```

SUBROUTINE TORT5(W1,W2,W3,CJ0,CJ1,CY0,CY1,AL,FX,FY,FZ)
  DIMENSION T(6,16),F(6)
  COMPLEX SK, J1, O2, O3, FX, FY, FZ, SX, SY, SZ, AL
  WL=0.261
  SL=0.2
  M=49
  DO 20 J=1,M
  CALL TORT1(W1,W2,W3,WL,CJ0,CJ1,CY0,CY1,T(1,J),T(2,J),T(3,J),T(4,J),
1  T(5,J),T(6,J),SK,AL)
20  WL=WL+SL
  DO 30 I=1,6
  N=M-1
  K=M-2
  ODD=0.0
  EVEN=0.0
  DO 30 J=2,N,2
  EVEN=EVEN+T(I,J)
  DO 40 J=3,K,2
  ODD=ODD+T(I,J)
  F(I)=SL/3.*(T(I,1)+4.*EVEN+2.*ODD+T(I,M))
  SX=CMPLX(F(1),F(2))
  SY=CMPLX(F(3),F(4))
  SZ=CMPLX(F(5),F(6))
  C7=SQRT(W3**2+W1**2)
  C8=W1**2+W2**2+W3**2
  D1=-SK*(W1**2)*(W2**2)*3.14159/(2.*C7*C8)
  D2=SK*W1*W2*C7*3.14159/(2.*C8)
  D3=-SK*W1*(W2**2)*W3*3.14159/(2.*C7*C8)
  FX=SX+D1
  FY=SY+D2
  FZ=SZ+D3
  RETURN
  END

```

```

SUBROUTINE TORT1(RK1,RK2,RK3,RL,BJ0,BJ1,BY0,BY1,XR,XI,YR,YI,ZR,ZI,
1SA,BL)
DIMENSION S(3),B0(3),B1(3),R(3)
COMPLEX S,UA,UB,VA,VB,WA,WB,A,B,X,Y,Z,SA,B-
R(1)=RK1+RL
R(2)=RK1-RL
R(3)=RK1
WLL=RL
R1=R(1)
R2=ABS(R(2))
CALL BESJ(R1,0,B0(1),.000001,IER)
CALL BESJ(R1,1,B1(1),.000001,IER)
CALL BESJ(R2,0,B0(2),.000001,IER)
CALL BESJ(R2,1,B1(2),.000001,IER)
IF(R(2).LT.0.0) B1(2)=-B1(2)
B0(3)=BJ0
B1(3)=BJ1
CALL BESJ(WLL,0,B0(3),.000001,IER)
CALL BESJ(WLL,1,B1(3),.000001,IER)
DO 40 I=1,3
S(I)=BL*(B0(I)+(0.0,-1.0)*B1(I))+(0.0,1.0)*RK1*B1(I)/R(I)
C1=SQRT(RK3**2+(RK1+RL)**2)
C2=SQRT(RK3**2+(RK1-RL)**2)
C3=2.*C1*((C1+RL)**2+RK2**2)
C4=2.*C2*((C2+RL)**2+RK2**2)
C5=RK1+RL
C6=RK1-RL
UA=S(1)*RK2*RK3*(C1+RK1)/(RL*C3)
UB=S(2)*RK2*RK3*(C2-RK1)/(RL*C4)
VA=-S(1)*RK3*(C1+RL)/C3
VB=S(2)*RK3*(C2+RL)/C4
WA=-S(1)*C5*RK2*(C1+C5)/(RL*C3)
WB=-S(2)*C6*RK2*(C2-C6)/(RL*C4)
A=-S(3)*RK2*RK3/(RL*(RK1**2+RK2**2+RK3**2))
B=S(3)*RK1*RK2/(RL*(RK1**2+RK2**2+RK3**2))
X=(0.0,1.0)*BL0*(-RK3*(VA+VB)+RK2*(WA+WB)+RK2*B)+BL1*(-RK3*(VA-VB)
1+RK2*(WA-WB))
Y=(0.0,1.0)*BL0*(RK3*(UA+UB)-RK1*(WA+WB)+RK3*A-RK1*B)+BL1*(RK3*(UA
1-UB)-RK1*(WA-WB))
Z=(0.0,1.0)*BL0*(-RK2*(JA+UB)+RK1*(VA+VB)-RK2*A)+BL1*(-RK2*(UA-UB)
1+RK1*(VA-VB))
XR=REAL(X)
XI=AIMAG(X)
YR=REAL(Y)
YI=AIMAG(Y)
ZR=REAL(Z)
ZI=AIMAG(Z)
SA=S(3)
RETURN
END

```